A dynamic Turing model of digit patterning

A Turing mechanism modulated by Positional Information underlies digit specification

Luciano Marcon

TESI DOCTORAL UPF / ANY 2013

DIRECTOR DE LA TESI
James Sharpe - Departament of Systems Biology
EMBL/CRG

This thesis is dedicated to my family and to my girlfriend Jelena

"The pressure of occupation and the incessant streams of impressions pouring into our consciousness trough all the gateway of knowledge make modern existence hazardous in many ways."

Nikola Tesla

Acknowledgments

Thank to all the fantastic people that shared their science and their feelings with me during these years, you have allowed me to see life in all his complexity. At times this has been quite tough but thanks to you I can see every day a new part of reality. I would like to thank in particular my supervisor James, who has not only been my mentor during these years but has also been a real friend. I will never be grateful enough to him for hiring Jelena, I love her since the first moment. I would like to thank my family for teaching me to never give up my ideals. They dedicated their whole life to fight for my right to be safe and free. This thesis also goes to those people that are still fighting. I hope that you will never give up.

Abstract

The specification of the vertebrate limb skeleton is a classical model to study pattern formation during development. Two different theories have been proposed to explain this process: the Turing mechanism and the Positional Information model. This thesis uses computational modeling to explores to which extent these two theories can be combined to explain digit patterning. The main result of this work is a computational model of digit patterning that suggests that a Turing mechanism modulated by Hox genes and Fgf-signaling underlies digit specification. By comparing simulations and experimental data we show that the Turing mechanism is implemented by Bmps, Sox9 and Wnts. The model shows that a combination of Positional Information and Turing can implement an extremely reliable patterning mechanism and suggests that Fgf-singling coordinates patterning and growth.

Resum

L'especificació de l'esquelet de las extremitats dels vertebrats és un model clàssic per estudiar la formació de patróns durant el desenvolupament. Dues diferents teories van propusarse per explicar aquest procés: el mecanisme de reacció-difusió de Turing i el model de Positional Information. Aquesta tesi utilitza modelos computacionals per explorar si aquestas dues teories es poden combinar per explicar el patron dels dits. El resultat principal és un model computacional que suggereix que un mecanisme de Turing modulat per Hox genes i Fgfs controla l'especificació dels dits. Comparant simulacions amb dades experimentals aconseguim demostrar que el mecanisme de Turing és implementat per Bmps, Sox9 i Wnts. A mes, el model mostra que una combinació de un mecanisme de Turing i Positional Information aconsegueix especificar al patró de manera extremadament fiable i suggereix que els Fgfs coordinen la formació del patró amb el creixement.

Sumari

List of Figures

List of Tables

Chapter 1

INTRODUCTION

Modern Developmental biology is rooted on fundamental questions raised by ancient Greek philosophy. As early as the eight century B.C., Greek philosophers had already established a field called "generation" that focused on the study of the origin of organisms. Aristotle in the fourth century B.C. was already performing classical embryology experiments by opening chicken eggs at different times to observe the progressive development of the embryo [Balme, 2002]. Aristotle was the first to challenge the preformationist theories that believed that a miniature version of the embryo ("Homunculus") was preexisting in the father's semen. Strong of his observations in chick, he proposed an alternative model called "epigenesis" that described the embryo as a mass of undifferentiated substance where the parts were created in a nested hierarchical order. Over the centuries, various philosophers and scientists supported Aristotle's view and found conceptual problems deriving from preformationism notions. A well- known problem of preformationism was the recursive application of the "Humunculus" assumption that implied that every embryo contained an infinite series of Russian-doll "Homonculi". Also Leonardo Da Vinci in the 15th century raised doubts against preformationism by highlighting the evidence that both parents contributed almost equally to a child's aspect. However, it took a two thousand years long debate to accept Aristotle's "epigenesis" and eventually his theory was only revived in 1759 by the German zoologist C.F Wolff.

During the nineteenth century with the development of cell theory and the discovery of the mammalian ovum by Karl Ernst von Baer the study of embryogenesis was revolutionized. It was then clear that the germ cells of both parents contributed equally to form the zygote that by successive cell divisions generated all the somatic cells of the embryo. These concepts founded the basis of modern developmental biology and lead to a main questions of the field: How does a complex multicellular organism with different organs and tissues develops form a single fertilized cell? How cells differentiate and achieve spatial organization?

This process is known as pattern formation and is the main topic of this study. This thesis is focused on the early development of the vertebrate limb and in particular on the molecular mechanisms that drive the specification of the digits. The final outcome of this work is a computational model of limb development which provides evidence that a Turing mechanism modulated by Positional Information specifies the periodic pattern of the digits. An interesting aspect of this this study is the use of a systems biology approach to the study morphogenesis and patterning, which shows that a combination of experiments and modeling is a convenient way to handle the spatio-temporal complexity of development.

The thesis is organized as follows:

- The first chapter provides a general overview on pattern-formation, morphogenesis and limb development. Each section of this chapter is concluded with a summary that helps the reader to contextualize the literature with my original work. The first section focuses on pattern formation and gives an historical introduction on Turing mechanisms and Positional Information. I give particular attention to Turing mechanisms which forms the basis of the two models of digit patterning presented in the third chapter. This section is best understood by people with a mathematical background. Readers with a biological background may want to go directly to the last three subsections that include the first article presented with my thesis, which reviews the Turing models that have been proposed to study development. The second section introduces the concept of morphogenesis and its relation to patterning. Finally, the last section provides an introduction to limb development with a particular emphasis on the theoretical and computational models of digit patterning.

- The second chapter gives a brief summary of the goals and results of this thesis.

- The third chapter presents the original contributions of my work. The chapter starts with the second article included with my thesis, which provides the first strong evidence that a Turing mechanism controls digit patterning. This work is done in collaboration with the laboratory of Marian Ros at the University of Cantabria and shows that Distal Hox Genes modulate the wavelength of the Turing mechanism that patterns the digits. The chapter follows with the third article included in this thesis, which concerns the development of a realistic model of limb growth based on mouse clonal data and experimental mouse limb morphologies. The last section presents the main result of my thesis, which is a model of digit patterning that considers accurate limb growth, experimental gene expression data, Positional Information gradients and a three-reactant Turing model derived from molecular

data. By comparing the model against experimental data we provide the first evidence that Bmps, Sox9 and Wnts form the Turing gene network responsible for digit patterning.

- Finally, the fourth chapter provides a discussion and elaborates on the future directions of limb development modeling.

1.1 Pattern Formation

One of the first theories that was proposed to explain the early patterning of the embryo is the Mosaic Model proposed by Weissman in 1880s. In his model, Weissman hypothesized the presence of a number of determinants in the zygote nucleus that after cell division were unequally distributed among cells. A certain combination of factors represented a particular cell identity and a series of asymmetric cell divisions would be responsible for the spatial asymmetries. A first confirmation of this model came from the experimental work done by Willhem Roux in frog, where destruction of one cell at the two-cell stage of the zygote resulted in a half embryo. However, successive experiments from H. Driesch in sea urchins and the famous work by Spemann and Mangold revealed that cells had the plasticity to be respecified by cells located in instructive regions of the embryo like the Spemann organizer. At the same time the chromosomal theory of development had established and the interest on genes was growing. One of the first scientist that tried to reconcile the concept of genes and organizers was Waddington. In his book "genes and organizers" [Waddington, 1940] he stated that Development was a path from genotype to phenotype and believed that embryology had to be study under the light of genetics. After the 1950s, with the discovery of the DNA and advances in the field of molecular biology, developmental biology focused on the relation between genes and morphological changes trying highlight which genes determine each morphological change in the embryo. However, it was still not clear how cells communicated to achieve spatial organization.

1.1.1 Self-organizing reaction-diffusion model

Alan Turing, a British electrical engineer famous for establishing the foundations of computer science and for being a code breaker during the Second World War, was among the first to use mathematical models to study biology [Murray, 2012]. In 1952 he published a seminal paper called "The Chemical basis of Morphogenesis" [Turing, 1952] where he described a simple model based on diffusible substances that were able to self-organize in a periodic stable pattern. His mathematical analysis showed that under certain reacting conditions two or more diffusible

substances, that he called morphogens, could stabilize in a periodic spatial pattern due to diffusion and stochastic fluctuations. He proposed that this diffusion-driven instability could be responsible for the generation of spatial asymmetries during morphogenesis. Turing's theory was published only one year before the discovery of DNA structure and did not provide an exact meaning for the nature of morphogens. In his paper Turing relates the morphogens to the evocators proposed by Waddington [Waddington, 1940] but also proposes that genes and hormones may also be considered as morphogens because they function similarly to chemical reactants and control the production of other morphogens.

1.1.1.1 Turing's original reaction-diffusion model

In the model presented by Turing each cell contains a number of morphogens (M morphogens) that can diffuse and react according to normal law of diffusion and reaction. If this system is well-stirred, both reaction and diffusion depend only on the concentrations of the M morphogens and the state of a whole systems made of N cells can be describe by $N \times M$ numbers. If each cell is in the same state, namely they have same M concentrations, and the system is completely symmetrical (like in the spherical symmetry of the Blastula embryo stage) nothing will happen. However, if the system has some deviations from homogeneity (some irregularities) it may reach a state where these deviations tend to grow and form a new stable equilibrium with broken asymmetry. To explain how this phenomena can take place Turing used a simple example of two initially homogeneous cells with two morphogens X and Y. The production reactions for X and Y are governed by the following equations:

$$(X) = 5X - 6Y + 1 \tag{1.1}$$
$$(Y) = 6X - 7Y + 1 \tag{1.2}$$

and X diffuses at rate 0.5 (for unit difference of concentrations between cells)
and Y diffuses at rate 4.5.

According to (1.1) and (1.2) if $X = 1$ and $Y = 1$ the system remains unchanged because both production terms are zero and no diffusion occurs. However, if we suppose that the morphogen concentrations in the cells are slightly perturbed:

$$X_1 = 1.06\ Y_1 = 1.02 \text{ in the first cell}$$
$$X_2 = 0.94\ Y_2 = 0.98 \text{ in the second cell}$$

the rate of production for X and Y becomes respectively $+0.18$ and $+0.22$ in the first cells and -0.18 and -0.22 in the second cell, and the amount of diffusion

from the first cell to the second is 0.6 and 0.18 for X and Y respectively. Therefore, by summing both diffusion and reaction we have a flow from the second cell to the first cell of 0.12 and 0.04, for X and Y respectively, that increases the difference between the two cells. This difference increases exponentially at every step drifting away from the equilibrium condition and accentuating the asymmetry between the two cells.

Turing, extended this simple example to a system made by a ring of N cells with generic production equations for X and Y. In this more general example, for each cell r with $1 \leqslant r \leqslant N$ there could be diffusion with the two neighboring cells $r-1$ and $r+1$. He denoted concentration of X and Y in a r cells as X_r and Y_r and wrote the equations defining their evolution over time as:

$$\frac{\partial X_r}{\partial t} = f(X_r, Y_r) + \mu(X_{r+1} - 2X_r + X_{r-1}) \tag{1.3}$$

$$\frac{\partial Y_r}{\partial t} = g(X_r, Y_r) + \nu(Y_{r+1} - 2Y_r + Y_{r-1}) \tag{1.4}$$

where $f(X, Y)$ and $g(X, Y)$ are production function with a general form and μ and ν are diffusion constant of X and Y respectively.

The behavior of the system was analyzed considering a perturbation of the equilibrium steady state $f(h, k), g(h, k) = 0$ that writes $X_r = h + x_r, Y_r = k + y_r$. In this state close to equilibrium $f(h + x, y + k)$ can be approximated as a linear combination of x and y that writes $ax + by$. Similarly, $g(h + x, y + k)$ can be approximated to $cx + dy$ and the system can be rewritten as:

$$\frac{\partial x_r}{\partial t} = ax_r + by_r + \mu(x_{r+1} - 2x_r + x_{r-1}) \tag{1.5}$$

$$\frac{\partial y_r}{\partial t} = cx_r + dy_r + \nu(y_{r+1} - 2y_r + y_{r-1}) \tag{1.6}$$

Turing solved this system analytically and found four types of spatial waves (four different behaviors) that the system can exhibit as the parameters a, b, c, d, μ, ν are changed:

(a). *Stationary homogeneous (extreme long wave-length)*
The cells are all the same, there is no flow from one cell to the other and they behave like isolated. Example of parameters: $\mu = \nu = \frac{1}{4}, b = c = 1, a = d$

(b). *Oscillatory (extreme long wave-length)*
The system oscillates homogeneously.
Example of parameters: $\mu = \nu = \frac{1}{4}, b = -c = 1, a = d$

(c). *Stationary waves (extreme short wave-length)*
Cells have alternated identities like in a chessboard pattern or in a lateral inhibition pattern (E.g Notch-Delta signaling).
Example of parameters: $\mu = 1, \nu = 0, b = -c = 1, d = I, a = I - 1,$

(d). ***Stationary waves (finite wave-length)***
Cells show a periodic stationary wave pattern in space. The number of peaks formed depends on the radius of the ring of cells and the diffusion constants.
Example of parameters: $\frac{\mu}{\mu'} = \frac{\nu}{\nu'} = (\frac{N}{2\pi\rho})^2, \nu = 0, a = I - 2, b = 2.5, c = -1.25, d = I + 1.5$

With the addition of a third morphogen two other behaviors were possible, namely: *(e) Traveling waves* and *(f) Out phase oscillations*; and these are all the possible behaviors that can be obtained by a reaction-diffusion mechanism. The behavior (d) is the main result of Turing and is usually referred as Turing instability or diffusion-driven instability. Figure 1.1 shows A Turing's original numerical simulations that forms a diffusion-driven instability starting from homogeneous initial conditions.

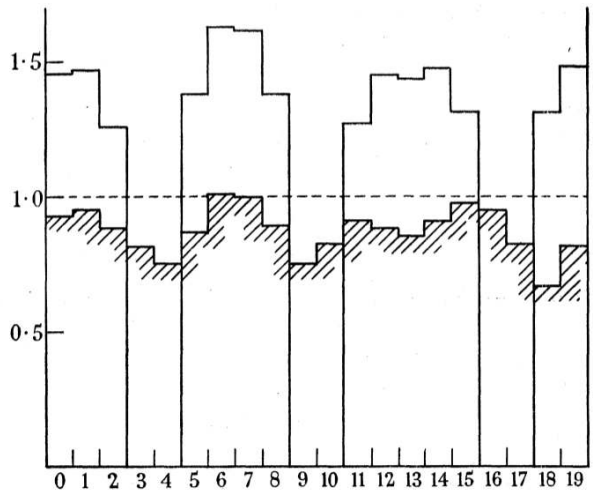

Figure 1.1: Concentration of Y in a numerical simulation performed by Turing. The horizontal dash line is the starting homogeneous steady state, the continuous line is the final state. The line highlighted by oblique lines is an intermediate state (Figure taken from [Turing, 1952]) .

Interestingly, by the time when Turing published his paper, a Russian scientist named Boris Belousov was struggling to publish his results regarding a

chemical reaction that could oscillate between two states, see Figure 1.2. The work of Belousov was considered too controversial and was rejected twice for publication because it showed that chemical reactions could behave according to non-equilibrium thermodynamics. At the time, the work of Alan Turing was largely unknown to the scientific community and no connection between the Belousov's work and the reaction-diffusion models type (b) was made. Eventually, Belousov's work was published in a non reviewed journal [Belousov, 1959] and re-discovered only in the early sixties by a graduate student named Anatol Zhabotinsky [Zhabotinsky, 1964]. In the following three decades, a number of theoretical models like the Brusselator [Prigogine and Lefever, 1968] and the Oregonator [Field and Noyes, 1974] were developed to explain such chemical oscillations. Moreover it was also recognize that the dynamics behind chemical oscillations were the same as those exhibited by the predator-prey model of Lotka and Volterra [Lotka, 1910] published at beginning of the century. This anecdote highlights the initial resistance that Turing and others had to face to convince the scientific community. Nevertheless, Turing's and Belusov's work were just the beginning of a long series of models and experiments that would confirm the importance of reaction-diffusion in biology and chemistry.

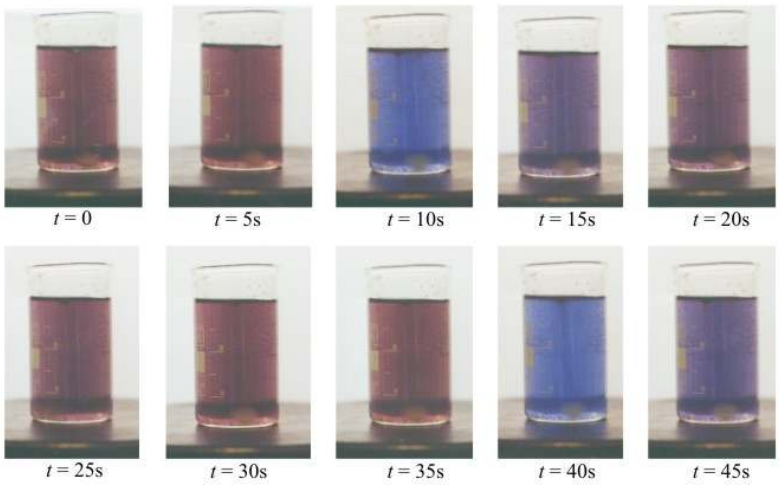

Figure 1.2: A stirred Belousov-Zhabotinsky reaction mixture showing changes in color over time (oscillations). (Figure taken from [Wikipedia, 1])

1.1.1.2 Reaction diffusion models after Turing

The reaction-diffusion models that were published in the two decades following Turing's paper focused either on type (d) models (periodic patterns) or on type (b) models (oscillations) based on the idea of Belousov and Zhabotinsky. Eventually, these two schools converged and many of the type (b) oscillating models were re-analyzed for their type (d) behavior and vice versa.

A famous contribution regarding type (d) reaction diffusion models is the work by Gierer and Meinhardt [Gierer and Meinhardt, 1972] that proposed more realistic models made of two morphogens: one acting as an activator and another having an inhibitory effect. According to Gierer and Meinhardt [Gierer, 1981, Gierer and Meinhardt, 1972, Meinhardt, 1982] two qualitative phenomena are required to obtain a diffusion-driven instability: (a) short range auto-activation, (b) long range lateral inhibition. The first phenomena implies that the activator has to promote its own activation locally to allow some local initial advantages to develop in an activated region. The second, means that the inhibitory effect has to spread on a wider area than the activator in order to limit its over-all expansion. Gierer in [Gierer, 1981] provided a more formal description of these two concepts as follows, given a system of two reaction diffusion equations:

$$\frac{\partial u}{\partial t} = f(u,v) + D_u(u) \tag{1.7}$$

$$\frac{\partial v}{\partial t} = g(u,v) + D_v(v) \tag{1.8}$$

where $D_u(u)$ and $D_v(v)$ describe the diffusion of the morphogens, for example in the one dimensional continuous case thy are: $D_u(u)$=$k_u \frac{\partial^2 u}{\partial x^2}$ $D_u(u)$=$k_v \frac{\partial^2 v}{\partial x^2}$

to get stable pattern formation, the uniform solution $f(u_0, v_0) = g(u_0, v_0) = 0$ has to be: stable for uniform distributions of u and v (including their spatial averages when there are small perturbations) and unstable for local deviations. According the Gierer, this happens when the following conditions are satisfied:

- u has to auto-activate itself.
- v has to cross-inhibit u to prevent u explosion and to maintain average u and v near the uniform steady state.
- The inhibition from v has to be strong enough to maintain the stability of the uniform steady state.
- The inhibition from v has to be relatively fast compare to the activation.

- The half decay length of u, that is $\sqrt{k_u/\mu_u}$ (where μ_u is a first order decay of u), has to be lower than the domain size.
- The half decay length of v, that is $\sqrt{k_v/\mu_v}$ (where μ_v is a first order decay of v), has to be large in comparison with the one of u.

Following these assumptions, if the reaction-diffusion equations are re-written to consider explicitly production P_u, P_v and degradation Q_u, Q_v terms:

$$\frac{\partial u}{\partial t} = P_u(u,v) - Q_u(u,v) + D_u(u) \tag{1.9}$$
$$\frac{\partial v}{\partial t} = P_v(u,v) - Q_v(u,v) + D_v(v) \tag{1.10}$$

and if we assume the terms can be approximated as:
$P_u \sim u^{i_1}v^{i_2}$; $Q_u \sim u^{i_3}v^{i_4}$; $P_v \sim u^{i_5}v^{i_6}$; $Q_v \sim u^{i_7}v^{i_8}$

models that respect the diffusion-driven instability conditions presented above can be generated considering the term orders $i_k, k = 1..8$ as follows:

- $i_1 > i_3$ to make sure that u manages to auto-activate itself
- $i_8 > i_6$ to make sure that v grows to cross inhibit
- $i_2 < i_4, i_5 > i_7$ to ensure cross-inhibition or alternatively $i_2 > i_4, i_5 < i_7$ to implement the inhibition by depletion of v by u and activation of u by v.

Using these criteria Gierer and Meinhardt developed two class of models:

- the *Activator-Inhibitor* (AI) model with conditions $i_2 < i_4, i_5 > i_7$, where an activator u auto-activate itself and stimulates the production of its own inhibitor v. This model is equivalent to the original model presented by Turing and a popular version of its equations is:

$$\frac{\partial u}{\partial t} = \rho_u \frac{u^2}{(1+k_u u^2)v} - \mu_u u + \sigma_u + D_u \nabla^2 u \tag{1.11}$$
$$\frac{\partial v}{\partial t} = \rho_v u^2 - \mu_v v + \sigma_v + D_v \nabla^2 v \tag{1.12}$$

  where the term $\frac{u^2}{(1+k_u u^2)v}$ in equation (1.11) represents the u auto-activation (u^2), the inhibition from v (that is at the denominator) and a saturation on the auto-activation depending on k_u. Starting from the homogeneous steady state (case with no diffusion) in a one-dimensional row of thirty cells a

periodic pattern of u and v emerges, see the left panel in Figure 1.3. In the final pattern, peaks of high concentration of u and v are in the same place, the two patterns are in phase.

Gierer and Meinhardt were also the first to show two-dimensional computer simulations of a diffusion-driven instability. In two dimensions the Activator-Inhibitor model showed two different types of patterns: spots or stripes, see the right part of Figure 1.3. The former developed when the auto-activation did not saturate ($k_u = 0$) and an activated region could freely grow and promote enough inhibitor to make a stable spot configuration. This is easy to understand as a natural extension of a 1D model to every 2D direction. Stripes were instead formed when the auto-activation saturated ($k_u > 0$). According to [Scholarpedia, 1] stripes develops because the activator peak height can no longer increase but the spatial extension of a region carrying a high activator concentration can still increase. Since the mechanism is based on lateral inhibition, a stripe-like distribution is preferred and each activated cell will have activated neighbor but also non-activated neighbors in the vicinity to dumped inhibitor.

- the *Substrate-Depletion* (SD) model, with conditions $i_2 > i_4, i_5 < i_7$ where an activator u auto-activate itself by depleting a substrate v. One of the implementations of this model is the following:

$$\frac{\partial u}{\partial t} = \rho_u \frac{u^2 v}{(1 + k_u u^2)} - \mu_u u + \sigma_u + D_u \nabla^2 u \tag{1.13}$$

$$\frac{\partial v}{\partial t} = -\rho_v \frac{u^2 v}{(1 + k_u u^2)} + \sigma_v + D_v \nabla^2 v \tag{1.14}$$

  where the term $\frac{u^2 v}{(1+k_u u^2)}$ in both equations (1.13) and (1.14) represents the fact that u auto-activate itself (u^2) by consuming the substrate v with a saturation that depends on k_u. A one-dimensional simulation in a row of thirty cells shows again an emerging periodic pattern of u and v, see left panel in Figure 1.4. However, this time the peaks of u are spatially complementary to those of v, the two patterns are out-phase. This happens because where u grows v is consumed. Similarly to the previous case the peaks of v are wider than those of u due to its greater diffusion constant.

  In two dimensions, the model exhibited a behavior similar to the Activator-Inhibitor model, see right panel in Figure 1.4. As in the AI model, when there was no saturation ($k_u = 0$) the pattern of u showed spots. With this

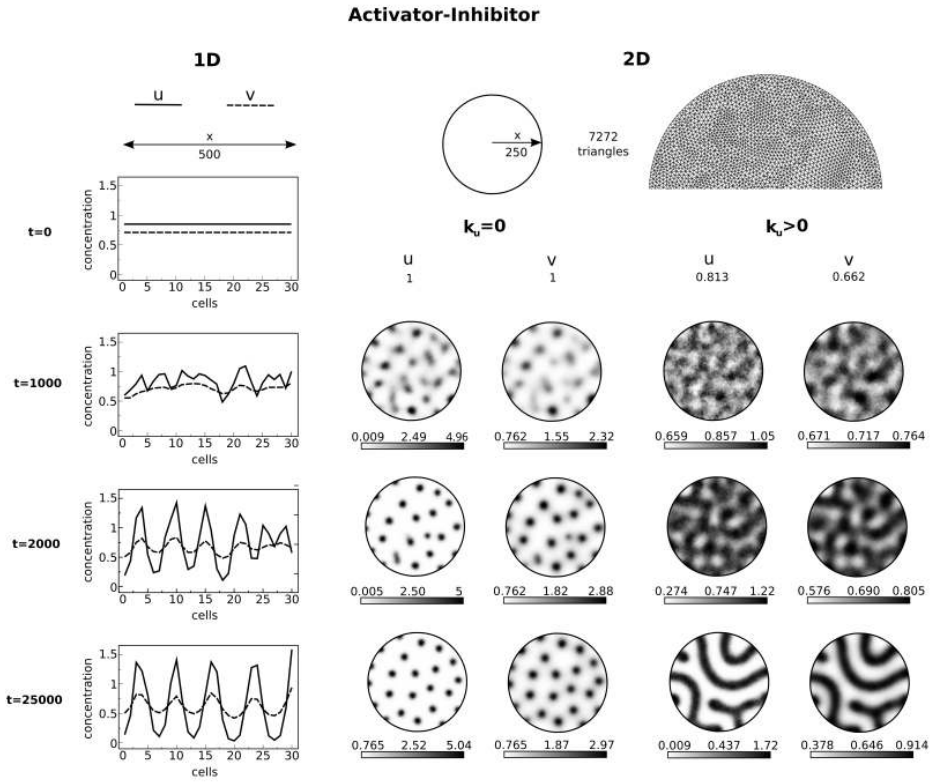

Figure 1.3: On the left: a 1D simulation on a row of 30 cells (long 500 space units) of the Activator-Inhibitor model proposed by Gierer and Meinhardt. The activator u is shown by continuous line and the inhibitor v by dashed line. Four different time points corresponding to t=0 (initial conditions), t=1000, t=2000 t=50000 are shown. On the right: same time-points for simulations on a 2D circular domain made of 7272 triangles with radius of 250 space units. High concentrations are shown in black color and low concentration in white, the minimum, medium and maximum concentration values are provided. The left part shows the simulation with no saturation $k_u = 0$: spots are formed. The right part shows the simulation with saturation $k_u > 0$: a labyrinthine pattern is formed. All the simulation show that u and v have an in-phase pattern and that v is spatially more extended.

parameters the model converged more quickly than the AI model to a regular spot configuration. This is due to the fact that the substrate v has a pattern of highly-connected stripes (rather than spots) and quickly organizes in a hexagonal-like honey bee pattern. When there was saturation and $k_u > 0$ a labyrinth-like pattern of stripes was created for both u and v. In both cases the patterns of u and v were out of phase (complementary patterns).

In parallel to the work of Gierer and Meinhardt, a number of models inspired by the oscillations of the Belousov-Zhabotinsky reaction were modified to consider diffusion and extended into Turing models:

- *Brusselator* - The first theoretical model was proposed by Prigogine [Prigogine and Lefever, 1968] at the Université Libre de Bruxelles and was named Brusselator after the city where it was developed. This model was made to capture the oscillating dynamics of the following hypothetical reactions:

$$\begin{aligned} A &\xrightarrow{k_1} X \\ B + X &\xrightarrow{k_2} Y + D \\ 2X + Y &\xrightarrow{k_3} 3X \\ X &\xrightarrow{k_4} E \end{aligned}$$

where X and Y are internal reactants with variable concentration and A, B and D are external reactants with fixed concentrations

from these reactions, the following Ordinary Differential Equations (ODEs) governing the systems can be derived for X and Y:

$$\frac{dX}{dt} = k_1 A - k_2 BX + k_3 X^2 Y - K_4 X \tag{1.15}$$

$$\frac{dY}{dt} = k_2 BX - k_3 X^2 Y \tag{1.16}$$

Prigogine described analytically the limit cycle behavior (oscillations) that this system can exhibit. Successively, Nicolis in [Nicolis, 1970] highlighted that a remarkable characteristic of systems far of equilibrium, like the Brusselator, is the capacity to form a new type of instability that can generate

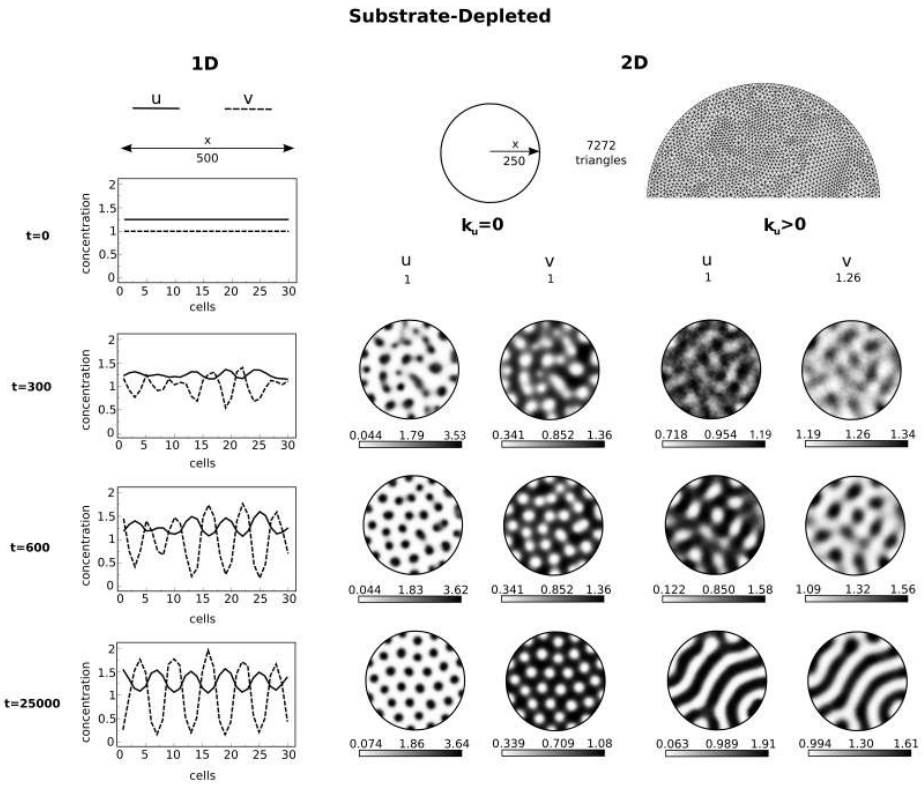

Figure 1.4: On the left: a 1D simulation on a row of 30 cells (long 500 space units) of the Substrate-Depletion model proposed by Gierer and Meinhardt. The activator u is shown by continuous line and the substrate v by dashed line. Four different time points corresponding to t=0 (initial conditions), t=300, t=600 t=25000 are shown. On the right: same time-points for simulations on a 2D circular domain made of 7272 triangles with radius of 250 space units. High concentrations are shown in black color and low concentration in white, the minimum, medium and maximum concentration values are provided. The left part shows the simulation with no saturation $k_u = 0$: u forms spots and v forms an hexagonal-like honey bee pattern. The right part shows the simulation with saturation $k_u > 0$: for both u and v a labyrinth-like pattern of stripes is formed. All the simulation show that u and v have an out of phase pattern (complementary).

non-equilibrium structures. Such structures are maintained trough the continuous exchange of energy and matter from the outside world and for this reason he call them "dissipative structures". Systems capable of diffusion-driven instabilities are typical examples of dissipative structures and indeed the Brusselator model itself can be transformed in a set of Partial Differential Equation that behaves like a reaction-diffusion type (d) model [Nicolis and Prigogine, 1977]. For example, equation (1.15) and (1.16) can be conveniently rewritten and transformed in PDEs as following:

by considering the following transformation
$X = u, Y = v, t = tk_3, \frac{D_x}{k_3} = D_u, \frac{D_y}{k_3} = D_v, \alpha = A\frac{k_1}{k_3}, \beta = B\frac{k_2}{k_3}$

$$\frac{\partial u}{\partial t} = \alpha - (\beta + 1)u + u^2 v + D_u \nabla^2 u \tag{1.17}$$
$$\frac{\partial Y}{\partial t} = \beta u - u^2 v + + D_v \nabla^2 v \tag{1.18}$$

this system has homogeneous steady state $(u_0, v_0) = (\alpha, \frac{\beta}{\alpha})$ and shows type (b) behavior for $\beta > 1 + \alpha^2$ and Turing diffusion-driven type (d) instability when $\beta > (1 + \alpha\sqrt{\frac{D_u}{D_v}})^2$. This system shows an out of phase pattern for u and v similar to the Substrate-Depletion model of Gierer Meinhardt. An interesting aspect of this model is that when the type (d) instability condition is satisfied, by changing the parameter α the pattern can smoothly change from a configuration where u shows spots and v shows stripes, to the opposite configuration where v show spots and u show stripes. In between these two configurations there exist one that resembles the one of Substrate-Depletion model with $k_u > 0$ and where both u and v show stripes.

- *Oregonator* - Another famous reaction-diffusion type (b) model is the Oregonator presented by Field and Noye in [Field and Noyes, 1974] at the University of Oregon just few years after the Brusselator. This model was not just inspired by the Belusov-Zhabotinsky system but aimed to explicitly mimic its reactions. The original model was derived from a set of five reactions:

$$
\begin{aligned}
A + Y &\xrightarrow{k_1} X + P \\
X + Y &\xrightarrow{k_2} 2P \\
A + X &\xrightarrow{k_3} 2X + 2Z \\
2X &\xrightarrow{k_4} A + P \\
B + Z &\xrightarrow{k_c} \frac{1}{2} fY
\end{aligned}
$$

where X, Y, Z are internal reactants with variable concentration and A, B and P are external reactants with fixed concentrations

from these reactions the following Ordinary Differential Equations (ODEs) system can be derived for X, Y and Z:

$$\frac{dX}{dt} = k_1 AY - k_2 XY + k_3 AX - 2k_4 X^2 \tag{1.19}$$

$$\frac{dY}{dt} = -k_1 AY - k_2 XY + \frac{1}{2} k_c f BZ \tag{1.20}$$

$$\frac{dZ}{dt} = 2k_3 AX - k_c BZ \tag{1.21}$$

This system gives rise oscillations and traveling waves that are consistent with the experiments of Belusov and Zhabotinsky. Moreover, it can be transformed in a system of PDEs that can form stationary type (d) Turing Patterns [Becker and Field, 1985]. A simplified version of the Oregonator model known as the two-variable Oregonator [Nicolis and Prigogine, 1977] writes:

$$\frac{\partial u}{\partial t} = \frac{1}{\varepsilon}(u - u^2 - fv\frac{u - q}{u + q}) + D_u \nabla^2 u \tag{1.22}$$

$$\frac{\partial v}{\partial t} = u - v + D_v \nabla^2 v \tag{1.23}$$

the system has steady state $u_0 = v_0 = \frac{1-f-q+\sqrt{(1-f-q)^2+4q(1+f)}}{2}$ and shows type (b) behavior when $0 < \varepsilon < 1$ and Turing diffusion-driven type (d) instability when $\varepsilon = 1$. This system shows an in phase pattern for u and v. Similarly to the case of the Brusselator by changing the parameter f the pattern can smoothly change from a configuration where u shows spots and v shows stripes, to the opposite configuration, v show spots and u show stripes.

- *Schnakenberg* - A more general study on the chemical reactions that can exhibit reaction-diffusion type (b) behavior was made by Schnakenberg in [Schnakenberg, 1979]. The purpose of this study was to find the simplest set of reactions capable of a limit cycle behavior. Schnakenberg demonstrates analytically that the simplest system (even simpler than the Brusselator) that is capable of oscillation writes:

$$\begin{aligned} 2X + Y &\rightarrow 3X \\ A &\rightarrow Y \\ X &\rightleftarrows B \end{aligned}$$

where X and Y are internal reactants with variable concentration and A, B are external reactants with fixed concentrations

from these reactions the following ODEs can be derived for X and Y:

$$\frac{dX}{dt} = X^2Y - X - B \tag{1.24}$$

$$\frac{dY}{dt} = -X^2Y + A \tag{1.25}$$

Such system exhibits a type (d) oscillations behavior when $0 < B \ll A$ and $\sqrt{2} - 1 < A < 1$ and can be extended with diffusion to a system of PDEs as following:

$$\frac{\partial u}{\partial t} = u^2v - u - \beta + D_u\nabla^2 u \tag{1.26}$$

$$\frac{\partial v}{\partial t} = -u^2v + \alpha + D_v\nabla^2 v \tag{1.27}$$

where $X = u, Y = v, \alpha \sim A$ and $\beta \sim B$

the system has homogeneous steady state $(u_0, v_0) = (\alpha + \beta, \frac{\alpha}{(\alpha+\beta)^2})$ and can produce Turing diffusion-driven (d) instability [Iron et al., 2004]. The pattern of u and v is out of phase as in the Substrate-Depletion model of Gierer and Meinhardt. Again by changing the parameters α and β it is possible to smoothly change a configuration where u shows spots and v shows stripes, to the opposite configuration, v show spots and u show stripes.

- *Gray Scott* - A more recent model capable of reaction-diffusion type (b) behavior was proposed by Gray and Scott in [Gray and Scott, 1985]. Again the starting point of the model is a set of hypothetical reactions that highly resemble the minimal set of reactions proposed by Schnakenberg:

$$Y + 2X \xrightarrow{k_1} 3X$$
$$X \xrightarrow{k_2} A$$

where X and Y are internal reactants with variable concentration and A is an external reactant product

from these reaction the following ODEs can be derived for X and Y:

$$\frac{dX}{dt} = k_1 X^2 Y - k_2 X + k_f(x_0 - X) \tag{1.28}$$
$$\frac{dY}{dt} = -k_1 X^2 Y + k_f(y_0 - Y) \tag{1.29}$$

where (x_0, y_0) is the steady state and $k_f = \frac{1}{t_{res}}$ and t_{res} is the mean residence time

Such system shows a limit cycle behavior with oscillations and can be transformed in a non-dimensional version of PDEs as shown in [Pearson, 1993]:

$$\frac{\partial u}{\partial t} = u^2 v - (F + k)u + D_u \nabla^2 u \tag{1.30}$$
$$\frac{\partial v}{\partial t} = -u^2 v + F(1 - v) + D_v \nabla^2 v \tag{1.31}$$

where $X = u, Y = v$

this system has homogeneous steady state $(u_0, v_0) = (0, 1)$ and can produce a range of different behaviors by varying the two control parameters F and k, including oscillations and reaction-diffusion type (d) Turing instability. An extensive numerical study of the patterns produced by this model was

presented by Pearson in [Pearson, 1993]. In previous reaction-diffusion numerical studies a slight perturbation of the homogeneous steady state was used as initial condition. Pearson instead used a strong squared perturbation in the center of the domain with value $(u, v) = (0.25, 0.3)$. This perturbation grows and spread on the whole domain producing the different patterns as F, k are varied. The pattern of u and v is out of phase as in the Substrate-Depletion model of Gierer Meinhardt. Turing patterns can range from configuration where u shows spots and v stripes to the opposite configuration. Interestingly, the excitation induced by the initial perturbation is also able to produce propagating stripe-like structures and replicating spots. This phenomena are qualitatively different from a stable Turing patterns and are related e to the reaction-diffusion type (e) behavior. In this configuration the initial excitation produces a dissipative structures (as named by Prigogine) that behave as a propagating waves. An example of such propagating waves are the traveling waves created by the action-potential neuronal model of the Fitzhugh-Nagumo equations [Fitzhugh, 1961], see also the discussion about waves in excitable media presented in [Murray, 1989]. The behavior of this kind of structures is also referred as autosolitons or dissipative solitons and has been extensively characterized by Kerner and Osipov [Kerner and Osipov, 1994].

1.1.1.3 General conditions for diffusion-driven instability

In conclusion, both the studies that followed the work of Turing and those that followed the work Belusov and Zhabotinsky converged to models made of two reactants (two species) that showed similar reaction-diffusion type (d) behaviors. Indeed, by the end of the eighties a more general theory that could be applied to all these models was developed by Murray, see the reaction-diffusion stability analysis in [Murray, 1989]. In this study Murray formalized the two conditions for a diffusion-driven instability that were originally given by Turing and successively by Gierer:

- the system has to be linearly stable in the case of no diffusion
- the system has to be unstable for spatial perturbations

The first condition was formalized as follows:

given the reaction-diffusion system

$$\frac{\partial u}{\partial t} = \gamma f(u, v) + \nabla^2 u \tag{1.32}$$

$$\frac{\partial v}{\partial t} = \gamma g(u, v) + d\nabla^2 v \tag{1.33}$$

with zero flux boundary condition: r on ∂B where B is the boundary

the system can be linearized around the homogeneous steady state solution (u_0, v_0) in the following way:

$$\mathbf{w} = \begin{pmatrix} u - u_0 \\ v - v_0 \end{pmatrix} \tag{1.34}$$

when the vector $|w|$ (the fluctuations) is small, the system (1.32),(1.33) can be written in matrix form as

$$\frac{\partial \mathbf{w}}{\partial t} = \gamma A \mathbf{w}, \quad A = \begin{pmatrix} f_u & f_v \\ g_u & g_v \end{pmatrix}_{u_0, v_0} \tag{1.35}$$

A is called the stability matrix and f_u, f_v, g_u, g_v are the partial derivative of f and g at steady state. Let's consider the solution $\mathbf{w}$ of the system as proportional to $e^{\lambda t}$ where λ is the vector of eigenvalues. The steady state $\mathbf{w} = 0$ is linearly stable if the real part of the eigenvalues λ satisfies $\lambda < 0$. The eigenvalues λ are calculated as:

$$\begin{aligned} |\gamma A - \lambda I| &= \begin{vmatrix} \gamma f_u - \lambda & \gamma f_v \\ \gamma g_u & \gamma g_v - \lambda \end{vmatrix} = 0 \\ \Rightarrow \lambda^2 - \gamma(f_u + g_v)\lambda + \gamma^2(f_u g_v - f_v g_u) &= 0 \\ \Rightarrow \lambda_1, \lambda_2 = \frac{1}{2}\gamma[(f_u + g_v) \pm \sqrt{(f_u + g_v)^2 - 4(f_u g_v - f_v g_u)}] & \end{aligned} \tag{1.36}$$

according to (1.36) the real part of the eigenvalues λ satisfies the condition $\lambda < 0$ when

$$f_u + g_v < 0, \quad f_u g_v - f_v g_u \quad > 0 \tag{1.37}$$

condition for the stability of the homogeneous steady state

The second condition required for a diffusion-driven instability is to be unstable for spatial perturbations. This was formalize as follows:

again the whole system (including diffusion) is linearized around the steady state $\mathbf{w} = 0$:

$$\frac{\partial \mathbf{w}}{\partial t} = \gamma A \mathbf{w} + D\nabla^2 \mathbf{w}, \quad D = \begin{pmatrix} 1 & 0 \\ 0 & d \end{pmatrix} \tag{1.38}$$

to solve this system with zero-flux boundary conditions, let's first consider the solution $\mathbf{W}(\mathbf{r})$ associated with the following eigenvalue problem:

(Note: an eigenvalue problem is the problem of finding an eigenvector v that satisfies $Av = \lambda Bv$ where A and B are matrices and λ the eigenvalue of A, B)

$$\nabla^2 \mathbf{W} = k^2 \mathbf{W} \tag{1.39}$$

where k is the eigenvalue

For example in a 1D domain $0 \leq x \leq a$, a solution $\mathbf{W}$ of this system that satisfies the zero flux boundary conditions is proportional to $cos(k)$ where $k = \frac{n\pi x}{a}$ with n being an integer. k is usually referred as wavenumber and is inverse proportional to the wavelength $\omega = \frac{2\pi}{k}$. For this eigenvalue problem a discrete number of k will exist. Let's consider $\mathbf{W}_k(r)$ as the eigenfunction of a k number, the solution of the whole system (1.38) can be written as:

$$\mathbf{w}(r,t) = \sum_k c_k e^{\lambda t} \mathbf{W}_k(r) \tag{1.40}$$

for the whole system to be unstable to spatial perturbations, the real part of the solution $\lambda(k)$ has to satisfy $\lambda(k) > 0$. It can be shown (see [Murray, 1989]) that this is satisfied when following conditions are true:

$$df_u + g_v > 0 \quad \frac{(df_u + g_v)^2}{4d} > |A| \tag{1.41}$$

condition for the instability to spatial perturbations

In conclusion Murray in [Murray, 1989] showed that a system in the form (1.32),(1.33) can undergo diffusion-driven instability when (1.37) and (1.41) are satisfied. In summary, putting together (1.37) and (1.41), a diffusion-driven instability is possible when:

$$\begin{aligned} f_u + g_v < 0, \quad & f_u g_v - f_v g_u > 0 \\ df_u + g_v > 0, \quad & (df_u + g_v)^2 - 4d(f_u g_v - f_v g_u) > 0 \end{aligned} \tag{1.42}$$

condition for diffusion-driven instability

the conditions (1.42) imply that:

- $f_u > 0$ and $g_v < 0$, this means that u has to have a positive influence on itself and that v has to have a negative influence on itself.

- $d > 1$, that means that v has to diffuse more than u.
- f_v has to have opposite sign to g_v. This leaves with two possibilities $f_v > 0, g_u < 0$ or $f_v < 0, g_u > 0$, see the two A matrices in Figure 1.5. Interestingly these are the two possibilities found by Gierer and Meinhardt. The first $f_v > 0, g_u < 0$ corresponds to the Activator-Inhibitor model and will produce periodic in-phase patterns of u and v. The second corresponds to the Substrate-Depletion model and will produce periodic out-of-phase patterns of u and v. In summary the two matrices A capable to produce a diffusion-driven instability are:

$$A = \begin{pmatrix} f_u & f_v \\ g_u & g_v \end{pmatrix}$$
$$\text{AI model} = \begin{pmatrix} + & + \\ - & - \end{pmatrix}, \quad \text{SD model} = \begin{pmatrix} + & - \\ + & - \end{pmatrix} \tag{1.43}$$

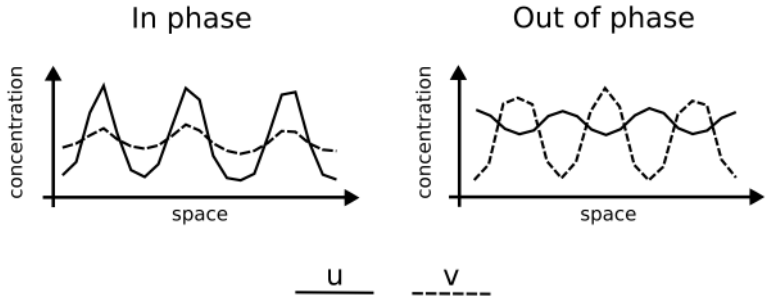

Figure 1.5: The two A matrices derived by Murray and the corresponding two class of models: AI models with in-phase pattern of u and v and SD models with an out of phase pattern of u and v.

More recently, starting from the theory proposed by Murray, Barrio and colleagues derived in [Barrio et al., 1999] a general Turing model by expanding with a Taylor series the two functions f and g that respected the conditions (1.42). The equations derived were the following:

$$\begin{aligned} \frac{\partial u}{\partial t} &= \alpha u(1 - r_1 v^2) + v(1 - r_2 u) + d\nabla^2 u \\ \frac{\partial v}{\partial t} &= \beta v(1 + \frac{\alpha r_1}{\beta} uv) + u(\gamma + r_2 u) + \nabla^2 v \end{aligned} \tag{1.44}$$

when $\alpha = -\gamma$ this system has homogeneous steady state at $(u_0, v_0) = (0, 0)$. The conditions for the stability the homogeneous steady state (1.37) are satisfied when:

$$\alpha \geqslant 0, \quad \beta \leqslant -\alpha$$

or

$$\alpha \leqslant 0, \quad \beta \leqslant -1$$

The condition for the instability to spatial perturbation (1.41) are satisfied when:

$$\alpha - 2\sqrt{\alpha d} > \beta d$$

By changing α, β and d different modes (wave-numbers) could be obtained. For example the following set of parameters $\alpha = 0.899, \beta = -0.91, D = 0.516$, that respects the conditions presented above, gives a wavenumber $k = 0.42$. The other two parameters r_1 and r_2 in (1.44) represent the strength of the different non-linear terms: r_1 is the strength of cubic term and favors stripes while r_2 is the strength of the quadratic term and favors spots. This system produces an in-phase pattern of u and v similar to the Activator-inhibitor model proposed by Gierer and Meinhardt.

In biological terms, the most interesting result of the linear stability analysis of Murray are the two matrices showed in (1.43) that represent the only two alternatives topologies capable of a reaction-diffusion type (d) behavior in a network of two reactants. These two topologies show different qualitative patterns: the AI topology shows an in phase pattern for u and v and the SD topology shows an out of phase pattern for u and v, see Figure 1.5. All the two-species models presented in the previous section can be related to one of these two topologies, see Figure 1.6.

1.1.1.4 Reaction-diffusion and levels of abstraction

As Turing also admitted in the conclusion of his paper, even if simple reaction-diffusion models capture some biological aspects of pattern formation, a biological implementation of a diffusion-driven instability will not be as simple as a two-reactant network. A real system will probably have a big number of reactants that interact with several feedbacks. Nevertheless, fewer reaction-diffusion models with more than two reactants can be found in literature. Gierer in [Gierer, 1981] was the first to formalize some of the conditions required for diffusion-driven instability in a general system made of N reactants. More recently, a formal derivation of the conditions required for diffusion-driven instability in system of N reactants that interact according to simple linear terms was presented [Satnoianu et al.,

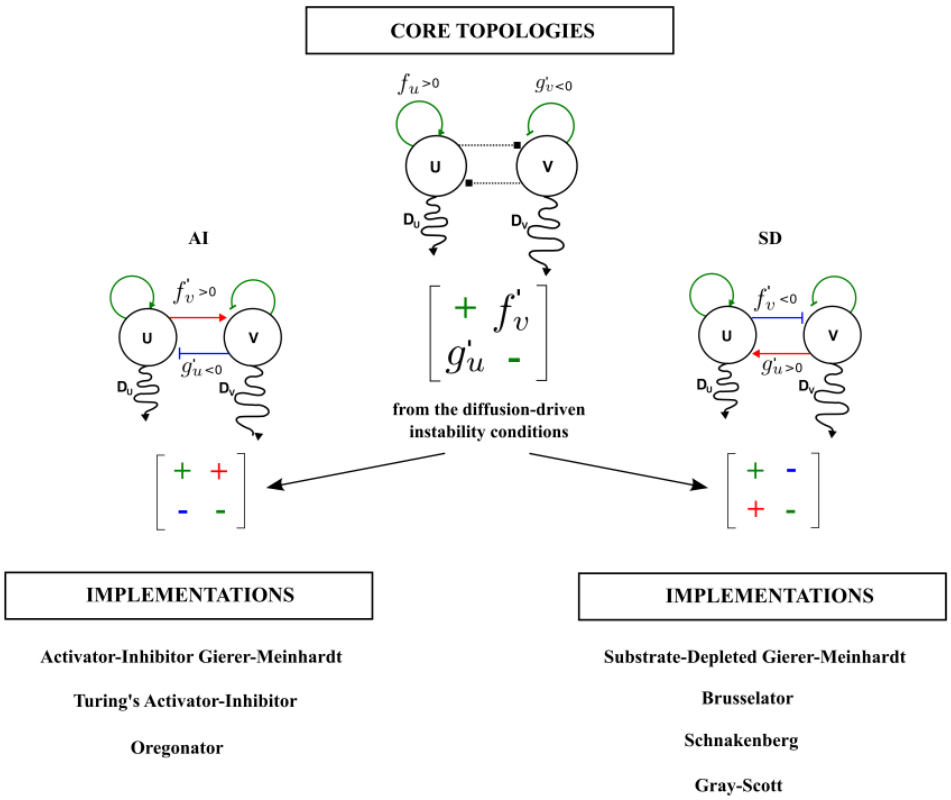

Figure 1.6: In the upper part, the two core topologies derived from the conditions for diffusion-driven stability derived by Murray. The topology on the left correspond to the Activator-Inhibitor model (AI), the one one the right to the Substrate-Depletion model (SD). Green arrows show the interactions that are common to both core-topologies. Red and Blue interactions represent the cross-regulation terms that are inverted in the two core topologies. On the lower part, the different implementation of these two core topologies.

2000]. Murray in [Qian and Murray, 2001] formalized the conditions required for a diffusion-driven instability in general systems made of three reacting species. However, a robust theory to easily derive the conditions for diffusion-driven instability of general systems made of N reactants is still missing. For this reason a limited number of Turing models with more than two species can be found in literature. The few examples include ecological models, see [White and Gilligan, 1998], and models developed by Meinhardt in [Meinhardt, 2004] .

This is due to the fact that as the number of species (reactants) increases the derivation of the conditions required for a diffusion-driven instability becomes more challenging. Moreover, when a complex system is studied, as it is often the case in biology or in physics, it is usually preferable to develop the simplest model that is able to reproduce a desired behavior. This strategy is sometimes referred as coarse-grained modeling and it consists in using a high level of abstraction. On one side, this is a safe and conservative strategy to develop models with the minimum number of "ingredients" required to explain a behavior. On the other side, a minimal model has a reduced number of parameters and it is usually easier to study. However, abstract models have also limited prediction capabilities and are more difficult to compare with reality.

To explain better how different levels of abstractions can affect biological modeling, I will use an example of the Drosophila circadian clock that has a well-known underlying biological network. The biological interactions that drive the Circadian clock in Drosophila depend on protein phosphorylation states, translocation of proteins in the nucleus, protein complex formation, protein degradations and gene regulation, see the schema in Figure 1.7A. This schema can be entirely translated into a model, see for example [Leloup et al., 1999], and we will obtain a model with at least ten ordinary differential equations and with more then twenty parameters. With the right set of parameters this model will exhibit oscillations of the proteins *Per* and *Tim* that reflect the Circadian clock. However, we could also build a model with a greater level of abstraction that captures only key interactions: for example the fact that *Per* and *Tim* form a protein complex that eventually inhibits their own expression, see Figure 1.7B. In this case, the model would have only five ordinary differential equations but again, with the right parameters set, the model will exhibit oscillations. The level of abstraction could be further increased by considering that the dynamics of the two proteins *Per* and *Tim* are coupled, see Figure 1.7C. Finally, we could even consider the simplest model capable of oscillation by approximating proteins and mRNAs with a single reactant and by implementing the negative feedback with a single delayed self-inhibition, see Figure 1.7D.

Each of this models is capable of oscillations and it is correct under the as-

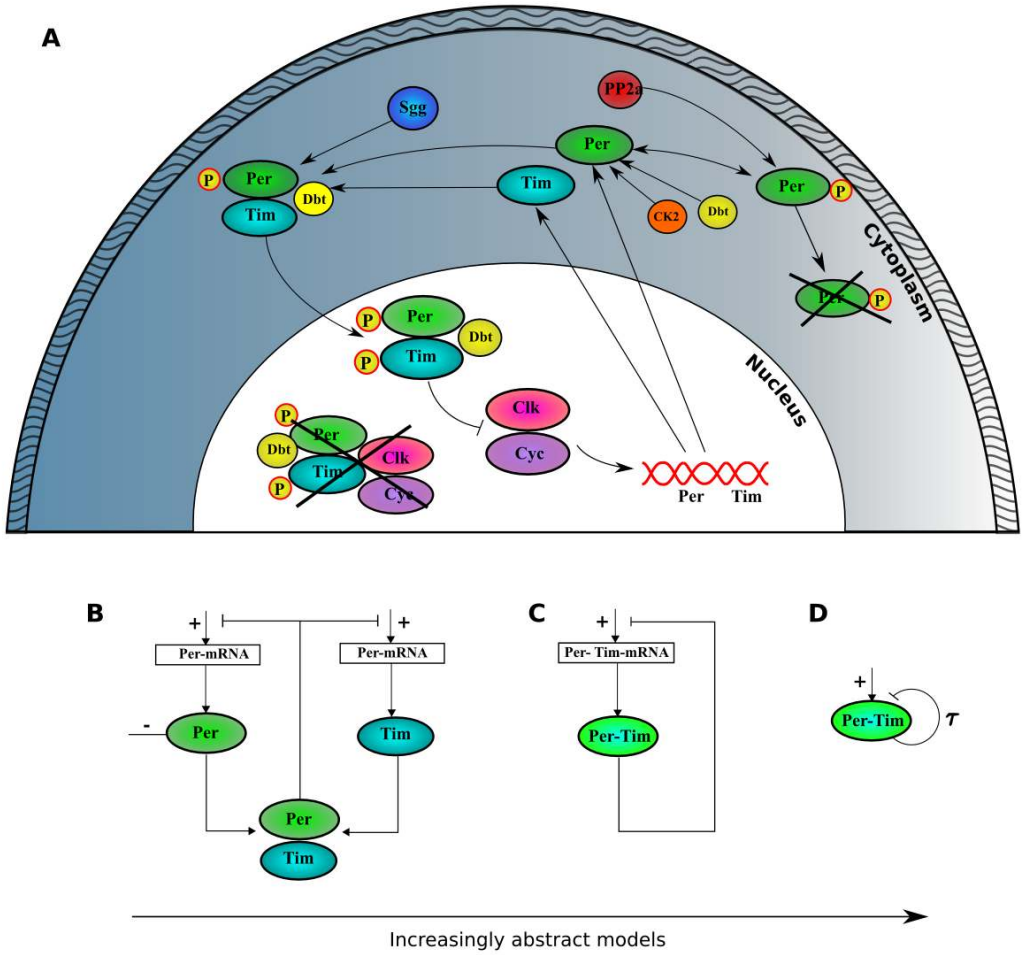

Figure 1.7: (A) A schema of the biological network responsible for the Circadian rhythm in Drosophila (adapted from [Hardin, 2005]), the concentrations of *Per* and *Tim* oscillate over time. A detailed model that mimics all these interactions with a set of ten differential equation was presented in [Leloup et al., 1999]. (B) A more abstract schema of the Circadian clock that considers only protein and mRNA concentrations of *Per* and *Tim*. The two proteins form a complex that inhibits the mRNA production. (C) An increasingly abstract schema that couples the concentration of *Per* and *Tim* because they depend on the same feedback. (D) A schema that approximate mRNAs and proteins with a single reactant. The feedback on transcription is implemented with a delayed auto-inhibition. This is the highest level of abstraction that can capture the oscillating behavior.

sumption that are taken. Nevertheless, from the biological point of view not all the models allow to address the same type of questions. For example if we are interested in predicting the effects of a reduction in the *Dbt* protein or if we want to predict the concentration of a specific nuclear protein complex, only the more detailed model will be suitable. However, even the simplest model showed in Figure 1.7D, that contains only a delayed negative feedback, can provide some unintuitive predictions about the real system. For example, it allows us to predict in which way the basal production of the proteins versus the degree of delay in the negative feedback can affect the period of the oscillations.

To conclude, regarding reaction-diffusion systems, Turing provided an abstract model for pattern formation, in the Circadian clock example corresponds to the model in Figure 1.7D, and the current challenge is to develop more realistic models that reflects the biology that underlies development, corresponding to Figure 1.7A in the Circadian clock example. In this thesis, I take a step towards this direction by developing a more realistic three-species Turing model that aims to explain limb skeletal patterning. The model is presented in the third section of the Results chapter and a more detailed discussion on the level of abstractions of Turing models is presented in the last chapter.

1.1.1.5 Experimental evidences

Although theoretical models predicted that the oscillating Belousov-Zhabotinsky reaction could in principle produce a diffusion-driven instability, later studies found that the diffusion coefficients that were required contrasted with the physical constrains of the systems [Rovinskii, 1987]. The first experimental evidence for a stable reaction-diffusion type (d) pattern was found only a few years later at the University of Bordeaux [De Kepper et al., 1991]. In this study, De kepper and colleagues observed the emergence of a stationary Turing pattern in a tiny gel reactor in which malonic acid was added to a variation of the chlorite-iodide reaction which was known to have a rich dynamic behavior. This system, usually referred as CIMA, produced a series of parallel stripes that eventually broke into spots, see Figure 1.8A. Following studies, see [Szalai et al., 2012] for a review, confirmed the impressive correlation between the patterns produced by the CIMA reaction and those produced by a Turing system, see Figure 1.8B.

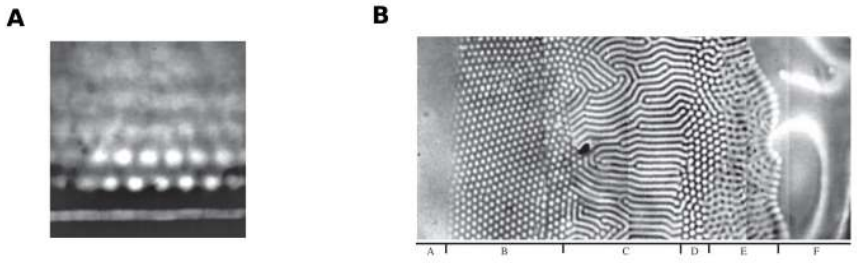

Figure 1.8: (A) an example of Turing pattern obtained in the original chlorite-iodide malconic acid reaction (CIMA). (B) Different types of Turing pattern that can be obtained by playing with the parameters of the CIMA reaction. Figures taken from [Szalai et al., 2012].

The CIMA systems was the first demonstration that Turing patterns could indeed be formed by simple chemical reactions. This reconfirmed the relevance of Turing mechanisms for patterning in development. However, only in recent years it has been shown that various developmental systems behave like Turing models. In the following paper I review some of these developmental systems.

1.1.1.6 First article: Turing Patterns in Development: What About the Horse Part?

Marcon L, Sharpe J. Turing patterns in development: what about the horse part?
Curr Opin Genet Dev. 2012 Dec; 22(6): 578-84. DOI: 10.1016/j.gde.2012.11.013

1.1.1.7 Conclusions and discussion

In this section, I presented the original reaction-diffusion model proposed by Turing and I gave an historical overview of the reaction-diffusion models that were proposed after him. I presented the mathematical conditions derived by Murray that have to be satisfied to form a Turing pattern. I showed that these two conditions correspond to the two informal requirements introduced by Gierer and Meinhardt: local auto-activation and long range lateral inhibition. According to these conditions, two minimal models made of two reactants can generate a Turing pattern: the Activator-Inhibitor model (AI) the Substrate-Depletion model (SD). In the first model, the two reactants form periodic spatial patterns that are in phase (overlapping), while in the second model they develop periodic spatial pattern that are out of phase (complementary). I also showed that all the reaction-diffusion models presented after Turing can be related to one of these two core models.

I continued the section with a discussion about the different level of abstraction that can be used to model biological systems. In particular, I showed that depending on the abstraction level, only certain biological questions can be addressed. In the following section, I presented an overview of the biological systems that are currently believed to be patterned by Turing models. Although, several studies showed a striking correlation between abstract Turing models and experimental patterns, in most cases the Turing molecules have not yet been identified. Only two recent studies have developed more realistic models by considering specific signaling molecules: the lung branching model presented in [Menshykau et al., 2012] and the model of hair follicle formation presented in [Klika et al., 2012]. The first study reproduced the qualitative behavior observed during lung branching but it was not tested against experimental perturbations. The second study demonstrated that, in contrast to what was previously reported, a model implemented by Eda and Bmp-signaling was not able to produce a stable Turing pattern. This negative result highlights that the development of more realistic models can indeed be key to identify the molecules may implement the Turing network.

In this thesis, I propose two Turing models to elucidate the mechanisms that underlie digit patterning in the vertebrate limb. The first model is based on an abstract Activator-Inhibitor model and it is used to show that a combination of reaction-diffusion and Positional Information underlies digit patterning. The second model is derived from literature and experimental perturbations and it is used to show that a Turing network implemented by Bmps, Wnts and Sox9 controls the patterning of the digits.

1.1.2 Positional Information model

At the beginning of the XX century most of the work in embryology was focused in understanding how regional specificity was induced during development. Inspired by the work of Driesch, two Swedish scientists, Runnström and Hörstadius, were interested to find the mechanism that induced cell fates during sea-urchin development [Hörstadius, 1936, Olsson, 2007]. Experiments performed by Hörstadius showed that at early stages of development, the cell fates were specified in graded manner: cells in the anterior pole of the embryo had a graded fate of animalness (epidermal determination) and those in the posterior pole had a graded fate of vegetalness (endodermal determination). From this evidence the two scientists concluded that cell fates had to be controlled by two opposing gradients. This idea was further developed by Grunenberg [Grüneberg, 1951] and Child [Child, 1941] that proposed the controversial idea of a morphogenetic field that depended on the concentration of a graded inducer.

1.1.2.1 French Flag Problem

In the late sixties, the idea of a gradient as inducer was formalized and extended by Lewis Wolpert, a British scientist that was interested in understanding the induction of cell fates in Hydra and sea-urchin. Wolpert in [Wolpert, 1968, 1969] proposed a model based on a graded inducer that was called the French Flag Problem and that later will be known as the Positional Information Model. The model described a mechanism of cell fate induction that consisted in two phases:

- *Specification*: In a first phase a gradient of a substance, that Wolpert calls morphogen using the term introduced by Turing, is established along the space. The gradient can be formed by alternative mechanisms, for example by local production and diffusion or by active transport. Different mechanism can produce different gradient profiles. The original example presented by Wolpert in [Wolpert, 1968] was based on local morphogen production at one extreme coupled with local sink at the other extreme and diffusion. According to Wolpert when the morphogen concentrations at the production site and at the sink side are fixed a linear gradient is formed, see Figure 1.9A. More recent implementations of the gradients are inspired by biological examples and assume local production, uniform first order decay and diffusion to generate an exponential gradient profile, see Figure 1.9B.

- *Interpretation*: In a second phase the gradient acts as a coordinate system for the cells and drives their differentiation. In particular, the genome of the cells encodes a mechanisms that react differently according to different morphogen concentrations. In this way different thresholds of the morphogen,

for example α_1 and α_2 in Figure 1.9, can be interpreted to form a spatial pattern, see the French Flag example in Figure 1.9 .

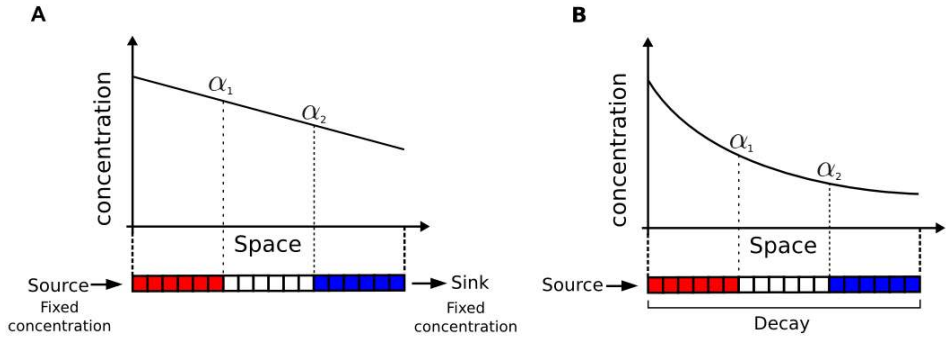

Figure 1.9: Positional Information model. The two graphs show morphogen profile along the space, α_1 and α_2 are two morphogen thresholds. The colored region in red, white and blue represent three different cell fates. A) A linear morphogen gradient created by local morphogen production at one extreme and a local sink at the other extreme. B) An exponential gradient created by local production, uniform first order decay and diffusion.

It is worth of attention, that the first phase (*specification*) requires diffusion or cell communication, while the second phase (*interpretation*), in the simple formulation proposed in [Wolpert, 1968, 1969], is cell-autonomous. Positional Information Models are commonly referred as "hierarchical mechanism" to highlight that in their simple formulation the interpretation phase is usually considered cell autonomous and does not feedback to the specification gradient.

1.1.2.2 Experimental evidence

The first experimental evidences that supported the Positional Information model was found in the chick limb. First, Summerbell and Wolpert [Summerbell et al., 1973] showed that a gradient coming the distal ectoderm of the limb (the Apical Ectodermal Ridge) provided positional values to pattern the proximal-distal axis. However, they proposed that the interpretation phase relied on a timing mechanism rather than a simple threshold-response. Successively, Tickle and colleagues [Tickle et al., 1976, 1975] showed evidence that the posterior region of the limb emanated a gradient that was responsible for the specification of the digits, when the gradient was duplicated a mirror duplication of the digits occurred. The

Proximal-Distal (P-D) and the Anterior-posterior (A-P) patterning of the limb are discussed in more detail in section 1.3. Another classical model that was studied in the context of Positional Information was the regeneration of Hydra [Wolpert et al., 1972].

While evidence existed for the involvement of gradients in early embryo patterning, the dynamics of the specification phase (formation of the gradients) remained largely unknown. The system in which the specification phase is best understood is the determination of the basic body plan of Drosophila during the blastodermal stage [Johnston and Nüsslein-Volhard, 1992]. Several studies [Frohnhöfer and Nüsslein-Volhard, 1986, Johnston et al., 1989] identified that a maternal gene called Bicoid (Bcd) was expressed in a graded manner along the Anterior-Posterior axis of the Drosophila egg and that was responsible for the patterning of the body plan. Many parameters of this morphogen are currently known, for example its the decay rate [Drocco et al., 2011, Liu et al., 2011, Liu and Ma, 2010] and its diffusion constant [Abu-Arish et al., 2010, Porcher et al., 2010], and it is clear that Bcd forms a negative exponential gradient from maternal deposited mRNA. It is however still controversial to which extent the gradient reaches a steady state [Porcher and Dostatni, 2010] and it has been proposed that pre-steady sate dynamics may be relevant for the interpretation phase [De Lachapelle and Bergmann, 2010].

The Drosophila body plan determination is also a classic system to study the interpretation phase. The patterning mechanisms that are best understood are the Dorso-Ventral (D-V) patterning and the segmentation of the Anterior-Posterior axis (A-P). The first is based on the interpretation of the Dorsal (Dl) morphogen to pattern the embryonic germ layers [Morisalo and Anderson, 1995, Moussian and Roth, 2005]. The second is based on the interpretation of the Bcd gradient and posterior determinants to pattern gap, pair-rule and segment polarity genes [Akam, 1987, Ingham, 1988]. This system is the best example of hierarchical system and consists of consecutive and independent steps that are responsible for segment patterning: from the initial maternal gradient to segment polarity gene expression, see Figure 1.10A . The step that is better described is the gap gene network system, that implements the first interpretation phase to drive the expression of broad non-overlapping gap gene domains from the morphogen concentrations [Jaeger, 2011]. In recent years a model of the gap gene network was reversed-engineered from data [Reinitz et al., 1998] and it was showed that it could replicate the gap gene dynamics by interpreting the morphogens in a purely cell-autonomous manner (without cell-communication). This model also managed to show that the spatial shift of gap gene domains, that is known to occur over time, could be explained only with cell-autonomous mutual inhibitions [Jaeger and Martinez-Arias, 2009], see Figure 1.10B . This result highlighted that a cell-autonomous model based on the original threshold-response postulated by Wolpert could indeed account for the complex gene expression dynamics observed during development.

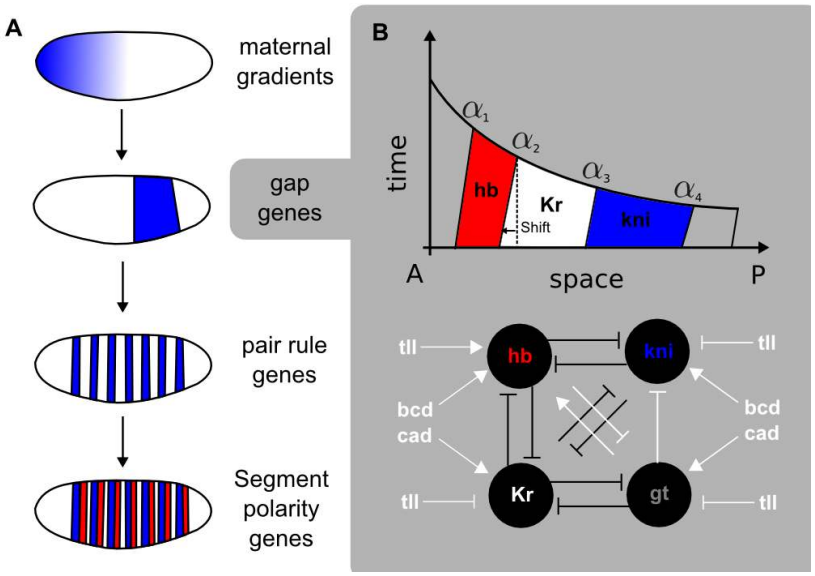

Figure 1.10: A) The segmentation network of the Drosophila. From to bottom, the consecutive step that allow to interpret the maternal gradients to express the segment polarity genes. B) The first step of interpretation that drives the expression of the gap gene system. The graph on top shows the interpretation of the Bcd gradient to express three gap genes: Hunchback in red, Krupple in white and Knirps in blue. On the bottom, the gene network that drive such interpretation. The mutual inhibitions highlighted with black colored lines are the one responsible for the anterior shift of the gap genes.

However, recent studies [Kerszberg and Wolpert, 2007, Nahmad and Stathopoulos, 2009, Ochoa-Espinosa et al., 2009] have challenged the original Positional Information model proposing that in many system a morphogen gradient would be too noisy and unable to drive precise and reliable patterning based on thresholds. It was instead proposed that the interpretation phase may involve temporal integration and that therefore different patterning regions could be specified according to the morphogen exposure time. A recent study provided good experimental evidence that such temporal integration is indeed involved in the interpretation of Sonic Hedge Hog to pattern the five different regions of neural tube [Balaskas et al., 2012]. Finally, also in limb development, classic positional information systems as the Proximal-Distal (P-D) and the Anterior-Posterior (A-P) patterning are being extended to consider growth and temporal integration [Towers et al., 2008], this is discussed in detail in section 1.3.

To conclude, the four decades of experiments that followed the initial model proposed by Wolpert have provided good evidence that morphogen gradients are

involved in the patterning of the embryo. However, they have also raised doubts against the simple interpretation based on morphogen thresholds. This simple model was often found to be unable to account for the precision and robustness that is observed in development. For this reason, the field in currently proposing models with more sophisticated interpretation-phases that consider growth or temporal integration.

1.1.2.3 Conclusions and discussion

In this section I presented the Positional Information model of Lewis Wolpert [Wolpert, 1969]. The two phases that are at the base of the Positional Information model were described: the specification phase, namely the formation of a morphogen gradient trough cell-communication (E.g diffusion), and the interpretation phase, that describes the way in which cells react to different morphogen concentration. I showed that in the simplest Positional Information formulation the interpretation phase is based on morphogen thresholds and is cell-autonomous. Several studies have shown that a simple threshold response model was unable to account for robustness and precision of patterning. For this reason more complex models that involve more sophisticated interpretation dynamics are currently being developed.

Positional Information models are often described as hierarchical mechanism, highlighting the fact that the interpretation-phase is usually cell-autonomous and does not feedback to the specification phase (the spatial coordinates). This constitutes the mayor difference between Positional Information and Turing models. Conceptually, the Positional Information model relies on a pre-existing asymmetry to explain how the breaking asymmetry takes place (E.g an organizing region releasing a morphogen). The recursive application of this assumption invokes eventually the presence of some pre-existing asymmetries already in the egg, that encode the information at the base of the whole development, see for example the maternal gradient of Bicoid (Bcd) in the segmentation network in Drosophila (Figure 1.10). In contrast, a Turing model does not require prior asymmetries and the specification can occur only trough the amplification of random initial fluctuations coupled with cell communication. This fact does not imply however that Turing mechanism and Positional Information can take place together.

Interestingly, already in the late eighties [Wolpert, 1989] Wolpert describes the possibility that a wave-like pre-patterning mechanism (Turing) could work in combination with Positional Information. Wolpert analyzes the pro and cons of the two models and recognizes that for isomorphic periodic patterns, like the digits in the limb, a wave-like pre-patterning mechanism would be more robust and easier to evolve. One argument that Wolpert uses in favor of Turing system, is that for the formation of N identical structures the Positional Information model would

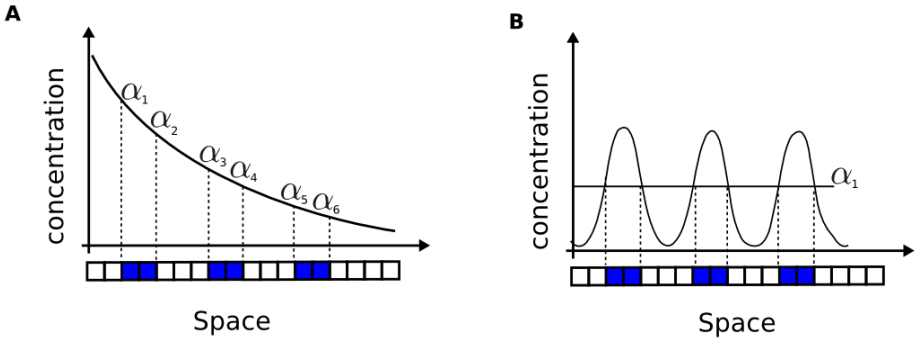

Figure 1.11: A) To specify three isomorphic fates along the space (blue regions) the positional information model require to interpret 6 thresholds, α_1 to α_6. B) A Turing mechanism produces an isomorphic periodic pattern along the space. The three blue regions can be interpreted with only one threshold α_1.

require the ability to interpret at least $2N$ thresholds of the morphogen gradient, see Figure 1.11. Moreover, to perform the interpretation robustly, a Positional Information model will require a large number of interactions that are less likely to be evolved than a wave-like pre-patterning mechanism "ab initio". Therefore, Wolpert suggests that a combination of a wave-like spacing mechanism with the Positional Information model may be more suitable to explain the variety of patterns shown in the embryos. In the case of digits for example, a Turing mechanism could specify the presence of the digits (periodic pattern) and a Positional Information model based on an Anterior-Posterior gradient could be responsible for digit identity. More Recently the idea of combining a Turing mechanism and the Positional-Information model to explain development has gained new popularity [Kondo and Miura, 2010, Miura, 2013].

It is becoming increasingly clear that the developmental program that drives the patterning of the early embryo is more complex that we previously thought and often relies on a combination of Positional Informations, Turing mechanisms and morphogenetic events, all being orchestrated to account for robustness and precision. The model of limb development that I propose in last section of the Results chapter represents a first attempt to combine a Turing mechanism, Positional Information signals and realistic growth to explain patterning. We show that such model can robustly reproduce the dynamics of digit patterning.

In the next section I introduce the concept of morphogenesis and I discuss its relation to the Positional Information model and the Turing mechanism.

1.2 Morphogenesis

Scientists have always been fascinated by the variety of morphologies that are produced during development. The first attempt to formalize the general principles that underlie morphogenesis were made at the beginning of the XX century by D'Arcy Thompson [D'Arcy, 1963]. Traditionally, the term morphogenesis referred to the whole process of creation of organs an tissues, including the patterning events that lead to cellular differentiation. In recent years however, with the advance of imaging technology, the study of morphogenesis has mainly focused on describing the cellular behavior that drive tissue movements observed in development [Bénazéraf et al., 2010, Keller, 2013, Wyngaarden et al., 2010].

There are two types of quantitative data that describe tissue movements [Sharpe, 2011]: tracking data, where tissue points are tracked over time with live microscopy, and fate maps, that consist in labeling a population of cells (or a single cell) and to follow its spatial evolution over time. The fist type of data can be used to extract the displacement vectors (or velocity vector field) of the tissue points over time, see Figure 1.12A . The second type of data provides information about the local deformations that a part of tissue undergoes, see Figure 1.12B. Studies of the morphogenesis in Arabidopsis [Kuchen et al., 2012, Rolland-Lagan et al., 2003] have shown that these two type information are mathematically related. In particular, when the time between the fate map labeling and its observation is small, the deformations of the labeled populations become a good approximation for the tensors of the correspondent velocity vector field. In other words, from tracking data it is possible to derive the displacement velocity vectors and from fate maps it is possible to derive its tensors, see Figure 1.12.

When the imaging technique provides singe-cell resolution of the whole organ, it is possible to track the behavior of each individual cell. This is the ideal scenario to study morphogenesis and it is the best way to relate single cell behaviors with the final morphology of the organ. However, it is commonly the case that the tracking data has a much lower spatio-temporal resolution and provides only a description of the global tissue movements. In this case, the associated velocity vector field abstracts the underlying cellular behaviors and represents only global tissue movements. These global movements can be obtained by different cellular behaviors, for example the velocity vector field associated with directional outgrowth can equally result from directed cell divisions or from cell migration.

Fate maps and its tensors provide instead relative/local information and are easier to relate to local cell-behaviors. A tensor contains three types of information: growth, anisotropic deformation and rotation, see Figure 1.12B. The first is

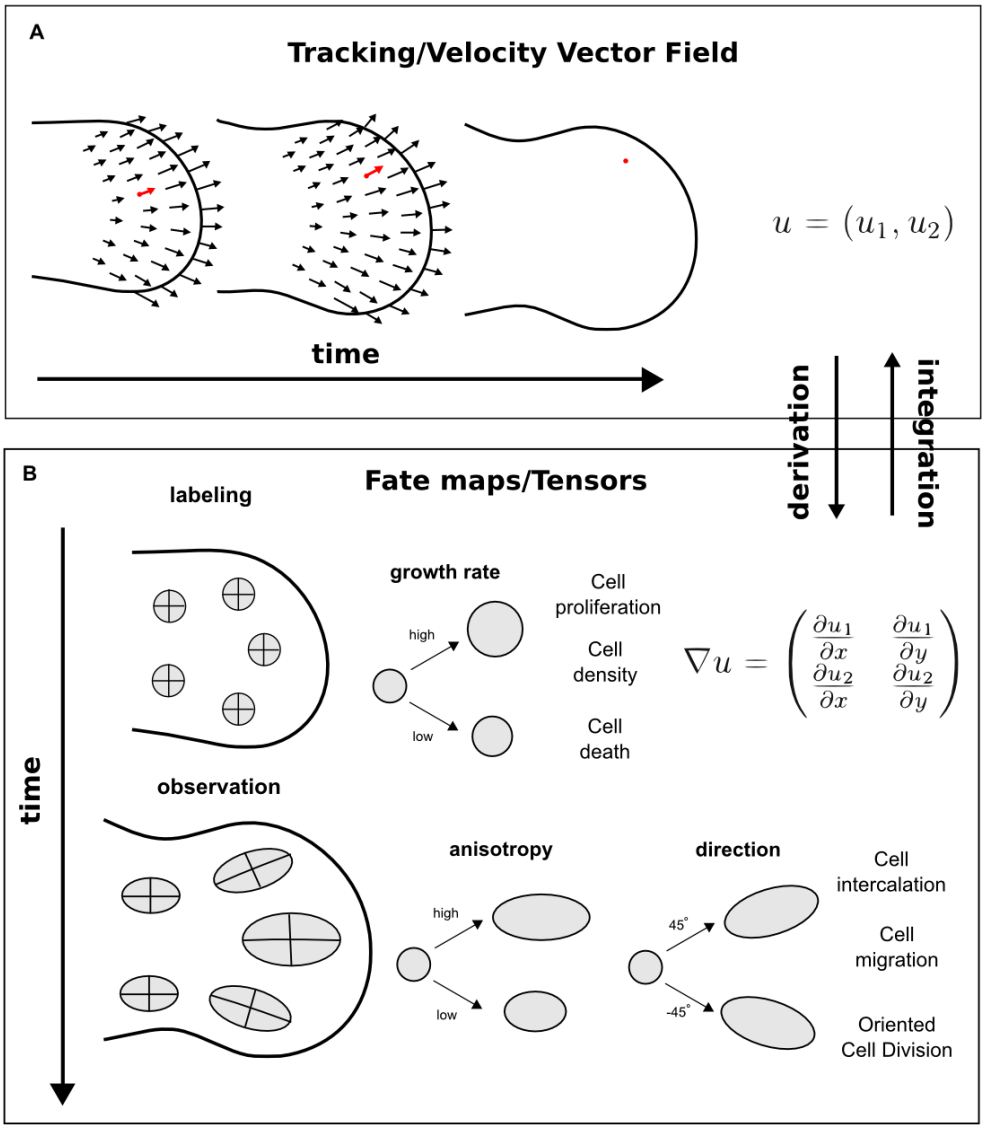

Figure 1.12: Two types of tissue movement data: an example is shown for the two-dimensional case. A) Tracking and live imaging can be used to derive the displacement velocity vector field (the arrows and corresponding function u). The red point and the arrows highlight the tracking of a single tissue point over time. B) Left: on top cell populations are labeled at an early time in development, on the bottom the labeled cell population have deformed because of morphogenesis. Right: different characteristic of the deformed labeled populations encode for the various tensor components of the velocity vector field, growth, anisotropy and rotation. The first component relates with cell proliferation, cell death or cell density. The last two components relate with directional cell behaviors like cell migration, oriented cell division or intercalation.

often related with cell proliferation or cell density, while the last two behaviors can be obtained by different directed cellular behavior like oriented cell-division, intercalation or migration, see Figure 1.12B.

1.2.1 Morphogenesis and patterning: Morphostatic vs Morphodynamic

It is quite common to consider morphogenesis and patterning as two distinct parts of development [Wilkins, 2002]. The first is assumed to deal with the change of cellular arrangements that drive shape change, the second is focused on the molecular interaction that drive the change of cell states (gene expression). However, it is clear that in most developmental systems both processes are happening simultaneously and are tightly coupled. In this cases, even if a very short development times are considered it appears that no temporal hierarchy between these two processes can be established. Developmental systems where a clear hierarchy between patterning and morphogenesi can be traced (it is commonly assumed that patterning comes first) have been called Morphostatic, systems where an interplay between the two exists have been called Morphodynamic [Salazar-Ciudad et al., 2003]. These two class of systems are profoundly different, in Morphostatic systems the change in form is basically a read-out of the change in cell- states while in Morphodynamic systems the change in form and the change in cell-states feedback into each other, see Figure 1.13.

Morphodynamic developmental systems can only be study by analyzing both morphogenesis and patterning simultaneously.

1.2.2 Mutliscale-Modeling

Although morphogenesis and patterning are very often simultaneous, the timescale at which considerable morphological or cell-state changes happen can differ greatly. It is often the case, that changes in cellular behavior are slower that changes in gene expression. In addition, cell-states or morphological events can have different impacts at different spatial scale: cells, tissues or organs. For this reason, computational models of development have to deal with different time and spatial scales. This type of modeling is known as multiscale-modeling [Grima, 2008] and in recent years has gained increasing popularity. The main challenges of multiscale-modeling are computational and technical. It is indeed computational expensive to model the whole system at the lowest spatial and temporal scales. Therefore, multiscale-modeling is the art of finding the best trade-off between spatio-temporal precision, right abstraction level and computational load.

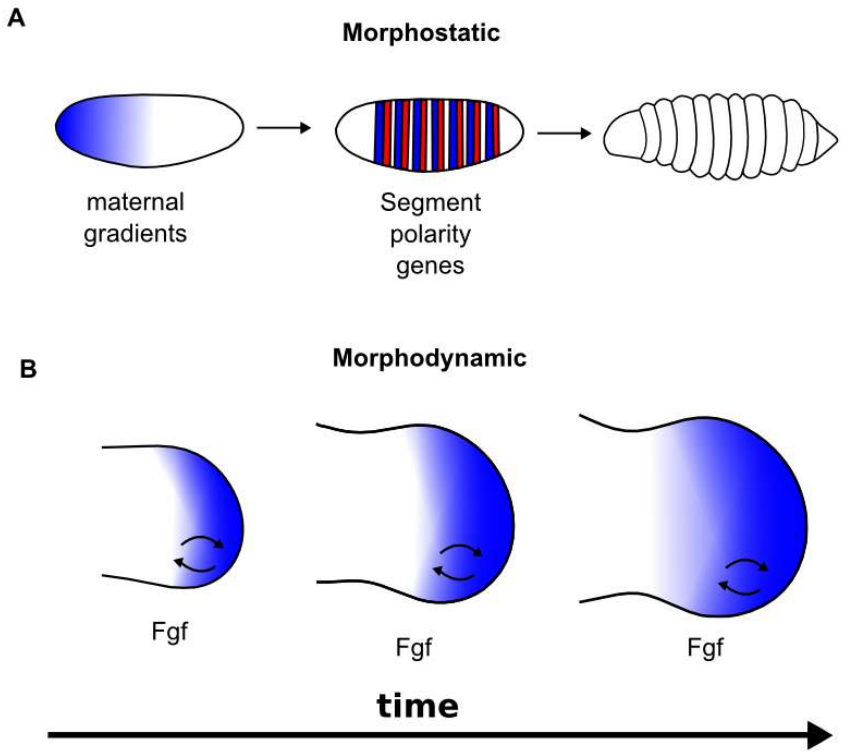

Figure 1.13: Examples of Morphostatic and Morphodynamic systems. A) The Droshophila segmentation is a Morphostatic process. Segment polarity genes are specified first and morphogenetic events occur after. B) Limb development is a Morphodynamic system: Fgfs promote proliferation that changes the limb shape. The cell that experiment Fgf-signaling continuously change overtime because of growth. The arrows represent the continuous feedback between morphogenesis and cell-states.

1.2.3 Positional Information and growth

In section 1.1.2, I presented the original Positional Informational Model proposed by Lewis Wolpert. In its simple formulation this model considers a Morphostatic scenario where the cells receive positional values by a steady state gradient. However, already in his original work [Wolpert, 1969] Wolpert was concerned with the coordination between positional information and growth and in particular with problem of scale-invariance, that is how embryos with different sizes could produce similar patterns with likely the same Positional Information system. Wolpert suggests that smaller organism would have shorter gradients and bigger organism gradients with longer ranges. In addition, the interpretation along one axis could be coupled with the level of a morphogen along another axis in order to maintain the overall proportions, see the left part in Figure 1.14A.

In flies, experimental evidence that the Bcd maternal gradient has longer range in bigger flies and shorter range in smaller flies was indeed found [Gregor et al., 2005]. However, other studies showed that the position of gap genes was less dependent on Bcd dose variation than expected [Houchmandzadeh et al., 2002, 2005]. It was therefore proposed that scaling could be obtained by specific gap gene interactions [Vakulenko et al., 2009] but this hypothesis has never been validated experimentally.

Finally, the French Flag Problem also predicts that if the parameters are unchanged and the domain is increased no structure will be formed behind the last interpreted threshold, see the left part in in Figure 1.14B.

1.2.4 Turing mechanism and growth

Turing mechanisms from a pattern with an intrinsic length-scale (wavelength) that depends on the parameters. The length-scale determines the spatial periodicity of the pattern and therefore the number of peaks that are formed in a spatial domain. Similarly to the case of Positional Information, scale invariance in reaction-diffusion system can be obtained by decreasing the wavelength in smaller organism and increasing the wavelength in bigger organism. This can be done by coupling the parameters that control the wavelength with domain size. The advantage of Turing mechanisms on Positional Information models is that the maintenance of proportions along the different axis is inherently provided, see right part 1.14B.

If the parameters are unchanged and the domain is increased, more peaks are formed, see right part in Figure 1.14B. If the domain is growing continuously new peaks are formed either by peak insertion or by peak splitting. In one dimension this has been shown to depend on the speed of growth [Crampin et al., 1999]

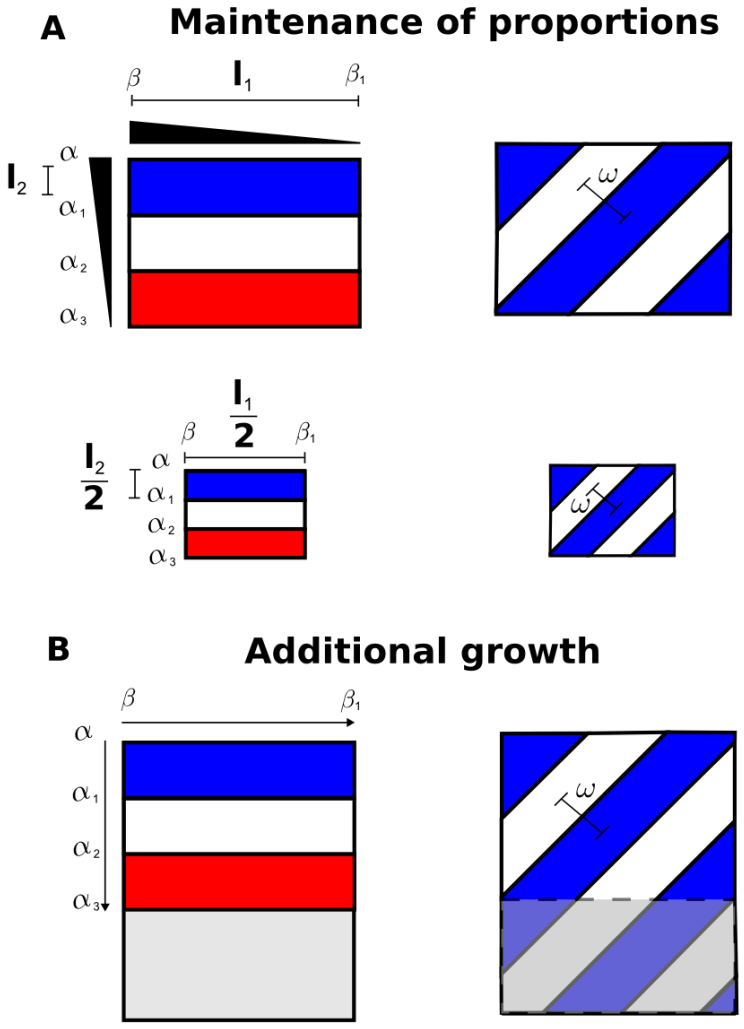

Figure 1.14: A) Left column: on top, a Positional Information model specifies a pattern along two axis with characteristic lengths l_1 and l_2 obtained by interpreting two independent morphogens, α_1, β_1 represent the interpreted thresholds; on bottom, to obtain a smaller pattern with the same proportions, the two interpreted thresholds α_1, β_1 have to change in a combined manner such that the characteristic lengths are reduced proportionally. Right column: on top, a reaction-diffusion model forms stripes in two dimension (blue stripes), the pattern has an intrinsic wavelength ω; on bottom, scale invariance on a smaller domain can be obtained by reducing the wavelength ω and proportions are automatically maintained. B) Left: when the domain is increased in the Positional Information case, no pattern is formed behind the last interpreted threshold α_3. Right: when the domain is increased the Turing mechanism forms additional stripes.

and in the models proposed by Gierer and Meinhardt [Meinhardt, 1982] on the saturation of the auto-catalysis, see Figure 1.15.

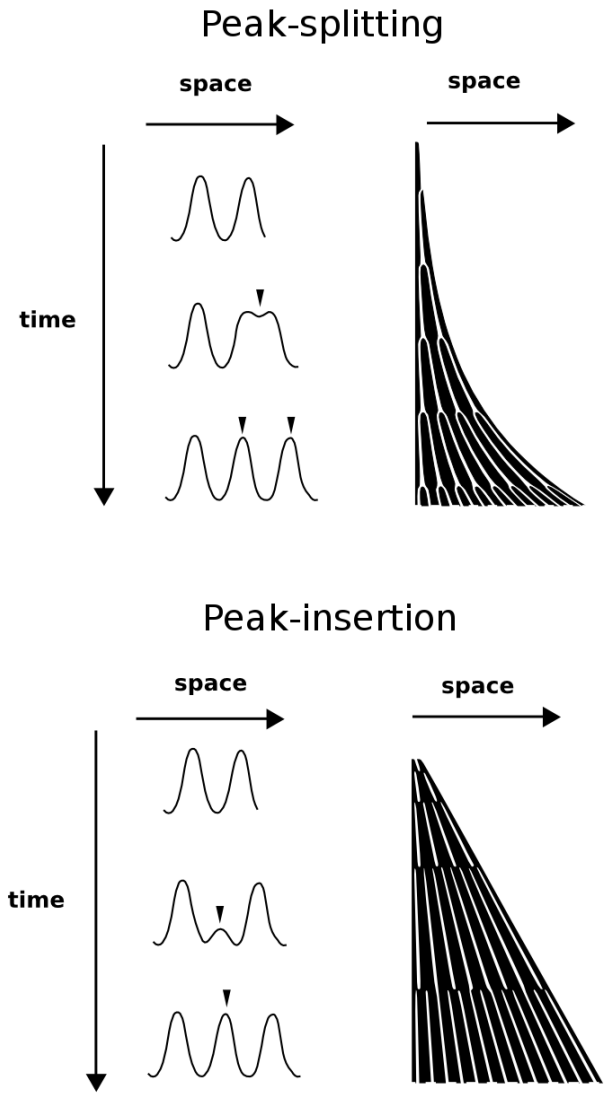

Figure 1.15: Reaction diffusion simulations inside one-dimensional growing domains. Top row: peak splitting as highlighted by the black arrow happens with the Substrate-Depletion model (left) or with exponential growth (right). Bottom row: peak insertion as highlighted by the black arrow happens with the Activator-Inhibitor model (left) or with linear growth (right).

1.2.5 Conclusions and discussion

In this section I introduced the concept of morphogenesis and the two types of data that can be used to study tissue movements: tracking data and fate maps. I showed, that these two data type can be respectively described by velocity vector field and by tensors and that the two descriptions are mathematically related. A velocity vector field can be used to describe either single-cell tracking data or a global tissue movements. In the second case the velocity vector field abstracts from the underlying cell behaviors.

Successively, I introduced the difference between Morphostatic and Morphodynamic systems highlighting that in Morphodynamic systems patterning and morphogenesis have to be study simultaneously. Multi-scale modeling was presented as a way to handle the complexity of models that combine both patterning and morphogenesis. Finally, I showed how Positional Information and Turing models react when coupled with growth and I discussed the problem of scale-invariance.

In the third section of the Results chapter, I present a multi-scale Morphodynamic model of limb development that combines Positional Information gradients, a Turing model and realistic growth to explore digit patterning. It is showed that this model captures the dynamics of digit patterning and it is able to maintain proportions and account for scale-invariance.

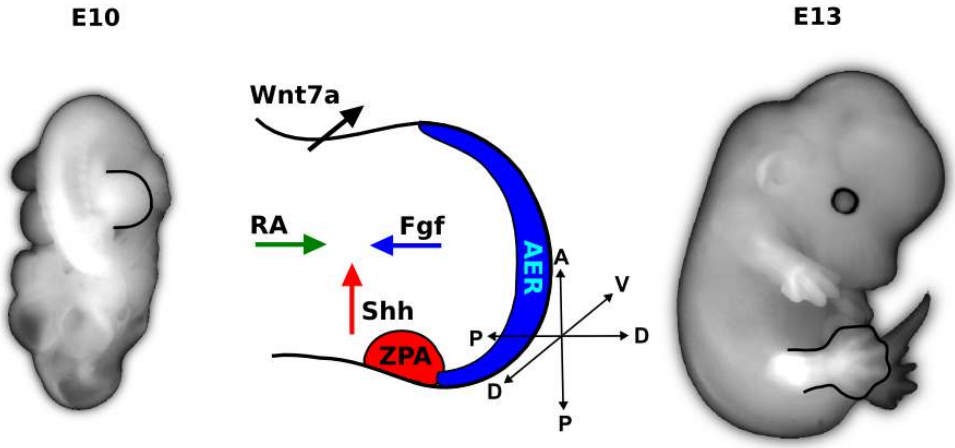

Figure 1.16: On the left, a mouse embryo at 10 days post fertilization, the limb bud (outlined with a black line) protrudes from the body flank as a bulge of undifferentiated mesenchymal cells covered with an ectodermal layer. In the middle, a schema of the limb bud: the three main axis P-D, A-P, D-V and the organizer AER, ZPA, body flank (RA) and dorsal ectoderm (Wnt7a) are highlighted. On the right, a mouse embryo at 13 days post fertilization, the limb bud (outlined with a black line) has developed to form tendons, skeleton and nerves.

1.3 Limb development

Vertebrate Limb development is a classical system to study patterning and morphogenesis and has contributed to various seminal discovery in developmental biology. Its development begins with the protrusion, from the flank of the embryo, of a bulge of undifferentiated cells known as the limb bud, shown Figure 1.16. The limb bud is a precursor of the adult limb made of mesenchymal cells covered with an ectodermal layer, which in the mouse appears around 9.5 days post fertilization and in less than 72h is able to growth and form most of the tissues that are present in the adult limb: tendons, skeleton, and nerves. This process happens along three axis: the Proximal-Distal axis (P-D) the Anterior-Posterior axis (A-P) and the Dorso-Ventral axis (D-V), see Figure 1.16 .

Over the last fifty years, various organizing regions have been identified in the limb. The first organizer to be discovered was the Apical Ectodermal Ridge (AER) [Saunders, 1948] a thickening of the ectoderm at the distal tip which produces Fibroblast Growth Factors (Fgs) that are essential for growth and patterning.

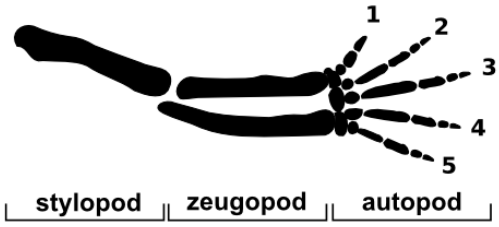

Figure 1.17: A typical skeletal of a tetrapod limb. From left two right the three segments common to all tetrapod: stylopod with one element, zeugopod with two elements and autopod with five digits. The digits are identified with progressive numbers from anterior to posterior.

Another important organizer of the limb is the Zone of Polarizing Activity (ZPA) [Saunders and Gasseling, 1968] a region of cells in the posterior part of the limb that produces Sonic Hedge Hog (SHH) [Tickle et al., 1975] and is important for the correct A-P patterning of the limb. The body flank is another region of cells that is known to participate in patterning and it is believed to produce Retinoic Acid (RA) that is involved in P-D patterning. Finally, it was discovered that the dorsal ectoderm of the limb is important for correct D-V patterning [Geduspan and MacCabe, 1987, Geduspan and Maccabe, 1989, Saunders and Reuss, 1974] and that the difference between the dorsal and the ventral part of the limb is established early in development by restricting Wnt-signaling to the dorsal part [Loomis et al., 1996, Parr and McMahon, 1995, Riddle et al., 1995, Vogel et al., 1995]. This early asymmetry also defines a boundary that divides the limb in two compartments along D-V axis [Arques et al., 2007]. A summary of the organizing regions is shown in Figure 1.16.

1.3.1 Limb skeletal patterning

The Tetrapod limb skeleton can be considered as divided in three segments: the stylopod, that consists of one element (humerus in forelimb and femur in hind limb), the zeugopod made of two elements (radius and ulna in forelimb and tibia and fibula in hind limb) and the autopod that contains wrist and digits, see Figure 1.17. The specification of the skeleton is know to happen in a proximal to distal manner as the limb grows [Summerbell et al., 1973]: the stylopod is specified fist, then the zeugopod and finally the autopod.

Most tetrapods are pentadactyl and their digits have been identified according to the A-P position: fingers are numbered from 1 to 5 starting from the anterior

part of the limb, the thumb is digit 1 and the little finger digit 5, see Figure 1.17. In most tetrapods (E.g mouse and human) digit 1 has only two phalanges while the other have three. Other tetrapod systems like the chick wing, have only three digits with different phalanx numbers. In this case digit identity has often been asserted by counting the number of phalanges.

1.3.1.1 P-D patterning

The progressive appearance of more distal elements during limb development was originally discovered in chick by removing the AER at different developmental stages [Summerbell et al., 1973]. Depending on the time of AER removal more severe skeletal truncation were observed: early removal lead to limbs with only the stylopod and later removals to limbs with only stylopod/zeugopod or with all the three segments. This experiment was the base for the first historical model of limb patterning: the Progress Zone Model [Summerbell et al., 1973]. This model postulated that a permissive signal coming from the AER maintained a clock in the underlying mesenchymal cells. As the limb grew cells exited the region under the influence of the AER (Progress Zone) and according to the time they had spent inside the Progress Zone acquired different P-D fates: the longer they staid inside this zone the more distal fates they acquired, see Figure 1.18A. Another classic experiment that supported the Progress Zone model consisted in irradiating the chick limb mesenchyme with X-ray at different developmental stages: early irradiation lead to loss of proximal structure and late irradiation to more distal structure [Wolpert et al., 1979]. In the context of the Progress Zone Model, it was interpreted that the X-ray irradiation affected the pool of undifferentiated cells in the Progress Zone and therefore compromised the development of more distal structures as time was passing.

Fibroblast Growth factors (Fgfs), that are expressed in the AER and are able to rescue growth after AER removal, were successively identified as good candidates for the AER signal. There are four Fgf ligands expressed in the limb: Fgf8 and Fgf4-9-17, the first is expressed along the whole AER and the last three begin to be expressed posteriorly and expand to the anterior part as the limb grows [Martin, 1998].

The genetic removal of Fgf8 [Lewandoski et al., 2000, Moon and Capecchi, 2000] exhibited an unexpected loss of the stylopod alone. It was successively showed that when Fgf8 was missing, Fgf4 was up-regulated and the transient loss of proximal structure related to the time required for Fgf8 compensation [Lu et al., 2006, Sun et al., 2002]. Consistently, mutants that lack both Fgf8 and Fgf4 were

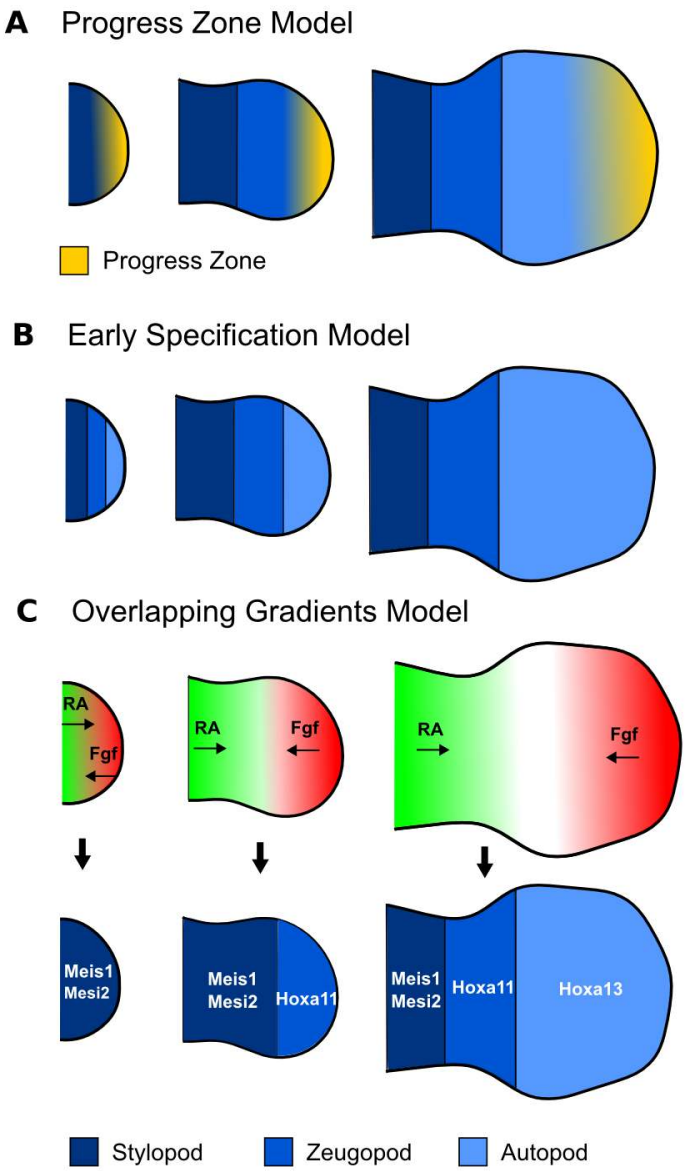

Figure 1.18: Three different models of P-D patterning. A) Progress Zone Model: as the limb bud grows cells exit from the Progress Zone (yellow region): the more time cells spend inside the Progress zone the more distal fates they assume. In this way the three P-D segments are progressively specified. B) Early Specification Model: the three P-D segments are specified early in development and successively expand due to proliferation. C) Overlapping Gradient Model: a balance of Fgf-signaling (in red) and RA signaling (in green) specify the three P-D segments as marked by genetic markers: Meis1/Meis2 mark the stylopod, Hoxa11 the zeugopod and Hoxa13 the autopod.

unable to develop a normal limb [Boulet et al., 2004, Sun et al., 2002]. However, transient expression of Fgf8 and Fgf4 at early stages was enough to correctly pattern the Proximal-Distal axis of the limb.

These results were difficult to explain with the Progress Zone Model. In addition, a recent re-evaluation of the classic X-ray irradiation experiments showed that lost of skeletal elements is not a patterning defect but it is rather due to loss of the skeletal progenitors that are necessary to form condensation [Galloway et al., 2009]. This lead to the idea that a different mechanism was responsible for the dynamic specification of the three P-D segments. It was proposed that the specification of the three P-D segments could happen at early stages of limb development and that the segments successively expanded because of growth [Dudley et al., 2002], see Figure 1.18B. This hypothesis was called the Early Specification model and was used to re-interpret the phenotype of the AER removal by showing that a $300\mu m$ long distal region, that was assumed to progressively overlap with less P-D segments, was undergoing apoptosis when the AER was removed. The X-ray irradiation experiment was instead interpreted assuming that at later stages, when the autopod becomes larger, the probability to lose distal structures became higher. Finally, this model was also supported by experiments that showed a relatively early ability of cells to sort out according to their P-D identity [Barna and Niswander, 2007].

The Early Specification Model proposed a new time window for the definition of the P-D segments but did not provide an explanation for how the regionalization was implemented. A more mechanistic model was proposed only later [Mercader et al., 2000] by showing that a gradient of RA coming from the body flank promoted proximal fates and that Fgf-signaling coming from the AER promoted distal fates. As the limb grew, an interplay between these two gradients was proposed to drive the specification of the P-D segments and three genetic markers: Meis1/Meis2, Hoxa11 and Hoxa13 were proposed as read-outs for the three segments [Mercader et al., 2009], see Figure 1.18C. The model was successively named the Overlapping Gradients Model [Tabin and Wolpert, 2007] and it was proposed that degree of overlap and dose of the gradients could underline the patterning of the three markers.

1.3.1.2 A-P patterning

The study of the patterning along the Anterior-Posterior limb axis has mainly focused on the digits. This has been historically motivated by the pioneering discovery in chick that a mirror-image duplication of the digits was induced when a portion of the posterior mesenchyme, called the Zone of Polarizing Activity (ZPA), was graft in the anterior part of the limb [Saunders and Gasseling, 1968]. This experiment was proposed as the first strong evidence that a Positional Information

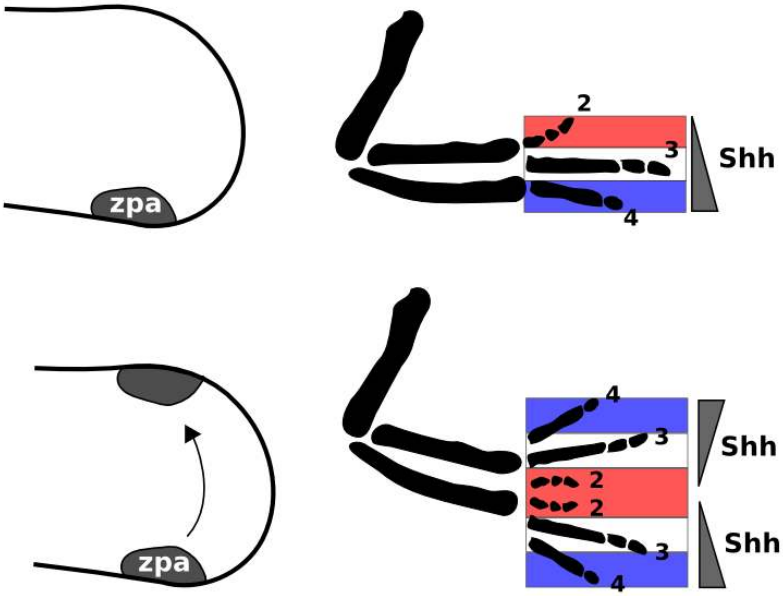

Figure 1.19: The classic ZPA grafting experiment in chick forms the basis for the Positional Information model responsible for digit patterning. On top, the Zone of Polarizing Activity (ZPA) in the chick wing provides a gradient along the A-P axis that instructs the tissue to form the different digits (French flag colors). On bottom, when part of the ZPA is grafted anteriorly, the specification gradient is duplicated and a mirror image duplication of the digits occurs.

gradient patterned the digits according to the French Flag problem proposed by Lewis Wolpert [Tickle et al., 1975], see Figure 1.19. Since then, several studies have focused in finding the morphogen gradient and its interpretation rules, see [Tickle, 2005] for a review. Nevertheless, evidence supporting Sonic Hedge Hog (Shh) as the morphogen came only twenty years after the discovery of the ZPA [Riddle et al., 1993].

Traditionally, limb development experiments were conducted in chick limb, where it was easier to perform manipulations. The chick wing and hind limb have respectively three and four digits with different number of phalanges. Digits in the wing were traditionally numbered from anterior to posterior as digit 2, digit 3 (both with two phalanges) and digit 4 (that has only one phalanx). However, in a recent study [Carkett et al., 2011] the digits of the wing have been re-numbered as digit 1, digit 2 and digit 3. Digits of the chick hind limb are numbered from

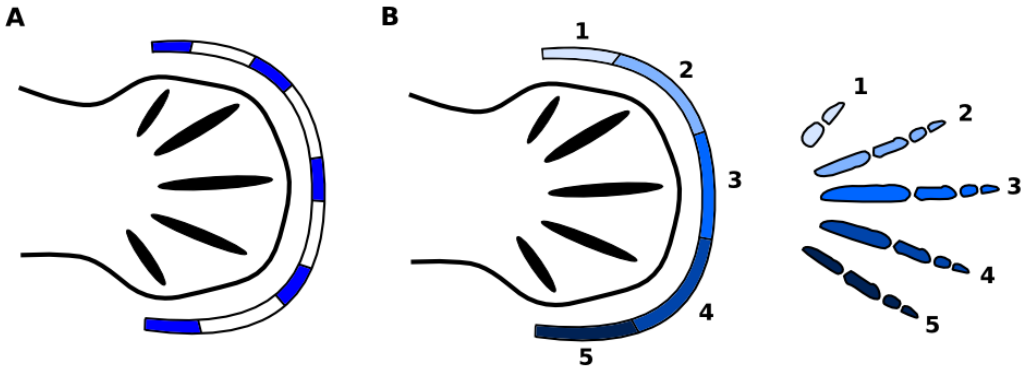

Figure 1.20: Difference between digit specification and digit identity specification. A) Digit specification defines the sequence of digital (blue) versus interdigital (white) fate along the A-P axis. B) Digit identity specification defines the fates along the A-P axis (different blue colors) that drive the specification of phalanx number and the final digit morphology, showed on the right.

anterior to posterior as digit 1 and digit 2 (that have three phalanges), digit 3 (that has four phalanges) and digit 4 (that has five phalanges). Because of the different number of phalanges, even in the case of ectopic digit formation, it was always easy to assess digit identity. For this reason, even though Wolpert had already discussed the difference between digit identity and digit specification (see section 1.1.2.3 and Figure 1.20), for a long time these two concepts were conceptually coupled. In other words, for a long time Positional Information models based on Shh were not only assumed to be responsible for digit identity but also for the specification of the digital vs inter-digital fates.

Recent genetic manipulation in mouse, highlighted that the first asymmetry that is established along the A-P axis of the limb is the anterior expression of Gli3R and the posterior expression of Hand2 [Ros et al., 1996]. These two genes mutually repress one each other [te Welscher et al., 2002] and several studies have shown that Hand2 is required for Shh activation [Cohn, 2000]. 5' Distal Hoxd genes (including the zeugopod marker Hoxa11 and the autopod marker Hoxd13) have also been shown to be essential for Shh activation [Tarchini et al., 2006] and there is evidence that they may act by directly enhancing Shh expression [Capellini et al., 2006]. This suggests that in the onset of limb development Hand2 may promote or interact with 5' Distal Hoxd genes to promote Shh. Once expressed in the posterior part of the limb, Shh forms a gradient along anterior posterior axis and signals by activation of Gli1 and Gli2 and repression of Gli3R,

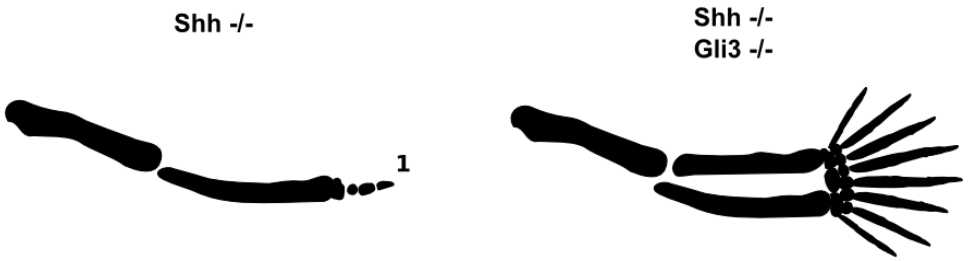

Figure 1.21: On the left, the presence of only one element in the zeugopod and autopod in the Shh mutant is consistent with the Positional Information model based on a Shh gradient. The only digit that is formed is commonly considered to be digit 1. On the right, when both Shh and Gli3 are genetically removed eight digits without identity are formed supporting a Turing mechanism for the specification of the periodic digital A-P patterning.

the repressing form of Gli3 [Varjosalo and Taipale, 2008]. Shh signaling is important for the maintenance of 5' Hoxd Genes and when a bead soaked in Shh is implanted anteriorly, 5' Hoxd Genes are ectopically expressed. Consistently with its role as A-P organizer, when Shh is genetically removed the zeugopod and the autopod form only one element that are usually interpreted as being Shh independent [Chiang et al., 2001, Kraus et al., 2001], see Figure 1.21. In addition, Shh deficient mouse have smaller limbs because the increase in Gli3R is known to inhibit cell-proliferation.

Gli1 and Gli2 deficient mouse form normal limbs suggesting that the main Shh signaling pathway goes trough the repression of Gli3R formation from Gli3 [Litingtung et al., 2002]. Unexpectedly, mouse that lack Gli3 form bigger limbs with eight un-patterned digits and the same result is observed when both Gli3 and Shh are removed [Litingtung et al., 2002], see Figure 1.21. This important result suggests that Shh signaling is not required for digit specification. In agreement with this experiment, previous theoretical studies [Newman and Frisch, 1979, Wolpert, 1989] proposed that the isomorphic pattern of digital vs interdigital fates could be specified by a Turing mechanism (see section 1.1.2.3) and that the main roles of Shh was to provide identity to already specified digits. When the space is increased a Turing mechanism predicts the formation of additional peaks (see section 1.2.4) and this could explain why bigger limbs lacking Gli3 would form more digits (polydactyly). The proposal that a self-organizing Turing mechanism is responsible for digit specification also helps to explain another classic manipulation

experiment: the re-aggregation experiment, that shows a capacity of the limb mesenchyme to self-regulate [Zwilling, 1964]. This experiment consists in removing and mixing limb mesenchymal cells from a donor limb bud and to graft them inside another ectodermal layer to a neutral side of the embryo. The re-aggregated limb buds in chick form relatively normal limbs with two digits, showing that cells that have already received positional cues form organizers are able to re-assemble and to be respecified, see Figure 1.22A. The same experiment in Xenopus lead to to the astonishing formation of limbs with up to 30 digits [Yokoyama et al., 1998]. This not only confirmed the self-regulatory capacity of the mesenchyme but provided a strong evidence for a periodic pattern formation of digits. Finally, another evidence that shows that the limb mesenchyme is able self-organize is the formation of periodic structures in the Micromass culture system [Cottrill et al., 1987], a culture of limb mesenchymal cells that spontaneously forms a chondrogenic periodic pattern reminiscent of a two dimensional Turing simulation, see Figure 1.22B.

While substantial evidences existed for a reaction-diffusion mechanism responsible for digit specification, most studies focused on the extension of the classical Positional Information model to account for the phenotypes observed upon Shh perturbations. The first extension was based on fate-mapping experiments that showed that the descendant of the Shh expressing cells in the ZPA overlapped with the half of the limb encompassing digit 5,4 and 3 [Harfe et al., 2004]. It was proposed that the time of Shh expression rather than Shh-signaling thresholds was the important factor for digit specification. This model was named temporal-spatial-gradient model [Zeller, 2004] and by comparing the Shh expressing region with its progeny it was proposed that cells that expressed Shh for a short time formed digit 3, while cells that progressively expressed Shh for longer time formed digit 4 and digit 5. Finally, since digit 1 was considered to be the Shh-independent digit observed in the Shh mutant, the model considered that digit 2 was the only digit to be patterned exclusively by Shh signaling, while digit 3 was somehow patterned by a combination of Shh-signaling and time of Shh expression. This model was supported by experiments that showed a lack of digit 2 in mouse mutants that had reduced Shh signaling range [Scherz et al., 2007]. The temporal-spatial-gradient Model implicitly assumed that Shh not only specified digit identity but that had at least a permissive role for digit formation. A second extension to the classic Shh Positional Information model was based on the sequence of digit loss observed upon Shh removal at progressively later times. In these experiments digit loss order was opposite to the normal order of digit specification: digits 3 was lost first, than digit 5, successively digit 2 and finally digit

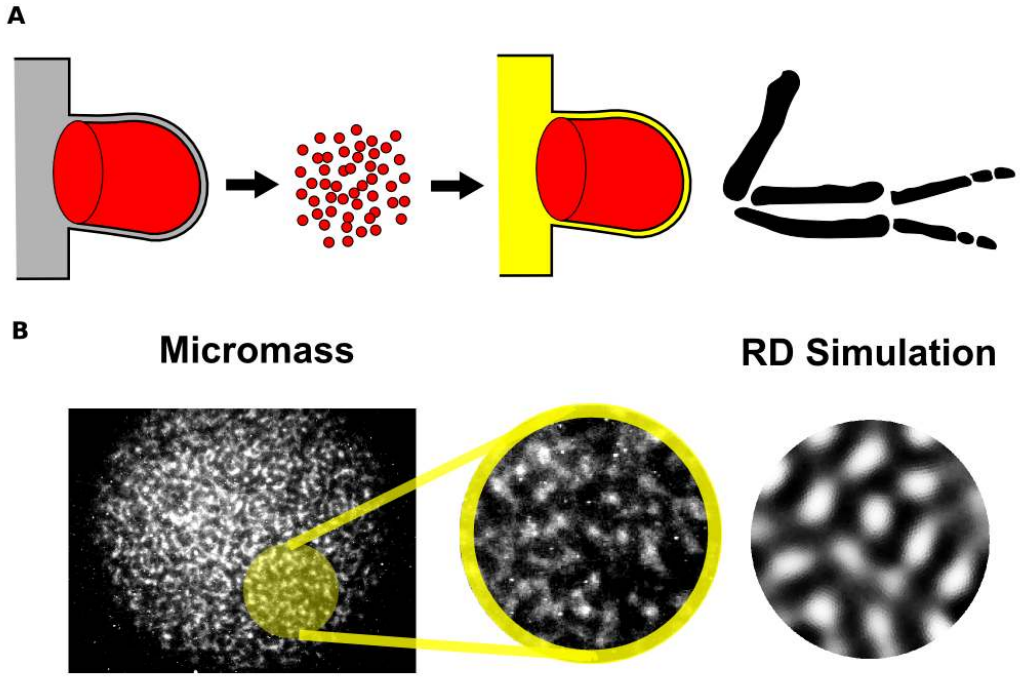

Figure 1.22: A) Re-aggregation experiment in chick limb. From left to right, the mesoderm (red) is removed from a donor limb bud (gray), cells are mixed and re-aggregated (red points), the re-aggregated mesenchymal cells are placed inside another ectodermal jacket (yellow) and graft to a neutral side of the embryo. Eventually, a limb with two digits forms. B) On the left, a Micromass culture system after 20h, a labyrinth-like pattern of condensations showed by Sox9 immuno-staining (left) is reminiscent of a Turing simulation (right).

4. This evidence was used to formulate a model where in an initial phase, Shh specified digits and their identity, and in a second phase it was required for the maintenance of sufficient digit progenitors to form condensations. The order of digits loss was therefore assumed to be the sequence with which condensations took place [Zhu et al., 2008]. Again an implicit requirement for Shh as permissive signal for digit formation contrasted the dispensability of Shh [Litingtung et al., 2002]. Finally, a third model that integrated proliferation and digit specification was formulated by observing that the application of a Shh inhibitor at progressively earlier stages resulted in the loss of more posterior digits and that inhibition of proliferation lead to limbs with only posterior digits. The model was called the Growth-Morphogen model [Towers et al., 2008] and assumed that the duration and dose of Shh exposure was coupled with growth to specify the digits.

In general, the studies mentioned above assumed that digit specification and digit identity specification happen at similar developmental stages. However, experiments performed in chick have provided evidence that digit identity is specified much later in development [Dahn and Fallon, 2000]. In late phases of limb development when fingers have already been specified, a region of high Bmp-signaling activity, known as Phalanx Forming Region (PFR), is established at the digit tips. The level of Bmp activity is specified in a graded manner along the A-P axis and determines the number of phalanges that are formed. For each digit, the posterior neighboring part of interdigital tissue determines the Bmp activity level and there is evidence that also Fgf-signaling participates in the regulation of phalanx number [Sanz-Ezquerro and Tickle, 2003], see Figure 1.23.

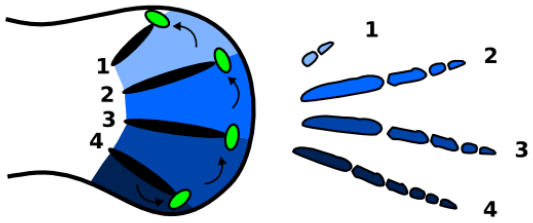

Figure 1.23: On the left, posterior interdigital regions (different blue colors) modulate the activity of the Phalanx Forming Regions - PFR (green) at the digit tips. This results in the specification of different digit identities that drive the formation of the final digit morphologies showed on the right.

1.3.2 Sox9 regulation and skeletal patterning

One of the earliest markers of skeletal patterning is the Sox9 transcription factor [Akiyama, 2008, Akiyama et al., 2002, Chimal-Monroy et al., 2003]. At early times after Sox9 expression, cells are still undifferentiated but their fate is committed to form the skeleton or soft tissue. Conditional inactivation of Sox9 in the limb results in a complete lack of patterning and chondrogenic differentiation [Akiyama et al., 2002] suggesting that Sox9 plays a central role in both processes. However, the genetic network that control Sox9 expression is not fully understood.

Secreted molecules of the Tgf-β family have been identified as important chondrogenic regulators. Among them Tgf-βs, Activins and Bone Morphogenetic Proteins (Bmps) are known to promote chondrogenesis [Barna and Niswander, 2007, Ganan et al., 1996, Leonard et al., 1991, Merino et al., 1999, Miura and Shiota, 2000, Montero et al., 2008, Pizette and Niswander, 2000]. Three Bmp's are expressed in the limb bud, Bmp2, Bmp4, and Bmp7 [Robert, 2007], and their signaling is mediated by two Bmp receptors, BmpRIA that is ubiquitously expressed and BmpRIB that is expressed in the digital region [Bandyopadhyay et al., 2006]. Conditional knockout of BmpRIA results in the absence of digits and severe defects in Sox9 expression [Ovchinnikov et al., 2006], while mutants that lack BmpRIB show normal Sox9 expression but defects in later chondrogenic events [Yi et al., 2000]. Bmp2/Bmp4 double mutants lack Sox9 expression and patterning in the most posterior digits (2 in forelimb, 3 in hindlimb) [Bandyopadhyay et al., 2006]. In contrast, over-expression of Bmp2 and Bmp4 in chick limb lead to an increased volume of cartilage elements [Duprez et al., 1996]. It has been proposed that Bmp-signaling promotes Sox9 expression through p38 pathway and that the Smad pathway is necessary for Sox9 activity [Pan et al., 2008].

Other important regulators of chondrogenesis and of Sox9 are the genes of the Wnt family [Day et al., 2005, Hens et al., 2005, Hill et al., 2005, Hu et al., 2005]. Seven different Wnts are expressed in the limb [Parr et al., 1993, Summerhurst et al., 2008] and their signaling is mediated by Frizzled and LRP receptors [Mikels and Nusse, 2006]. The canonical Wnt pathway is transduced by stabilization of Beta-catenin that accumulates in the nucleus and binds LEF/TCF transcription factors to regulate target genes [Nelson and Nusse, 2004]. Besides the importance of Beta-catenin as a transcription factor, complexes between Beta-catenin and cadherins participate in the formation of adherents junctions at the cell wall that are involved in cell to cell interactions during mesenchymal condensation [Delise and Tuan, 2002, Hülsken et al., 1994, Kemler, 1993]. In the limb, conditional Beta-catenin gain of function results in arrest of chondrogenesis and down-regulation of Sox9 expression, while loss-of-function mutations increase chondrogenesis and up-regulate Sox9 [Hill et al., 2005]. Similarly, Beta-catenin knock out in Micromass culture increase expression of Sox9, while Beta-catenin

gain-of-function inhibit Sox9 expression and suppress chondrogenesis [Grigoryan et al., 2008]. Ectodermal Wnts in the limb inhibit chondrogenesis and Sox9 expression and they promote proliferation [ten Berge et al., 2008]. Finally, it has been showed that Sox9 inhibits Beta-catenin activity in chondrocytes and stimulates Beta-catenin degradation in the nucleus [Akiyama et al., 2004, Topol et al., 2009].

1.3.3 Limb outgrowth

In mouse, limb outgrowth starts around 9 days post fertilization at specific sites along the lateral plate mesoderm (LPM). Current evidence supports Retinoic Acid (RA) as the mayor signaling that specifies the position of limb initiation sites [Niederreither et al., 1999, 2002]. RA drives the expression of different Hox genes along the LPM that in turn promote the expression of specific T-box family genes in the putative limb regions: Tbx5 marks the forelimb and Tbx4 marks the hind limb [Gibson-Brown et al., 1996, Logan, 2003, Minguillon et al., 2005]. Limb bud initiation is then established by canonical WNT signaling that restricts the expression of Fgf10 in the limb initiation site. Fgf10 is a Fibroblast growth factor that is expressed in the mesoderm and signals to the neighboring ectoderm driving expression of WNT ectodermal genes that promote Fgf8 expression and formation of the AER [Barrow et al., 2003, Kawakami et al., 2001]. Once the AER is formed, the limb begins to growth preferentially in the distal direction resulting in limb bud elongation. Several cellular behaviors have been proposed to underly limb outgrowth. For a long time, the most prominent hypothesis was that a proliferation gradient promoted by the AER was responsible for the growth in the distal direction [Ede and Law, 1969, Searls and Janners, 1971]. However, a recent computer simulation based on careful quantification of limb bud shape and cell cycle times has showed the implausibility of this hypothesis [Boehm et al., 2010]. This study showed that the difference in cell cycle along the P-D axis was minimal and proved that a model that was based only on cell proliferation would required very drastic differences to achieve elongation. Moreover, evidence that cells close to the ectoderm were polarized suggested the possibility that directed cell behaviors could instead be responsible for limb elongation. Single cell tracking and live imaging were successively used [Wyngaarden et al., 2010] to confirm this hypothesis and it was proposed that Wnt5a could be responsible for cell polarization [Gros et al., 2010]. To conclude, it is currently believed that growth anisotropies derive from directed cell behaviors rather than differences in cell proliferation.

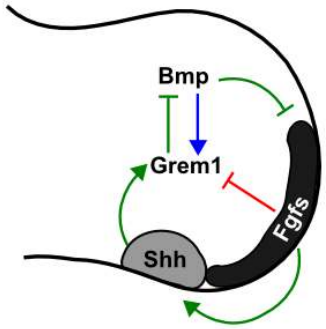

Figure 1.24: The feedback responsible for the coordination between AER and ZPA. Bmp promotes its own inhibitor Gremlin1 (blue interaction) and initiate that positive feedback loop between Shh, Gremlin1 and Fgfs (green interactions) that drives Fgfs expansion and growth. Finally Fgfs grow beyond a certain threshold and inhibit Gremlin1 (red interaction) and terminate the positive feedback.

1.3.4 Coordination between the P-D and the A-P axis

Classic ZPA grafting experiments [Tickle, 1981] showed that ZPA grafts had stronger effects when placed close to the AER. This revealed that AER and ZPA activities were coupled and suggested that these two organizers could cross-talk to implement coordination between P-D and A-P development. A first confirmation of this hypothesis was provided by showing that in the absence of the AER, Fgf beads were able to rescue Shh expression and that Shh beads were able to induce the AER and Fgf expression [Niswander, 2002, Tickle, 2005]. Successively, it was discovered that the positive feedback loop between mesenchymal ZPA cells and epithelial AER cells was mediated by Gremlin1, a Bmp antagonist expressed in the mesoderm [Khokha et al., 2003, Michos et al., 2004]. Gremlin1 mutants showed smaller limb buds, lack Fgf4-9-17 and had a reduced expression of Fgf8 and Shh. It was therefore proposed that the reduction of Bmp Activity by Gremlin1 was essential for the maintenance of the positive feedback loop between Shh and Fgfs [Bénazet et al., 2009, Michos et al., 2004]. Counterintuitively, Bmp signaling was known to be required for early AER induction [Ahn et al., 2001] but it was also known to promote Gremlin1 expression [Nissim et al., 2006] and to reduce Shh expression that promotes Gremlin1 [Bastida et al., 2009]. It has been proposed, that the negative feedback implemented by Gremlin1 allows the initial up-regulation of Fgfs and it is responsible for the initiation of the positive feedback loop between Fgfs and Shh [Bénazet et al., 2009], see Figure 1.24.

Successively, Shh, Fgfs and Gremlin form a positive feedback loop that is terminated when Fgfs increase beyond a certain threshold and lead to Gremlin1 inhibition [Scherz et al., 2004, Verheyden and Sun, 2008], see Figure 1.24. This complex self-regulatory network coordinates the patterning along the A-P and P-D axis and controls limb growth to achieve typical limb shape and size.

1.3.5 Models of Limb Development

Not only limb development has lead to pioneering discoveries in developmental biology but it is also the earliest complex biological organ that has been simulated in a computer. In this chapter, I will review in chronological order most of the computational and mathematical models that have been developed to study limb development. These models come in all sort of flavors and focus on different aspects of limb patterning and morphogenesis. In order to facilitate the reader, each model is accompanied with a label that summarize its characteristics:

- Dimensionality can be either *1D*, *2D* or *3D*.
- The model can consider only limb morphogenesis *Mor*, only limb patterning *Pat* or both *MorPat*.
- The model can use abstract limb shapes *AbsShp* or realistic/experimental limb shapes *RealShp*.
- The model includes experimental data *ExpDat* or is purely theoretical *Theo*.
- The model is based on a Positional Information model *PI*, a reaction-diffusion model *RD*, both *PIRD* or none (label not present).

An example of label is *2D-Morp-AbstShp-Teo-PI* and represents a two-dimensional (*2D*) model that is focused on morphogenesis (*Morp*), that uses abstract limb shapes (*AbsShp*), that is purely theoretical (*Theo*) and it is based on a Positional Information model (*PI*). Models that are particularly important for this thesis have been highlighted with a *. The goal of this review is to give an overview of the state of the art and to highlight the different questions that have been investigated with modeling. All the figures included in this section are adapted from the correspondent studies. A summary and a discussion is given at the end of the section.

1.3.5.1 A brief history of limb models

1969 - *2D-Mor-RealShp-Theo*

Already in the late 60s, a Scottish scientist called Donald Ede and his colleagues had developed a pioneering computer simulation of limb morphogenesis [Ede and

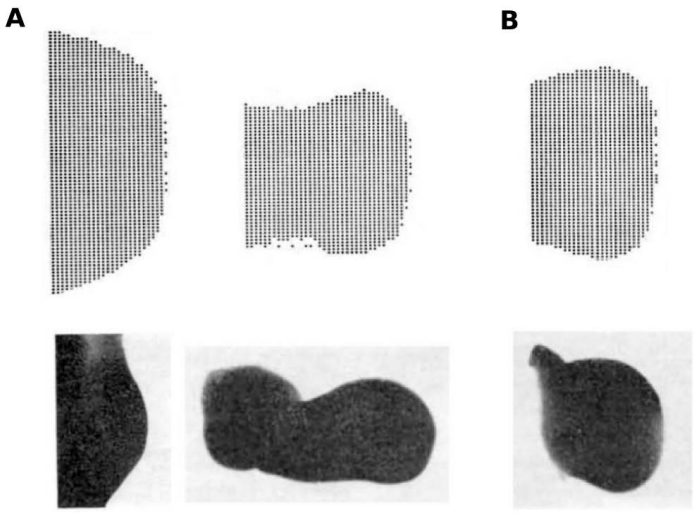

Figure 1.25: A) On top, the results of the Cellular Automaton model proposed to explain limb growth: on the left a young limb bud shape, on the right the final limb bud shape obtained by simulating cell-proliferation and cell-movements. On the bottom, similar shapes are observed in real chick limb bud. B) On top, when cell-movements are decreased in the simulation a shorter and fatter limb is obtained. On the bottom, a similar limb shape is observed in the Talpid chick mutant.

Law, 1969] to study if directional behaviors were required to achieve limb elongation. The model was based on a Cellular Automaton that simulated growth by considering two cellular behaviors: cell proliferation and cell movements. Simulation were used to find which combination of cellular behaviors could reproduce better the shape change observed in the real limb, see Figure 1.25A. The model proved that directed cell movements were necessary to drive limb elongation and proposed that the shorter and fatter limb bud of the Talpid chick mutant [Davey et al., 2006] could be obtained if directed cell behaviors were diminished, see Figure 1.25B.

1975 - *1D-Mor-AbsShp-ExpDat*

Another model of Limb elongation was proposed in [Lewis, 1975] to investigate to which extent a proliferation gradient could drive limb elongation. The model used the quantitative data of cell proliferation and cell density presented in [Hornbruch and Wolpert, 1970, Summerbell and Wolpert, 1972] and predicted with a simple mathematical formulation a one-dimensional time-course of fate maps along P-D

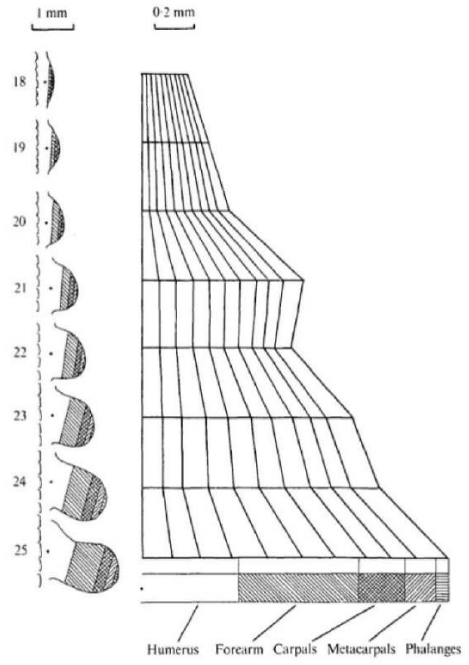

Figure 1.26: On the right, a one dimensional time-course of simulated fate maps extrapolated from experimental mitotic index and cell density data

axis, see Figure 1.26. In contrast with experimental fate maps, the predicted fate maps expanded quite uniformly over the P-D axis. This study concluded that discrepancies were due to the limited spatial and temporal resolution of the approach and supported the cell proliferation gradient as the mayor force driving elongation. The main limitation of this model was the one-dimensional approximation that did not took into consideration tissue movements along the D-V and A-P axis.

1975 - *1D-Pat-AbsShp-ExpDat-PI*

A one dimensional model [Summerbell and Lewis, 1975] was also developed to test the validity of the Progress Zone Model proposed by Lewis Wolpert. This model described with partial differential equations the change in P-D positional values as a function of time and distance from the AER (Progress Zone). The model was used to show that the Progress Zone Model could predict the outcome of the grafting experiments.

1975 - *2D-Pat-RealShp-Theo-RD* *

The first genuine two-dimensional simulation that focused on limb skeletal patterning was presented in [Wilby and Ede, 1975]. This study proposed a self-organizing Cellular Automaton model reminiscent of a Turing mechanism to explain skeletal patterning along the P-D and the A-P axis of the limb. In contrast to a normal reaction-diffusion mechanism, this model considered only one diffusible morphogen that induced cells to act either as morphogen producer or as a morphogen sink. By default cells were all morphogen producers but when a certain morphogen threshold was reached they switched the behavior to become morphogen sinks. When coupled with noise, this mechanism produced periodic patterns that were similar to those that could be obtained by a Turing mechanism, with the only difference that cell states were irreversible (once cells became morphogen sink could not revert their state). Similarities between this Cellular Automaton model and a Turing mechanism can be traced by observing that the two ingredients required to form a diffusion-driven instability are implemented in the following way: local auto-activation is implemented by the fact that the morphogen stimulates cells to produce more morphogen, lateral inhibition is implemented by cells acting as morphogen sink. Moreover, the two cell-states implements two behaviors that correspond to the two reactants of a typical abstract Turing model. The model was simulated inside a series of two-dimensional Cellular Automaton grids that corresponded to different P-D parts of the limb, see Figure 1.27A. The different grids were obtained by partitioning a realistic chick limb shape and reflected the assumption that during limb development patterning was only active in a narrow distal region. When the results of the simulations were re-composed together a series of skeletal elements that was in agreement with the skeletal of the chick was observed, see Figure 1.27B. Moreover when a limb shape corresponding to the polydactyly Talpid mutant was used, the model produced more digits due to the increased A-P size of the limb, see Figure. Finally, the model was also used to show that different skeletal patterns in evolution could be obtained by varying limb morphologies.

1977 - *1D-Mor-AbsShp-ExpDat*

Two years later, the mechanisms underlying distal limb elongation were studied again with a one-dimensional simulation, but this time a more sophisticated Cellular Automaton model was employed [Wilby, 1977]. This model considered that cells along the P-D axis could divide with a probability related to the concentration of a morphogen gradient. The morphogen gradient was formed by ubiquitous production, diffusion and a local sink at the distal tip of the limb. The resulting

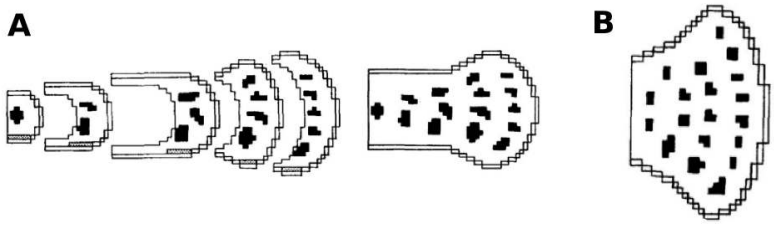

Figure 1.27: A) On the left, a chick limb is divided in several parts along the P-D axis. In each part, a Cellular Automaton simulation produces a periodic array of elements. On the right, the simulation recapitulates as a whole the skeletal pattern of the chick limb. B) When a similar simulation is performed in the morphology the Talpid chick mutant more digits are formed.

gradient was higher in the proximal region and lower in the distal part. Cell could randomly divide in any direction and when they divided along the A-P or D-V axis no change was introduced since the simulation considered only the P-D expansion. In addition, directed cell behavior were implemented by considering that a higher bias for P-D cell divisions existed where the morphogen had higher concentrations. By Comparing predicted growth rates with experimental data, this model was able to show that directed cell-behaviors were necessary to achieve enough elongation.

1979 - *2D-Pat-AbsShp-Theo-RD* *

Another two-dimensional reaction-diffusion simulation of digit patterning was proposed in [Newman and Frisch, 1979]. This time a genuine Turing model was used to simulate limb skeletal patterning inside a squared limb shape. Like in the Cellular Automaton model presented four years before the overall skeletal pattern was simulated by dividing the limb in different parts along the P-D axis. However, this time only three P-D profiles that corresponded to stylopod, zeugopod, and autopod were considered. For each profile a two-dimensional simulation that corresponded to an AP-DV section was performed, see Figure 1.28A. As in the previous model, this choice underlies the assumption that skeletal patterning was active only in a very narrow region distal region. The model showed that if the right parameter was changed over time the Turing model could form one element in the stylopod, two elements in the zeugopod and three elements in the autopod, see Figure 1.28B.

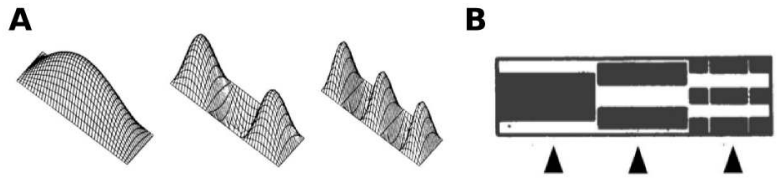

Figure 1.28: A) Reaction-diffusion simulation inside three two-dimensional squares corresponding to three AP-DV sections. B) The varying parameter in each section produced one element in the stylopod section, two elements in the zeugopod section and three elements in the autopod section.

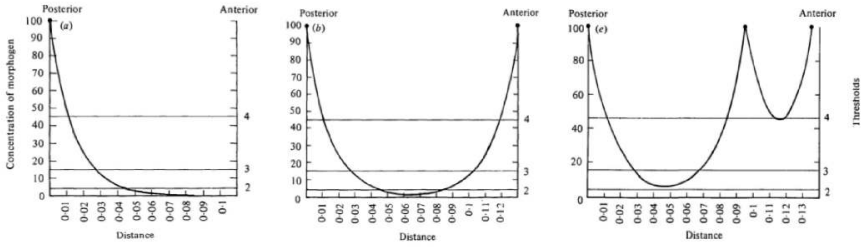

Figure 1.29: From left to right, a graph showing a simulated morphogen gradient in the wild type, a graph showing the morphogen gradient when another ZPA is grafter anteriorly and a graph showing the morphogen gradient when less ZPA cell are grafted anteriorly. By fitting digit threshold to the wild type case, the model was used to produce semi-quantitative prediction in the other cases.

1981 - *1D-Pat-AbsShp-Theo-PI*

A more simple one-dimensional model was used to show that a formalized version of the French Flag Model proposed by Wolpert could account for the digital patterns observed in different ZPA grafting experiments [Wolpert and Hornbruch, 1981]. By Simulating the gradients of different ZPA grafting situations, the model predicted the qualitative patterns of perturbations, see Figure 1.29.

1983-88 - *2D-Pat-AbsShp-Theo*

Another self-organizing two-dimensional patterning model [Oster et al., 1983] proposed that cellular behaviors, rather than changes in cell-state, could drive the formation of skeletal elements. The model considered various cellular behaviors like random cell movements, cell division rates and cellular haptotaxis (tendency of cells to move towards region of more cell density) and showed that if these

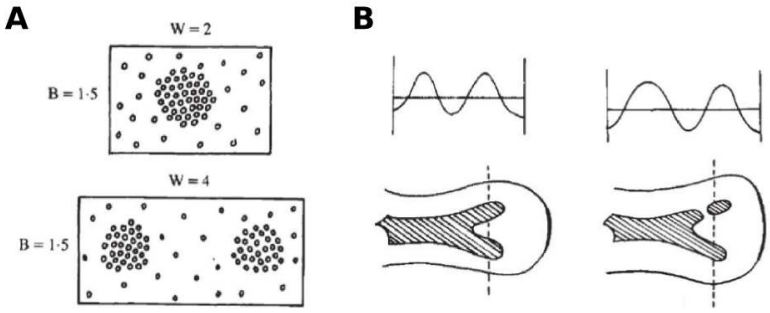

Figure 1.30: A) On top a Mechanochemically model based on cell movements, cell divisions and haptotaxis predict the spontaneous creation of one high cell density cluster. On bottom, if the space is doubled two clusters are formed. B) The same model was used to explain how branching bifurcations (on the left) and axial bifurcation (on the right) could arise in evolution.

processes were coupled in the right way, points of higher cell density (skeletal elements) could arise. Similarly to the case of reaction-diffusion (RD) models, simulations were used to show that if the space increased more elements were formed, see Figure 1.31A. A following study [Murray et al., 1988] suggested that this model could also explain the two type of skeletal element branching that were observed during limb evolution, see Figure 1.31B. This type of models were called Mechanochemical (MC) models and for a while competed with Turing models to explain skeletal patterning [Maini, 1991, Murray and Maini, 1989]. However, subsequent theoretical work showed that the abstract mathematical formulation of RD and MC models was equivalent [Maini and Solursh, 1991] and supported the idea that in the absence of more concrete knowledge about cell-behaviors and cell-states, RD models offered a general framework to study pattern formation based on local-autoactivation and lateral-inhibition.

1992 - *1D-Pat-AbsShp-Theo-PIRD* *

The first model that formalized the idea that Positional Information and Turing models could work in conjunction was presented in [Maini et al., 1992]. In this study, a global gradient was used to modulate the parameters of a one-dimensional Schnakenberg Turing system. The width of the peaks that were formed by the model varied according to the morphogen concentration, see Figure 1.31. Similarly to ZPA grafting experiments in real limbs, duplication of the morphogen gradient produced duplication of the peaks, see Figure 1.31. This study not only

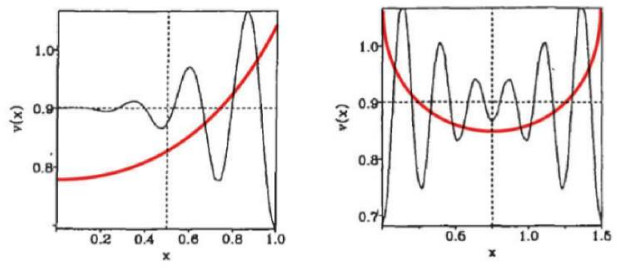

Figure 1.31: A model that combine a morphogen gradient (in red) with a Turing mechanism (in black). On the left, the gradient scales in a concentration-dependent manner the reaction-diffusion peaks by controlling one reaction-diffusion parameter. On the right, if the gradient is duplicated like in ZPA grafting experiments the peaks are also duplicated.

provided a first concrete example of how to combine Positional Information and a Turing mechanism but also showed that the randomness exhibited by Turing patterns could be overcome by modulating reaction-diffusion parameters in a graded manner. Successively, other studies proposed that similar effects could be achieved with boundary conditions [Dillon et al., 1994] or growth [Crampin et al., 1999].

1999 - *2D-MorpPat-RealShp-ExpDat-PI* *

The first model that combined realistic simulation of morphogenesis and patterning was developed in [Dillon and Othmer, 1999]. In this study a grid that represented and early limb bud was deformed by simulating each grid point as a visco-elastic material that could generate mass by cell proliferation. Cell proliferation was governed by signals coming from the AER and the ZPA, that were tuned to obtain realistic limb shape changes, see Figure 1.32. In addition, springs running along the A-P axis were used to provide a containing force that simulated the ectoderm. Limb elongation was therefore achieved by combining two assumptions: the proliferation gradient hypothesis and the assumption that the ectoderm provided physical containing forces to the mesenchyme. The first hypothesis was ruled-out years later (See section 1.3.3) the second assumption had been in fact already confuted by ectoderm-removal experiments [Saunders, 1948]. Despite the discrepancies with real limb outgrowth, the comparison between experimental fate maps and the growth model was assumed to be qualitatively correct. Successively, the model was used to predict which interpretation of the AER and the ZPA

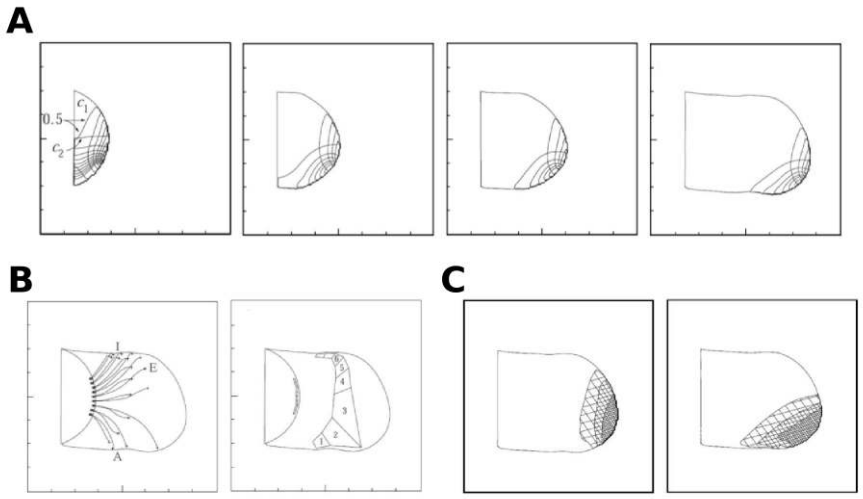

Figure 1.32: A) Signals from the AER and the ZPA (showed with contours) promote growth in a visco-elastic model. The model produces realistic limb shape change. B) Tracking of tissue movement points over time. C) Simulated Hoxd genes patterns deriving from hypothetical interactions with AER and ZPA signals. On the left the Hoxd genes are promoted by the AER and on the right are promoted by the ZPA.

signals was able to reproduce the experimental expression pattern of Hox genes, see Figure 1.32. The advantage of this pioneering Morphodynamic model was that fates of different part of tissue could be traced over time and compared with gene expression patterns.

2004 - *2D-Pat-AbsShp-Theo-RD*

More recently, a partial differential equation model that used a combination of a Turing mechanism and a Mechanochemical model [Hentschel et al., 2004] was developed to simulate limb skeletal patterning in a way that was reminiscent of the early work done by Frisch and Newmann [Newman and Frisch, 1979]. This study considered a general Schnakenberg model that drove changes in Fgf receptors and in cell density. Simulations were performed in a two-dimensional squared limb shape where the skeletal patterning was active only in an narrow distal region, see Figure 1.33. Similarly to the model presented two decades earlier when the right parameter was changed more elements could be form to account for the formation of the two elements of the zeugopod and three elements of the autopod, see Figure

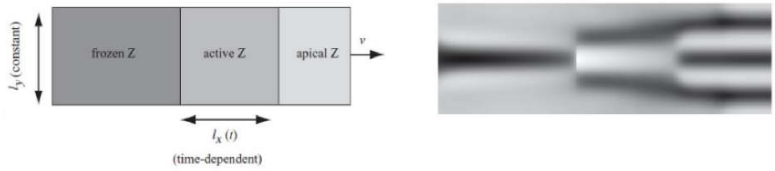

Figure 1.33: Simulation of a reaction-diffusion model coupled with a Mechanochemical model simulated on a squared limb shape. On the left, the squared limb shape is divided in three zones: frozen, active and apical. Skeletal patterning occurs only in the active-zone that shrinks over time. On the right, the final skeletal pattern that is obtained with a simulation where a parameter is changed over time to form one element in the stylopod, two elements in the zeugopod and three in the autopod.

1.33. The change in cell density was in effect only a downstream read-out of the Turing molecule concentrations.

2004 - *2D-Pat-AbsShp-Theo-RD*

In the same year, a more sophisticated model that simulated the behavior of single cells by using a Cellular Potts Model [Graner and Glazier, 1992] was presented in [Izaguirre et al., 2004]. This model recapitulated and extended the results of the Turing model presented in [Hentschel et al., 2004] to explicitly consider cell condensations. Again an abstract squared-like limb shape was used for the simulation but growth this time was implemented by adding new cells to the distal end of the limb, see Figure 1.34.

2004 - *2D-Pat-AbsShp-Theo-RD*

Other three studies ulteriorly extended the model presented in [Hentschel et al., 2004]. A first study aimed to reduce its complexity by showing that the entire Turing-Mechanochemical model could be reduced to a Morphostatic model that did not include cellular behaviors [Alber et al., 2008]. Other two studies [Chaturvedi et al., 2004, Cickovski et al., 2005] extended the model in three dimension. In both studies the three-limb axis were in effect approximated by a series of two-dimensional AP-DV sections over time, see Figure 1.35A, but in [Cickovski et al., 2005] a genuine three-dimensional Cellular Pots Model was used

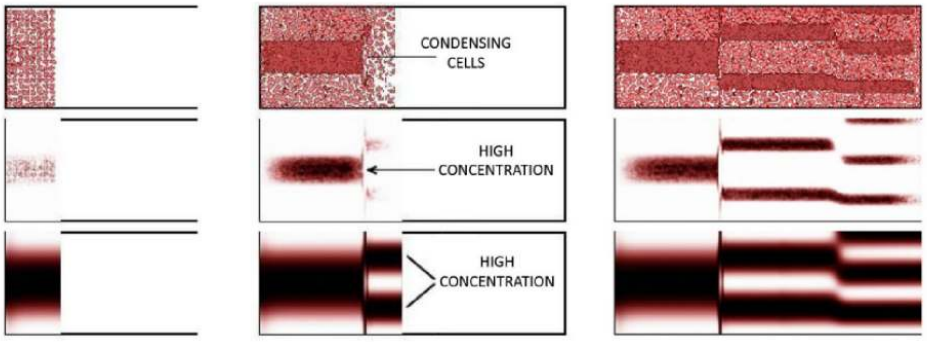

Figure 1.34: A Reaction-diffusion model coupled with a Cellular Potts Model that simulates cell condensations. Top row, simulated cells condense to form skeletal elements and are added to the distal part of the squared-limb to account for growth. Middle and bottom row show respectively the concentrations of the activator and the concentrations of the inhibitor in the reaction-diffusion model.

to simulate condensations1.35B. However, along the P-D axis both approaches consider a one-dimensional active-zone that corresponded to the AP-DV sections that were simulated.

2006 - *1D-Pat-AbsShp-Theo-RD*

A more simple one-dimensional Turing model was used to explain the thin-thick digit alternation observed in the Doublefoot mouse mutant [Miura et al., 2006]. The model employed a set of reaction-diffusion equations implemented with simple step-like functions and was simulated inside a growing domain. It was showed that certain parameters made the system more prone to the thick-thin digit alternation, see Figure 1.36.

2007-08 - *2D-Mor-AbsShp-Theo*

A Cellular Potts Model was also used to simulate limb growth and elongation [Popławski et al., 2007]. Like done two decades before [Dillon and Othmer, 1999] the model explored if limb elongation could be obtained by a gradient of cell-proliferation promoted by AER signals. The model simulated the behavior of each single cells and was able to produce elongation by promoting proliferation in a narrow distal region under the AER, see Figure 1.37. Similar results

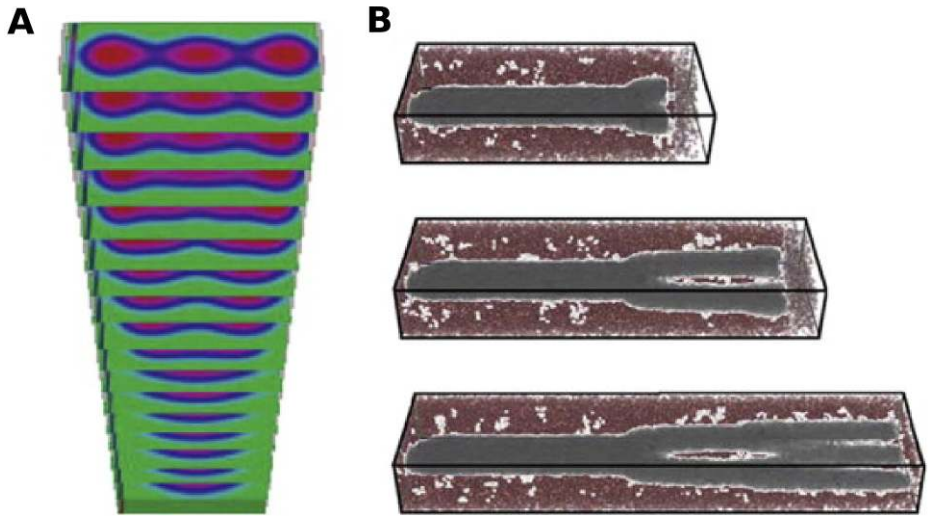

Figure 1.35: A) A Turing-Mechanochemical model simulated in a series of two-dimensional simulation that reflect AP-DV sections. The number of skeletal elements is increased by varying one parameter in the model. B) A three-dimensional Cellular Potts model simulation of the same model.

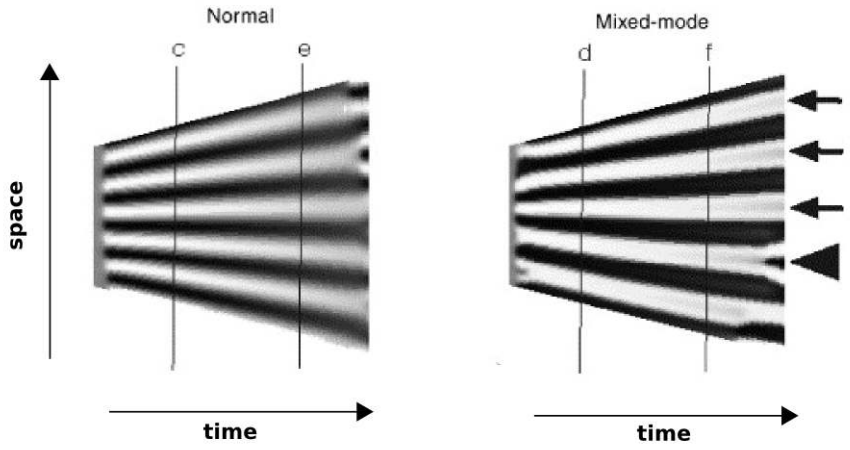

Figure 1.36: A one-dimensional Turing simulation in a growing domain, the black color corresponds to regions of high concentration. On the left, a normal Turing pattern with peaks of the same width is formed. On the right, with certain parameters a mixed-mode Turing pattern arises and thin stripes are formed as pointed by the black arrows. This behavior is reminiscent of the Doublefoot mouse mutant.

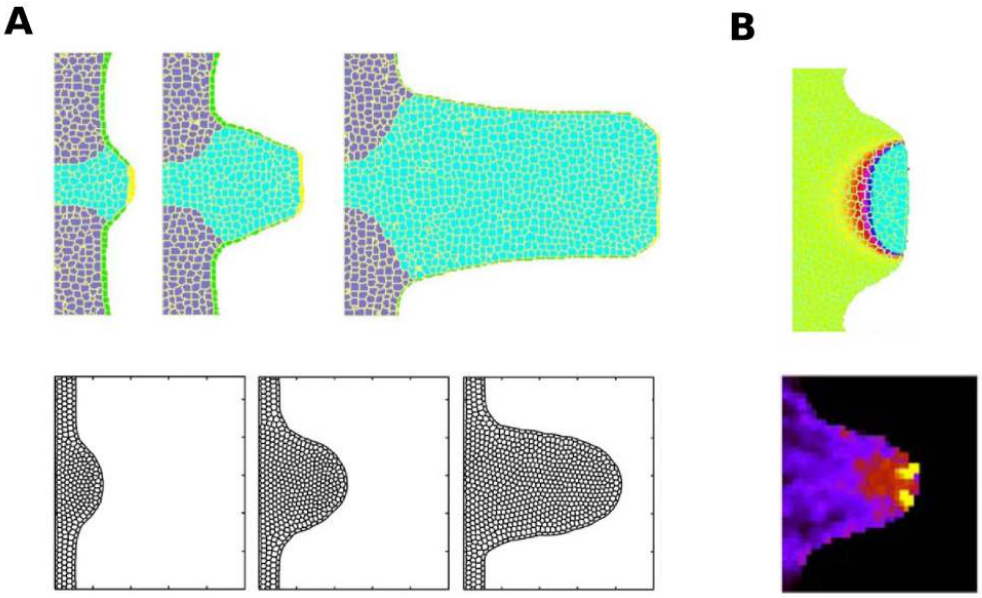

Figure 1.37: A) Top row, a growing limb simulated with a Cellular Potts Model. Bottom row, a similar simulation implemented with a spring model. B) In both models a proliferation gradient promoted by the AER is assumed to be responsible for limb elongation. Top and bottom figures show the simulated AER signals in the two models respectively.

where obtained one year later with a different formalism [Morishita and Iwasa, 2008]. However, later studies [Boehm et al., 2010] quantified cell proliferation and showed that the extreme difference in cell-proliferation along the P-D axis required for elongation was unrealistic.

2009-10 - *2D-Pat-AbsShap-Theo-RD*

Two of the most recent models of limb patterning [Zhu et al., 2010, 2009] are again based on the idea that a Turing mechanism responsible for skeletal patterning is active only in a very narrow region close to the AER. As it has been proposed in previous models, these studies consider a general Turing model which parameters vary over time to produce one peak in the stylopod, two peaks in the zeugopod and three peaks in the digits, see Figure 1.38A. However, this time the models define an active patterning region that can growth and deform producing different morphologies. Similarly to the work done in the pioneering model presented in

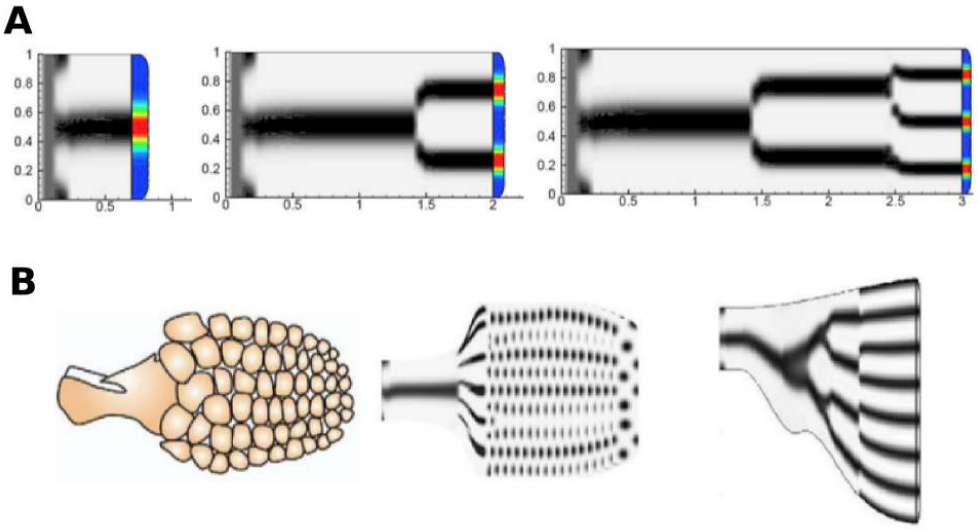

Figure 1.38: A) A Reaction-diffusion simulation in a squared limb shape. Similarly to previous models, the patterning Turing mechanism is active only on in a narrow distal region (colored region), over time by more elements are obtained by changing the relevant parameters. B) The active-region is deformed over time to produce different limb morphologies and patterns. A sketch of the limb morphology of the Ichtyosaur fossil (on the right) is compared with a simulations (in the middle). On the right, another simulation produces a different morphology that correspond to the limb of the Sauripterus fossil.

[Wilby and Ede, 1975], different limbs fossil morphologies were simulated and it was proposed that morphological changes could underly limb skeletal evolution, see Figure 1.38B.

2010 - *3D-Mor-RealShap-ExpDat*

The first genuine three-dimensional model based on quantified limb shapes was presented in [Boehm et al., 2010]. Like previous studies, this work aimed to check if limb elongation could be explained by a P-D gradient of cell-proliferation. To this extent cell-cycle times across different limb region were carefully quantified in three-dimension and were given in input to a visco-elastic three-dimensional model similar to the two-dimensional model propose in 1999 [Dillon and Othmer, 1999]. An experimental three-dimensional limb shape obtained with Optical Projection Tomography (OPT) was used as starting point for the growth simulation.

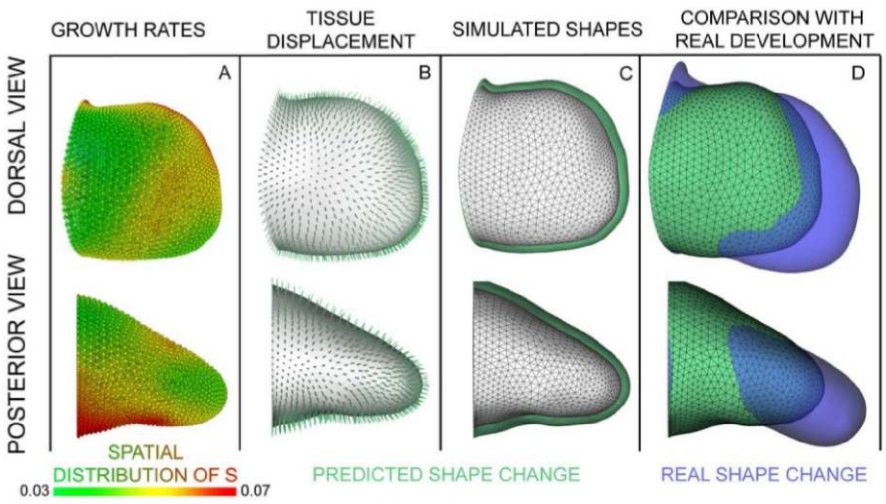

Figure 1.39: A) A three-dimensional model of limb growth based on a realistic cell-proliferation gradient. The first column shows a 3D quantification of cell-proliferation coming from BrdU/IddU labeling. Second and third column show the initial experimental 3D shape used for the simulation (white shapes), the predicted velocity vector field (green arrows) and final limb shape (green shape). The fourth column compares the predicted limb shape (green) with an experimental limb shape at the same stage (blue).

The final simulated shape was then compared with an experimental shape at a similar stage, see Figure 1.39. As it was proposed almost four decades earlier [Ede and Law, 1969] the simulation confirmed that a proliferation gradient alone was not enough to explain elongation and that directed cell-behaviors were required.

2011 - *2D-Pat-AbsShap-ExpDat-PI*

A more recent model [Probst et al., 2011] of limb patterning used a growing two-dimensional simulation to study the signals that control the distal progression of limb development. The model approximated growth as a simple stretching limb shapes and simulated the interaction between Fgf, Shh and RA, see Figure 1.40. The simulations were compared with molecular data and the model was used to replicate the increase in RA production observed in the Shh mutant, see Figure 1.40.

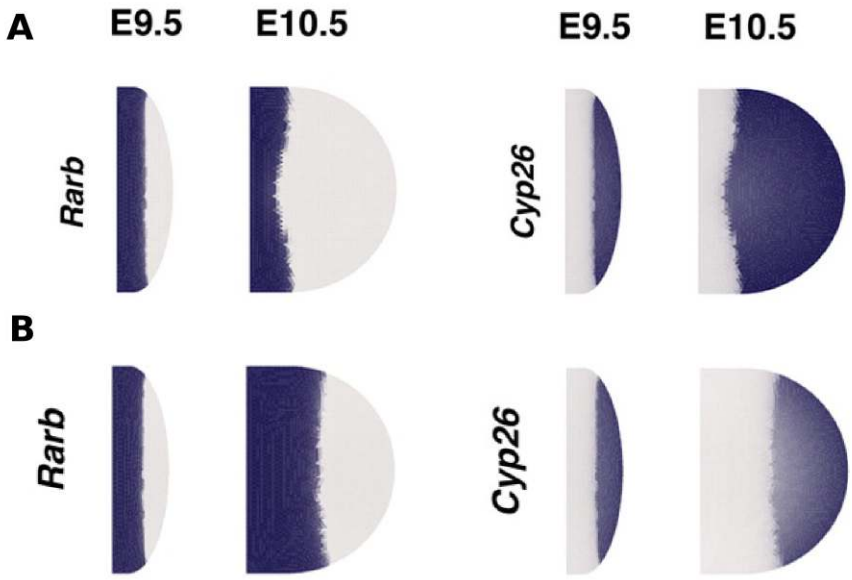

Figure 1.40: Simulations of distal limb developmente patterning at stage E9.5 and stage E10.5. A) Simulated wild type expression patterns for $Rarb$, an enzyme that produces Retinoic Acid, and $Cyp26$ which is promoted by Fgf. B) Simulated expression patterns for $Rarb$ and $Cyp26$ in the Shh mutant.

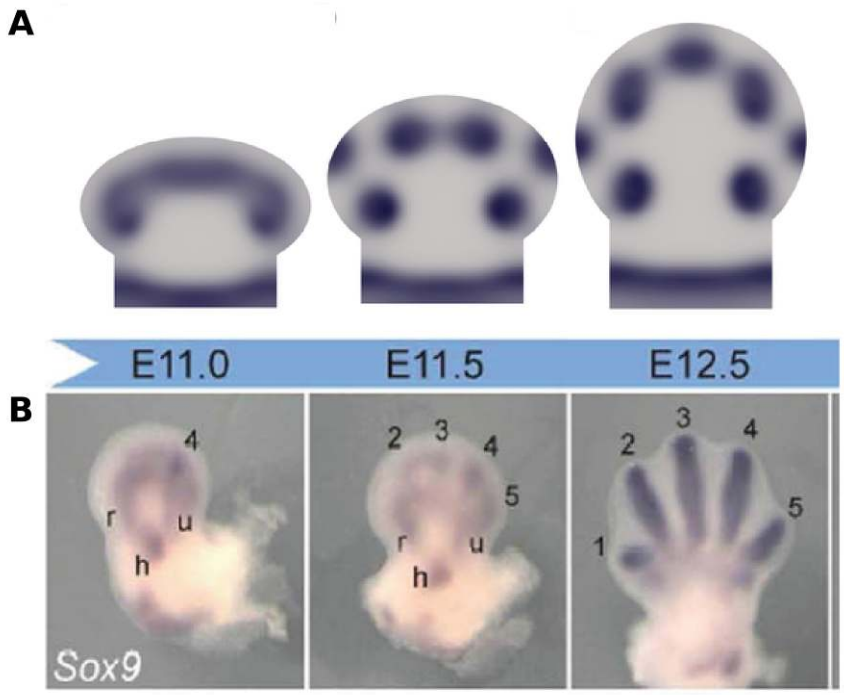

Figure 1.41: A) Simulation of a reaction-diffusion model based on Bmps and their receptors inside a stretching limb bud. The simulation shows the regions of high Bmp-signaling. B) Experimental patterns of Sox9 are compared with the simulation.

2012 - *2D-Pat-AbsShap-ExpDat-RD* *

The most recent model of limb development [Badugu et al., 2012] is a genuine two-dimensional Turing model that focuses only on digit patterning rather than on the whole skeletal pattern. Similar to the model presented in [Probst et al., 2011] a simple stretching limb bud shape was used to simulate growth. Inside, this two-dimensional growing domain a reaction-diffusion mechanism based on hypothetical interactions between Bone Morphogenetic Proteins and their receptors was simulated. The model produced a two-dimensional spot pattern which progressive appearance was related to the progressive patterning of Sox9, see Figure 1.41.

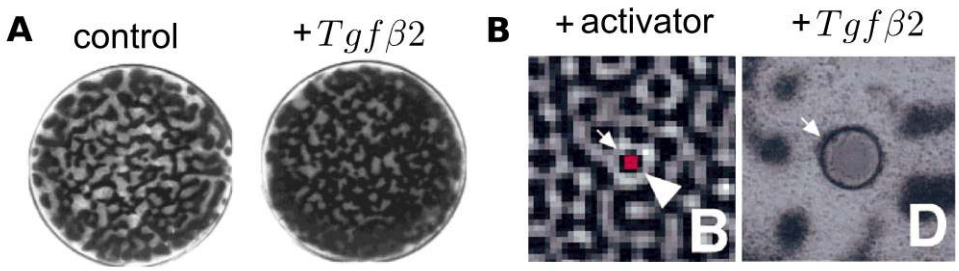

Figure 1.42: A) Periodic chondrogenic patterns in Micromass cultures: on the left a normal situation, on the right increase chondrogenesis after Tgf-β2 addition. B) On the left, a reaction-diffusion simulation with a bead of Activator. On the right, a bead of Tgf-β2 is added to the Micromass culture. In both cases inhibition is observed in the region surrounding the bead.

1.3.5.2 Models of Micromass culture

While most skeletal patterning models focused on limb development, few other studies focused in modeling the spontaneous pattern formation that was observed in the Micromass culture system, see Figure 1.22B. The striking correlation between the periodic chondrogenic Micromass patterns and Turing patterns has been repeatedly used to suggest that a self-organizing Turing mechanism was underlying skeletal patterning [Newman, 1996]. The first study that investigated this hypothesis [Leonard et al., 1991] provided experimental evidence that a transforming growth factor called Tgf-β1 acted as an activator in a Turing system. Another study [Miura and Shiota, 2000] used a combination of experimental work and modeling showed that another growth factor, this time Tgf-β2, satisfied the conditions required to be an activator. This study showed that ectopic addition of Tgf-β2 increased chondrogenesis and explained the counterintuitive fact that Tgf-β2 beads inhibited chondrogenesis as an increase in lateral inhibition promoted by the "Activator", see Figure 1.42. In addition, this study showed that cell-sorting was occurring both in-vitro and in-vivo and proposed that the self-organizing chondrogenic patterns were likely to be made by cell-sorting behaviors under the control of a Turing pre-pattern.

The idea that both a Turing mechanism and cell-rearrangements were responsible for the final Micromass pattern was further developed in [Kiskowski et al., 2004] with a combination of modeling and experiments. The model presented in this study was based on an Activator-Inhibitor model implemented by $Tgf\beta$ and one hypothetical inhibitor. In addition, random cell movements were modeled using a

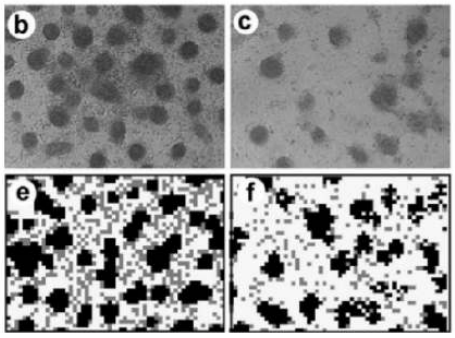

Figure 1.43: Left column: on top, condensation patterns in a Micromass culture, on bottom, a simulation produces similar condensations. Right column: on top, condensations in a Micromass culture with 15% cell dilution, on bottom, a similar pattern is obtained in a simulation with 50% less cell density.

Cellular Automaton formalism. High Tgf-β concentrations were coupled with a reduction of random cell movements that was assumed to result from an increase in Fibronecting (FN). This model was able to explain the Micromass Cultures patterns that were obtained when different initial densities were used, see Figure 1.43.

In the same year, another study [Miura and Maini, 2004] revealed that addition of ectopic Fgf4 increased the speed of pattern appearance and reduced chondrogenesis in Micromass cultures, see Figure 1.44. A comprehensive mathematical analysis showed that this behavior was consistent with an increase in lateral inhibition strength in a Turing model.

Finally a more recent study [Christley et al., 2007] extended and improved the CA model presented in [Kiskowski et al., 2004] and showed that with certain parameters the simulation could produce oscillating behaviors but so far no evidence for oscillations have been found in the limb.

1.3.6 Conclusion and discussion

In this section I presented a brief overview of limb patterning and limb morphogenesis. I reviewed the main limb organizers and their role in pattern formation and growth. I gave particular attention to the skeletal patterning as it is the first asymmetry that is establish in the limb mesenchyme and is the main topic of this

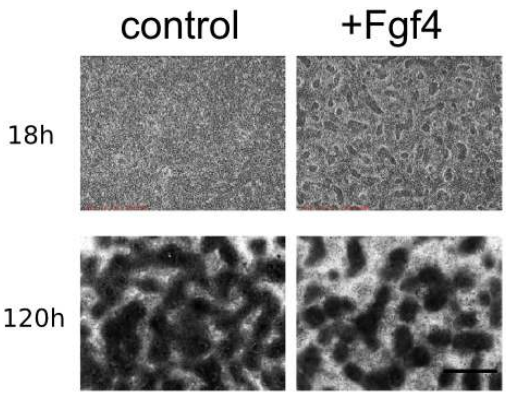

Figure 1.44: Left column, Micromass condensation patterns in control situation at 18h (visualized with phase contrast) and at 120h. Right column, Micromass condensation patterns when $Fgf4$ is added. The pattern appears already at 18h compared to control and the final pattern (120h) shows reduced chondrogenesis.

thesis. I reviewed the different P-D patterning models and showed that current evidence supports the dynamic specification of the three P-D segments of the skeleton via an interplay between RA and Fgf-signaling. The A-P patterning was mainly discussed in the context digit patterning in the autopod. In particular, I reviewed the distinction between digit specification and digit identity, the first being the sequence of isomorphic digital vs interdigital fates along the A-P and the second the specification of the different digit morphologies. I discussed how these two concepts have been coupled in the classic Positional Information models based on Shh and reviewed the evidence for a Turing self-organizing mechanism responsible for digit specification. Finally, I presented the current knowledge about limb bud initiation, limb bud termination and control of limb outgrowth.

Next, I reviewed and categorized the existing models of limb development, the review highlights three different observations. First, most of the early models focused on limb morphogenesis and in particular on the cellular mechanisms underlying limb elongation. This topic returned in fashion only in recent years motivated by the appealing idea to model limb growth at the cellular level. Paradoxically, the earliest model [Ede and Law, 1969] was more successful that its successors to suggest that cell-proliferation alone was unable to drive limb elongation. The most recent and most complete three-dimension model of limb growth traced similar conclusions. Secondly, only one model [Dillon and Othmer, 1999] combined limb growth and patterning. However, this work was limited to the study of distal Hoxd genes and did not focus on the skeletal patterning.

In general, the models that focused on skeletal patterning were theoretical and

did not considered realistic growth, realistic limb shapes or experimental data. Even recent models simulate skeletal patterning inside squared limb shapes that elongates in one direction over time. Moreover, the patterning mechanism is often set to be active only in a very narrow region of the limb, that in practice correspond to reduces most of the two-dimensional models to one-dimensional models plus time. Similarly to the case of morphogenesis, the oldest patterning model [Wilby and Ede, 1975] was under certain aspects more advance that its successors as it used geometries that were derived from experimental limb shapes. Turing models are very sensitive to the spatial domain that is considered, therefore the quasi one-dimensional approximation given by a narrow active region can cover some important aspects of the real skeletal patterning in the limb. For example, a Turing model produces peaks in a one-dimensional domain but in a two-dimensional domain can produce either spots or stripes depending on the parameters. When stripes are formed, they are usually randomly oriented and create a labyrinthine pattern. Therefore any two-dimensional simulation that forms stripes has to consider the problem of stripe orientation. However, if the spatial domain is one-dimensional (or very narrow) the orientation becomes irrelevant and for this reason none of the simulations presented in this review had to deal with this problem. The most recent Turing model [Badugu et al., 2012] is the only one that considers a complex two-dimensional geometry were the patterning mechanism is active everywhere. However, it considers a Turing system that produces spots, therefore it does not suffer from the orientation problem mentioned above but that is also more difficult to re-conciliate with the obvious stripy pattern of Sox9, see Figure 1.41.

Third an last, only one study explored with one-dimensional simulations the idea of combining Turing mechanism and Positional Information gradients. This study provided evidence that a combined model was able to produce a more robust Turing pattern that was less dependent on random fluctuations. Similar results were discussed in [Crampin et al., 1999] were it was shown that different type of growth could also stimulate a more robust pattern formation.

I continued this section by reviewing the mathematical models and the experiments that were developed to study the chondrogenic patterns formed in Micromass Cultures. In all studies, a comparison between experiments and simulations was used to strengthen the hypothesis that a Turing mechanism was responsible for the periodic condensations observed in vivo. Two studies [Miura and Shiota, 2000] and [Miura and Maini, 2004] were able to provide good molecular evidence in vitro that Tgf-β2 and Fgf4 may be involved in the underlying Turing mechanism. Tgf-β2 promoted chondrogenesis and was prosed to act as an Activator in an Activator-Inhibitor Turing model. Fgf4 instead inhibited chondrogenesis but at the same time increased the speed of pattern appearance. A mathematical analysis

revealed that this behavior was consistent with a stronger lateral-inhibition in the Turing model.

In conclusion, limb development has a long tradition of mathematical and computational models that have mostly focused on exploring theoretical questions regarding patterning and morphogenesis. Recent studies are gradually starting to include more experimental data into the models. In the study of morphogenesis, this strategy has been key to resolve a long-standing debate on the practicability of the cell-proliferation gradient hypothesis. In the study of skeletal patterning, models are only recently starting to consider realistic abstraction for limb geometry and patterning events. For this reason, despite the large number of Turing models, the almost thirty years old hypothesis that skeletal patterning is driven by a Turing mechanism has been difficult to test. In this thesis I present two models of limb development. The first model is focused only on skeletal patterning and combines Positional Information signals with an abstract Turing model to provide the first strong evidence that a Turing mechanism is responsible for the digit patterning in vivo. Following the notation used in this section, the model label is *2D-Pat-RealShap-ExpDat-PIRD*. The second model can be seen as an extension of this first model to consider realistic limb growth, a three-reactant Turing model based on molecular data and experimental data encoding Positional Information signals, its label writes *2D-MorPat-RealShap-ExpDat-PIRD*. The model is compared against experimental data and is able to capture the dynamics of digit patterning as shown by the expression pattern of the Sox9 skeletal marker.

Chapter 2

OBJECTIVES OF THIS WORK

The aim of this thesis is to study the molecular mechanism that underlie the patterning of the digits in the vertebrate limb. Two alternative theories have been proposed to explain patterning in development: the Positional Information model and the Turing mechanism. In the limb, these two theories have been traditionally seen as competing but have been both used with success to explain different aspects of skeletal patterning. The main goal my thesis is to to explore if these two models can be reconciled to explain the spatio-temporal dynamics of digit patterning. This is done by developing a computational model of limb development that combines a Turing mechanism with Positional Information and limb growth to recapitulate the dynamics of the skeletal marker Sox9. The model is developed in three incremental steps.

First, I develop a simple Turing model of digit patterning simulated inside a static limb shape morphology. In collaboration with the laboratory of Marian Ros, I show that this model provides evidence that Distal Hox Genes and Fgfs modulate the Turing mechanism by changing its wave-length. For the first time we show that a Turing mechanism can be combined with Positional Information gradients to obtain reliable digit patterning.

Successively, I develop a novel way to model limb growth that uses experimental limb morphologies and clonal data. This allows me to address questions related to proximal-distal (P-D) patterning and supports the dynamic specification of the three P-D segments of the limb.

Finally, I build a model of limb development that combines realistic growth, experimental gene expression data, a simulated Positional Information gradient and a Turing mechanism to produce digit patterning dynamics that reflect the expression of the skeletal maker Sox9. This model together with descriptive and functional experiments allow us to identify some of the signaling molecules that form the Turing gene-network responsible for digit patterning. To conclude, I show that the model predicts that Fibroblast Growth Factors (Fgfs) in the limb act

as coordination signals to orchestrate growth and patterning.

Chapter 3

RESULTS

This chapter presents the main results of my thesis. The chapter is organized as following: in the first two sections I present two of my published articles and in the third section I present un-published work. The first paper consists in a static model of digit patterning that combines Positional Information and a Turing mechanism to investigate the phenotype of Distal Hox genes mutants. The second article introduces a limb growth model based on experimental data that investigates the relation between the patterning of the Proximal-Distal axis and limb outgrowth. Finally, the un-published work presented in the last section concerns the development of a digit patterning model that combines a Turing mechanism with Positional Information and limb growth to investigate the spatio-temporal regulation of Sox9. This final model is the main result of my PhD and combines the ideas presented in the previous two articles to develop a dynamic simulation of digit patterning. Together with experiments performed in our laboratory by Jelena Raspopovic, this model helps to identify the signaling molecules that implement the Turing network that drives digit patterning.

3.1 Second article: Hox Genes Regulate Digit Patterning by Controlling the Wavelength of a Turing-Type Mechanism

Sheth R, Marcon L, Bastida MF, Junco M, Quintana L, Dahn R et al. Hox genes regulate digit patterning by controlling the wavelength of a Turing-type mechanism. Science. 2012 Dec 14; 338(6113): 1476-80. DOI: 10.1126/science.1226804

3.2 Third article: A Computational Clonal Analysis of the developing Limb Bud

Marcon L, Arqués CG, Torres MS, Sharpe J. A computational clonal analysis of the developing mouse limb bud. PLoS Comput Biol. 2011 Feb 10; 7(2): e1001071. DOI: 10.1371/journal.pcbi.1001071

OPEN ACCESS Freely available online PLoS COMPUTATIONAL BIOLOGY

A Computational Clonal Analysis of the Developing Mouse Limb Bud

Luciano Marcon[1]*, Carlos G. Arqués[2], Miguel S. Torres[2], James Sharpe[1,3]*

1 EMBL-CRG Systems Biology Research Unit, Center for Genomic Regulation (CRG), Universitat Pompeu Fabra, Barcelona, Spain, **2** Departamento de Biología del Desarrollo Cardiovascular, Centro Nacional de Investigaciones Cardiovasculares (CNIC), Instituto de Salud Carlos III, Madrid, Spain, **3** ICREA Professor, Centre for Genomic Regulation (CRG), Universitat Pompeu Fabra, Barcelona, Spain

Abstract

A comprehensive spatio-temporal description of the tissue movements underlying organogenesis would be an extremely useful resource to developmental biology. Clonal analysis and fate mappings are popular experiments to study tissue movement during morphogenesis. Such experiments allow cell populations to be labeled at an early stage of development and to follow their spatial evolution over time. However, disentangling the cumulative effects of the multiple events responsible for the expansion of the labeled cell population is not always straightforward. To overcome this problem, we develop a novel computational method that combines accurate quantification of 2D limb bud morphologies and growth modeling to analyze mouse clonal data of early limb development. Firstly, we explore various tissue movements that match experimental limb bud shape changes. Secondly, by comparing computational clones with newly generated mouse clonal data we are able to choose and characterize the tissue movement map that better matches experimental data. Our computational analysis produces for the first time a two dimensional model of limb growth based on experimental data that can be used to better characterize limb tissue movement in space and time. The model shows that the distribution and shapes of clones can be described as a combination of anisotropic growth with isotropic cell mixing, without the need for lineage compartmentalization along the AP and PD axis. Lastly, we show that this comprehensive description can be used to reassess spatio-temporal gene regulations taking tissue movement into account and to investigate PD patterning hypothesis.

Citation: Marcon L, Arqués CG, Torres MS, Sharpe J (2011) A Computational Clonal Analysis of the Developing Mouse Limb Bud. PLoS Comput Biol 7(2): e1001071. doi:10.1371/journal.pcbi.1001071

Editor: Stanislav Shvartsman, Princeton University, United States of America

Received August 11, 2010; **Accepted** December 29, 2010; **Published** February 10, 2011

Funding: The work was funded by the MADRICEL grant from the Madrid Regional Government (S-SAL-0190-2006). The funders had no role in study design, data collection and analysis, decision to publish, or preparation of the manuscript.

Competing Interests: The authors have declared that no competing interests exist.

* E-mail: luciano.marcon@crg.es (LM); james.sharpe@crg.es (JS)

Introduction

The cellular processes by which a field of cells develops into a spatially-organized tissue have traditionally been split into two distinct questions: pattern formation and morphogenesis. The first focuses on the regulatory mechanisms underlying spatial and temporal cell fate specification. The second focuses on the cellular behaviors that physically drive growth and shaping of multicellular structures. While these two processes can indeed be considered to be conceptually separated, in practice they usually occur simultaneously and are believed to be tightly coordinated. The vertebrate limb is an excellent model system to study how these two processes work in combination [1]. In mouse, limb development starts around 9 days post fertilization with the protrusion of a mass of undifferentiated mesenchymal cells from the lateral plate mesoderm of the embryo. This structure, known as the limb bud, is able to grow and organize itself in less than 3 days to determine most of the structures found in the adult limb (tendons, skeleton, dermis etc.). Growth and patterning occur along three major axes: the proximal-distal axis (PD) that goes from the body to the finger tip; the anterior-posterior axis (AP) going from the thumb to the little finger and the dorsal-ventral axis (DV), going from the palm to the dorsal part of the limb. Important signaling centers of the limb, like the apical ectodermal ridge (AER) and the zone of polarizing activity (ZPA), are known to regulate both growth and patterning [2–4] and their activities are known to be highly coupled [5]. Moreover there is increasing evidence that tissue growth could play an important role for patterning [6]. Therefore a crucial step to better understand both limb morphogenesis and patterning is to accurately map tissue movements over space and time.

Several studies in chick [7–9] have produced fate maps which provide an important overview of the tissue movements in the mesenchyme and in the AER. In mouse, where in utero labeling is required, a first study was made in [10] by carbon particles injection and only more recently a first clonal analysis was performed by using a tamoxifen-inducible Cre reporter line to obtain cell labeling in the embryo [11]. However, the goal of these studies was not to build quantitatively-accurate maps of tissue movements, but rather to address specific questions about (a) the timing and mechanisms of regional fate determination, and (b) the possible presence of lineage-restriction compartments. It has been possible to draw clear conclusions regarding the second question: a clear compartment boundary restricting cells along the DV axis was found in [11], while no evidence for compartments along the other two axes was found (PD and AP). Indeed, both in chick and mouse a high degree of overlap was found between clones of the three PD regions corresponding to the stypolod, zeugopod and

Author Summary

A comprehensive mathematical description of the growth of an organ can be given by the velocity vectors defining the displacement of each tissue point in a fixed coordinate system plus a description of the degree of mixing between the cells. As an alternative to live imaging, a way to estimate the collection of such velocity vectors, known as velocity vector field, is to use cell-labeling experiments. However, this approach can be applied only when the labeled populations have been grown for small periods of time and the tensors of the velocity vector field can be estimated directly from the shape of the labeled population. Unfortunately, most of the available cell-labeling experiments of developmental systems have been generated considering a long clone expansion time that is more suitable for lineaging studies than for estimating velocity vector fields. In this study we present a new computational method that allows us to estimate the velocity vector field of limb tissue movement by using clonal data with long harvesting time and a sequence of experimental limb morphologies. The method results in the first realistic 2D model of limb outgrowth and establishes a powerful framework for numerical simulations of limb development.

autopod. However, regarding the first question, experimental results have led to conflicting interpretations. For example, the relationship between PD patterning and the underlying tissue movement remains unclear. On one hand, limb tissue movement data has been used to support the idea that the three PD segments are specified at early stages of limb development [12] and subsequently only expand because of growth. On the other hand, comparisons between fate maps and the expression of distal markers like Hox genes [9,13] have been used to support the idea that the PD patterning relies on complex spatio-temporal gene regulation coordinated with growth [14,15].

Discrepancies between different interpretations of tissue movement data are due to a few specific limitations of previous studies which we aim to address through the modeling framework presented here. Firstly, quantitative details matter. Although alternative hypotheses may be qualitatively different from each other (such as the Progress Zone Model (PZM) [16] versus the Early Specification Model (ESM) [12]), the empirical evidence that could distinguish them will often depend on quantitative details of timing. Previous projects have revealed the overall pattern of movements, but have not mapped out the quantitative details. Secondly, all real data sets are sparse – they provide observations about a discrete collection of positions in space and time. It is non-trivial to extrapolate from these observations to a comprehensive prediction of how any piece of tissue will move at any point in time. Thirdly, many projects have employed a large time interval between labeling the cells and assessing the distribution of descendants. The shapes of the final labeled regions are therefore the result of an accumulated history of different tissue movements over time. Again, deconstructing the full sequence of local movements which lead to the final result is non-trivial. In particular, a recent study [17] showed that the tissue movements that drive limb morphogenesis are more complex than previously thought and depend on anisotropic forces. This and other studies [18,19] also highlighted that limb mesenchymal cells have a complex shape and are capable of a wide range of cellular behaviors including oriented cell division and cell migration.

As an important step beyond the general overview given by previous fate maps, a formal numerical description of limb tissue movements over time would be of immense help to analyze the complex morphogenesis of the limb. Such a description could be defined by the velocity vectors defining the displacement of each tissue point in a fixed coordinate system. Ideally, the collection of these vectors, known as velocity vector field, would be directly measured by tracking tissue points during growth by time-lapse imaging. However, despite recent advances in live imaging of the mammalian limb bud [20,21], it is a challenging technique and a complete description of tissue movements is still not available. In plants, clonal analysis has been explored as an alternative to live imaging for studying the growth of 2D leaves and petals. Local growth tensors were derived directly from shapes of clones and these data were combined into a computational model to recreate a full map of the global tissue movements (the velocity vector field) over time [22]. Unfortunately, in the mouse limb most of the available fate maps and clonal analyses have been performed with a long time-interval between labeling and analysis. This is ideal for the more common purpose of fate-mapping, as it reveals the final positions and tissue types of cells which were labeled during their early patterning phase. However such long-term clone shapes are not suitable for directly inferring local growth tensors – instead labeled populations should have undergone only enough growth to reveal local anisotropies, i.e. a short time-interval between labeling and analysis [23]. Another complication compared to the 2D plant case is the extensive mixing of mesenchymal cells that leads to a strong dispersal of the cells over space. A velocity vector field alone would therefore be insufficient to fully describe cell movements.

Due to this lack of quantitative data on tissue movements, most of the existing 2D mathematical models of limb growth have been used as theoretical tools to explore possible cellular hypothesis explaining limb outgrowth [24,25]. These studies relied on the existing literature to suggest the underlying mechanics of limb growth, and consequently predicted tissue movement maps consistent with the proliferation gradient hypothesis [26], in which tissue expansion is concentrated at the distal tip. However, a recent simulation which performed a more rigorous comparison of this hypothesis against quantitative data on proliferation rates, has demonstrated the implausibility of this concept [17]. Since it is now clear that the cellular mechanics underlying outgrowth are complex and not well understood [19,27], we therefore wished to create a model of tissue movements which is based not on a mechanistic hypothesis, but which instead acts as a numerically-descriptive framework within which to integrate information from real clonal experiments. In particular we have developed a methodology which is not restricted to short-term clonal data, and which can interpret the available long-term clonal and predict cell movements across the full spatio-temporal extent of mouse limb bud development. The model is able to use 2 sources of data as empirical constraints to define a biologically-accurate tissue movement map: (i) a temporal sequence of experimental limb bud morphologies – a numerical shape description for every hour of development over a 72 hour period, and (ii) a collection of clonal data generated by a tamoxifen-inducible Cre transgenic mouse line.

The paper is organized as follows. In the first two sections of the results we introduce the new computational approach that was developed to explore different limb tissue movement maps matching experimental change in limb morphology. In the subsequent two sections we present a mouse clonal analysis of early limb development (from 9 to 12 days pf.) and we show how the tissue movement map that better matched the distribution and shapes of clones was selected. In the following section, the tissue movement map is modified to match the experimental degree of cell mixing observed in the experimental clones. In the

last section of the results we characterize the tissue movement map and relate it to traditional PD patterning hypothesis. Finally in the Discussion section we summarize the study and present the future applications of the model.

Results

We present here a new computational method that estimates the velocity vector field of limb tissue movement by using 2 experimental constraints: a sequence of experimental limb morphologies, and long-term clonal data. The main idea underlying the method is to generate a set of hypothetical velocity vector fields that are consistent with the first constraint (the experimental morphological changes), and then to select the one responsible for real limb outgrowth by comparing simulated fate maps with the second constraint (the experimental clonal data). In this respect our approach is analogous to a "reverse-engineering' method, as the data cannot lead to a direct calculation of tissue movements but can only constrain the possible forward simulations. The resulting velocity vector field was then used to derive the tensors of the velocity gradient which describe the local behaviors of the tissue movement. As an application of the model, a reverse version of the tissue movement map was generated to provide a relative estimate of the degree of mixing between the progenitors of three PD segments. Finally, by mapping a time course of Hoxd13 gene expression into the model, we were able reveal the contribution of tissue movement to the expansion of the Hoxd13 domain.

From 2D experimental morphologies to velocity vector fields

The shape of the limb bud at any point in time can be defined by a spline curve, but clear morphological features along this line are absent – the limb displays a smooth rounded shape. This lack of landmarks means that even a very precise knowledge of the shapes over time is insufficient to define the underlying tissue movements. This is true both for the internal tissue and also the limb boundary itself, as a particular point of tissue (or landmark) could slide along the boundary spline without altering the shape. Figure 1 illustrates the nature of the problem: a well-defined shape change is given (panel A), but numerous different tissue movement maps are all equally compatible with this observation, each of which has different combinations of local tissue speed and directionality (B–E). Despite these degrees-of-freedom, the temporal sequence of boundary shapes does nevertheless act as an important constraint on the full range of growth possibilities. To capture an accurate numerical description of these shape changes we therefore took advantage of a morphometric analysis performed in [28]. In that work, 600 limb buds of different ages were photographed in a standard orientation, cubic splines were fitted to the boundaries, average shapes were calculated for key timepoints, and shape interpolation was performed to calculate the intermediate shapes [28]. The result is an hour-by-hour sequence of 72 shapes which represents a standard trajectory of limb bud morphology over developmental time (from approximately E9 to E12) – see Figure S1. Each shape corresponds to a morphometric stage that is named as mE*dd*:*hh*, where *dd* is the morphometric embryonic day and *hh* is the morphometric embryonic hour. It is important to note that the morphometric stage notation is different from the standard embryonic day notation, for example the standard notation E10.5 translates into the morphometric stage mE10:12.

For this study we had to develop software that would allow the exploration of a set of possible velocity vector fields that can each reproduce the same observed boundary changes. In particular, different tissue movement maps are equivalent to considering the

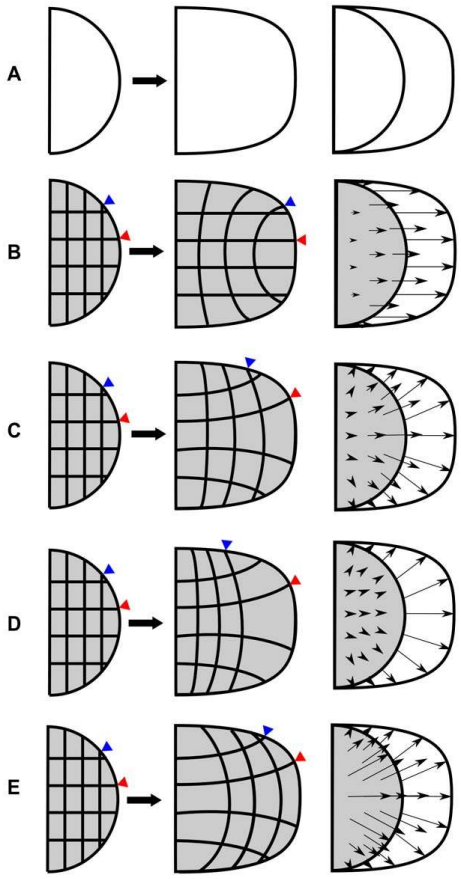

Figure 1. Different ways to make the same shape. (A) A simple semi circle (first column) grows into a defined shape (second column). The two shapes are aligned at their left boundary (third column). (B) A velocity vector field pointing in the distal direction with a vector magnitude distribution that leads to a uniform expansion. (C–E) A variety of velocity vector fields which can all create the same boundary shape change. The first magnitude distribution (C) defines uniform expansion, the second (D) defines a greater distal expansion and the third (E) a greater proximal expansion.
doi:10.1371/journal.pcbi.1001071.g001

2D limb shape as a rubber sheet or mesh, with different distributions of elastic deformation (e.g.. the various mesh deformations shown in Figure 1B–E). To cover the whole temporal sequence of development, a single complete map would include a sequence of slightly changing hour-by-hour deformations across all 72 shapes. We thus spatially discretized each of the limb bud shapes using an unstructured triangular grid. An example of the type of grid generated is given in Figure 2C. We then sought a convenient approach to parameterize the variety of possible mesh deformations across time, and devised a two-step method – the first step dealing with boundary, and the second with the internal tissue movements.

For the first step, in effect we must define a series of landmarks which explicitly map points in each boundary shape to their

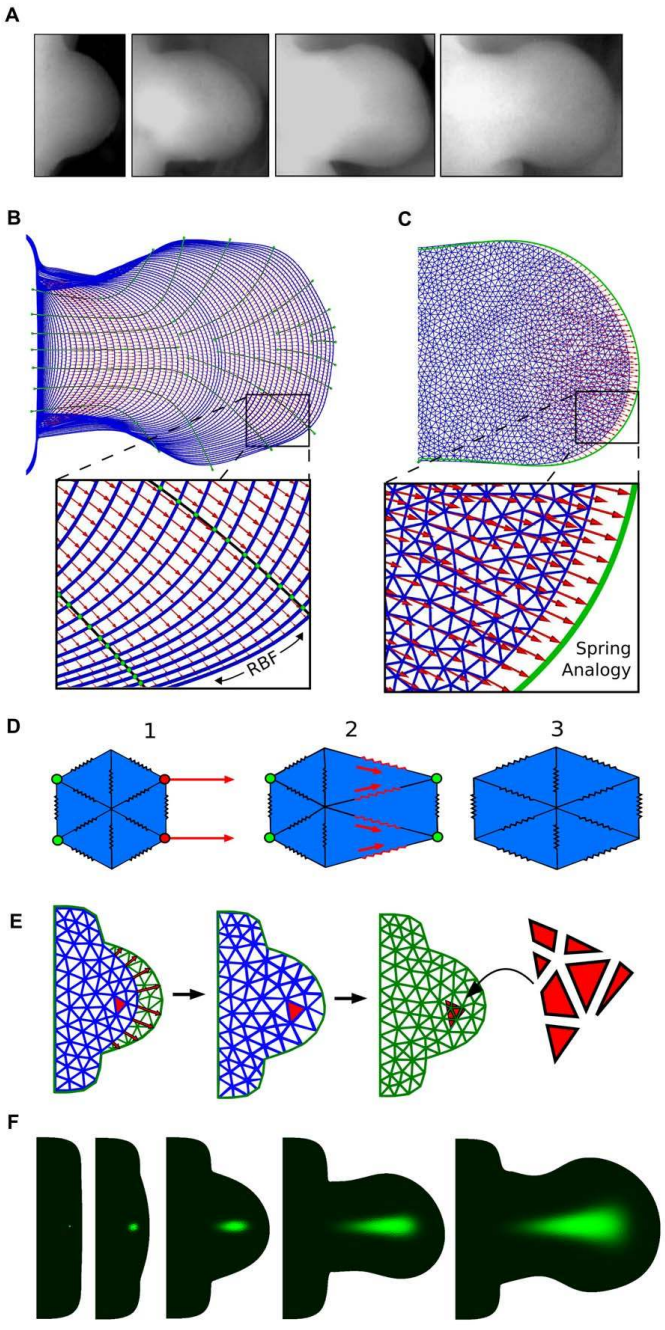
A
B
C
RBF
Spring
Analogy
D
1
2
3
E
F

Figure 2. From morphologies to velocity vector fields. (A) A sequence of limb photos at different developmental stages. (B)The chronological sequence of limb morphologies derived from [28] (blue color) is overlaid by the *boundary control splines* (black lines). Intersection points between control splines and limb morphologies (green dots) define a set of control vectors that are interpolated using radial basis functions (RBF) onto the boundary mesh points. In this way a series of velocity vector fields is obtained (red arrows) which define how to displace the boundary mesh points to match the following mesh in the sequence. (C) Starting from the boundary displacement, a velocity vector field that displaces internal mesh points (red arrows) is calculated by using an edge spring analogy. (D) An example of deformation obtained with an edge spring analogy. 1) A deformation is applied to the boundary points of the mesh (red points) and the displacements of mesh points of the left-most boundary are fixed to zero (green points). 2) Edge springs of the triangles close to the deformation exercise tension forces to the neighboring triangles. 3) Relaxation of the forces to reach equilibrium provides a smooth deformation of the mesh. (E) A mesh (blue mesh) is deformed to match the next mesh in the sequence (green mesh). A triangle (red triangle) of the deformed mesh is split into the overlapping triangles of the next mesh by considering the respective areas of overlap (seven red segments on the right). (F) An example of virtual fate map. A triangular element is labeled with a green dye (probability equal to one) at early stages of development and its fate is simulated using the sequence of deformations and interpolations.
doi:10.1371/journal.pcbi.1001071.g002

positions in the next shape (equivalent to controlling the blue and red triangles in Figure 1). To maximize the flexibility of the system we devised the concept of user-defined *boundary control splines*. A graphical user interface was developed to allow arbitrary positioning of these control splines onto the sequence of limb shapes (an example is shown in Figure 2B). Intersections between control splines and limb shapes (the green points in Figure 2B) determined, for each pair of contiguous limbs, a set of control vectors which defined how to displace points on a young limb shape in order to match a point on the next older one. Due to the intrinsic smooth curvature of these splines over space, they are a convenient method for defining smooth boundary movements over time (Figure 2B). Since the resulting control vectors were defined for arbitrary points of the limb boundaries they were interpolated onto all the mesh boundary points using radial basis functions (RBFs) with Gaussian basis. For each limb mesh, the N control vectors $\vec{V}_i,\ i \in 1..N$ (calculated from the intersection between the spline curves the limb morphologies) were used to derive two radial basis function interpolations $f_x(P)$ and $f_y(P)$ with the formula:

$$f(P) = \sum_{i=0}^{n} w_i \phi(\|P - c_i\|) \tag{1}$$

where the Gaussian basis $\phi(r) = e^{(-\beta r^2)}$ and c_i is the origin of the control vector V_i. Coefficients w_i were estimated using the matrix methods of linear least squares to fit the x components of the control vectors $\vec{V}_i$ in the case of $f_x(P)$ and the y components of the control vectors $\vec{V}_i$ in the case of $f_y(P)$. Interpolated velocity vectors $\vec{v}_P$ were thus calculated as $\vec{v}_P = \{f_x(P), f_y(P)\}$ for all the points on the mesh boundaries. This results in a series of velocity vector fields (the red arrows in Figure 2B) which define how to displace the boundary points of each limb mesh in order to match the following in the chronological sequence. We have thus created a method by which the user can conveniently define a variety of different mappings for the boundary, which are all consistent with the experimental shape changes.

For the second step we had to devise a way of defining the internal tissue movements (the velocity vector field), and in particular a method for exploring some variations on these maps. The internal movements must be consistent with a given boundary mapping (defined above) and we therefore chose to calculate internal velocity vectors using an edge spring analogy algorithm which can smoothly propagate a given set of displacements from the boundary into the internal points of each mesh. Spring analogy algorithms are a popular approach to deform mesh elements by modeling edges as lineal tension springs [29], Figure 2D. Although this approach is sometimes used to model the elastic mechanics of a tissue, in our case we are not assuming that it correctly represents the physical properties of the tissue – it is simply an efficient method for defining hypothetical displacement maps. The algorithm prevents node element collisions and for small deformations it ensures that the quality of mesh elements is maintained. In our model this approach exhibits particularly good performance due to the small time differences between contiguous limb morphologies (differing by just one hour of development). Moreover the smooth propagation of displacements translates into a smooth spatial distribution of tissue expansion in accord with the limb proliferation maps presented in [17]. Furthermore, since each spring in the mesh can be given a stiffness coefficient, it also presents a convenient method to explore variations to the tissue movement map, simply by varying the spatial distribution of the stiffness (explained in more detail below).

Our spring analogy method was implemented as follows: given a mesh M_k defined as $M_k = (V_k, B_k, B_k^l, E_k)$, where V_k are the mesh points, B_k the points on the mesh boundary, B_k^l the points on the left-most boundary and E_k the edges of the mesh, our algorithm proceeds as follows:

1. the displacement of all the boundary points on the left-most boundary are set to zero (representing the deep internal tissue of the body) and the displacements of the remaining mesh boundary points is set to the velocity vectors calculated with the radial basis function interpolation described above in equation (1):

$$\begin{aligned} &\forall v_i \in B_k^l, \overrightarrow{\delta_i} = \{0,0\} \\ &\forall v_i \in B_k \wedge v_i \notin B_k^l, \overrightarrow{\delta_i} = \{f_x(v_i), f_y(v_i)\} \end{aligned} \tag{2}$$

   where $\vec{\delta}_i$ is the displacement vector of the vertex v_i.
2. The following iterative formula is used to equilibrate the forces h times until the displacements are close to zero, ($lim_{h\to\infty} \overrightarrow{\delta_i^h} = 0$):

$$\forall v_i \in V_k \wedge v_i \notin B_k, \overrightarrow{\delta_i^{h+1}} = \frac{\sum_{j=0}^{v_i} \alpha_{ij} \overrightarrow{\delta_i^h}}{\sum_{j=0}^{v_i} \alpha_{ij}} \tag{3}$$

   where α_{ij} is the stiffness coefficient of the edge e_{ij} that connects the point v_i and v_j of the mesh.
3. Eventually the new vertex positions are calculated as:

$$\forall v_i \in V_k, v_i = v_i + \overrightarrow{\delta_i} \tag{4}$$

A small graphical example of the algorithm is shown in Figure 2D.

A variety of alternative movement maps which all fit to the given boundary displacements, can now easily be generated by altering the spatial distribution of the stiffness coefficient α_{ij}.

In conclusion, we can define a velocity vector field for each mesh in the chronological sequence (the red arrows in Figure 2C) representing a hypothetical tissue movement map connecting each pair of contiguous morphologies in the sequence, see Video S1. The displacements on the boundary can be altered through the use of the boundary control splines, while the internal displacements can be altered through changes in the spatial distribution of spring stiffness. The collection of 9 different maps explored extensively in this paper are described later.

Triangle interpolation map and virtual fate maps

In this section we wish to generate virtual clone experiments, which can later be compared to real clonal data. Although the velocity vector fields defined above are smooth across time, to create virtual clones the resulting hour-by-hour mesh deformations must be linked together to allow tracking the fates of individual tissue regions over time.

Each of the 72 velocity vector fields defines how to deform a limb mesh in order to match the following mesh in the sequence, and the complete set of fields describes a hypothetical computational tissue movement map that matches the entire sequence of experimental morphologies. To track a region of tissue over the full 72 hours, we must determine how the triangular elements of each mesh will map to the different set of triangles of the 1-hour older mesh. In particular, we must calculate a triangle-interpolation map from mesh to mesh. A graphical representation of this process is provided in Figure 2E. On the left of this panel, a blue mesh is deformed according to its velocity vector field (red arrows), in the second column of the figure, the deformed blue mesh is perfectly overlapping the next green mesh in the sequence. On the right of the panel, a triangle of the blue mesh (red labeled triangle) is split in 7 parts. Each of these parts represents the area of overlap between the original triangle of the blue mesh and a triangle of the next green mesh. In the course of a numerical simulation, numerical values associated with the triangle of the blue mesh are transferred to the triangles of the next green mesh according to the area of overlap.

Repeating this operation for each pair of contiguous meshes, we generate a correspondence map that defines the fate of each triangle of the first mesh in the sequence (stage E9) with respect to a set of triangles on the last mesh in the sequence (stage E12). This map is a computational implementation of an experimental fate map. The interpolation is conservative and is based upon the velocity vector fields that define the whole virtual tissue movement. A virtual fate map can be performed by marking a triangle with a "virtual clonal dye" – in practice by assigning the triangle a probability of one and then following the evolution of the probability distribution over time, see Figure 2F and Video S2. Experimental clones can be seen as a stochastic simulation of these probability distributions. (Further details on the use and meaning of this map are provided in Text S3).

This approach has also a more general application, since it defines the basis for any kind of numerical simulation on a growing triangular mesh representing limb growth. Indeed, by interpolating numerical values on a newly generated mesh at every hour of development we are effectively implementing a global re-meshing scheme that avoids the large element deformations that a grid would undergo over the whole 72 hours of limb development. It is well known that frequent re-meshing introduces a source of spatial diffusion in numerical solutions [30,31]. This is not however a problem in the context of virtual fate maps of the limb bud – clonal data of mouse and chick show a high degree of cell mixing even for short time intervals after clone induction. In the virtual fate maps, the probability distribution represents the local density of labeled cells, with a value of one corresponding to a region where every cell is labeled. The local decrease of labeled cell density which is modeled as diffusion therefore corresponds to cell mixing. Determining the appropriate levels of cell diffusion/mixing for the model is discussed in a later section.

Mouse clonal data

In this section we present a mouse clonal analysis of early hind limb development, which will subsequently be used to compare with hypothetical virtual clones. These experimental results are compared with previously published fate maps in chick and implications on PD patterning are discussed.

We used the tamoxifen inducible Cre-line presented in [11] to conduct a mouse clonal analysis from stage E9 to stage E12 of development. The clones were induced by injecting low tamoxifen concentration at E8 (0.10mg) so that random recombination events would produce single cell labeling events within the embryos. 24 hind-limbs showing suitable monoclonal labeling were used for the clonal analysis. To compensate for the variation in development between embryos of the same litter and the uncertainty of the injection day, we staged each limb using the staging system presented in [28] and adjusted the estimation of the injection day accordingly. The PD and AP clone lengths relative to the maximum PD and AP length of the limb were measured as shown in Figure 3A (See also Figure S2). From the quantification of clone lengths, two graphs representing respectively PD and AP clone expansion were produced, an example is shown in Figure 3B. All clone lengths were mapped at stage E12 by considering prospective or retrospective lengths as shown in Figure 3B. PD and AP lengths at E12 were visualized representing each clone as a rectangle centered in its AP and PD midpoint (in Figure 3C). In this way we were able to cluster the clones in two groups according to their position and shape: a) isotropically expanding clones in the proximal and distal part of the limb that showed similar AP and PD expansion rate (highlighted in blue), b) anisotropic clones that expanded more along the PD axis than the AP axis (highlighted in green and red). Plotting the ratio between PD and AP lengths a similar behavior was revealed (Figure 3D). In accord with a previous study [11] we found no clear evidence for AP and PD compartments. Indeed, a high degree of cell mixing was observed across the whole limb. Consistently with previous studies in chick [8,9] we found that clones expanded across one or two PD segments but never span across the whole PD axis of the limb, see Figure 3E. Remarkably, no clones were found restricted to the zeugopod alone – all clones found in this zone also overlapped with the autopod or the stylopod regions.

Tissue movement map estimation

Now that we have (i) a method for generating virtual clones on hypothetical growth maps, and (ii) a suitable set of experimental clone data, the next task is to use the latter to infer a biologically-realistic growth map for the mouse limb bud. This task can be split into two parts: firstly defining a suitable set of hypothetical velocity maps, and secondly developing a method to systematically compare each map against the experimental clone data.

The space of all possible movement maps is highly multidimensional and potentially very large, (as exemplified in Figure 1). Exhaustively exploring all theoretically-possible maps would have a prohibitive computational cost, and the challenge is therefore to find a good match in an efficient manner. However, when experimentally-derived assumptions about limb development are considered – for example that tissue never moves backwards towards the body, and that the distribution of tissue growth varies smoothly over space – in fact the available options reduce to a basic set of possible asymmetries, as summarized by the following

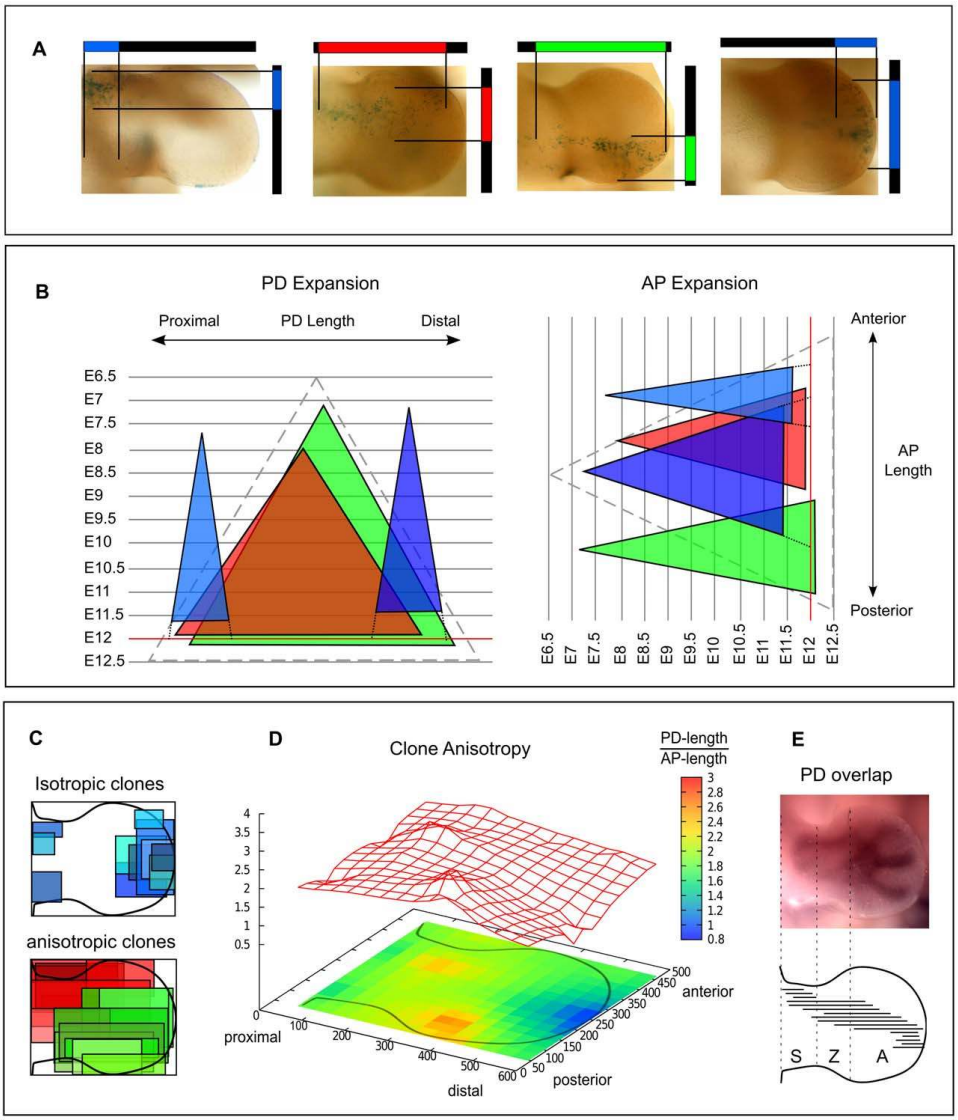

Figure 3. Clonal analysis. (A) Four clones showing the quantification of the AP and PD clone lengths. (B) In order to compensate for the variation in developmental stage between different embryos each limb was staged and the tamoxifen injection time was adjusted accordingly. Large triangles represent the AP and PD clone expansion over space and time. PD and AP lengths were mapped at E12 (red line) considering prospective (dotted line) or retrospective lengths. (C) Each rectangle represents the AP and PD length of one clone. Clones were clustered into two groups: isotropically expanding clones, with comparable AP and PD length (blue rectangles), and an-isotropically expanding clones having the PD length greater than AP length (red and green rectangles). (D) A graph showing the degree of clone anisotropy in the limb, PD length over the AP length. Blue means low anisotropy and red high anisotropy. (E) Top: In-situ of Sox9, a known early skeletal marker showing the position of the three PD segments (S = stylopod, Z = zeugopod, A = autopod) Bottom: 16 clones showing the degree of overlap between clones spanning across different PD segments.
doi:10.1371/journal.pcbi.1001071.g003

questions: Is there asymmetric growth along the AP axis? E.g. does the posterior tissue expand faster or slower than the anterior tissue? Similarly, does the distal region expand faster or slower than the proximal region? Finally, does the tissue grow fairly straight distally, or alternatively does it fan-out along the AP axis into the autopod?

Using the two levels of manual control described in a previous section of results (the boundary control splines, and the spring stiffness distribution) we were able to create a collection of 9 maps which represent the main plausible asymmetries in limb bud development (Figure 4). Since the control splines are oriented substantially along the PD axis, varying their positions primarily affects the AP distributions of growth. We were thus able to choose 3 sets of these control splines, which define either a fairly straight distally-oriented growth (Maps 1–3), a strong fanning-out movement into the distal autopod region (Maps 4–6), or a posteriorly-biased map in which growth is preferentially twisted into the posterior region (Maps 7–9). Using the second level of control – the spring stiffness distribution – we could vary the PD growth pattern. The stiffness coefficient for each edge of the mesh was given a spatial distribution in the following way:

$$\forall e_{ij} \in E_k, \alpha_{ij} = \frac{1}{l_{ij}} P(e_{ij}^x) \quad (5)$$

where α_{ij} is the stiffness coefficient of the edge e_{ij} that connects the point v_i and v_j of the mesh, l_{ij} is the length of the edge e_{ij} and $P(e_{ij}^x)$ is a scaling function used to vary the distribution of the stiffness coefficients according to e_{ij}^x, the x coordinate of the edge.

We explored a number of scaling functions, $P(e_{ij}^x)$ in equation (5), to vary the stiffness coefficients along the PD axis (the x axis), and chose 3 which display different degrees of bias towards the distal end of the limb. The first function used was an inverted sigmoid (with respect to x) that defined lower stiffness coefficients in the distal part of the limb (Maps 1, 4, 7), i.e. allowing greater expansion of distal tissue. The second function was a constant value defining no change in stiffness along the PD axis (Maps 2, 5, 8). The third function was a sigmoid that defined higher stiffness coefficients in the distal part of the meshes (Maps 3, 6, 9), i.e.. restricting distal growth along the PD axis. The combination of the 3 AP variations, and the 3 PD variations resulted in 9 maps to be explored in detail. Additional details regarding the maps and the scaling functions are provided in Text S1. As an important control, proliferation patterns were derived from the velocity vector gradients of each map and the ranges were ensure to be biologically realistic, see Figure S3.

The second step was to evaluate which of the 9 hypothetical tissue movement maps best fitted the experimental data. We mapped the 13 clone pictures having better contrast and best capturing the main features of the clonal data set onto the last triangular mesh in the sequence (stage E12). This was done by manually aligning the limb morphologies of the thresholded clone pictures on the last mesh boundary. Results are shown in Figure S4. Next we implemented an algorithm to systematically compare all possible virtual clones for a given map with the 13 experimental clones. The youngest timepoint (E9) is represented by a mesh with 3156 triangles, and so this is also the number of virtual clones which could be calculated for each of the 9 maps. Evaluating the score of a given map therefore involved over 40 thousand clonal comparisons, which were calculated in the following way:

Given a set of triangles representing a virtual clone v and a set of triangles representing an experimental clone e, each virtual clone was scored with the formula:

$$S_e(v) = \sum_{i=1}^{N} p_i \sum_{i=1}^{N} \frac{1}{M} \quad (6)$$

where N is the number of common triangles between e and the virtual clone v, p_i is the probability value associated with the triangle i of the virtual clone and M is the number of triangles of the experimental clone e. The first part of the scoring function represents the probability that the experimental clone is obtained from the spatial probability distribution of the virtual clone. The second part acts as a penalty for cells founds outside the domain of the virtual clone. It calculates a score between 0 and 1 describing the proportion of triangles of the experimental clone contained in the virtual clone.

Figure 5A shows the positions that scored the best for three experimental clones on three different maps. Experimental clones are shown in white while virtual clones are visualized with colored

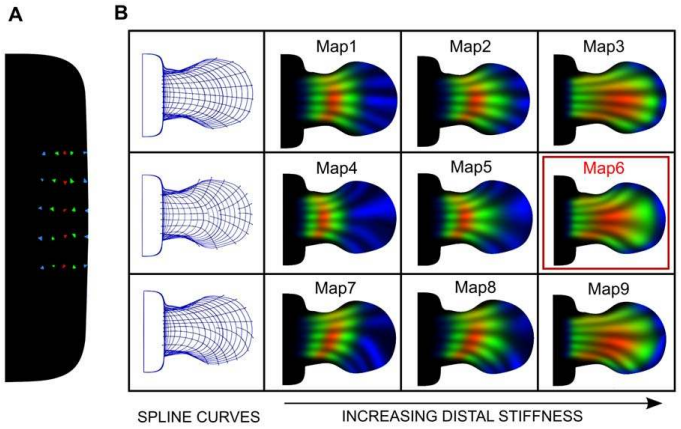

Figure 4. A collection of tissue movement maps. (A) Initial conditions used for the comparison between the tissue movement maps. Clones are positioned on a grid along the AP and PD axis and are colored according to the PD position, from proximal to distal: blue, green,red, green and blue. (B) Virtual fate maps resulting from 9 different maps obtained combining different stiffness coefficient distributions and spline curves (described in more detail in the main text). The left column shows the control spline curves. The stiffness of the distal springs is increasing from left to right. The tissue movement map outlined in red (Map6) is the one that best matched the mouse clonal data.
doi:10.1371/journal.pcbi.1001071.g004

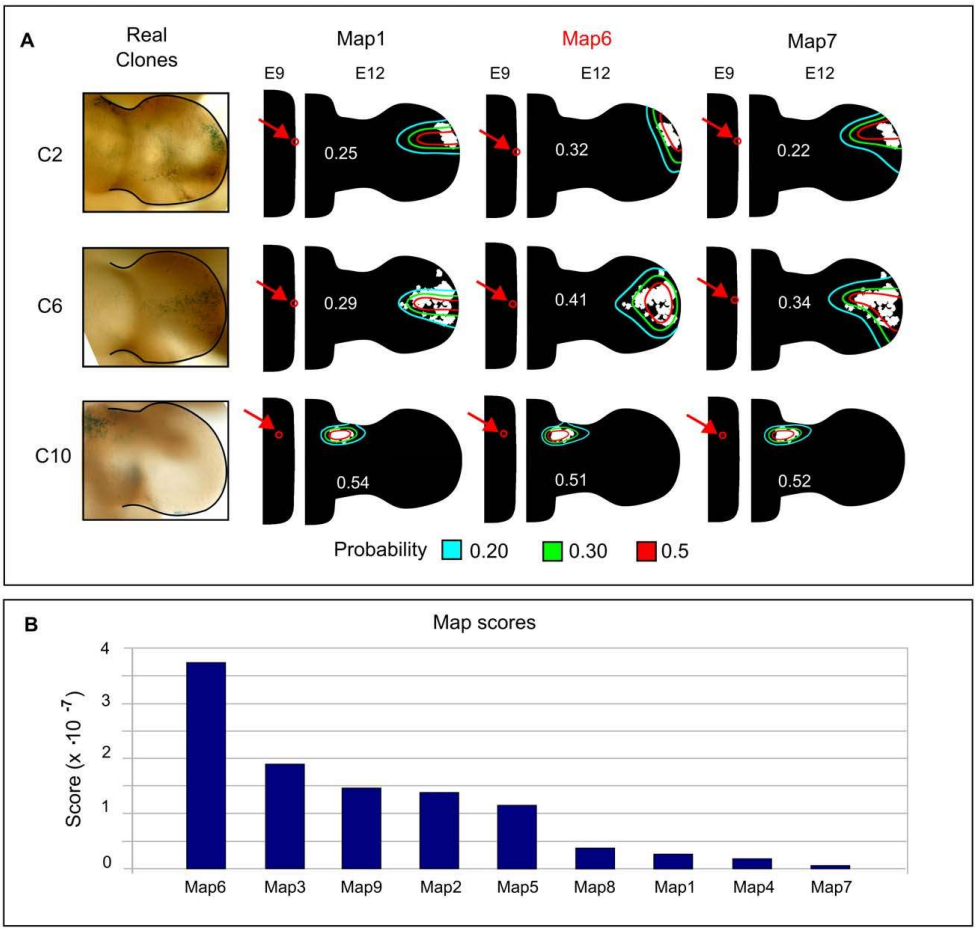

Figure 5. Virtual clone scores. (A) The left column shows pictures of experimental clones. The remaining columns show numerical comparisons between the experimental clones (white shapes) and the best matching virtual clone (colored contour lines). The comparison is made for three different maps (Map1, Map6, Map7). The contour lines define three regions of probability of the virtual clones: the area enclosed by the red line contain the 50% of the clone probability, the area between the green and the red contour the 30% and the area between the blue and the green contour the 20%. The number in white is the score value for each virtual clone. Limb shapes at stage E9 show the initial triangle associated with the virtual clone. (B) A comparison between the total scores of the 9 virtual tissue movement maps. Map6 scores almost 2-fold better than all the other maps.
doi:10.1371/journal.pcbi.1001071.g005

contour lines that define three regions of probability: the area enclosed by the red line contains the 50% of the clone probability, the area between the green and the red contour the 30% and the area between the blue and the green contour the 20%. Detailed clone scores for map are shown in Figure S5. The total score for each map was calculated by using the formula:

$$S_m^j = \prod_{i=1}^{13} S_c^{ij} \qquad (7)$$

where S_c^{ij} is the best score found for the clone i on the map j using the formula (6). We calculated the product between the clone scores (S_c) in order to give higher score to the maps that better matched all the experimental clones. Figure 5B shows the total score for each map. In conclusion, Map6 scored almost two-fold better than the other maps and was therefore selected as the one the best represented hind-limb tissue movement. As a test of robustness of this result, we chose to remodel the tissue movements of Map6, but on a finer mesh (starting with 5678 triangles at E9, instead of the previous 3156). These results (shown in Text S2) highlight that the same positions and orientations of virtual clones were obtained irrespective of the mesh resolution.

Cell mixing estimation

As mentioned in the previous sections, the hourly global re-meshing process introduces an inherent source of diffusion to the

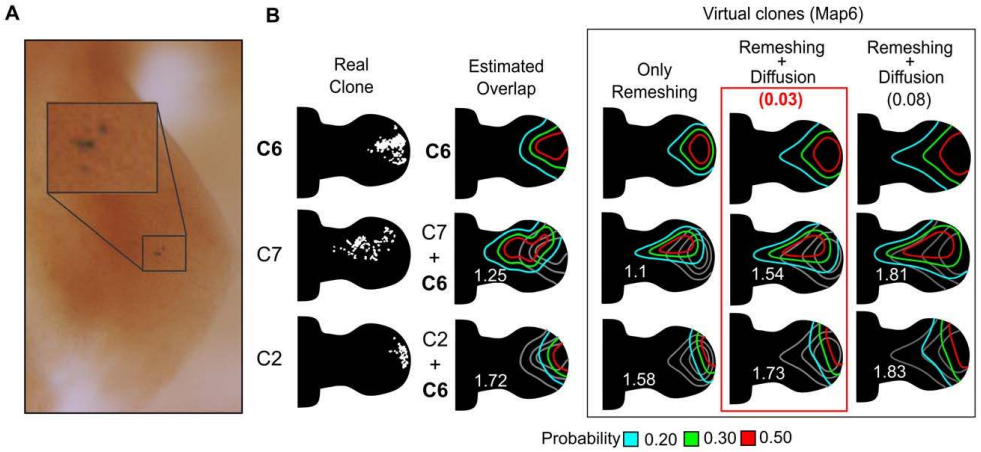

Figure 6. Re-meshing and cell mixing. (A) A picture showing the degree of cell mixing observed at early times after clone induction. (B) The first column shows 3 experimental clones used for this analysis. The second column shows the estimated probability distributions of experimental clones obtained by a mean filter. The second and the third row of this column show a quantification of the overlap between pairs of experimental clone distributions – C6-C7 and C6-C2. The number in white is the score representing the amount of overlap. In the three right-hand columns the overlap between the correspondent virtual clones from Map6 is calculated by considering different amount of additional diffusion: no additional diffusion (first column), a diffusion constant of 0.03 (second column) and a diffusion constant of 0.08 (third column). It can be seen that addition of some diffusion improves the score (compare with the "Estimated overlap" column), while too much extra diffusion makes the scores worse again.
doi:10.1371/journal.pcbi.1001071.g006

numerical simulation, which we consider equivalent to the redistribution in the density of labeled cells. This is in agreement with our clonal data that clearly shows a decrease of labeled cell density during early phases of clone expansion resulting from the mixing between labeled and non-labeled mesenchymal cells, see Figure 6A. An accurate quantification of the degree of mixing between mesenchymal cells would require a larger collection of clonal data, but we nevertheless wished to provide a rough estimate of the experimental degree of cell mixing and compare it with the amount of cell mixing introduced by the re-meshing process. Taking advantage of our model, we decided to estimate cell mixing by quantifying the degree of overlap between the experimental clones. The quantification was performed in two steps.

First, we estimated the spatial probability distribution of three different clones. This was done by applying a mean filter to the experimental clones as they were mapped into the mesh at stage E12. The mean filter averaged the value of each triangle with its direct neighbors and normalized the overall spatial distribution to 1. By iteratively applying the filter we smooth the distribution of the labeled triangles until the data did not present any spatial discontinuities. The estimated probability distributions of three experimental clones is presented in the second column of Figure 6B.

Secondly, we defined a score to quantify the degree of overlap between clone probabilities distributions. Given two clones $c1$ and $c2$, the score was defined as:

$$S_o(c1,c2) = \sum_{i=1}^{N} p_i^{c1} + p_i^{c2} \qquad (8)$$

where N is the number of common triangles between the two clones, p_i^{c1} is the probability value associated with the triangle i of the clone $c1$ and p_i^{c2} is the probability value associated with the triangle i of the clone $c2$. The overlap between two pairs of experimental clones was quantified using this formula (Figure 6B, second column). Results were then compared with the quantifications of the overlap between the correspondent virtual clones of Map6, see the third column in Figure 6B. Our estimations of overlap suggested that the amount of cell mixing introduced by the global re-meshing process was not enough to mimic the real degree of clone overlap consistent with the experimental data.

We therefore introduced an additional diffusion term that would model a higher degree of cell mixing. The quantification of the clone overlap was repeated multiple times with different degrees of extra-diffusion. In this way we were able to provide a rough estimate of the diffusion constant that better fitted the experimental clone overlap (see the two columns on the right in Figure 6B), and importantly to show that the unavoidable diffusion introduced by our global re-meshing scheme must in fact be augmented with extra diffusion to reach biologically-realistic levels.

In conclusion, the refined version of Map6 with the extra-diffusion not only matched the shape and distribution of the clonal data but was also matched the relative positing and spatial extension of the clones. A qualitative comparison between the experimental and the virtual clones obtained with this map is shown in Figure 7A. A simulation showing a number of clones that match the distribution and shape of the experimental clonal data is shown in Figure 7B and Video S3.

Applications of the model

In this section we present some applications of the growth model that highlight the power of mathematical modeling in characterizing limb outgrowth in space and time.

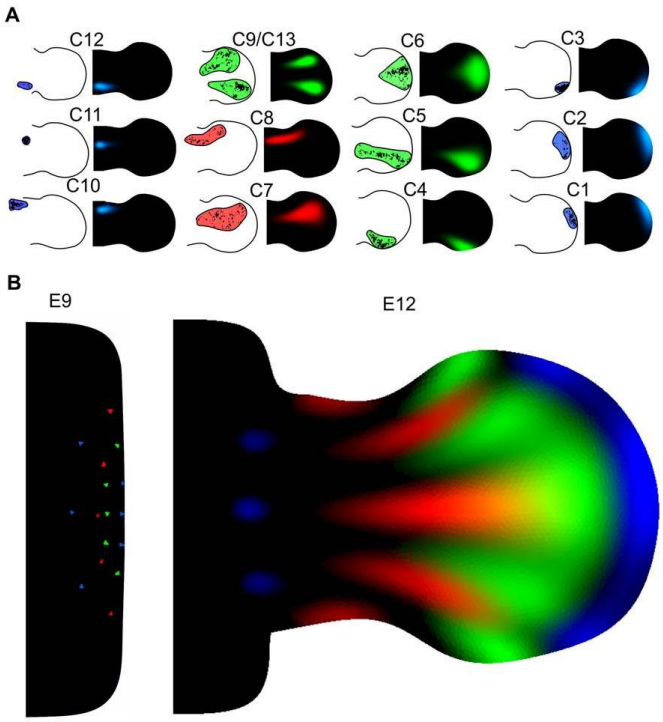

Figure 7. The matching map. (A) A direct comparison between experimental clones (white background) and simulated clones (black background). Experimental clones have been thresholded and the clone shape has been highlighted. (B) A collection of clones matching the distribution and shape of the experimental clonal data. Blue clones expand isotropically on the PD and the AP axis, and green and red clones expand more on the PD axis. On the left, the initial conditions of the fates are shown.
doi:10.1371/journal.pcbi.1001071.g007

A first interesting application of the model was to derive and visualize the local tissue behaviors that contributed to the global tissue movement responsible for limb outgrowth. In the model, local tissue behaviors can be represented by the growth tensors associated with each mesh triangle. Tensors were derived from the spatial gradient of the velocity vector field and provided three useful pieces of information: tissue growth rate, anisotropy and rotation [32]. The first of these can be directly related to proliferation and we translated these values into cell cycle time by considering the time required to double the area of a triangle. A similar approach was taken in [17] by assuming that the cell cycle time was equivalent to the time required to double the volume of a tetrahedron in a 3D limb tetrahedral mesh. Tensors were calculated for each time point and expansion rates were visualized using heat maps, see Figure 8B. Our model predicted a proliferation distribution with shorter cell cycle times in the distal region, with an average value of 9h, and longer cell cycle times on the proximal part of the limb, with an average value of 24h. The difference between the two regions was more evident from the stage E11 onwards with an average maximum difference of 12h in agreement with published experimental proliferation maps [17]. The other two components of the tensor were visualized using ellipsoids that were scaled and rotated according to the anisotropy and the rotation, see Figure 8C. The model predicted an initial relatively uniform anisotropy (until stage mE10.18) that was oriented towards the distal tip of the limb. This reflected the initial phase of elongation and protrusion of the limb and confirmed the results presented in [17] that showed that the elongation of the limb bud cannot depend only on differential isotropic cell proliferation but has to depend on anisotropic tissue movement. The model also revealed a second late phase, after mE10.18, in which the anisotropy under the distal ectoderm close to the AER was higher than in the central tissue. Interestingly, within the most distal/central region of this sub-ridge mesenchyme the direction of anisotropy was parallel to the AER, whereas it was perpendicular to the AER in more anterior and posterior regions. Taken together these results suggested the possibility that during autopod expansion, signals coming from the distal AER could act promoting a higher proliferation rate and an anisotropic behavior of the cells that result in the expansion of the autopod along the AP axis.

The second application of the model focused on the PD patterning of the limb. In particular we used our model to address a matter of debate for the last two decades: that is to identify at which stage the three PD segments of the limb can be specified. The problem has been addressed numerous times in the chick by creating fate maps to study two different aspects: the degree of mixing between cells of the prospective segments, and to follow the lineage of cells expressing markers of the three PD segments, like Hoxa13 and Hoxd13 for the autopod. An early study using both

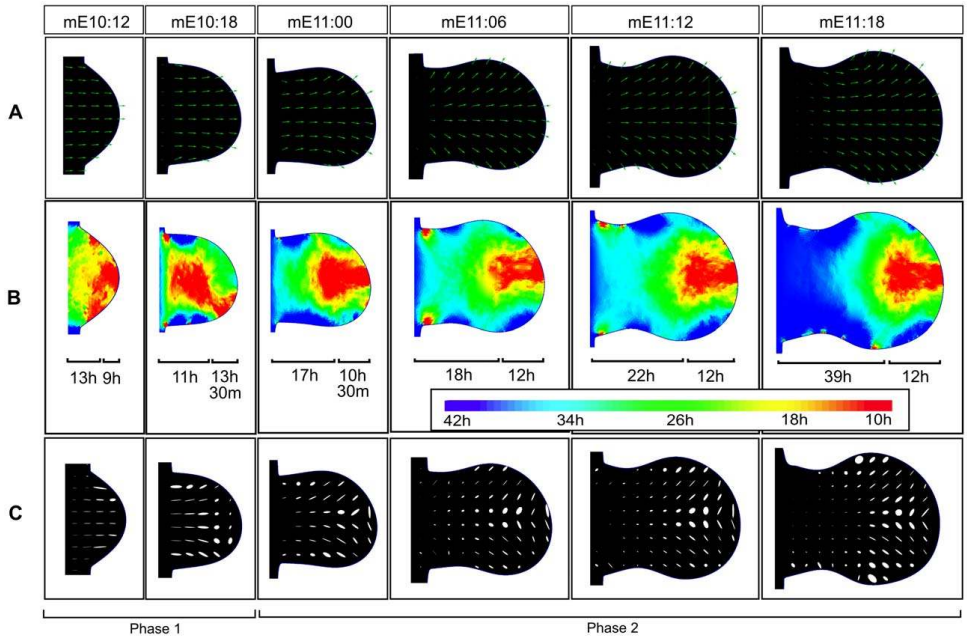

Figure 8. Derivation of growth tensors. (A) The velocity vector field of the map that best recapitulates limb tissue movement. Velocities have been normalized for clarity. (B) A heat map visualizing the expansion rate of each triangle. Red corresponds to high expansion rate (low cell cycle time of 10h) and blue to low expansion rate (high cell cycle 42h). Average cell cycle times of distal (1/3 of the PD axis from the tip) and proximal parts (remaining 2/3 of the PD axis) are shown for each time point. (C) Ellipses visualizing the anisotropy and rotation of different parts of the tissue. During an initial phase of development the anisotropy is relatively uniform (until stage mE10.18) and oriented towards the distal tip of the limb. After this stage the anisotropy is non-uniformly distributed, and is higher in the region under the influence of the AER. In the central sub-ridge region the direction of the anisotropy is parallel to the AER, while in more anterior or posterior regions it is perpendicular to the AER.
doi:10.1371/journal.pcbi.1001071.g008

approaches [7] concluded that the degree of mixing between the prospective PD segments was low and that the anterior expansion of the distal marker Hoxa13 was mainly due to growth. In other words this study suggested that the distal segment was specified early during development and that it subsequently expanded due to growth. A similar idea was further developed in [12] where it was proposed, based on the observation that early fate maps were almost always confine to a single segment, that the three segments were specified early in development and that their expansion was again mainly due to limb growth. This idea became known as the Early Specification Model. In contrast, a more recent study in chick [9] concluded that the mixing between zeugopod and autopod was higher than that between stylopod and zeugopod at early stages. This together with analysis of Hoxa13 and Hoxa11 expressions suggested that the two more proximal segments were specified early while the distal segment was specified later during development. However, another study in chick [8] found no strict barriers between all the three segments at early stages. Recent results in mouse [13] also supported a similar view by showing that cells expressing known markers of three segments were capable of altering their expression to match the local environments where they were moved. This supported the idea proposed in [14,15] that identities were progressively specified over time by active regulation along the entire limb despite cell transit between the segments.

Considering some of the controversies mentioned above we decided to use our model in two ways: firstly to give an estimation of the degree of mixing along the PD axis, and secondly to estimate the extent to which limb tissue movement could be responsible for the expansion of the Hoxd13 domain, one of the known distal marker of the autopod.

For the first question we used the model to compute a reverse version of the tissue movement map. This would allow us to start by marking the three PD segments at the oldest timepoint (E12), and then work backwards to determine which regions of the young limb bud could contribute to the 3 segments. Importantly, this is not equivalent to running a clonal experiment backwards in time. As in a traditional heat diffusion problem, individual virtual clones cannot be reverse simulated to discover where they came from. On the contrary, if a clone was reverse simulated from its final spatial distribution back to the young limb bud the corresponding region on the young shape will be proportionally larger than the final clone. This is clearly the opposite of the normal forward simulation, which starts with a region much smaller than the final clone – a single triangle. This distinction is explained in more detail in Text S3. The purpose of this reverse map is therefore instead to find the full distribution of possible progenitor regions for a given final PD zone, e.g. to find the possible distribution of all zeugopod progenitors at E10. Due to the effective diffusion caused by cell mixing, the potential progenitor region for a given segment

will always be proportionally larger than the final segment. As an example, if diffusion was high enough there would be a moment in the early limb bud when any single cell across the whole bud could provide descendants contributing to all 3 PD zones of the late bud. In other words, the progenitor region for any point of the older limb would be the whole young limb.

The positions of the PD segments at E12 were determined by the expression of the Sox9 skeletal marker, see Figure 9B. Based on the degree of cell mixing seen in real clones, our reverse model revealed the existence of regions having high probability to contribute to two or three segments at early stages of development (around stage E10 in Figure 9C) when most of the fate maps discussed above have been performed. In other words, assuming a spatially-uniform cell mixing that matches the observed overlaps of experimental clones, our model clearly suggests that the degree of mixing between the three PD segments does not allow an early specification of the PD identities even as late as E10.

For the second analysis of PD patterning we investigated the possible contribution of tissue movement to the known expansion of the Hoxd13 distal marker. First we mapped into the model a gene expression time course of Hoxd13 that was obtained from in-situ hybridization at 7 different developmental stages, see Figure 10A. This was done by staging each limb with the morphometric staging system presented in [28] and by mapping the domain of expression into the correspondent time point of the model. Secondly, we used the model to expand or shrink each experimental domain of expression into the following or the previous experimental time point, see Figure 10B,C. By computing the difference between the predicted and the experimental domains we were able to disentangle the active regulation of Hoxd13 from the underlying tissue movement. Our model showed that there were periods of growth during which the change in Hoxd13 domain was fairly consistent with the underlying tissue movements. However, two particular periods stood out from this trend during which there was strong active up-regulation of the gene. The first period was from stage mE10:15 to stage mE10:19, when the Hoxd13 domain undergoes a quick expansion from the posterior to the anterior part of the limb, and the second period was from stage mE11:1 to mE11:18, when the gene was up-regulated proximally. Interestingly, these phases seemed to correlate well with (a) the up-regulation of some of the FGFs expressed by the AER that have been described to expand from the posterior to anterior part of the distal ectorderm in an initial phase around E10.5, and (b) a later phase when FGFs expression is up-regulated around stage E11:5. These observations also fitted with the model proposed in [14] where FGF signaling was proposed as a candidate for the regulation of distal markers like Hoxa13.

In conclusion, our model predicts that the degree of mixing observed in mouse is too high to support the Early Specification Model as a realistic description of PD region specification. Moreover we have also shown that the expansion of the Hoxd13 domain, one of the genes proposed as a distal marker of the limb, cannot be explained considering tissue movement only but has to involve active up-regulation in at least two distinct phases of the development.

Discussion

In this study we present a novel computational method which combines a sequence of experimental 2D limb morphologies and clonal data to estimate a comprehensive description of the tissue movement map responsible for limb morphogenesis. We present a mouse clonal analysis of early hind limb development and show how this allows us to estimate a 2D descriptive model of limb outgrowth that fits the experimental data. In practice, our approach is a reverse-engineering method. It is important to note that the spring analogy algorithm is used as a convenient tool for creating a variety of different hypothetical growth maps, but is not employed to represent the mechanical properties of the tissue.

A major advantage of our model over previous fate maps is the resulting comprehensive prediction of tissue movements over time and space. Previously, the behavior of a point of tissue had to be inferred by manual comparison to its closest experimental clone.

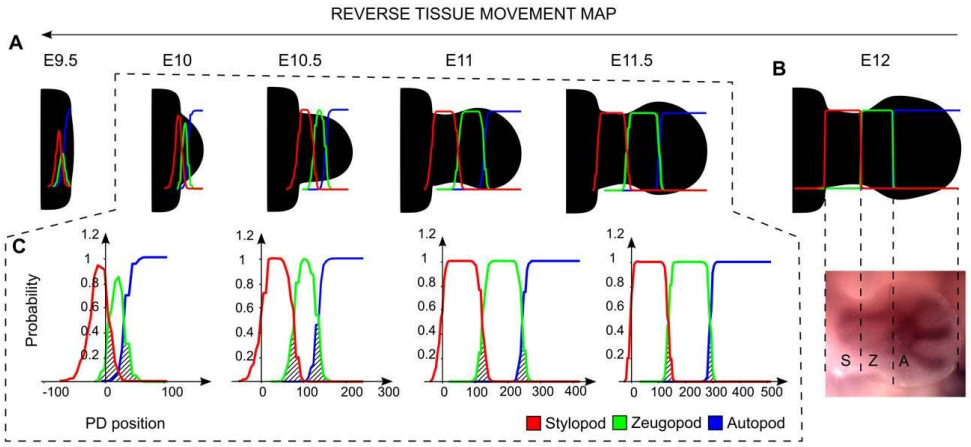

Figure 9. PD segments progenitors. (A) A reverse tissue movement map was calculated in order to identify the progenitor regions for the three PD segments. In the graphs, the stylopod is highlighted in red, the zeugopod in green and the autopod in blue. (B) On the top, the initial position of the three PD segments is specified as shown by an in situ hybridization at stage E12 of the Sox9 skeletal marker, on the bottom. (C) Graphs showing the retrospective probability to belong to the three segments along the proximal distal axis. The regions having a high probability to belong to more than one segment are highlighted with diagonal black lines.
doi:10.1371/journal.pcbi.1001071.g009

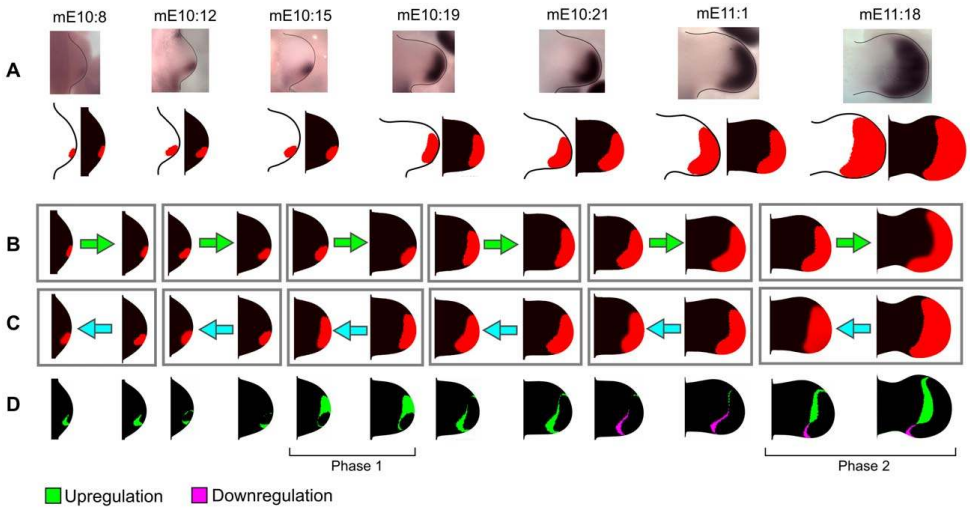

Figure 10. Hoxd13 domain expansion. (A) Top row: a sequence of 7 in-situ hybridizations of Hoxd13 with corresponding stage given by the morphometric staging system [17]. Bottom row: the thresholded gene expressions (limb with white background) are mapped into the triangular meshes of the model (limb with black background). (B) A set of distinct simulations (gray rectangles) showing how the gene expression domains of each time point would change if only passively carried along by tissue movements, i.e. with no active cellular up-regulation. (C) A similar set of simulations, but this time in reverse for each time point. (D) Differences between the experimental patterns and the "growth-only" simulated patterns in the correspondent column. The green regions are predicted to be up-regulated and the magenta regions to be down-regulated. This indicates that the Hoxd13 domain expansion requires active up-regulation on the anterior part around stage mE10.19 (phase 1) and on the proximal part around sage mE11:18 (phase 2).
doi:10.1371/journal.pcbi.1001071.g010

By contrast, in our new map the movement of every piece of tissue is described numerically across the whole period of development. A related advantage is the temporal accuracy – the state of any hypothetical clone can be predicted at any intermediate time point – not only at the beginning or end of a virtual clonal experiment. The spatio-temporal comprehensiveness of the model gives it the power to make more concrete predictions about PD patterning. To the best of our knowledge, this is the first comprehensive 2D model of limb outgrowth derived from experimental data.

Many aspects of our clonal analysis agree with previous results in mouse [11] and with fate maps in chick [9], in particular that clones expand across one or two PD segments but never span across the whole PD axis of the limb. By measuring the degree of overlap between clones at different PD position we found that clones spanning the zeugopod had a higher degree of overlap – in fact not a single zeugopod-restricted clone was found. A quantification of the ratio between AP and PD clone lengths highlighted a range of behaviors, but which could be broadly split into two type: isotropic clones on the distal and proximal part of the limb, and anisotropic clones in the bulk of the tissue showing greater PD length than AP length (Figure 3). Interestingly, in contrast to fate maps in chick [8,9], we found that some distal clones expanded more on the AP axis than the PD axis (e.g. C2 in Figure 5A). This was also reflected in the fitting of the hypothetic growth maps to the clonal data. The map which fitted best (Map6) displayed specific features regarding AP and PD growth: along the PD axis it was one of the maps with a distally-restricted PD elongation. On its own, this information would appear to contradict the knowledge that proliferation rates are highest distally, however Map6 was also the one with a strong distal "fanning-out" movement along the AP axis (central row in Figure 4B). This compensates the low PD expansion resulting in a strong AP-oriented anisotropy, such that predicted proliferation rates are maintained at high levels in this region (see Figure 8). Interestingly, although this feature may be stronger in mouse than chick (resulting in a wider mouse autopod) recent reports have suggested that the AP expansion of the chick and gecko autopod could be driven at least in part by AP-oriented cell diffusions [33]. Taking advantage of our computer model we can calculate the growth tensors directly revealing the AP anisotropy of the distal tissue. However, the tensors also show that tissue movements of the most anterior and the most posterior regions of the sub-ridge mesenchyme are perpendicular to the AER, rather than parallel (Figure 8C). This is an unexpected observation that will require more attention in future studies.

Another interesting observation regards the general construction of our model. By representing the local density of labeled cells as a probability distribution which can diffuse through a smoothly deforming mesh, we shows that biologically-realistic tissue movements can be captured through the combination of anisotropic velocity vector field, with isotropic diffusion. This could suggest that the cellular properties which govern mixing, such as cell-cell adhesion, may not themselves display any cell polarity. In other words, it is theoretically plausible that cells are subject to two types of activity: directional movements (such as oriented cell divisions or convergent extension) which are responsible for the tissue-level shape changes, and non-directional cell mixing. However, in reality, alternative scenarios may also be equally compatible with our model. For example, it is likely that oriented movements naturally lead to the intercalation and therefore to the mixing of cells, such that directional movement and cell mixing cannot be conceptually uncoupled.

Finally, we used the model to clarify the relation between mouse limb tissue movement and the existing PD patterning hypothesis. Firstly we showed, by using a reverse version of the model, that there is a considerable degree of mixing between the progenitors of the three PD segments (Figure 9). In contrast to the Early Specification Model, our model predicts that at early stages there are regions where cells have a high probability to contribute to more than one PD segment. Secondly we showed, by mapping a time course of Hoxd13 expression in the model, that the expansion of the Hoxd13 domain cannot be explained only by tissue movement but requires active gene regulation, Figure 10. The model gave specific predictions of the type of spatial and temporal active regulation of Hoxa13 required suggesting, as proposed in [14], that distal markers could be under the control of the FGF signaling coming from the AER. Taken together these two results prove that limb growth modeling is a valuable resource to extract maximum information from clonal data and to make specific predictions about the spatio-temporal dynamic of limb morphogenesis.

To conclude, the software that we developed will allow us to easily integrate, inside a realistic 2D model of limb growth, numerical simulations of gene regulatory networks and morphogen gradients taking a big step forward in the study of limb development by using a systems biology approach.

Materials and Methods

Ethics statement

All animals were handled in strict accordance with good animal practice as defined by the relevant national and/or local animal welfare bodies, and all animal work was approved by the appropriate committee.

Clonal data

The clonal data was produced using the tamoxifen inducible Cre-line presented in [11]. Lineage tracing at clonal resolution was obtained by injecting low dose of tamoxifen (0.10mg) to reduce the probability of polyclonal origin as described in [11]. Female pregnant females were injected at approximately 8 days pf. and embryos were extracted at 12 pf. LacZ clone staining was performed as described in [34] and embryos were post-fixed in 4% para-formaldehyde (PFA) and stored in 80% glycerol, 4% PFA.

Limb morphologies

72 limb morphologies were extracted from an extended version of the standard morphological trajectory presented in [28]. Each limb morphology was represented by an array of curvature values that were averaged from more than 600 outlines of real limb buds at different stages. We geometrically reconstructed 72 limb shapes from the standard morphological trajectory and added an artificial body of $150 \times 610 \mu m$ to each shape, see Figure S1. We thus spatially discretized each of the limb bud shapes using the unstructured triangular mesh generator presented in [35]. The meshes used to build the 9 tissue movement maps in Figure 4 were obtained with an element length of $8 \mu m$ and the finer version of the meshes in Figure S2 with an element length of $6 \mu m$.

Gene expression data

The Hoxd13 gene expression time course in Figure 10 and the Sox9 expression in Figure 3 were made using C57Bl/6J mouse embryos, fixed in 4%PFA and dehydrated into MetOH. Whole Mount In situ hybridizations were stained using NBT/BCIP and performed using a Hoxd13 antisense probe, kindly provided by Denis Duboule, and a Sox9 antisense probe.

Virtual tissue movment maps

Software to generate the virtual tissue movement maps was written in Java and used the free visualization library vtk [36] to implement the graphical user interface that allowed the user to specify the *boundary control splines*. Virtual tissue movement maps were stored on a re-usable data structure called *MorphoMovie* that was defined by a series of velocity vector fields and a series of triangle interpolation maps, one for each triangular mesh in the sequence. We developed a generic partial differential equation solver that was able to simulate virtual clones on a given *MorphoMovie*. The solver used an Euler method for time discretization and a Finite Volume Method [37,38] on unstructured triangular meshes for the space discretization.

Supporting Information

Figure S1 Standard morphological trajectory. The 72 experimental limb bud morphologies describing mouse hind-limb development from stage E9 to stage E12.
Found at: doi:10.1371/journal.pcbi.1001071.s001 (0.33 MB PDF)

Figure S2 Analysis of the clonal data (PD and AP length measurement). The clonal data that was generated using the tamoxifen inducible CRE transgenic mouse line. Clones are divided in two groups: isotropically expanding clones and an-isotropically expanding clones. The PD and AP clone lengths relative to the maximum PD and AP length of the limb are measured. Colored triangles represent the AP and PD clone expansion.
Found at: doi:10.1371/journal.pcbi.1001071.s002 (1.17 MB PDF)

Figure S3 Proliferation patterns of the maps shown in Figure 4. The proliferation patterns of the 9 virtual tissue movement maps in Figure 4. Triangle expansion rate are converted to cell cycle time and are visualized by using a heat map, red corresponds to low cell cycle times (11h) and blue to high cell cycle times (43h).
Found at: doi:10.1371/journal.pcbi.1001071.s003 (0.40 MB PDF)

Figure S4 Experimental clone registration. The collection of 13 experimental clones that were mapped into the last triangular mesh of the sequence (stage E12).
Found at: doi:10.1371/journal.pcbi.1001071.s004 (0.66 MB PDF)

Figure S5 Clone scores of the tissue movement maps in Figure 4. For each of the 9 virtual tissue movement maps, the collection of virtual clones that best matched the 13 experimental clones. Virtual clones are shown with colored contour lines and experimental clones are shown in white color. The text in white color is the virtual clone score. Finally, a bar diagram summarizing the clone scores.
Found at: doi:10.1371/journal.pcbi.1001071.s005 (1.68 MB PDF)

Text S1 Description of the tissue movement maps in Figure 4. A description of the spline curves and stiffness distributions used to generate the 9 virtual tissue movement maps in Figure 4.
Found at: doi:10.1371/journal.pcbi.1001071.s006 (0.04 MB PDF)

Text S2 Simulation with a refined triangular mesh. The 13 virtual clone positions in Map6 that best matched the experimental data were used to simulate virtual clones on a version of Map6 with a refined mesh.
Found at: doi:10.1371/journal.pcbi.1001071.s007 (0.46 MB PDF)

Text S3 Forward and backward maps. A description of the different information that can be extrapolated from a virtual tissue movement map: fate maps vs progenitor regions. The PD segment progenitor prediction shown in Figure 9 is also recalculated by using Map6 without additional diffusion.
Found at: doi:10.1371/journal.pcbi.1001071.s008 (1.00 MB PDF)

Video S1 Mesh deformation video. Part of the sequence of triangular meshes that was derived from the experimental limb bud morphologies. Each mesh is deformed to match the next mesh in the sequence from which the simulation continues.
Found at: doi:10.1371/journal.pcbi.1001071.s009 (5.46 MB AVI)

Video S2 Virtual fate map video. A video showing a virtual fate map. The spatial probability distribution of the fate is colored with a heat map, red represents a high probability and blue a low probability. A discrete number of triangle-interpolation steps can be appreciated in the video.
Found at: doi:10.1371/journal.pcbi.1001071.s010 (3.21 MB AVI)

Video S3 Video of the simulation in Figure 7B. A video showing a number of clones that match the distribution and shape of the experimental clonal data. Blue clones expand isotropically on the AP and the PD axis, red and green clones expand more on the PD axis.
Found at: doi:10.1371/journal.pcbi.1001071.s011 (2.70 MB AVI)

Acknowledgments

We wish to thank Laura Quintana for the photos of the Hoxd13 in-situs patterns, Jelena Raspopovic for the Sox9 in-situ, Bernd Boehm for help with the limb bud shapes and Jim Swoger for the useful discussion.

Author Contributions

Conceived and designed the experiments: LM CGA MST JS. Performed the experiments: LM CGA. Analyzed the data: LM JS. Contributed reagents/materials/analysis tools: LM. Wrote the paper: LM JS.

References

1. Yang Y (2009) Growth and patterning in the limb: Signaling gradients make the decision. Development 2: pe3.
2. Tickle C (2003) Patterning systems-from one end of the limb to the other. Dev Cell 4: 449–458.
3. Tickle C (2006) Making digit patterns in the vertebrate limb. Nat Rev Mol Cell Biol 7: 45–53.
4. Zeller R, López-Ríos J, Zuniga A (2009) Vertebrate limb bud development: moving towards integrative analysis of organogenesis. Nat Rev Genet 10: 845–858.
5. Bénazet J, Zeller R (2009) Vertebrate limb development: moving from classical morphogen gradients to an integrated 4-dimensional patterning system. Cold Spring Harb Perspect Biol 1: a001339.
6. Towers M, Tickle C (2009) Growing models of vertebrate limb development. Development 136: 179–190.
7. Vargesson N, Clarke JD, Vincent K, Coles C, Wolpert L, et al. (1997) Cell fate in the chick limb bud and relationship to gene expression. Development 124: 1909–1918.
8. Pearse R, Scherz P, Campbell J, Tabin C (2007) A cellular lineage analysis of the chick limb bud. Dev Biol 310: 388–400.
9. Sato K, Koizumi Y, Takahashi M, Kuroiwa A, Tamura K (2007) Specification of cell fate along the proximal-distal axis in the developing chick limb bud. Development 134: 1397–1406.
10. Muneoka K, Wane N, Bryant S (1989) Mammalian limb bud development: In situ fate maps of early hindlimb buds. J Exp Zool 249: 50–54.
11. Arques C, Doohan R, Sharpe J, Torres M (2007) Cell tracing reveals a dorsoventral lineage restriction plane in the mouse limb bud mesenchyme. Development 134: 3713–3722.
12. Dudley A, Ros M, Tabin C (2002) A re-examination of proximodistal patterning during vertebrate limb development. Nature 418: 539–544.
13. Wyngaarden L, Sevan H (2008) Plasticity of proximal-distal cell fate in the mammalian limb bud. Dev Biol 313: 225–233.
14. Mercader N, Leonardo E, Piedra M, Martinez A, Ros A, et al. (2000) Opposing ra and fgf signals control proximodistal vertebrate limb development through regulation of meis genes. Development 127: 3961–3970.
15. Tabin C, Wolpert L (2007) Rethinking the proximodistal axis of the vertebrate limb in the molecular era. Development 21: 1433–1442.
16. Summerbell D, Lewis J, Wolpert L (1973) Positional information in chick limb morphogenesis. Nature 244: 492–496.
17. Bohm B, Lesnicar-Pucko G, Sharpe J (2010) The role of spatially controlled cell proliferation in limb bud morphogenesis. PLoS Biol 8: e1000420.
18. Li S, Muneoka K (1999) Cell migration and chick limb development: Chemotactic action of fgf-4 and the aer. Dev Biol 211: 335–347.
19. Wyngaarden L, Sevan H (2010) Oriented cell motility and division underlie early limb bud morphogenesis. Development 8: e1000420.
20. Boot MJ, Westerberg C, Sanz-Ezquerro J, Cotterell J, Schweitzer R, et al. (2008) In vitro whole-organ imaging: 4d quantification of growing mouse limb buds. Nat Methods 5: 609–612.
21. Colas J, Sharpe J (2009) Live optical projection tomography. Organogenesis 5: 129–134.
22. Rolland-Lagan A, Bangham J, Coen E (2003) Growth dynamics underlying petal shape and asymmetry. Nature 422: 161–163.
23. Rolland-Lagan AG, Coen E, Impey S, Bangham J (2005) A computational method for inferring growth parameters and shape changes during development based on clonal analysis. J Theor Biol 232: 157–177.
24. Morishita Y, Iwasa Y (2008) Growth based morphogenesis of vertebrate limb bud. J Theor Biol 70: 1957–1978.
25. Dillon R, Othmer HG (1999) A mathematical model for outgrowth and spatial patterning of the vertebrate limb bud. J Theor Biol 197: 295–330.
26. Ede D, Law J (1969) Computer simulation of vertebrate limb morphogenesis. Nature 221: 244–248.
27. Gros JJ, abdHu, Vinegoni C, Feruglio P, Weissleder R, Tabin C (2010) Wnt5a/jnk and fgf/mapk pathways regulate the cellular events shaping the vertebrate limb bud. Curr Biol 20: 1993–2002.
28. Bohm B, Rautschka M, Raspopovic J, Quintana L, Jan Z, et al. (In press.) A landmark-free morphometric staging system for the mouse limb bud. Development.
29. FJ B (2000) Considerations on the spring analogy. Int J Numer Meth Fl 32: 647–668.
30. Van Loon R, Anderson PD, Van de Vosse FN, Sherwin SJ (2007) Comparison of various fluid-structure interaction methods for deformable bodies. Comput Struct 85: 833–843.
31. Chaniotis A, Poulikakos D, Koumoutsakos P (2002) Remeshed smoothed particle hydrodynamics for the simulation of viscous and heat conducting flows. J Comput Phys 182: 67–90.
32. Coen E, Rolland-Lagan A, Matthews M, Bangham J, Prusinkiewicz P (2004) The genetics of geometry. Proc Natl Acad Sci U S A 101: 4728–4735.
33. Sato K, Seki R, Noro M, Yokoyama H, Tamura K (2010) Morphogenetic change of the limb bud in the hand plate formation. J Exp Zool B Mol Dev Evol 314B: 539–551.
34. Torres M (1998) The use of embryonic stem cells for the genetic manipulation of the mouse. Curr Top Dev Biol 36: 99–114.
35. Geuzaine C, Remacle J (2009) Gmsh: a three-dimensional finite element mesh generator with built-in pre- and post-processing facilities. Int J Numer Meth Eng 79: 1309–1331.
36. Schroeder W, Martin K, Lorensen B (2006) The Visualization Toolkit An Object-Oriented Approach To 3D Graphics, 4th Edition Kitware, Inc. publishers.
37. LeVeque R (2005) Numerical Methods for Conservation Laws, 2nd ed. Birkhäuser Basel.
38. Eymard R, Gallouët T, Herbin R (2000) The finite volume method. Handbook of Numerical Analysis 7: 713–1020.

A computational clonal analysis of the developing mouse limb bud
Marcon L. et al.

Figure S1: The standard morphological trajectory – from E9 to E12

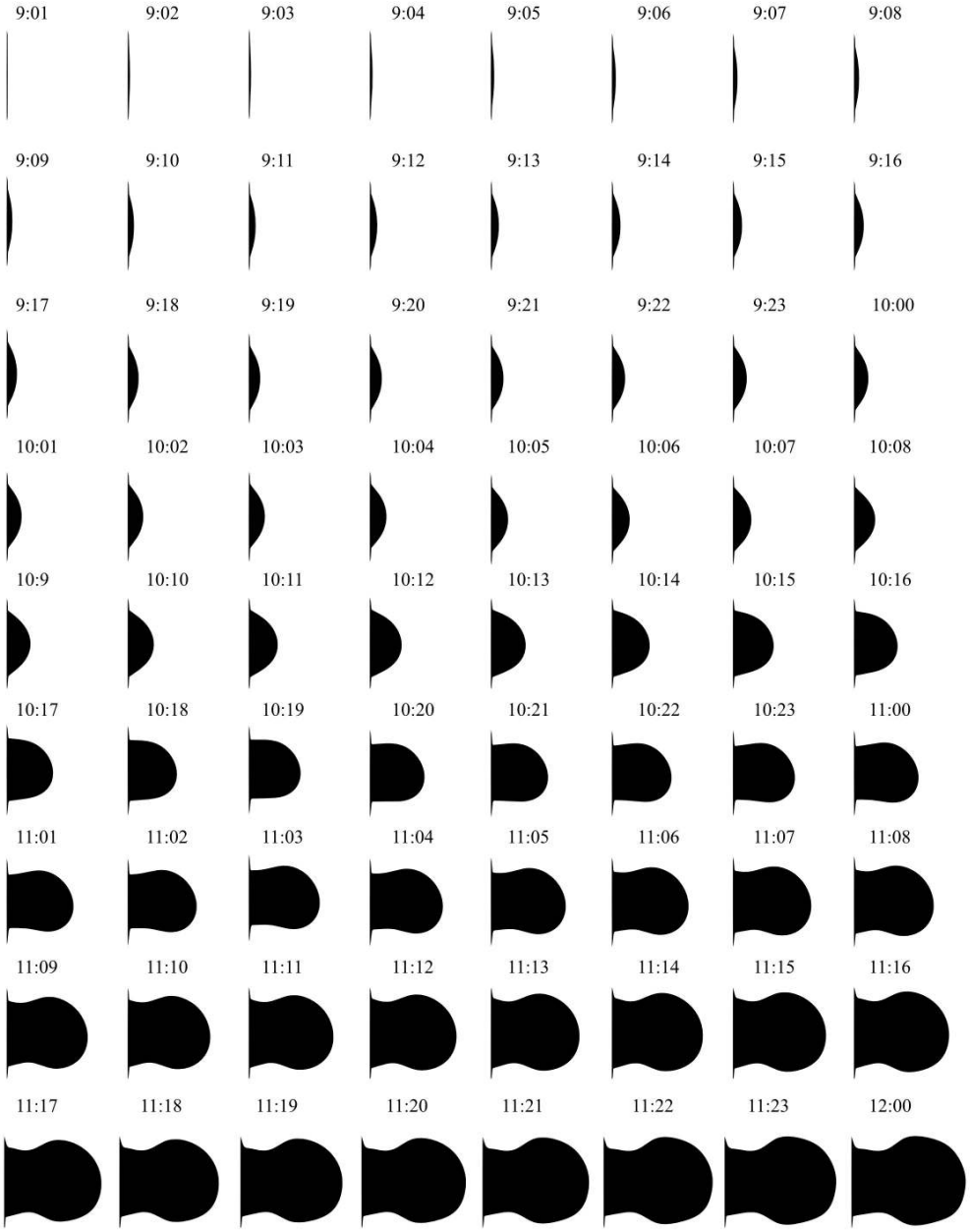

A computational clonal analysis of the developing mouse limb bud
Marcon L. et al.

Figure S2: Analysis of the clonal data (PD and AP length measurement)

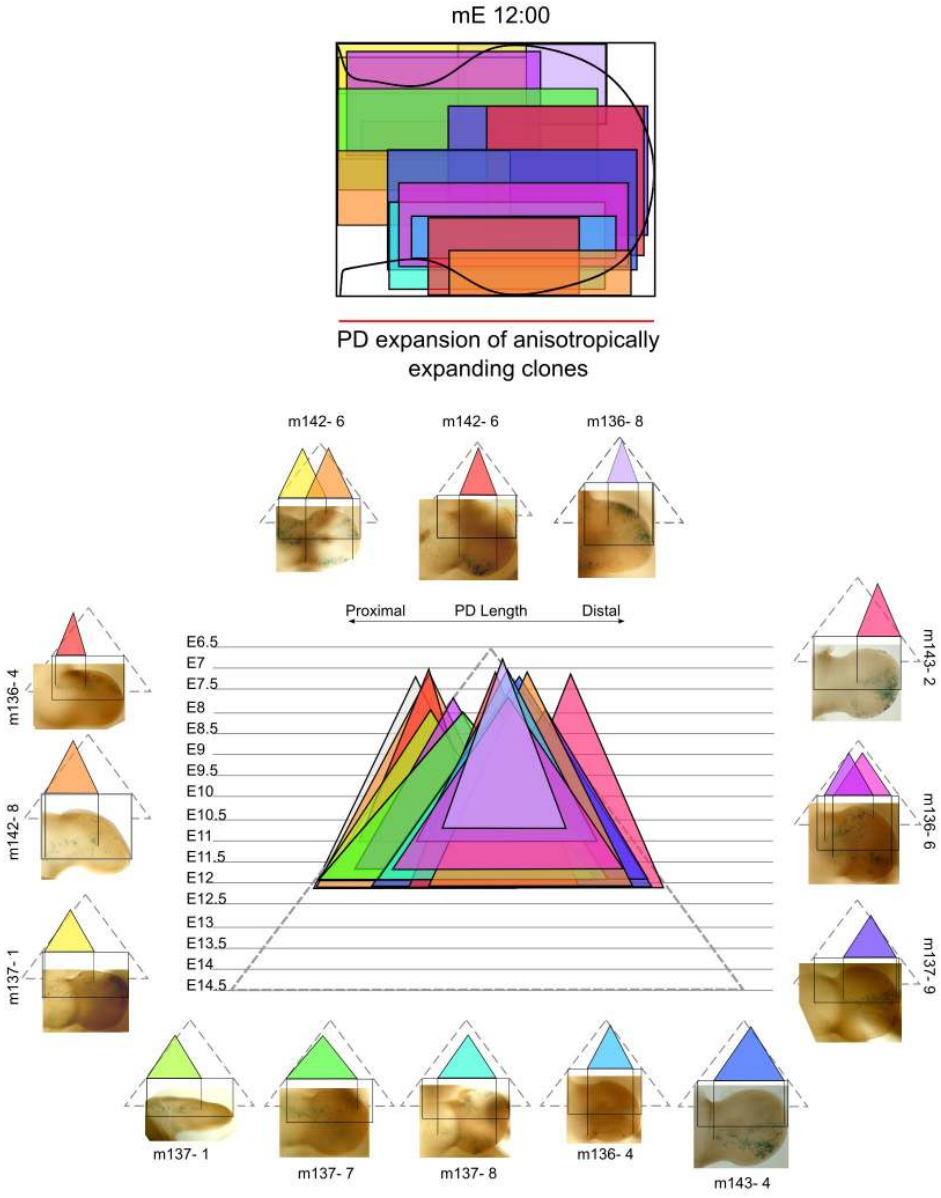

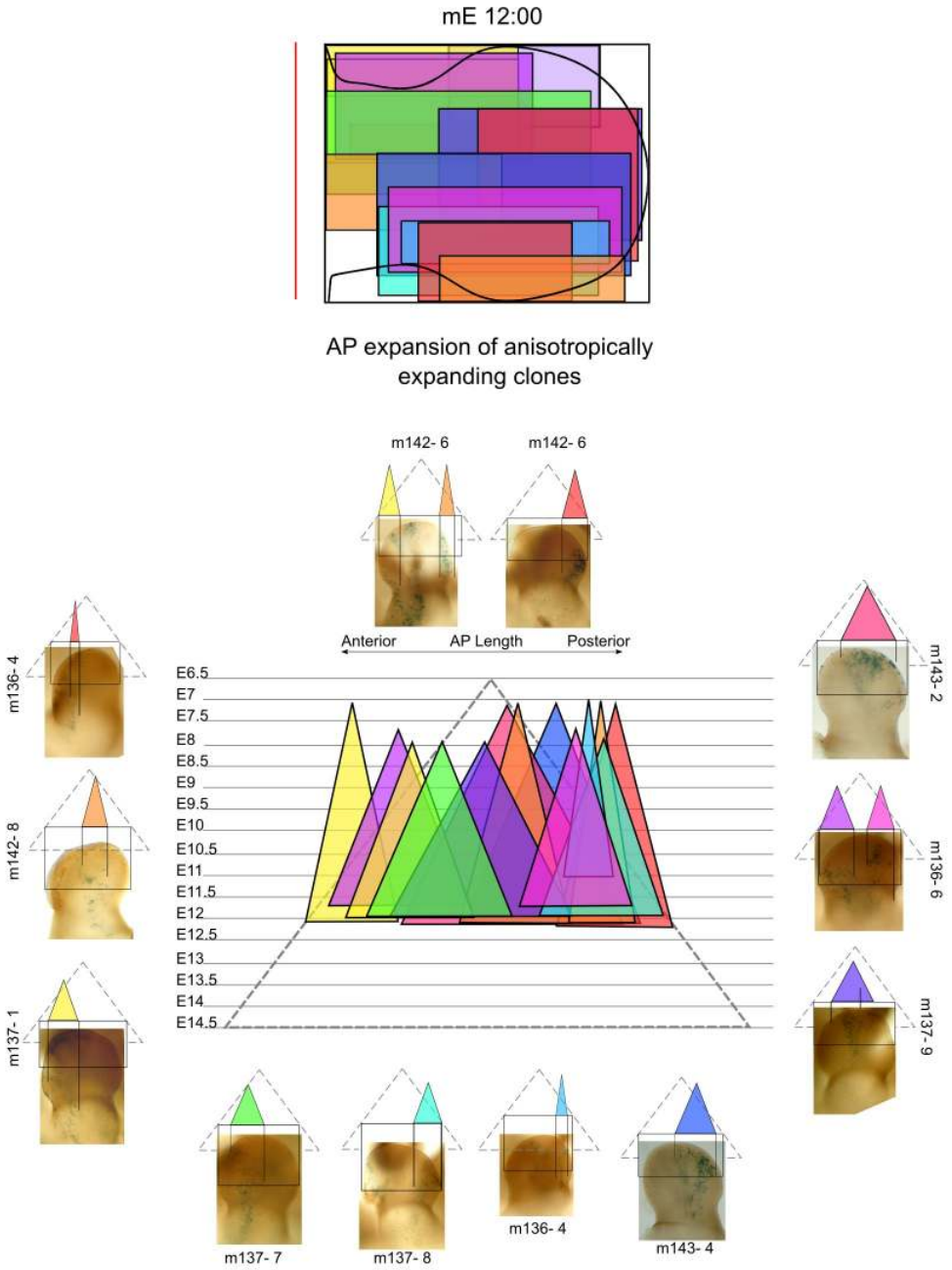
mE 12:00
AP expansion of anisotropically expanding clones
m142- 6
m142- 6
Anterior
AP Length
Posterior
m136- 4
m142- 8
m137- 1
m143- 2
m136- 6
m137- 9
E6.5
E7
E7.5
E8
E8.5
E9
E9.5
E10
E10.5
E11
E11.5
E12
E12.5
E13
E13.5
E14
E14.5
m137- 7
m137- 8
m136- 4
m143- 4

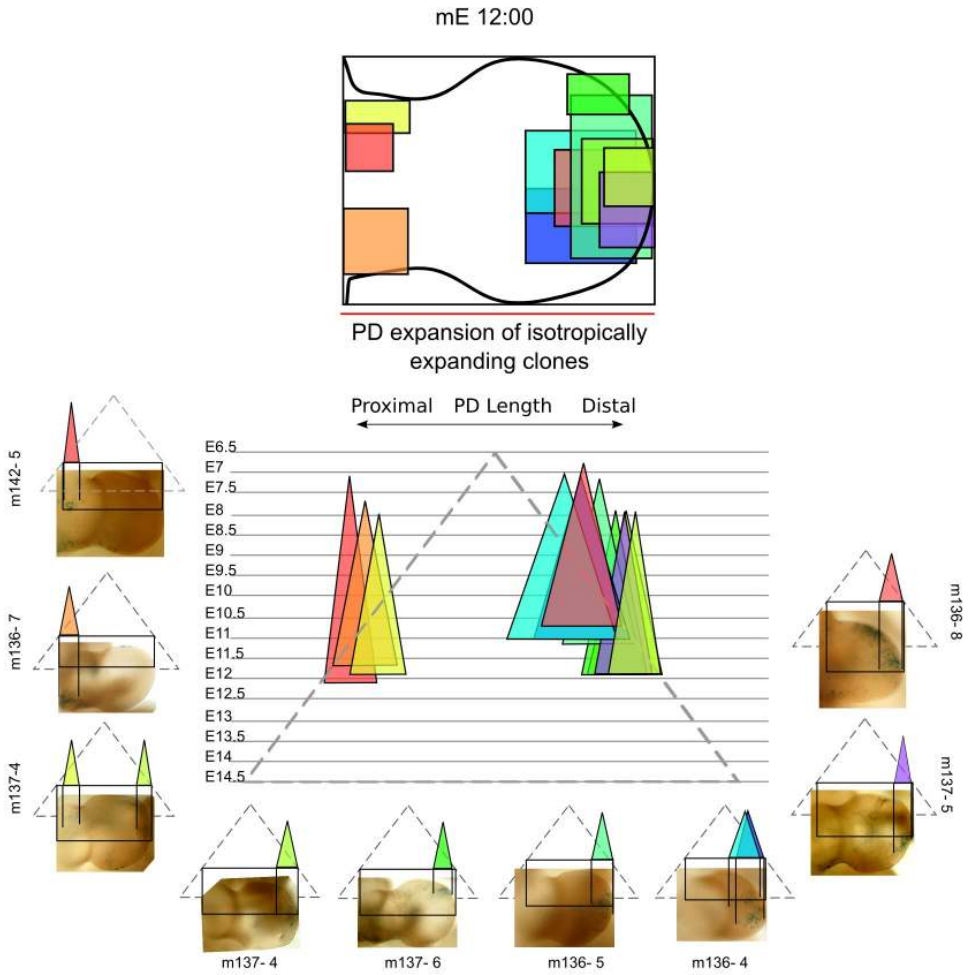
mE 12:00
PD expansion of isotropically expanding clones
Proximal
PD Length
Distal
E6.5
E7
E7.5
E8
E8.5
E9
E9.5
E10
E10.5
E11
E11.5
E12
E12.5
E13
E13.5
E14
E14.5
m142-5
m136-7
m137-4
m136-8
m137-5
m137-4
m137-6
m136-5
m136-4

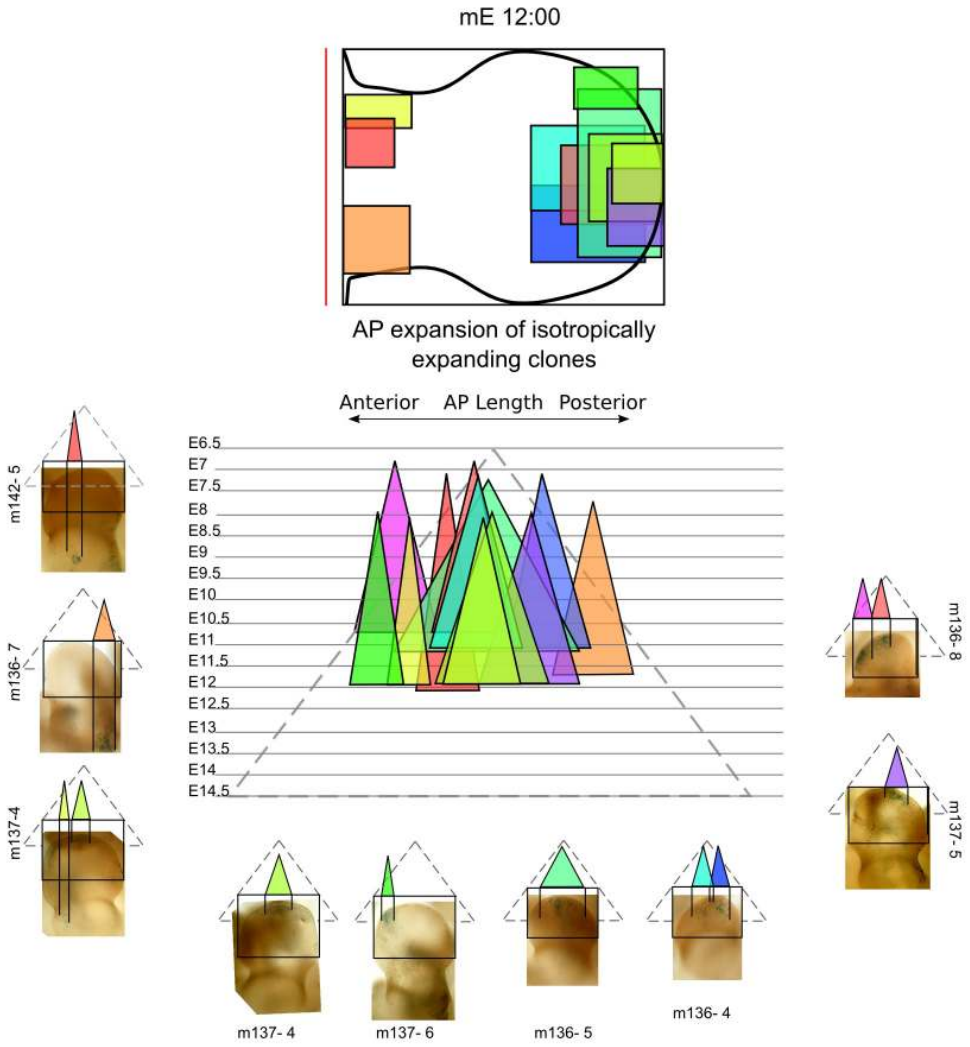
mE 12:00
AP expansion of isotropically expanding clones
Anterior AP Length Posterior
E6.5
E7
E7.5
E8
E8.5
E9
E9.5
E10
E10.5
E11
E11.5
E12
E12.5
E13
E13.5
E14
E14.5
m142- 5
m136- 7
m137-4
m136- 8
m137- 5
m137- 4
m137- 6
m136- 5
m136- 4

A computational clonal analysis of the developing mouse limb bud
Marcon L. et al.

Figure S3: Proliferation patterns of the maps shown in Figure 4

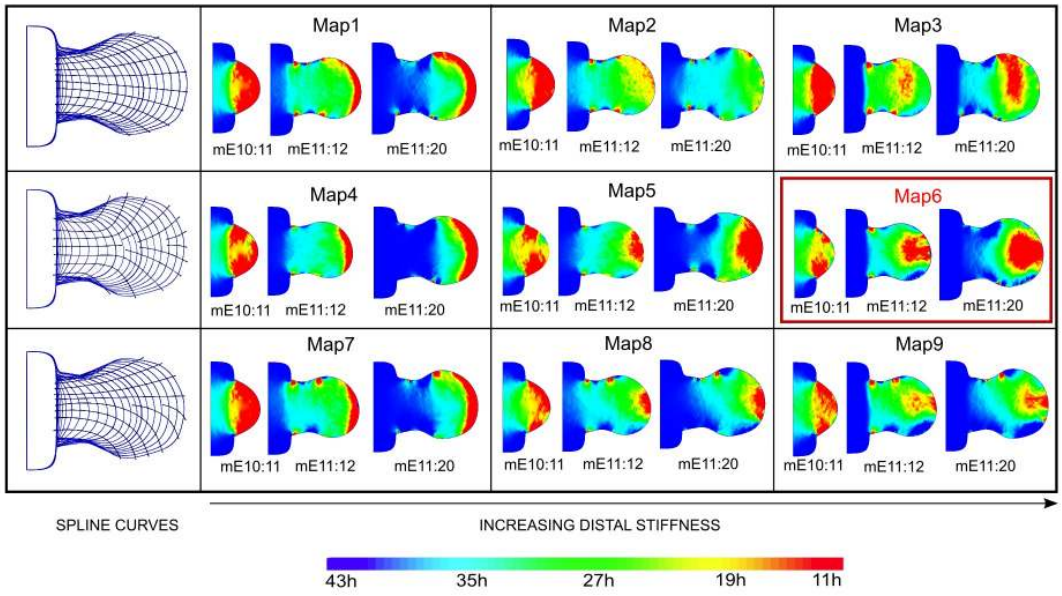

Figure S4: Experimental clone registration, triangular mesh at E12

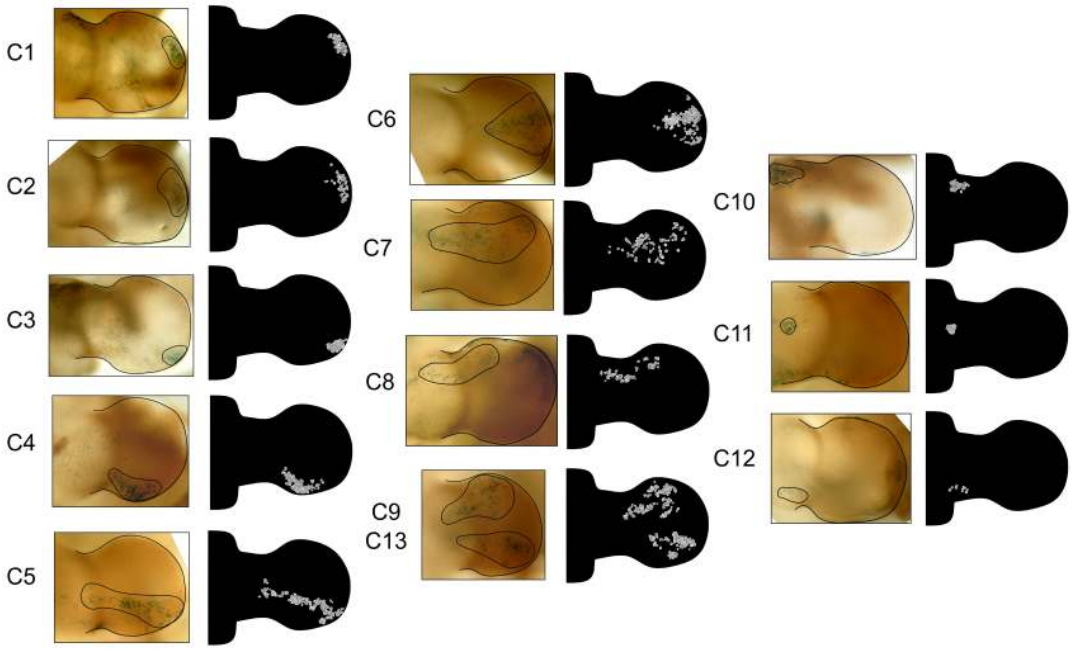

Figure S5: Clone scores of the tissue movement maps in Figure 4

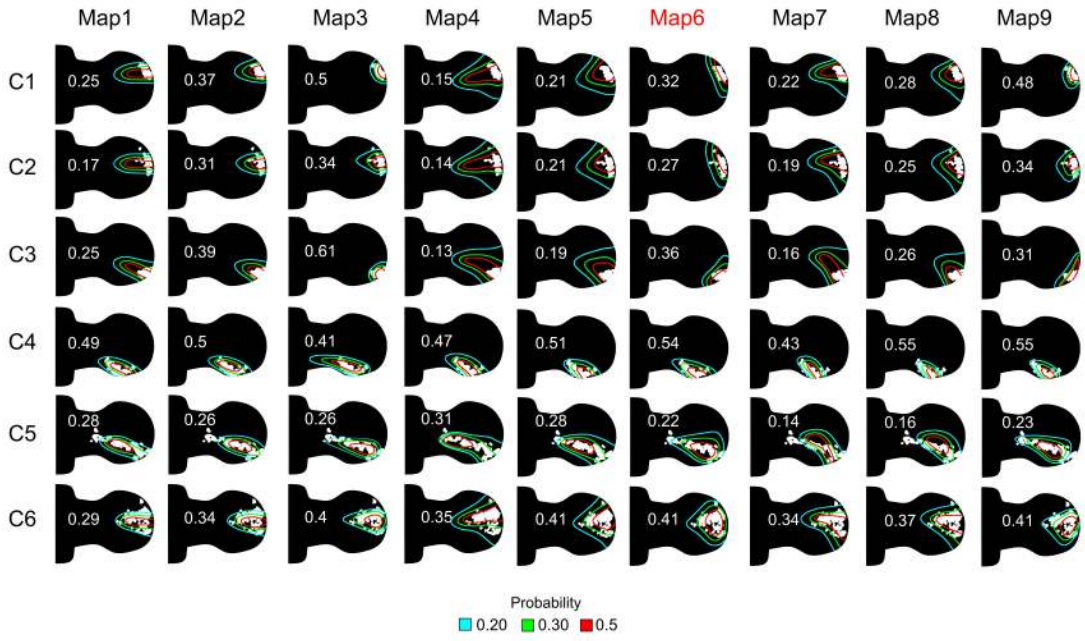

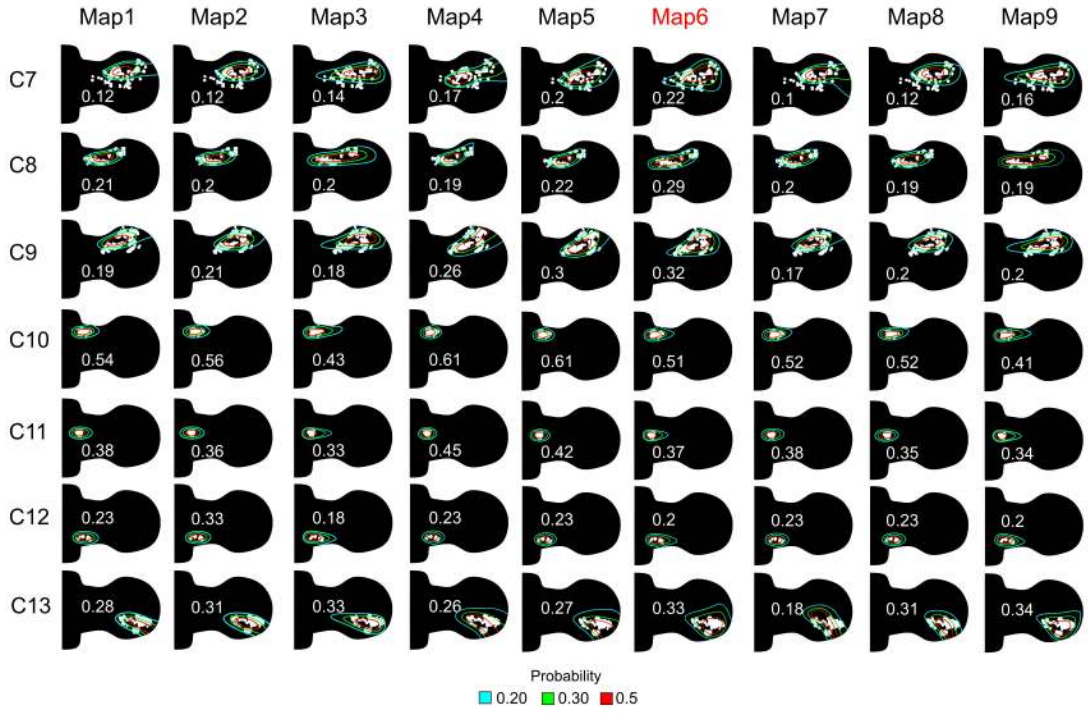
Map1
Map2
Map3
Map4
Map5
Map6
Map7
Map8
Map9
C7
0.12
0.12
0.14
0.17
0.2
0.22
0.1
0.12
0.16
C8
0.21
0.2
0.2
0.19
0.22
0.29
0.2
0.19
0.19
C9
0.19
0.21
0.18
0.26
0.3
0.32
0.17
0.2
0.2
C10
0.54
0.56
0.43
0.61
0.61
0.51
0.52
0.52
0.41
C11
0.38
0.36
0.33
0.45
0.42
0.37
0.38
0.35
0.34
C12
0.23
0.33
0.18
0.23
0.23
0.2
0.23
0.23
0.2
C13
0.28
0.31
0.33
0.26
0.27
0.33
0.18
0.31
0.34
Probability
0.20
0.30
0.5

Summary

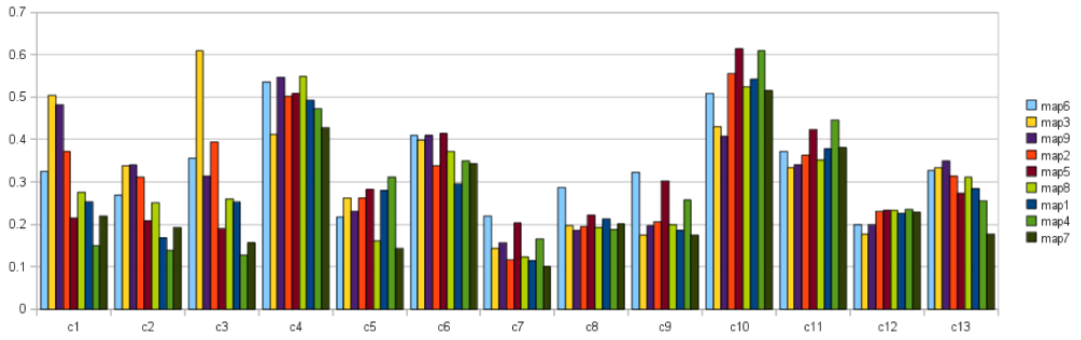
0.7
0.6
0.5
0.4
0.3
0.2
0.1
0
c1
c2
c3
c4
c5
c6
c7
c8
c9
c10
c11
c12
c13
map6
map3
map9
map2
map5
map8
map1
map4
map7

A computational clonal analysis of the developing mouse limb bud
Marcon L. et al.

Text S1: Description of the tissue movement maps in Figure 4

Tissue movement maps were generated by varying the directionality and the relative magnitude of the velocity vectors. A total of 9 maps (shown in Figure 4) were generated by using three different sets of spline curves and three different distributions of stiffness coefficients along the proximal-distal axis.

The three maps in the first row of Figure 4 (Map1, Map2, Map3) were obtained by using a set of spline curves that defined velocity vector fields with direction bias to the distal tip of the limb. The three maps of the second row (Map4, Map5, Map6) were obtained using a set of spline curves that defined velocity vectors that were progressively spreading-out more along the anterior-posterior axis of the limb. Finally, the spline curves that were used to generate the maps of the third row (Map7, Map8, Map9) defined a more asymmetric velocity vector field with posterior vectors bending to the posterior part of the limb and anterior vectors biased distally.

For each triangular mesh in the chronological sequence, edge stiffness coefficients were calculated using the formula:

$$\alpha_{ij} = \frac{1}{l_{ij}} P(e_x^{ij}) \tag{1}$$

where l_{ij} is the length of the edge connecting the vertex i and the vertex j and $P(e_x^{ij})$ is a scaling function P calculated on the x coordinate of the edge midpoint e_x^{ij}.

The three maps in the first column of Figure 4 (Map1,Map4,Map7) were generated using an inverted sigmoid as the scaling function P:

$$P(x) = \frac{1}{(1 + e^{-K_s * (-x + (m_x - d_x))})} \tag{2}$$

where K_s is a constant defining the steepness of the sigmoid, m_x is the maximum x coordinate of the mesh and d_x is a parameter used to translate the sigmoid proximally. This scaling function defined lower stiffness values for edges that were located distally, therefore allowing greater deformations on the distal part of the limb mesh.

The three maps in the second column of Figure 4 (Map2,Map5,Map7) were generated considering no change in stiffness coefficients along the proximal-distal

axis ($P(x) = 1$).

Finally, the three maps in the third column of Figure 4 (Map3,Map6,Map9) were generated using a sigmoid function P that was defined similarly to the scaling function (2) as:

$$P(x) = 1 + \frac{1}{(1 + e^{-K_s * (x - (m_x - d_x))})} \tag{3}$$

This scaling function defined higher stiffness coefficients for edges located distally, therefore allowing greater deformations on the proximal part of the mesh.

We also performed simulations using exponential and linear scaling function with similar monotonic behaviors to equations (2) and (4) and found similar mesh deformations in the first case but almost no change in mesh deformation from the constant fucntion ($P(x) = 1$) in the second case. This suggested that a non-linear scaling of the stiffness was essential to obtain a substantial difference in the mesh deformation.

The simulations that are shown in Figure 4 were performed using $K_s = 0.05$ and $d_x = 30$ and similar values of K_s and d_x showed little effect on the type of final deformation that was obtained. In addition in all the cases we also specified a greater stiffness for the part of the meshes correspondendt to the body. The space unit was μm and the maximum PD length given by the last mesh in the sequence was of $786\mu m$.

A computational clonal analysis of the developing mouse limb bud
Marcon L. et al.

Text S2: Simulation with a refined triangular mesh

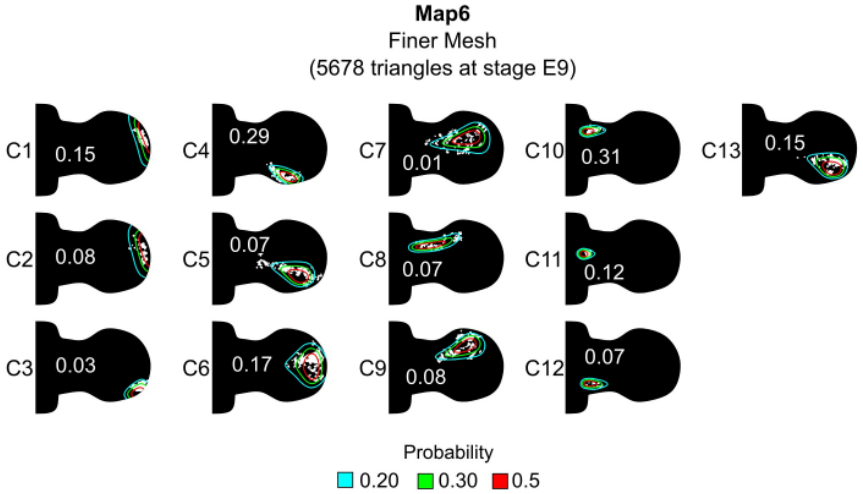

A version of Map6 with a finer mesh was generated. Using the initial positions that were optimized for the version of Map6 obtained with a coarser mesh, we computed and evaluated the 13 virtual clones on the finer mesh. Results were in agreement with the virtual clones obtained with the original mesh.

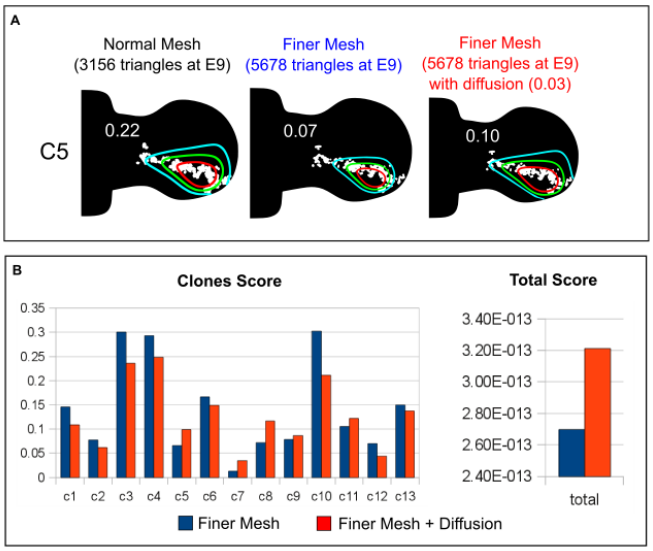

A) Example of clone generated with the Map6 on a finer Mesh and with Map6 on a finer mesh plus an additional diffusion term increasing cell mixing. **B)** Clone scores and Total score for Map6 on the finer mesh with and without diffusion.

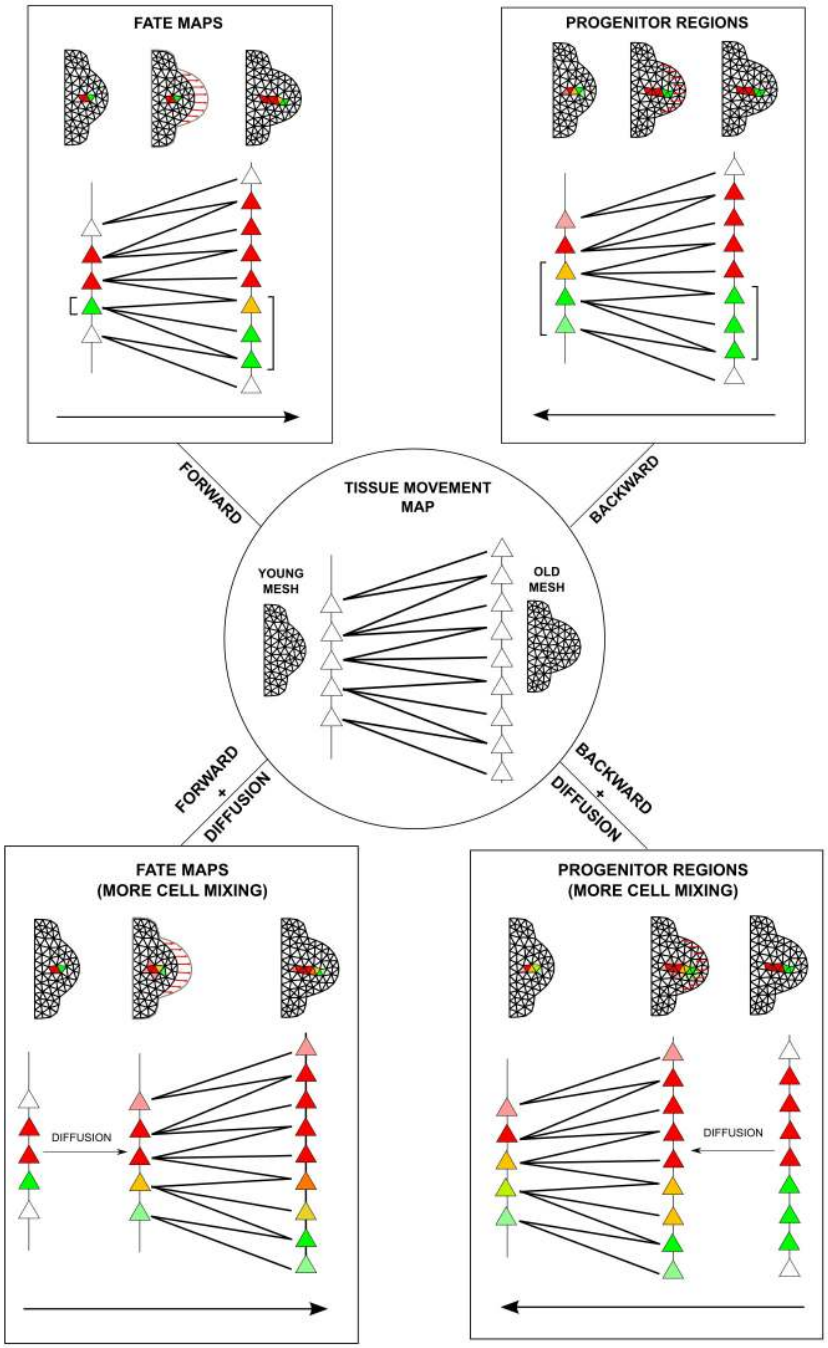
FATE MAPS
PROGENITOR REGIONS
FORWARD
BACKWARD
TISSUE MOVEMENT MAP
YOUNG MESH
OLD MESH
FORWARD + DIFFUSION
BACKWARD + DIFFUSION
FATE MAPS (MORE CELL MIXING)
PROGENITOR REGIONS (MORE CELL MIXING)
DIFFUSION
DIFFUSION

The above figure illustrates the type of information that can be obtained from a virtual tissue movement map. Inside the central circle, a tissue movement map is represented by a simplified mapping of 5 young-mesh triangles to 9 old-mesh triangles, based on their geometric overlap. This triangle map was generated starting from a velocity vector field of a hypothetical growth transform and provides information about the fate of each part of tissue (triangles) in the period of development between the two morphologies.

A tissue movement map of this type can be read in two different ways:

By reading it forward (*upper left-hand panel*) virtual fate maps can be performed by marking young-mesh triangles with a virtual dye and then observing the dye redistribution into the old-mesh triangles. In other words we use the map to explore the question: where can tissue in a triangle of the young mesh end up in the old mesh? In the specific example 2 triangles have been mapped with a red dye and 1 with a green dye. The map predicts that the red region will expand to occupy 5 triangles of the old mesh and the green region will grow into 3 triangles on the old mesh, one of which is in common between the two (yellow triangle). In biological terms the yellow triangle will contain cells labeled with green and red dye.

Conversely by reading it backwards (*upper right-hand panel*) progenitor regions can be identified by marking with a virtual dye a tissue region on the old mesh and then using the reversed triangle map to reveal the triangles from which this part of tissue could descend. In other words we are exploring the question: from which young triangles can an old triangle possibly descend? In the specific example, four triangles have been marked in the old mesh with a red dye and three triangles with a green dye. Redistributing the dye by using the reversed triangle map three triangles are predicted as the possible progenitors of the green marked tissue and three triangles as the possible progenitors of the red marked tissue, one of the triangles (in yellow) could be a progenitor of both regions.

These two interpretations are based on same triangle map but address two profoundly distinct questions. It is important to highlight that the reverse map does not provide a way to reverse a fate map, but only provides a way to identify progenitors. The fact that these are two different concepts becomes quite evident with another specific example: In the figure below, if we map the green triangles (old mesh) obtained by a fate map (on the left) into the old mesh of the backward map (on the right), we will find that the possible progenitor region identified is much broader than the original labeled region from which the fate map originated – 3 green triangles instead of 1.

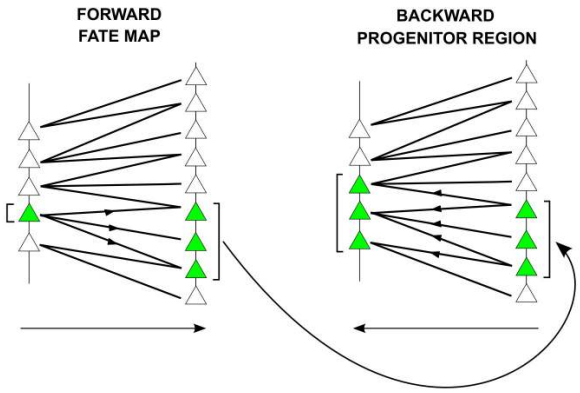

In addition the tissue movement map can also be read forward and backward considering additional levels of diffusion / cell mixing:

By reading it forward with additional diffusion (*lower left-hand panel*) fate maps can be computed as explained above but considering a higher degree of mixing between the cells. In the specific example (which represents only one of the 72 steps of mesh interpolation) the diffusion allows the dye values to spread into neighbouring triangles, during the 1 hour period when the younger mesh is being stretched, before the interpolation is performed. By diffusing the dyes before the interpolation a greater mix between fates is obtained. Similarly the same procedure can be performed in reverse (*lower right-hand panel)*.

As an extra control for the conclusions made in Figure 9, we have also re-done the reverse simulation without diffusion – to shown that these results do not depend on the extra degree of diffusion considered previously. Below we show the results of this "triangle-mapping-only" version of the reverse map (bottom row), in comparison to the previous version from Figure 9 (top row). Although the sizes of progenitor overlap regions are slightly smaller, they are still clearly evident, supporting our general conclusion that early specification of all PD zones is not an accurate description of limb bud development.

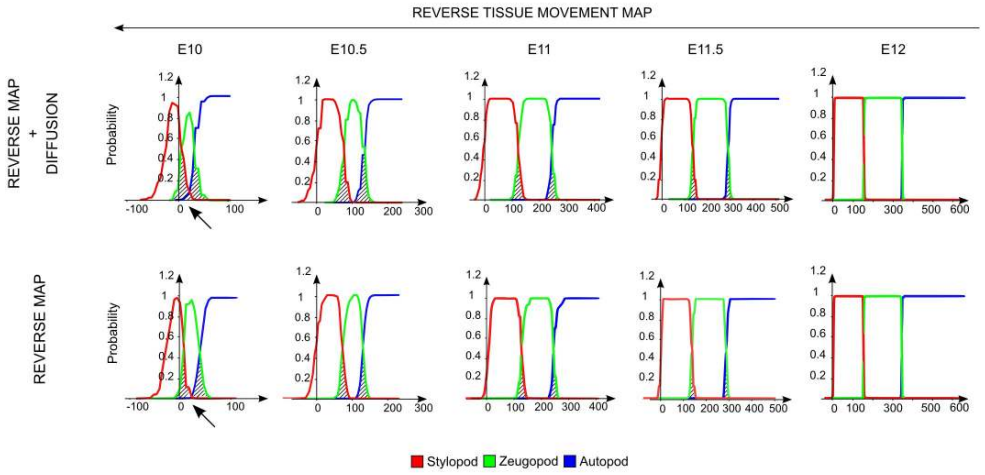

A considerable degree of mixing is observed also in the reverse map without diffusion. The black arrows highlight the major differences between the two reverse maps at E10.

3.3 A Turing model based on Bmps and Wnts explains Sox9 digit patterning

In section 3.1 we provided the first strong evidence that a Turing-type mechanism controls digit patterning. In particular, we showed that the polydactyly of various Distal Hox mutants could be explained as a change in wavelength of the Turing mechanism that specifies the periodic pattern of the digits. Which genes implement the Turing mechanism remains to be elucidated.

In this section, I combine experimental work with modeling to propose that Bmps, Sox9 and Wnts are the main components of this Turing network. The experimental work is done by Jelena Raspopovic another PhD student in our laboratory. My contribution to this work is the development of a new model of digit patterning that extend our previous results with realistic limb growth and a three-reactant Turing network based on molecular data. Similarly to the static model presented in section 3.1, the new model combines a Turing mechanism with Positional Information provided by Fgf-signaling and Hox genes. I show that this model robustly re-produces the experimental patterns of Sox9 inside a growing simulation.

This section is organized in the following way. In the first subsection, I present the evidence that supports Sox9 as being part of the Turing network. In the following subsection, I use experimental data and a mathematical analysis to develop a novel three-reactant Turing network based on Bmps, Sox9 and Wnts. In the third and fourth subsection, I characterize the effect of the different parameters in the model and I introduce an Fgf-signaling gradient and Hoxd13 experimental patterns into the growing model. These two signals are used to modulate the Turing network to obtain digit patterning dynamics that agree with the experimental expression of Sox9.

Finally in the last subsection, simulations are compared with experimental perturbations. A comprehensive discussion of the model is provided in the next chapter.

3.3.1 Sox9 is part of the reaction-diffusion mechanism

In the mouse the Sox9 expression pattern is the earliest asymmetry that reflects the skeletal pattern of the limb, see section 1.3.1. If a self-organizing Turing mechanism is responsible for digit-patterning, then the periodic digital pattern of Sox9 must be a direct reflection of this self-organizing process, see Figure 3.1.

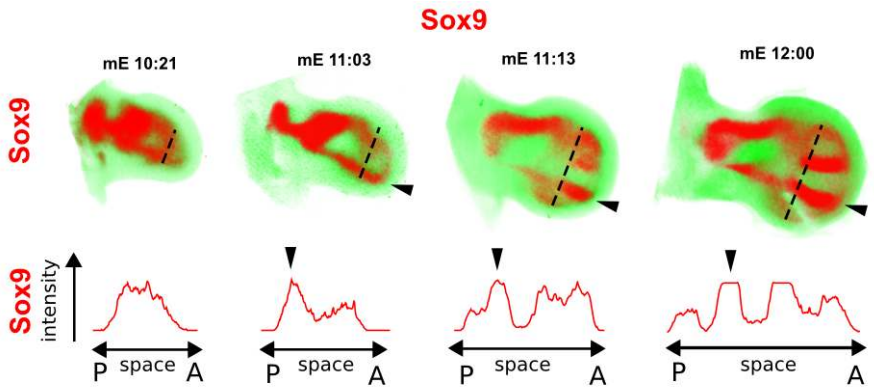

Figure 3.1: The progressive appearance Sox9 is a direct reflection of the self-organizing mechanism that drives digit patterning. Top row: Sox9 in-situ hybridization patterns scanned with OPT, Sox9 in red and the limb auto-fluorescence in green (a z-stack of the DV axis is showed). Bottom row: Sox9 concentration A-P profiles as shown by the dashed line above. The black arrows hilight digit 4 in the posterior part, Sox9 shows a periodic pattern along the AP-axis of the limb.

Two alternative scenarios can be formulates: either Sox9 is a readout of the Turing mechanism, see Figure 3.2A, or Sox9 itself is part of the Turing mechanism, see Figure 3.2B.

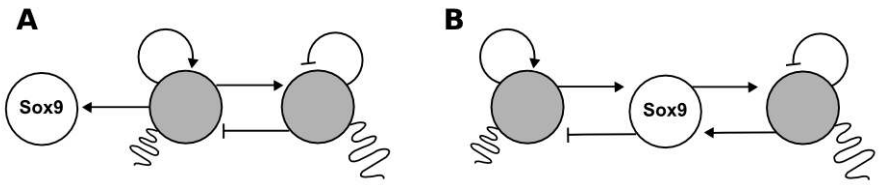

Figure 3.2: Two scenarios for the Sox9 skeletal marker. A) Sox9 is a simple readout of the Turing mechanism (represented by the gray nodes). B) Sox9 is involved in the main feedbacks of the Turing mechanism.

The complete lack of other skeletal markers (or morphological changes that reflect the digits) in the Sox9 mutant supports the second scenario (see section 1.3.2). Indeed, if Sox9 mediates the main reaction-diffusion feedbacks, its disruption will

result in a complete loss of patterning. In addition, the polydactyly observed in Sox9 mis-expression experiments [Akiyama et al., 2007] ulteriorly supports the fact that Sox9 feeds back on the Turing network.

If Sox9 is involved in the main feedback of the Turing mechanism, then its expression must be dynamically regulated as the digit pattern emerges. Evidence supporting this hypothesis comes from the fate mapping experiments presented in [Akiyama et al., 2005] where it was showed that the population of cells that express Sox9 is much broader that the Sox9-expressing population in later developmental stages. In other words, this result highlighted that over time Sox9 was dynamically down-regulated in the interdigital region. A similar observation can be made by comparing a virtual fate map of Sox9 with an experimental expression pattern (as it was done for Hoxd13 in the article presented in section 3.2), see Figure 3.3.

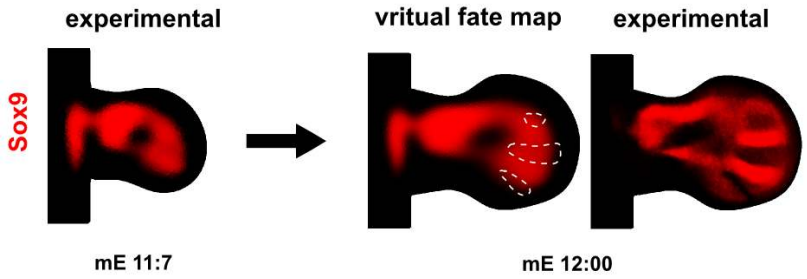

Figure 3.3: On the left, an experimental Sox9 pattern at mE11:7 is mapped into the growing model. On the right, a virtual fate map of Sox9 is computed at mE12 and compared with an experimental Sox9 pattern. In the region outlined by the white dashed line, Sox9 has to be down-regulated.

This degree of plasticity is in agreement with the dynamic regulation that is required to achieve self-organization in a Turing mechanism. To further confirm that Sox9 is dynamically regulated during patterning, we performed a Micromass culture with mesenchymal cells obtained from autopods of the Sox9-EGFP mouse, a mutant that carries an EGFP knock-in under the Sox9 promoter. By monitoring the culture we were able to observe for the first time the progressive appearance of the Sox9 pattern, see Figure 3.4A.

We compared the dynamics of Sox9 with a two-dimensional simulation of a simple Substrate-Depletion model that writes:

$$\frac{\partial a}{\partial t} = \alpha_a + k_1 a + k_2 s - a^3 + D_a \nabla^2 a \tag{3.1}$$

$$\frac{\partial s}{\partial t} = \alpha_s - k_3 a - k_4 s + D_s \nabla^2 a \tag{3.2}$$

where a and s are respectively the concentrations of the activator and the substrate and α_a, α_a their production terms. The negative cubic term $-a^3$ is introduced to have stable dynamics.

When this system is simulated inside a squared domain (edge length=1000) with reaction parameters values are $k_1 = 0.6, k_1 = k_3 = k_4 = 1, \alpha_a = \alpha_s = 0.1$ and diffusion constants $D_a = 250, D_s = 2500$, a labyrinthine pattern gradually emerges, see Figure 3.4B. The patterning dynamics of the reaction-diffusion system highly resembled those of Sox9 in the Micromass culture.

To confirm that the periodic expression of Sox9 was formed by a dynamic molecular patterning system, we performed Micromass cultures using FACS-sorted mesenchymal cells. When the culture was initiated with non-expressing Sox9 cells, the pattern still formed in less than 15 hours. Monitoring individual cells revealed that the pattern was established by a genuine spatially-controlled up-regulation of Sox9, see Figure 3.5A, rather than cell sorting. More strikingly, when the culture was initiated with highly-expressing cells, a similar periodic pattern emerged by spatially-controlled Sox9 down-regulation see Figure 3.5B. These experiments support the idea that Sox9 is dynamically regulated by a self-organizing Turing system based on cell-cell communication.

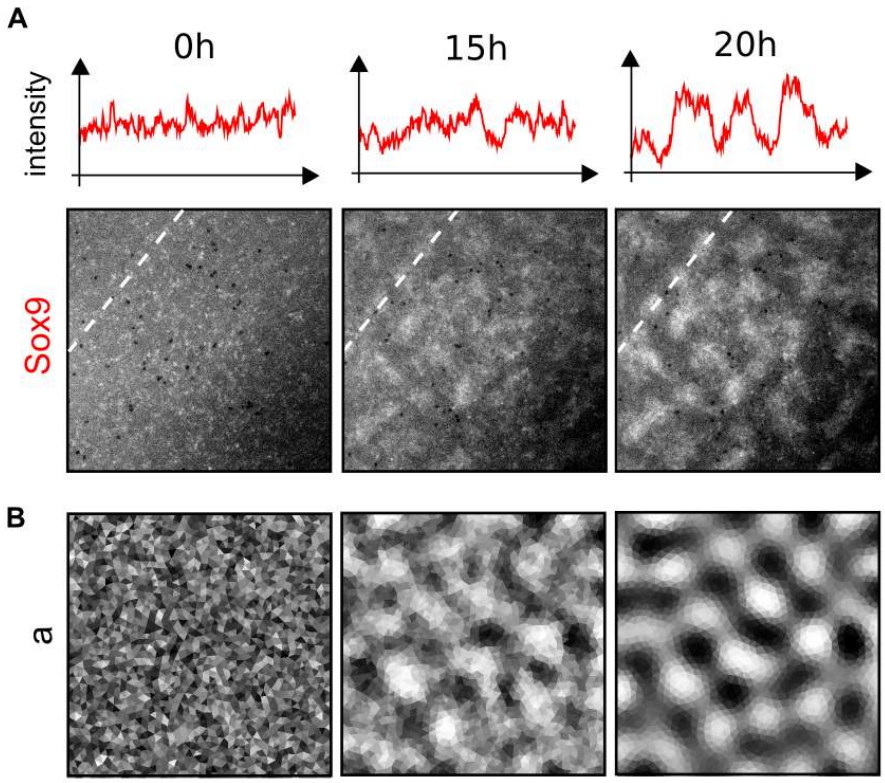

Figure 3.4: A) Bottom row: a time-lapse of a 20h Sox9-EGFP Micromass culture, a periodic chondrogenic pattern marked by Sox9 arises over time. Top row: graphs showing the Sox9-EGFP intensity along the profiles marked by the dashed white lines. B) A time course showing the concentration of the activator (a) in a two-dimensional simulation of a Substrate-Depletion Turing model.

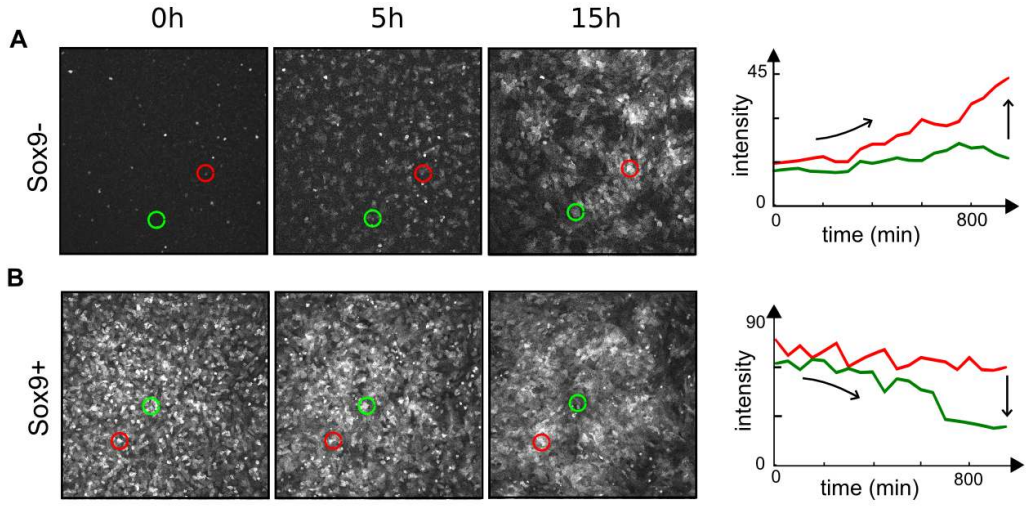

Figure 3.5: Micromass culture initiated with Sox9-EGFP FACS-sorted autopod cell, green and red circles track two cells which develop respectively low and high levels of Sox9. Graphs show Sox9 intensity change over time for both cells in each case. A-B) 15h time-lapse of a Micromass culture initiated with Sox9 negative cells and Sox9 positive cells, a periodic pattern is formed respectively by spatially-controlled up-regulation and down-regulation of Sox9.

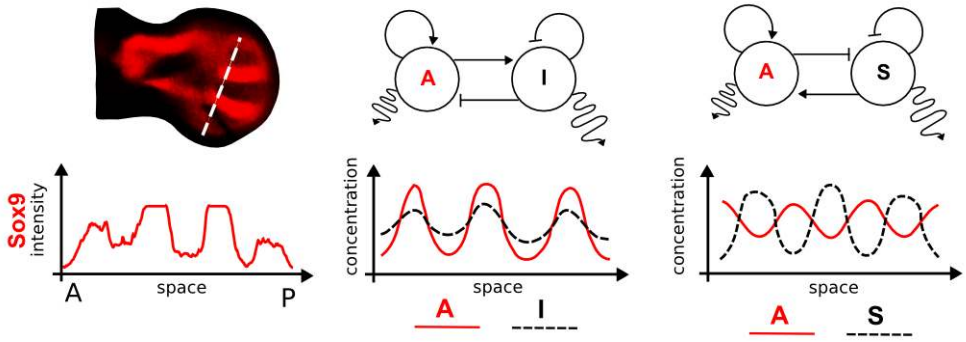

Figure 3.6: Genes that implement the Turing network will have a pattern that is either in-phase or out-of-phase with Sox9. On the left the experimental periodic expression pattern of Sox9. In the middle and on the right respectively: the Activator-Inhibitor (AI) topology and the Substrate-Depletion (SD) topology. The AI topology forms in-phase patterns and the SD topology forms out of phase patterns.

3.3.2 Identification of Turing molecules

In the previous section we provided several evidence that support Sox9 as being part of the Turing network. However, Sox9 is a non-diffusible transcription factor and at least two diffusible molecules are required to implement a minimal Turing model. The general conditions for diffusion-driven instability (see section 1.1.1.3) describe two minimal Turing topologies: the Activator-Inhibitor topology, where in-phase periodic patterns are formed by an auto-catalytic activator that promotes its own inhibitor, and the Substrate-Depletion topology, where out-of-phase patterns are formed by auto-catalytic activator that depletes a substrate. This means that genes that may implement the reaction-diffusion network in conjunction with Sox9 have to be diffusible molecules (E.g signaling molecules) that have either an in-phase of an out-of-phase pattern with Sox9, see Figure 3.6.

A detailed spatio-temporal characterization of the Sox9 pattern, see Figure 3.1, reveals that the periodic digital pattern appears for the first time around stage E11.5. To identify possible Turing-molecules, we dissected and FACS-sorted several limb autopods form E11.5 Sox9-EGFP specimens and performed a comparative microarray analysis to revel differentially expressed genes between Sox9 positive and Sox9 negative cells.

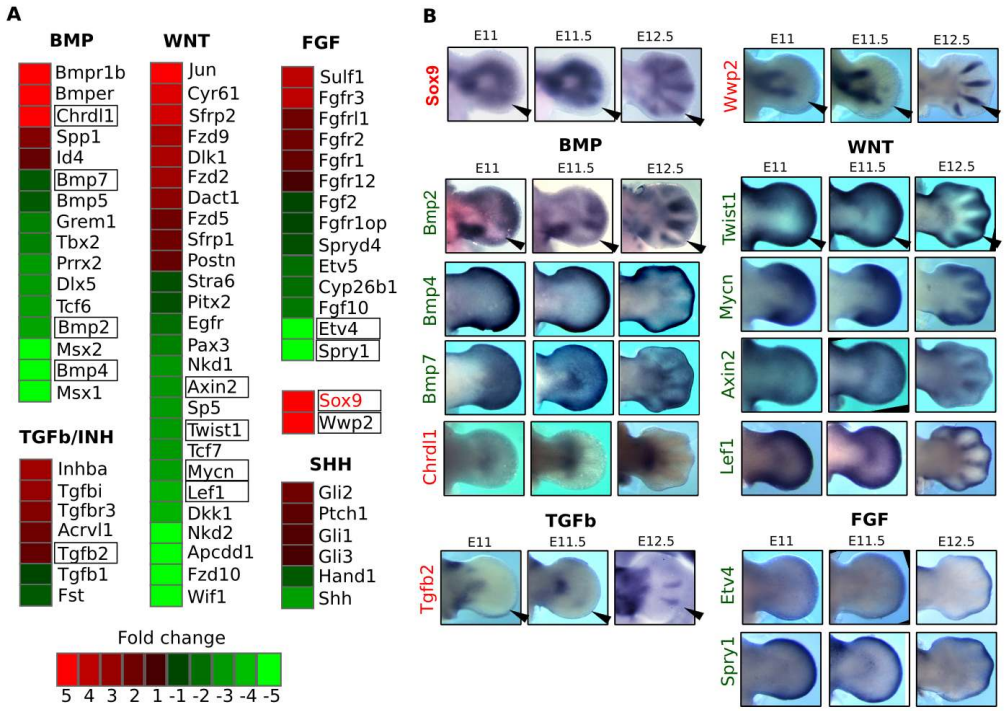

Figure 3.7: A) Microarray analysis that highlights identify differentially expressed genes between Sox9 positive (red) and Sox9 negative cells (green). Color intensity corresponds to fold change. The three major signaling pathways show a considerable number of differentially expressed genes: Bmp, Wnt and Fgf. Sox9 and its direct target Wwp2 are provided as a control. Genes highlighted by a rectangle were analyzed by in situ hybridization. B) Whole mount in situ hybridization time-courses to validate the microarray data. Three stages per gene are shown E11, E11.5 and E12.5. Digit 4 is highlighted with a black arrow.

Based on the number of differentially expressed genes and the fold-change magnitude, the pathways most strongly implicated in digit patterning were the Wnt, Bmp and Fgf pathways, see Figure 3.7A. Not all genes with a strong fold-change in the microarray will have a pattern completely in-phase or out-of-phase with Sox9. For example, Shh is strongly expressed in Sox9-negative cells but this is due to its restriction to the posterior mesenchyme outside the Sox9 domain. A second level of verification is thus required. We therefore analyzed the expression time-course of several genes by whole mount in-situ hybridization (WMISH) to check which patterns are genuinely in-phase or out-of-phase with Sox9, see Figure 3.7B. As a positive control, we checked the Sox9 target Wwp2, which scored highly in the microarray and is indeed expressed in-phase with Sox9, see Figure 3.7B. Regarding previously proposed candidate Turing molecules, neither Tgf-β2, nor any of the Galectins, showed strong differential expression in the microarray. We verified the negative microarray results for Tgf-β2, showing that its digital pattern only develops by E12.5, which is too late to participate in early patterning events. This suggests that Tgf-β2 is primarily involved in late chondrogenesis and differentiation events, despite its ability to induce extra digits when applied ectopically.

3.3.2.1 BMPs as a substrate in an SD system

Bone Morphogenetic Proteins (Bmps), are obvious Turing-molecule candidates as they are known to play an important role in skeletogenesis [Wan and Cao, 2005, Yoon and Lyons, 2004]. Our microarray analysis shows that Bmp2, Bmp4 and Bmp7 are highly expressed in Sox9 negative cells (Fig. 3.7A). Consistently, analysis of their expression patterns reveals that they are highly expressed in the distal mesenchyme surrounding the Sox9 domain. Moreover, Bmp2 has an expression pattern that is strikingly complementary to Sox9 at each stage of digit patterning (Fig. 3.7B). Although this is in agreement with the known role of Bmp-signaling as regulators of interdigital apoptosis [Zuzarte-Luis and Hurle, 2005], evidence also exist that Bmp-signaling promotes Sox9 and chondrogenesis [Bandyopadhyay et al., 2006, Pan et al., 2008, Zehentner et al., 1999]. At first glance, this seems difficult to reconcile with the complementary expression patterns of Bmps and Sox9. However, this non-intuitive behavior can be explained by considering that Sox9 and Bmps form a substrate-depletion model, in which Bmps acts as the substrate and Sox9 act as the activator. This would indeed result in complementary patterns despite the positive influence of Bmps on Sox9. In this model, Bmp activates Sox9 that in turn would represses Bmp expression, in this way final periodic pattern where Sox9 and Bmps are out of phase is formed, see the SD model in Figure 3.6 and Figure 3.8.

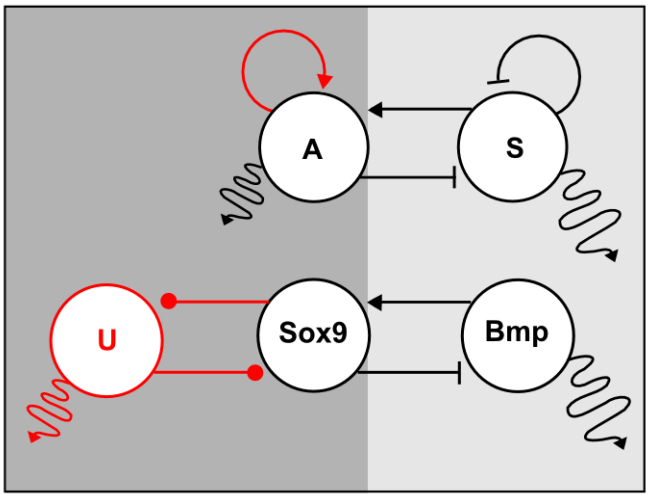

Figure 3.8: On top, a Substrate-Depletion model (SD), A is the activator and S is the substrate. On the bottom, a network where Bmp promotes Sox9 that in turn inhibits Bmp, this motif implements the right part (light gray background) of the SD model. To implement the other part (dark gray) Another diffusible molecule U that interacts with Sox9 is required (red node and arrows).

This hypothesis predicts that Bmp-signaling should be present in the digital tissue that expresses Sox9. To test this idea we assessed a time-course of canonical Bmp-signaling by performing immuno labeling against phosphorylated Smad1/5/8 (pSMAD) on cryosections of Sox9-EGFP limbs. By double-labeling for pSMAD and Sox9 (anti-EGFP), we found that Bmp-signaling activity correlates with the digital Sox9 expression pattern (starting with digit 4, and then including digit 3 and 2), see the Figure 3.9 that display the in-phase patterns of pSMAD and Sox9 along the A-P axis, together with the out-of-phase pattern of Bmp2 expression (mapped from an in-situ time-course). SMAD signaling is also known to be active in the distal phalanx forming regions at later stages, but this is long after the digits are already patterned [Montero et al., 2008, Suzuki et al., 2008].

To further test the positive influence of Bmps on Sox9, we used the Sox9-EGFP mouse to perform a number of manipulative experiments in limb and Micromass cultures. When Bmp2 protein-soaked beads were implanted into the interdigital region at E11.5, we observed a local up-regulation of Sox9 in less than

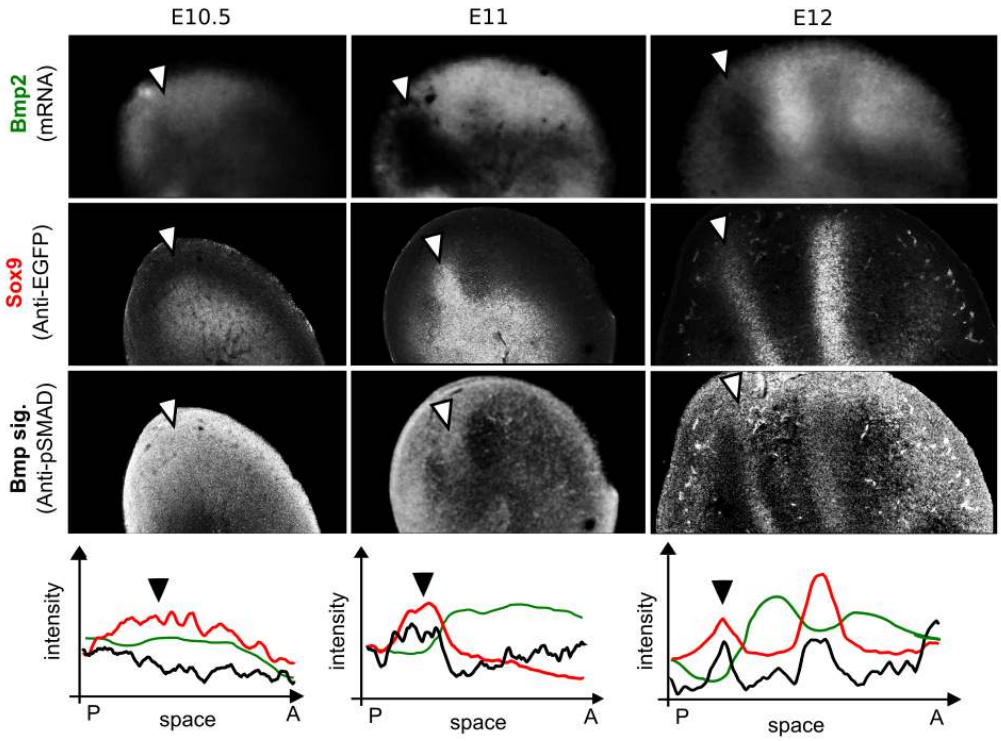

Figure 3.9: The first row shows Bmp2 expression at E10.5, E11 and E11.5. The second two rows show the same cryosections double-labeled for Sox9 (Anti-EGFP) and Bmp-signaling activity (Anti-pSMAD1/5/8). Digit 4 is highlighted with a white arrow, proximal is on the left and posterior is on the bottom. Graphs show AP-profiles of Bmp2 expression and fluorescence intensities. When the digit pattern starts to appear (E11) Bmp-signaling co-localizes with Sox9 while Bmp2 expression is out-of-phase at the level of the digits.

6 hours and similar result are observed when Bmp2 is added to the medium of Micromass cultures, see Figure 3.10A. In contrast when the Bmp-signaling inhibitor LDN-193189 (LDN) was added the medium of limb and Micromass cultures Sox9 was down-regulated, Figure 3.10B. Interestingly, in limb culture the down-regulation of Sox9 is mostly in the digital region Figure 3.10B. This in agreement with the phenotype of the Smad4 conditional mutant [Bénazet et al., 2012], where impairment of canonical Bmp-signaling in the limb mostly affects the autopod region and results in the absence of digits. Analysis of the expression pattern of Sox9 and Bmp2 in this mutant, reveals that while Sox9 expression is down-regulated, Bmp2 expression is up-regulated in comparison with the wild-type, see Figure 3.10C. This agrees with the hypothesis that Sox9 and Bmps from a Substrate-Depletion Turing mechanism where Bmp-signaling promotes Sox9 that in turns represses Bmp expression (topology in Figure 3.10C).

These functional experiments together with the complementarity of Bmp2 and Sox9 expression patterns provide evidence that Bmp2 act as a substrate and Sox9 as an activator in a Substrate-Depletion Turing model. However, a minimum of two diffusible molecules is required to produce a diffusion-driven instability. Since, Sox9 is a non-diffusible transcription factor, a third diffusible component is required. The experimental evidence supports the idea that Sox9 is involved in the main feedbacks of the reaction-diffusion network, therefore this third diffusible component has to interact with Sox9, see Figure 3.8. In the next two subsections, I develop a linear-stability analysis of a three-component reaction-diffusion system. This analysis reveals the possible topologies that can give rise to a diffusion-driven instability and help us to identify the third component.

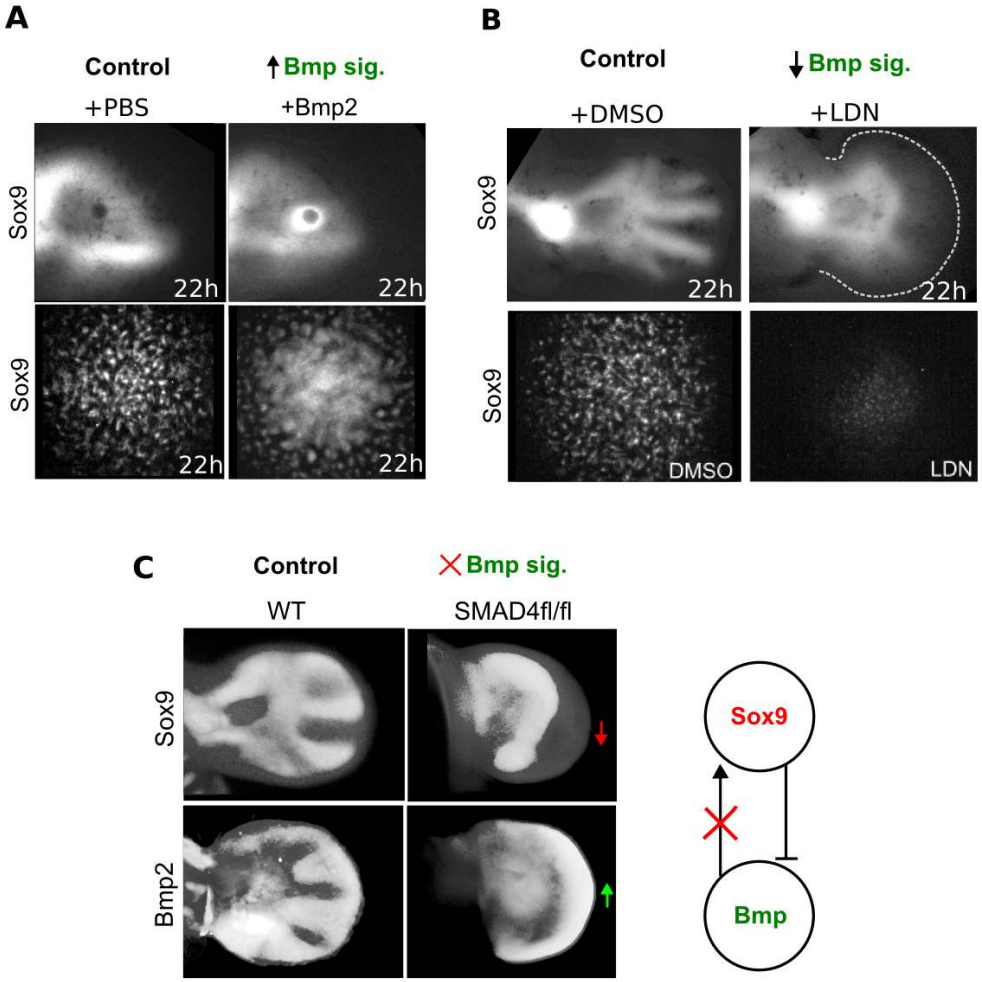

Figure 3.10: A) Top row: bead experiments in Sox9-EGFP limb cultures after 22h, a control PBS-soaked bead (left) and a Bmp2-soaked bead which promotes local Sox9 up-regulation (right). Bottom row: addition of BMP2 in the medium of Micromass culture up-regulates Sox9 in comparison with control. B) Addition of LDN in 22h Sox9-EGFP Micromass and limb cultures show a down-regulation of Sox9 and digit patterning loss. C) OPT scans of Sox9 and Bmp2 expression patterns in WT (left) and in the Prx1-CRE-Smad4fl/fl mutant [Bénazet et al., 2012] (right). In the Smad4fl/fl mutant abrogation of canonical Bmp-signaling causes loss of digit patterning with down-regulation of Sox9 (red arrow) and up-regulation of Bmp2 (green arrow). This behavior is consistent with deletion of Bmp-signaling (red cross) in a Substrate-Depletion network where Bmp activates Sox9 that in turns represses Bmp, network diagram on the right.

3.3.2.2 Linear stability analysis

In this subsection, I apply the linear-stability analysis presented in [White and Gilligan, 1998] to a reaction-diffusion system that represent the interactions between Bmp, Sox9 and an unknown diffusible molecule u. Let consider the following general reaction-diffusion equations for Bmp, Sox9 and u:

$$\begin{aligned}\frac{\partial sox9}{\partial t} &= f(sox9, bmp, u) + D_{sox9}\nabla^2 sox9 \\ \frac{\partial bmp}{\partial t} &= g(sox9, bmp, u) + D_{bmp}\nabla^2 bmp \\ \frac{\partial u}{\partial t} &= h(sox9, bmp, u) + D_u\nabla^2 u\end{aligned} \tag{3.3}$$

we can linearize the system around the steady
$f(sox9^*, bmp^*, u^*) = g(sox9^*, bmp^*, u^*) = h(sox9^*, bmp^*, u^*) = 0$
by setting the one-dimensional case with zero-flux boundary condition to:

$$\begin{aligned}sox9(x,t) &= sox9^* + \varepsilon_{sox9}(x,t) \\ bmp(x,t) &= bmp^* + \varepsilon_{bmp}(x,t) \\ u(x,t) &= u^* + \varepsilon_u(x,t)\end{aligned}$$

where $\varepsilon_{sox9}(x,t), \varepsilon_{bmp}(x,t), \varepsilon_u(x,t)$ define small partial perturbations written as:

$$\begin{aligned}\varepsilon_{sox9}(x,t) &= sox9_0 e^{\sigma t + ikx} \\ \varepsilon_{bmp}(x,t) &= bmp_0 e^{\sigma t + ikx} \\ \varepsilon_u(x,t) &= u_0 e^{\sigma t + ikx}\end{aligned}$$

the linearized system can be rewritten in matrix form (without considering terms that are of order higher than linear) as:

$$\begin{pmatrix} \sigma - f_{sox9} + D_{sox9}k^2 & -f_{bmp} & -f_u \\ -g_{sox9} & \sigma - g_{bmp} + D_{bmp}k^2 & -g_u \\ -h_{sox9} & -h_{bmp} & \sigma - h_u + D_u k^2 \end{pmatrix} \begin{pmatrix} sox9_0 \\ bmp_0 \\ u_0 \end{pmatrix} = 0,$$

where the terms in the form f_{sox9} denote the partial derivatives $\frac{\partial f}{\partial sox9}$ of f, g and h evaluated at steady state and the matrix on the left is the stability matrix A.

This system has solutions if $det(A) = 0$ which writes:

$$\sigma^3 + a_1(k^2)\sigma^2 + a_2(k^2)\sigma + a_3(k^2) = 0, \tag{3.4}$$

where the terms $a_1(k^2), a_2(k^2), a_3(k^2)$ are:

$$\begin{aligned}
a_1(k^2) &= -f_{sox9} - h_u - g_{bmp} + (D_{sox9} + D_{bmp} + D_u)k^2 \\
a_2(k^2) &= f_{sox9}h_u + f_{sox9}g_{bmp} + g_{bmp}h_u - h_{bmp}g_u - f_{bmp}g_{sox9} \\
&\quad - f_u h_{sox9} - k^2(D_u g_{bmp} + D_{bmp}h_u + D_{sox9}h_u \\
&\quad + D_{sox9}g_{bmp} + D_{bmp}f_{sox9} + D_u f_{sox9}) \\
&\quad + k^4(D_{bmp}D_u + D_{bmp}D_{sox9} + D_{sox9}D_u) \\
a_3(k^2) &= -f_{sox9}g_{bmp}h_u + f_{sox9}h_{bmp}g_u + f_{bmp}g_{sox9}h_u - f_{bmp}h_{sox9}g_u \\
&\quad - f_u g_{sox9}h_{bmp} + h_{sox9}g_{bmp}f_u + k^2(D_u f_{bmp}g_{sox9} \\
&\quad - D_{bmp}h_{sox9}f_u - D_{sox9}h_{bmp}g_u + D_{sox9}g_{bmp}h_u + D_{bmp}h_u f_{sox9} \\
&\quad + D_u g_{bmp}f_{sox9}) - k^4(D_{bmp}D_{sox9}h_u + D_{sox9}D_u g_{bmp} \\
&\quad + D_{bmp}D_u f_{sox9}) + k^6 D_{sox9}D_{bmp}D_u,
\end{aligned}$$

Similarly to a two-reactant system, see section 1.1.1.3, a diffusion-driven instability is formed when two conditions are satisfied:

- the system has to be linearly stable in the case of no diffusion
- The system has to be unstable for spatial perturbations

These two conditions correspond respectively to the existence of a negative and a positive real part in the solution σ of (3.4), that write:

$$Re(\sigma(k^2 = 0))) = 0 \tag{3.5}$$
$$Re(\sigma(k^2 > 0))) = 0 \tag{3.6}$$

By using the Routh-Hurwitz criteria [Murray, 1989] we can show that the condition (3.5) is satisfied when:

$$a_1(0) > 0, a_3(0) > 0, a_1(0)a_2(0) - a_3(0) > 0 \tag{3.7}$$

and the condition (3.6) is satisfied when at least one of the Routh-Hurwitz terms becomes negative for some $k^2 > 0$:

$$a_1(k^2) < 0 \vee a_3(k^2) < 0 \vee a_1(k^2)a_2(k^2) - a_3(k^2) < 0 \tag{3.8}$$

The second condition (3.8) cannot be solved analytically but can be simplified if one of the species is not diffusible [White and Gilligan, 1998]. If for example $D_{sox9} = 0$, the complex term $a_3(k^2)$ can be simplified to:

$$a_3(k^2) = -D_{bmp}D_u f_{sox9}k^4 + k^2(D_{bmp}[h_u f_{sox9} - h_{sox9}f_u] \tag{3.9}$$
$$+ D_u[g_{bmp}f_{sox9} - f_{bmp}g_{sox9}]) + a_3(0) \tag{3.10}$$

In this case, sufficient conditions that satisfy (3.8) by making $a_3(k^2) < 0$ can be derived according to the sign of f_{sox9} :

$$\text{if} \quad f_{sox9} > 0, \text{then} \quad a_3(k^2) \to -\infty \quad \text{(no diffusion-driven instability)} \tag{3.11}$$
$$\text{if} \quad f_{sox9} = 0, \text{then} \quad a_3(k^2) < 0 \quad \text{if} \quad D_{bmp}h_{sox9}f_u + D_u f_{bmp}g_{sox9} > 0 \tag{3.12}$$
$$\text{if} \quad f_{sox9} < 0, \text{then} \quad a_3(k^2) < 0 \quad \text{if} \quad F_1 < 0 F_2 > 0 \tag{3.13}$$

where

$$F_1 = D_{bmp}[h_u f_{sox9} - h_{sox9}f_u] + D_u[g_{bmp}f_{sox9} - f_{bmp}g_{sox9}], \tag{3.14}$$

and

$$F_2 = (D_{bmp}[h_u f_{sox9} - h_{sox9}f_u] + D_u[g_{bmp}f_{sox9} - f_{bmp}g_{sox9}] \\ + 4D_{bmp}D_u f_{sox9}a_3(0) > 0, \tag{3.15}$$

To summarize, in a three-component reaction-diffusion system with one non diffusible molecule ($D_{sox9} = 0$) the conditions (3.7)(3.12)(3.13) are necessary and sufficient to form a diffusion-driven instability.

3.3.2.3 Eight core topologies

Now that we have derived the necessary and sufficient conditions for a diffusion-driven instability in a three-component Turing system with one non-diffusible molecule, we can develop a simple linear model with a minimal number of interactions for Sox9,Bmp and u by defining f, g, h in (3.3) in the following way:

$$\begin{aligned} f(sox9, bmp, u) &= k_1 bmp + k_2 u \\ g(sox9, bmp, u) &= \alpha_{bmp} + k_3 sox9 - \mu_{bmp} bmp \\ h(sox9, bmp, u) &= \alpha_u + k_4 sox9 - \mu_u u \end{aligned} \tag{3.16}$$

were α_{bmp}, α_u and μ_{bmp}, μ_u are respectively production and first-order decay terms that provide stable dynamics to the system. The four constants k_1, k_2, k_3, k_4 define the strength of cross-regulation terms. A graphical representation of the systems is showed in Figure 3.11A. For simplicity I have ignored cross-regulation

terms between Bmp and u and I considered the simplest case where $sox9$ does not regulate itself.

This system has homogeneous steady state:

$$(sox9^*, bmp^*, u^*) = (-\frac{k_1\mu_u\alpha_{bmp} + k_2\mu_{bmp}\alpha_u}{k_2k_4\mu_{bmp} + k_1k_3\mu_u}, \\ -\frac{-k_2k_4\alpha_{bmp} + k_2k_3\alpha_u}{k_2k_4\mu_{bmp} + k_1k_3\mu_u}, \\ -\frac{k_1k_4\alpha_{bmp} - k_1k_3\alpha_u}{k_2k_4\mu_{bmp} + k_1k_3\mu_u})$$

Since $f_{sox9} = 0$, necessary and sufficient conditions for diffusion-driven instability can be obtained by combining (3.7) and (3.12), which nicely reduce to eight cases depending on $d = \frac{D_{bmp}}{D_u}$ and on the signs of k_1, k_2, k_3, k_4.

Let us define K as:

$$K = \begin{pmatrix} k_1 & k_2 \\ k_3 & k_4 \end{pmatrix}$$

if $\mu_{bmp} = \mu_u$, according to (3.7) and (3.12) a diffusion-driven instability occurs in any of the eight cases:

$$K = \begin{pmatrix} + & + \\ - & + \end{pmatrix} \quad \text{and} \quad k_1 > -\frac{k_2k_4}{k_3} \quad \text{and} \quad d > -\frac{k_1k_3}{k_2k_4} \tag{3.17}$$

$$K = \begin{pmatrix} + & - \\ - & - \end{pmatrix} \quad \text{and} \quad k_1 > -\frac{k_2k_4}{k_3} \quad \text{and} \quad d > -\frac{k_1k_3}{k_2k_4} \tag{3.18}$$

$$K = \begin{pmatrix} - & + \\ - & - \end{pmatrix} \quad \text{and} \quad k_1 > -\frac{k_2k_4}{k_3} \quad \text{and} \quad d < -\frac{k_1k_3}{k_2k_4} \tag{3.19}$$

$$K = \begin{pmatrix} - & - \\ - & + \end{pmatrix} \quad \text{and} \quad k_1 > -\frac{k_2k_4}{k_3} \quad \text{and} \quad d < -\frac{k_1k_3}{k_2k_4} \tag{3.20}$$

$$K = \begin{pmatrix} - & + \\ + & + \end{pmatrix} \quad \text{and} \quad k_1 < -\frac{k_2k_4}{k_3} \quad \text{and} \quad d > -\frac{k_1k_3}{k_2k_4} \tag{3.21}$$

$$K = \begin{pmatrix} - & - \\ + & - \end{pmatrix} \quad \text{and} \quad k_1 < -\frac{k_2k_4}{k_3} \quad \text{and} \quad d > -\frac{k_1k_3}{k_2k_4} \tag{3.22}$$

$$K = \begin{pmatrix} + & + \\ + & - \end{pmatrix} \quad \text{and} \quad k_1 < -\frac{k_2k_4}{k_3} \quad \text{and} \quad d < -\frac{k_1k_3}{k_2k_4} \tag{3.23}$$

$$K = \begin{pmatrix} + & - \\ + & + \end{pmatrix} \quad \text{and} \quad k_1 < -\frac{k_2k_4}{k_3} \quad \text{and} \quad d < -\frac{k_1k_3}{k_2k_4} \tag{3.24}$$

Conditions from (3.17) to (3.24) correspond to eight topologies that are able to produce all the different in-phase/out-of-phase periodic patterns for $sox9, bmp$ and u, see Figure 3.11B.

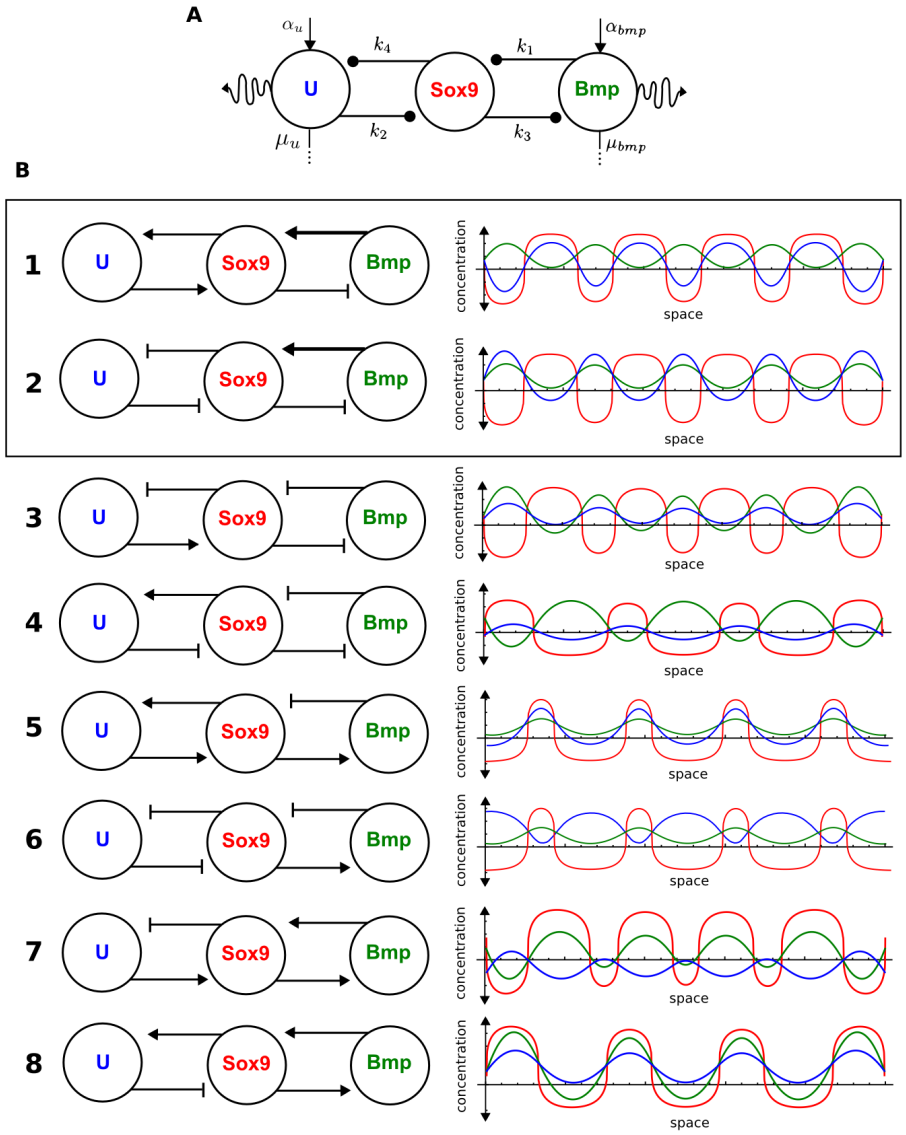

Figure 3.11: A) The linear three-component reaction-diffusion system presented in equations (3.16) B) Left column: the eight topologies capable of diffusion-driven instability in the $sox9, bmp, u$ reaction-diffusion system. Right column: one-dimensional simulations showing the in-phase/out-of-phase periodic patterns of $sox9, bmp$ and u. The first two-topologies that show out of phase patterns for $sox9$ and bmp are highlighted.

3.3.2.4 Wnt and Sox9 mutual inhibition

In section 3.3.2.1 we showed that Bmps promote Sox9 and that the expression patterns of Bmp2 and Sox9 are complementary. The only topologies that fit these observations are topology **1** and topology **2** in Figure 3.11B, that correspond respectively to conditions (3.17) and (3.18). Therefore, our mathematical analysis restricts the search for the third Turing molecule u to a diffusible molecule that participates either in a mutual activation or a mutual inhibition with Sox9. Moreover, it shows that in the first case the unknown molecule would have a pattern in phase with Sox9 and in the second case a pattern out-of-phase with Sox9.

Several studies, see section 1.3.2, show that Wnt-signaling inhibits chondrogenesis and participate in Sox9 regulation. For this reason, it is not surprising that components of the Wnt signaling pathway are highly represented in our microarray analysis, see Figure 3.7A. Unexpectedly, none of the Wnt ligands in the limb appears to be differentially expressed. We formulate the hypothesis that if Wnts are involved in the Turing network, regulation of their activity rather than their expression must be involved in the patterning process. Since the evidence in literature supports the idea that Wnt-signaling inhibits Sox9, in accord with the second topology presented in Figure 3.11B, Wnt-signaling should have a pattern out-of-phase of Sox9. Consistently with this hypothesis, we found that Twist1, Axin2, Mycn and Lef1, which are well known Wnt-signaling target genes, are highly expressed in Sox9-negative cells, see Figure 3.7B.

However, none of these genes showed an obvious complementary pattern at E11.5 as in the case of Bmp2. Since Wnt-signaling is a complex pathway with many receptors and rich dynamics, we chose to analyze Wnt-signaling activity more directly by immuno-labeling of β-catenin, which in the presence of Wnt-signaling accumulates in the cytoplasm and the nucleus to regulate target genes. We found a clear evidence that as soon as the digits are patterned, canonical Wnt-signaling activity was stronger in the interdigital region and formed a pattern that was complementary to Sox9 at all stages of development, see Figure 3.12.

To test the negative influence of Wnt-signaling on Sox9 we performed manipulative experiments in limb and Micromass cultures using the Sox9-EGFP mouse. When Wnt3a protein-soaked beads were implanted in the autopod at E11.5, we observed a local down-regulation of Sox9 within 6 hours, see Figure 3.13A. Similarly, when Wnt3a or BIO (6-bromoindirubin-3'-oxime) (an activator of β-catenin Wnt pathway) were added to Micromass cultures a general reduction of the Sox9

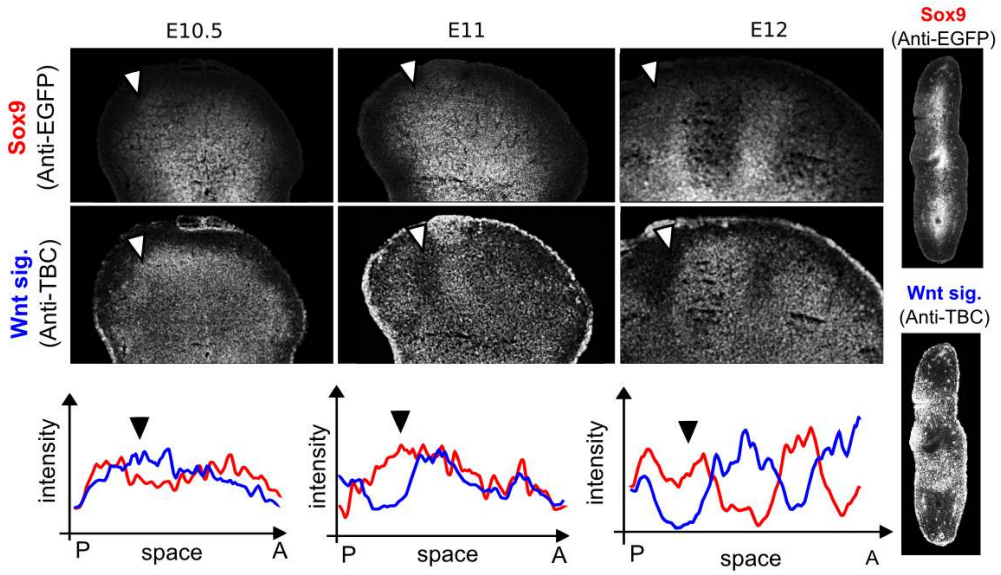

Figure 3.12: Series of cryosections double-labeled for Sox9 (Anti-EGFP) and Wnt-signaling (Anti-TBC) at E10.5, E11 and E11.5. Graphs show that canonical Wnt-signaling is out-of-phase with Sox9 as soon as the digit pattern appears. On the left dorsal view cryosections (left=proximal, bottom=posterior) and on the right distal view crysections (left=dorsal, bottom=posterior).

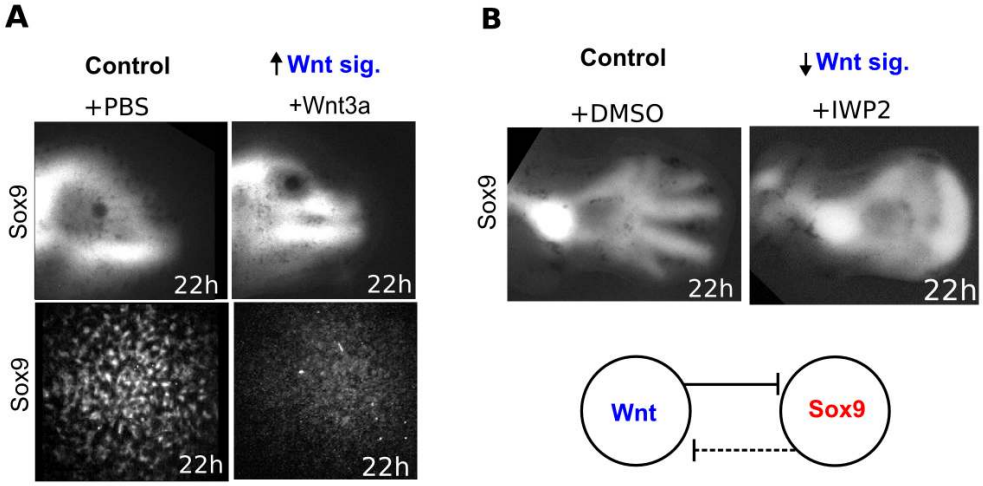

Figure 3.13: A) Top row: bead experiments in Sox9-EGFP limb cultures after 22h, a control PBS-soaked bead (left) and a Wnt3a-soaked bead which promotes local Sox9 down-regulation (right). Bottom row: addition of Wnt3a in the medium of Micromass culture down-regulates Sox9 in comparison with control. B) Top row: addition of IWP2 in Sox9-EGFP limb cultures up-regulates Sox9 in the interdigital region resulting in loss of digit patterning at 22h. Bottom row: this is consistent with a Turing model where a mutual-inhibition between Sox9 and Wnt-signaling is necessary for digit patterning.

levels was observed, see Figure 3.13A. Strikingly, addition of IWP2 in limb culture, which is an inhibitor of Wnt processing and secretion, causes a clear up-regulation of Sox9 in the interdigital region, resulting in the loss of the periodic digit pattern, see Figure 3.13B.

These experiments suggest that normal digit patterning requires interdigital inhibition of Sox9 by Wnt-signaling. Together with previously published genetic manipulations and our mathematical analysis, this suggests that Wnt-signaling participate in the Turing network by implementing a mutual-inhibition (double negative feedback) with Sox9.

3.3.3 The Bmp-Sox9-Wnt Turing model

Descriptive and functional experiments together with our mathematical analysis propose that Bmps, Sox9 and Wnts are the key players of the Turing network re-

sponsible for digit patterning. The network considers promotion of Sox9 by Bmp-signaling, repression of Bmp expression by Sox9 and a mutual inhibition between Wnt-signaling and Sox9, see Figure 3.14A. The reaction-diffusion equations of the model writes:

$$\begin{aligned}\frac{\partial sox9}{\partial t} &= k_1 bmp - k_2 wnt \\ \frac{\partial bmp}{\partial t} &= \alpha_{bmp} - k_3 sox9 - \mu_{bmp} bmp + D_{bmp}\nabla^2 bmp \\ \frac{\partial wnt}{\partial t} &= \alpha_{wnt} - k_4 sox9 - \mu_{wnt} wnt + D_{wnt}\nabla^2 wnt\end{aligned} \tag{3.25}$$

with the parameters showed in Table 3.1.

α_{bmp}	α_{wnt}	μ_{bmp}	μwnt	k_1	k_2	k_3	k_4	D_{bmp}	D_{wnt}
0.1	0.1	0.1	0.1	0.5	0.5	5.5	1	5000	500

Table 3.1: The parameter set used in the limb development simulations

Similarly to the static model presented in section 3.1, we add a negative cubic term ($sox9^3$) to the reaction term of Sox9 to limit the unbounded growth of the system. In one dimension, this model produces a periodic pattern where the peaks of Sox9 are out of phase of both Bmp and Wnt peaks, see Figure 3.14B. In a two-dimensional simulations, complementary labyrinth-like patterns are formed for the three species, see Figure 3.14C. This patterns are reminiscent of the periodic chondrogenic patterns observed in Micromass culture, see for example the striking similarity between a simulation and the complementary periodic patterns of Sox9 and Bmp (Figure 3.14D).

3.3.4 A Morphodynamic Turing model of digit patterning

In the previous sections I derived a Turing model with a topology that fits the qualitative patterns of Bmp-signaling, Wnt-signaling and Sox9, and that is consistent with experimental perturbations. In this section I develop a realistic model of limb development that recapitulates the experimental spatio-temporal dynamics of Sox9. This on one side shows that the Turing network presented in (3.25) is indeed able to drive the specification of the digits and on the other side provides perfect tool to predict the effect of perturbations. The model includes experimental data of the main factors that influence a Turing mechanism: growth (see section 1.2.4) and the geometry of the patterning field [Barrio et al., 1999, Crampin et al., 1999].

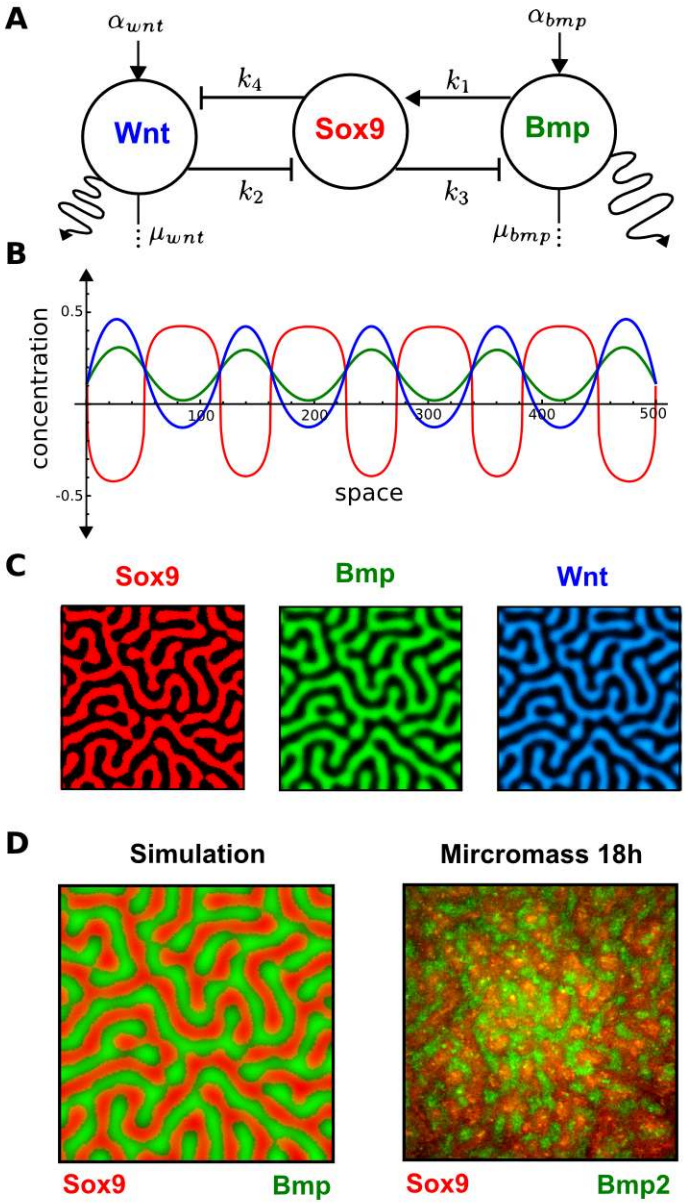

Figure 3.14: The Bmp-Sox9-Wnt reaction-diffusion model, Sox9 is showed in red, Bmp in green and Wnt in blue. A) The graphical representation of the model showed in equations (3.25) B) A one-dimensional simulation of the model, Bmp and Wnt are out of phase of Sox9. C) A two-dimensional simulation labyrinth-like pattern are formed. D) On the left a two-dimensional simulation showing Bmp (green) and (Sox9). On the right a Micromass Culture grown for 20h is stained for Sox9 (immuno-labeling against EGFP) and Bmp2 (in-situ hybridization).

Two different approaches can be used to develop a model based on experimental data: by using a reverse-engineering approach to fit the model to the data, see for example [Reinitz et al., 1998], or by using a step by step approach to build a model that captures the qualitative aspects of the data, see for example [Rolland-Lagan et al., 2003]. The first approach has the advantage of being completely unbiased because constrains the model trough an automatic process of optimization. However, for complex two-dimensional or three-dimensional systems, like vertebrate limb development, the optimization becomes impracticable because it requires prohibitive computational power and a large amount of quantitative data. The second approach consists of progressive model refinements which aim to identify the minimum number of "ingredients" required to reproduce certain qualitative aspects of the experimental data. In the next subsections, I use this approach to build in a step by step manner a model that reproduces the main qualitative features of the Sox9 expression pattern. As a first step I simulate the system (3.25) inside the limb growth model presented in section 3.2. Successively, I restrict the model to the digital region by using experimental expression patterns of Hoxd13 as autopod markers. Similarly to the static model presented in section 3.1, I find that a graded modulation of the wavelength is required to avoid distal bifurcations of the digits. Therefore, I explore the effect of spatially varying parameters in a static model and I introduce a graded modulation on the growing limb simulation by using an Fgf-signaling gradient. To conclude, I develop a model in which both Hoxd13 and Fgf-signaling modulate the Turing mechanism creating a pattern that captures the spatio-temporal dynamics of Sox9 both in the wild type and in perturbation.

All the numerical simulations presented in the next sections have zero-flux boundary conditions, use an adaptive time step for the numerical integration, start from the homogeneous initial conditions $(sox9^*, bmp^*, wnt^*) = (0, 1, 1)$ and have a 1% of Gaussian multiplicative noise added to Sox9, Bmp and Wnt at each time step. One time unit in the simulation corresponds to one minute in real developmental time. On a 2.30GHz CPU of an Intel Core i7-3610QM with 4GB of ram, a Turing simulation on a growing limb model with coarser meshes take approximately 1h (average $\delta t \approx 0.026$) and takes 6h on with finer meshes (average $\delta t \approx 0.011$). All the simulation showed in the following sections use finer meshes which have a resolution that is high enough to avoid deviations from the real solution. Similar results are indeed also obtained with coarser meshes. The low and high resolution growing limb models (MorphoMovies) are presented in Figure 3.15.

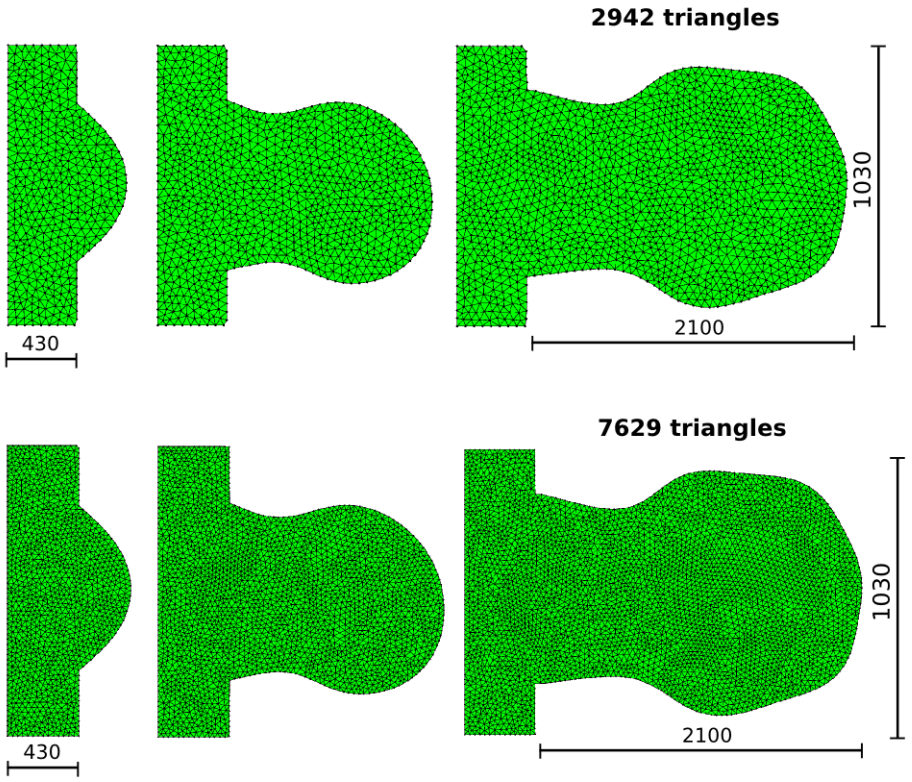

Figure 3.15: The two MorphoMovies used in the simulations. On top a MorphoMovie with coarse meshes and on the bottom the MorphoMovie with high resolution. The P-D length of the body and the AP/PD length of the limb bud shape at E12.5 are given.

3.3.4.1 Inside the growing limb model

As a first step, I test the behavior of the system (3.25) inside the growing limb model. In particular, I explore how the tissue movements specified by the Morphomovie can affect the Turing pattern. The influence of the Morphomovie will depend on the relative speed between the tissue movements and the reaction-diffusion patterning events. For this reason I rewrite the system (3.25) to consider a scaling factor λ that sets the speed of the reaction-diffusion mechanism:

$$\begin{aligned}
\frac{\partial sox9}{\partial t} &= \lambda(k_1 bmp - k_2 wnt - sox9^3) \\
\frac{\partial bmp}{\partial t} &= \lambda(\alpha_{bmp} - k_3 sox9 - \mu_{bmp} bmp + D_{bmp}\nabla^2 bmp) \\
\frac{\partial wnt}{\partial t} &= \lambda(\alpha_{wnt} - k_4 sox9 - \mu_{wnt} wnt + D_{wnt}\nabla^2 wnt)
\end{aligned} \tag{3.26}$$

This system is simulated inside the growing model for 2880 time units (minutes) that represent $48h$ of development in the period from $E10.5$ to $E12.5$. By changing λ, the speed of the reaction-diffusion system can be modified with respect to the speed of limb growth. I use the parameters presented in table 3.1 that according to the conditions derived in section 3.3.2.2 produce a diffusion-driven instability. The reaction-diffusion speed is changed by using three different values of λ: $\lambda = 0.25$, $\lambda = 1$ and $\lambda = 4$, see Figure 3.16

The simulations reveal a general trend where the faster is the Turing mechanism the more independent is the pattern with respect to limb growth. Indeed, when $\lambda = 0.25$ or $\lambda = 1$ the direction of the stripes is biased to the distal tip of the limb. This is due to the anisotropies that drive elongation in our growing model, see the top row in Figure 3.16. When $\lambda = 4$, the fast reaction-diffusion rates allow the pattern to re-arrange quickly at every time-point and the bias given by the tissue movement is lost. In this case the pattern depends only on the limb shape and on noise. Due to the lack of experimental information about the reaction-diffusion speed I perform the following simulations using the intermediate case with $\lambda = 1$, see Figure 3.17.

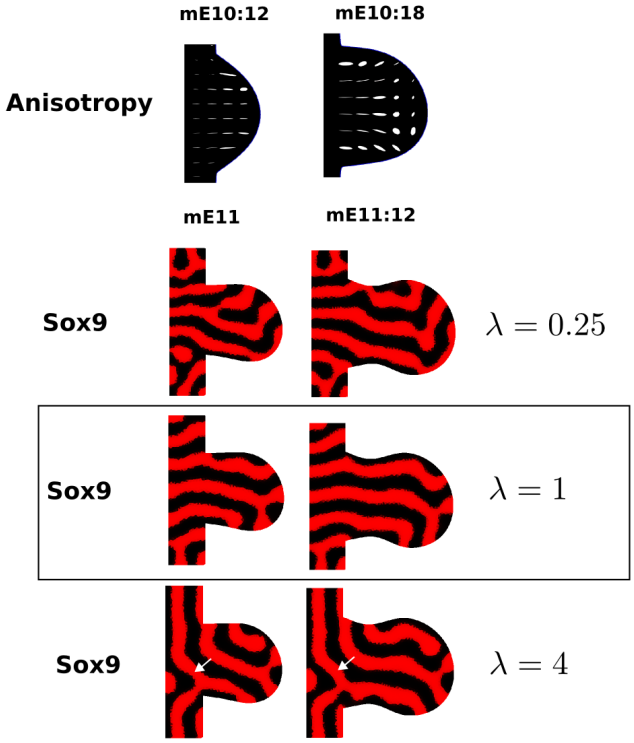

Figure 3.16: White ellipses show the anisotropies of the limb growth model (top row). The concentrations of Sox9 for the three simulations of the system (3.26) with $\lambda = 0.25, \lambda = 1$ and $\lambda = 4$ are shown in red color. When λ is high, the orientation of the stripes becomes more independent from the tissue movement, see the white arrow.

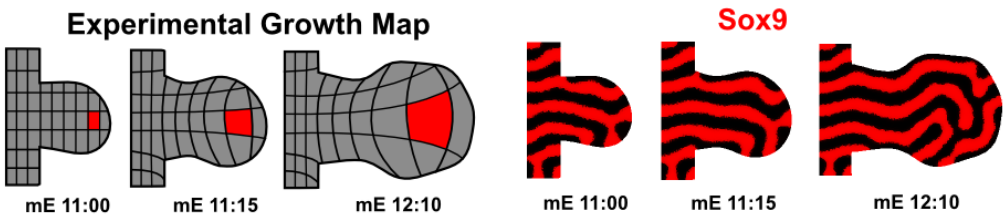

Figure 3.17: Left, a representation of the experimental limb growth model used in the simulations. Right, simulation of the Turing network inside the growth model with $\lambda = 1$. Sox9 concentrations (high values in red) show a labyrinthine pattern with stripes oriented towards the distal tip.

3.3.4.2 Using Hoxd13 as autopod marker

Distal Hox genes manipulations (see section 3.1), mutants of Bmp-signaling [Bénazet et al., 2012] and classic grafting experiments [Tickle et al., 1982] all suggest that digit patterning is relatively independent from the rest of the skeleton. Therefore it is reasonable to assume that the activity of the Turing mechanism may be restricted to the patterning of the digital region. I restrict the diffusion-driven instability to the autopod by mapping a time-course of experimental Hoxd13 expression patterns into the model, which marks the digit-forming region. This is done by manually segmenting a time course of in-situ hybridizations of Hoxd13 using the software Gimp [Gimp, 1] to remove the background and obtain a black and white images. Successively, the expression patterns are interpolated with the JavaMorph software [JavaMorph, 1] to derive patterns for the missing time-points. Then, each time-point is staged using the Morphometric staging system presented in [Boehm et al., 2011] and the expression patterns are mapped into the corresponding triangular mesh of the MorphoMovie by using the Vtk library [VTK, 1]. Finally, each expression pattern is normalized between 0 and 1. An overview of the whole pipeline is shown in Figure 3.18.

Scalar values associated with the expression of Hoxd13 can then be used to vary the reaction parameters of the system (3.25). To restrict the activity of the Turing mechanism to the autopod, I set the parameters to default values that do not produce a diffusion-driven instability and I move the system into the diffusion-instability space by using Hoxd13, see Figure 3.19.

This is be done by rewriting the system (3.25) as following:

$$\begin{aligned}
\frac{\partial sox9}{\partial t} &= k_1 bmp - k_2 wnt - sox9^3 \\
\frac{\partial bmp}{\partial t} &= \alpha_{bmp} - (k_3 - k^1_{hox} hoxd13) sox9 - \mu_{bmp} bmp + D_{bmp} \nabla^2 bmp \\
\frac{\partial wnt}{\partial t} &= \alpha_{wnt} - (k_4 + k^2_{hox} hoxd13) sox9 - \mu_{wnt} wnt + D_{wnt} \nabla^2 wnt
\end{aligned} \tag{3.27}$$

with the parameter set presented in Table 3.1 except for $k_3 = 7, k_4 = 0.45$ and with $k^1_{hox} = 1.5$, $k^2_{hox} = 0.55$. Simulations reveal that as Hoxd13 expands proximally and anteriorly, see the left part in Figure 3.20, distally oriented stripes are formed starting from the posterior part of the limb, see the right part of Figure 3.20. Moreover, the progressive expansion of Hoxd13 drastically reduces the variability of the patterns across different simulation runs, see Figure 3.21.

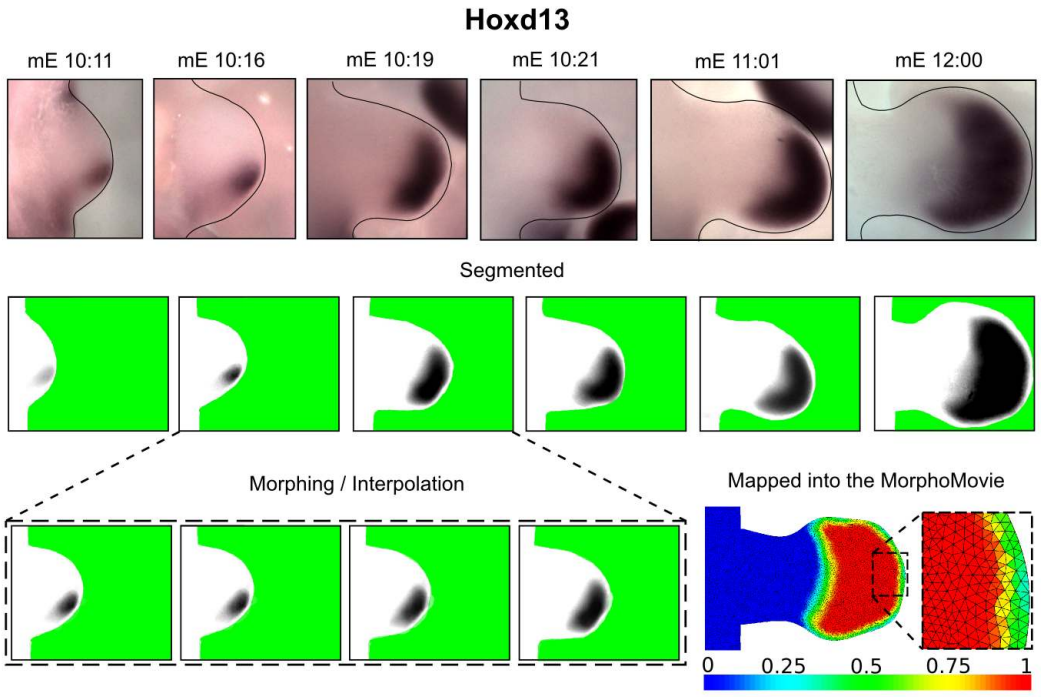

Figure 3.18: The first row shows a time course of Hoxd13 in-situ hybridization, the second row shows segmented expression patterns. In the third row, on the left an example of interpolated patterns obtained with JavaMorph and on the right an example of expression pattern mapped into the triangular mesh.

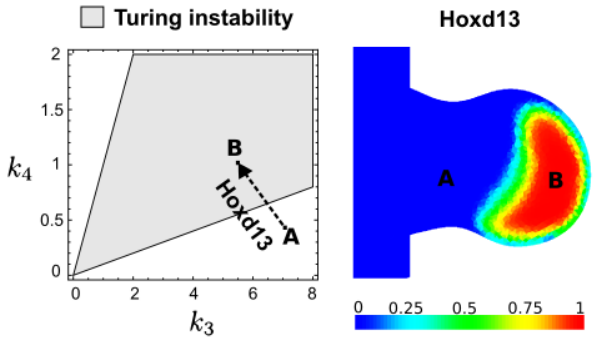

Figure 3.19: On the left, a graph shows the diffusion-driven instability region when k_3 and k_4 are varied (gray color) according to conditions derived in section 3.3.2.2. The black dashed line represents the change in k_3 and k_4 promoted by Hoxd13 to go from a region with no diffusion-driven instability (A) to a region with diffusion-driven instability (B). On the right, an Hoxd13 expression mapped into the model shows where the system move from (A) to (B).

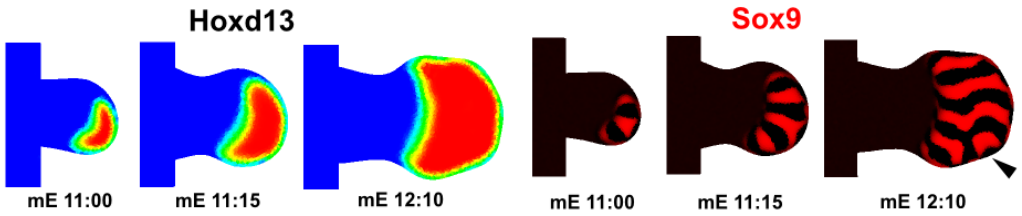

Figure 3.20: Left, experimental Hod13 expression mapped into the 2D growth model are shown with a blue to red color map (blue=0 and red=1). Right, a simulation with the Turing network active only in the Hoxd13 expressing region: concentration of Sox9 (red) reproduces a digit pattern but at mE12:10 the pattern forms new distal peaks (black arrow).

However, as the autopod expands along the AP-axis to produce its typical paddle shape, stripe splitting and stripe bifurcations are observed at the distal tip, see the black arrow in Figure 3.20. In the article presented in section 3.1, we showed that this behavior is naturally obtained when a Turing mechanism is simulated inside a static autopod-like geometry and we demonstrated that it could be avoided by scaling the wavelength in a PD-graded manner with Fgf-signaling. In the next section I extend this idea to the dynamic growing simulation.

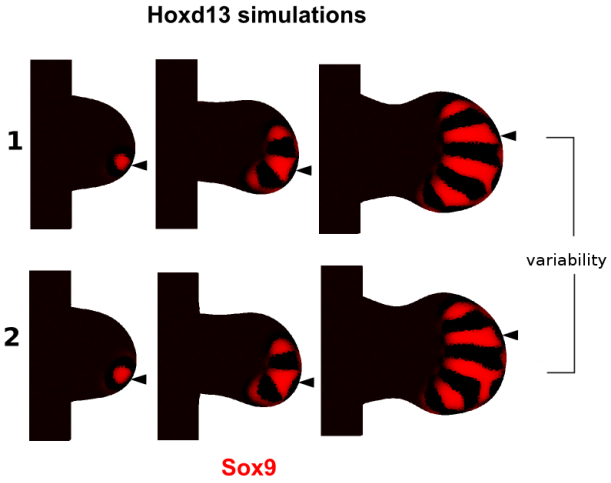

Figure 3.21: Two simulation runs with Hoxd13 that defines the autopod region where the diffusion-driven instability occurs. The progressive expansion of Hoxd13 creates a similar pattern in each simulation, see the black arrows.

3.3.4.3 Avoiding bifurcations by spatial modulation with Fgfs

To introduce a graded wavelength modulation in the limb growing model, I first need to gain a general overview of how the different reaction parameters affect the behavior of the system (3.25). To this end, I perform a number numerical simulations on a squared static mesh. Finally, I extend my observations to the dynamic growing simulation by introducing an Fgf-signaling gradient to vary parameters in a spatially graded manner.

The static simulations are performed setting $d = \frac{D_{bmp}}{D_{wnt}} = 10$ and considering the following initial parameter values:

α_{bmp}	α_{wnt}	μ_{bmp}	μwnt	k_1	k_2	k_3	k_4
0.1	0.1	0.1	0.1	0.5	0.5	2	0.5

Table 3.2: The parameter set used as a starting point for the analysis of spatially varying parameters

with these parameters the system has homogeneous steady state:

$$(sox9^*, bmp^*, wnt^*) = (0, 1, 1) \tag{3.28}$$

In the analysis of the two-reactant model presented in section 3.1, for each parameter couple I calculated the variation of the maximum eigenvalue λ_{max} and the wavelength ω. The analytical derivation of these two quantities is not possible in the three-components system (3.25). As an alternative, numerical simulations inside a squared domain where one parameter is changed along the x direction and other along the y direction can provide an overview of the qualitative patterns that are formed across the parameter space (E.g wavelength, spots vs stripes). A similar approach was taken in [Pearson, 1993] to sample the behavior of the Gray-Scott Turing model. The simulations have the homogeneous steady state (3.28) as initial conditions, have zero-flux boundary conditions and consider a 1% of multiplicative Gaussian noise that is added to the three species over time. The final results can be represented with a single plot for each parameter couple that includes the final time point of the numerical simulation overlapped with the Turing instability region, see Figure 3.22 and Figure3.23. These simulations also provide an idea of the effect of spatially varying parameters (E.g. if a graded parameter along x is able to align the stripes).

In agreement with (3.7) and (3.12) the static simulations reveal that the constant production rates α_{bmp} and α_{wnt} do not affect the capacity of the system to form a diffusion-driven instability, see Figure 3.22. However, they are key for the

type of spatial pattern that is formed: when $\alpha_{wnt} \gg \alpha_{bmp}$ spots are formed, when $\alpha_{wnt} \ll \alpha_{bmp}$ reverse spots are formed and when $\alpha_{wnt} \sim \alpha_{bmp}$ stripes are formed, see the top row in Figure 3.22. An analysis of the effect of the decay rates μ_{bmp} and μ_{bmp} predicts that if $\mu_{wnt} \ggg \mu_{bmp}$ or $\mu_{bmp} \ggg \mu_{wnt}$ the system exits from the diffusion-driven instability region, see the bottom row in Figure 3.22.

Regarding the main reaction parameters k_1, k_2, k_3, k_4, see Figure 3.23, numerical simulations are in agreement with the analytical derivation of the Turing spaces and show that within the diffusion-instability parameter space the system always produces stripes. As in the case of the two-reactant model presented in section 3.1 this is due to the reverse asymmetry provided by the cubic saturation term on the auto-activating reactant ($sox9^3$).

In addition, I found that either a decrease in k_1 or k_3 or an increase in $k2$ or k_4 increase the wavelength. When k_1 or k_2 are varied the stripes align parallel to the direction of change, while when k_3 and k_4 are varied the opposite aligning effect is observed: the stripes align towards to the direction of change (towards the gradient), see the simulations highlighted with a red outline in Figure 3.23 .

In summary, these numerical simulations suggest that k_3 and k_4 are the best parameter to achieve modulation of wavelength and to promote alignments of the stripes towards the gradient. To test these predictions inside the growing limb I modulate in a spatially graded manner the reaction parameters with a gradient that represents Fgf-signaling. The gradient is simulated by defining on each mesh of the Morphomovie two boundary regions that correspond to the parts of the AER that express Fgf8 and Fgf4-9-17. In the case of Fgf4-9-17 we use in-situ hybridization of Fgf4 as representative patterns, see the red line in Figure 3.24.

These boundary regions are then used to simulate a gradient of Fgf signaling, see Figure 3.24. The gradient is formed by local production, diffusion and decay according to the following equations:

$$\frac{\partial fgfsig}{\partial t} = \alpha_{fgf8} + \alpha_{fgf4} - \mu_{fgf} fgfsig + D_{fgf} \nabla^2 fgf \tag{3.29}$$

where $\mu_{fgf} = 0.1$, $D_{fgf} = 30000$ and the two production terms $\alpha_{fgf8}, \alpha_{fgf4}$ are set to $\alpha_{fgf4} = 0.7$ and $\alpha_{fgf4} = 0.3$ in the triangles underneath the $Fgf8$ and $Fgf4$ expressing region (they are equal to 0 elsewhere). Eventually, the gradient is normalized between 0 and 1, results are showed in Figure 3.24.

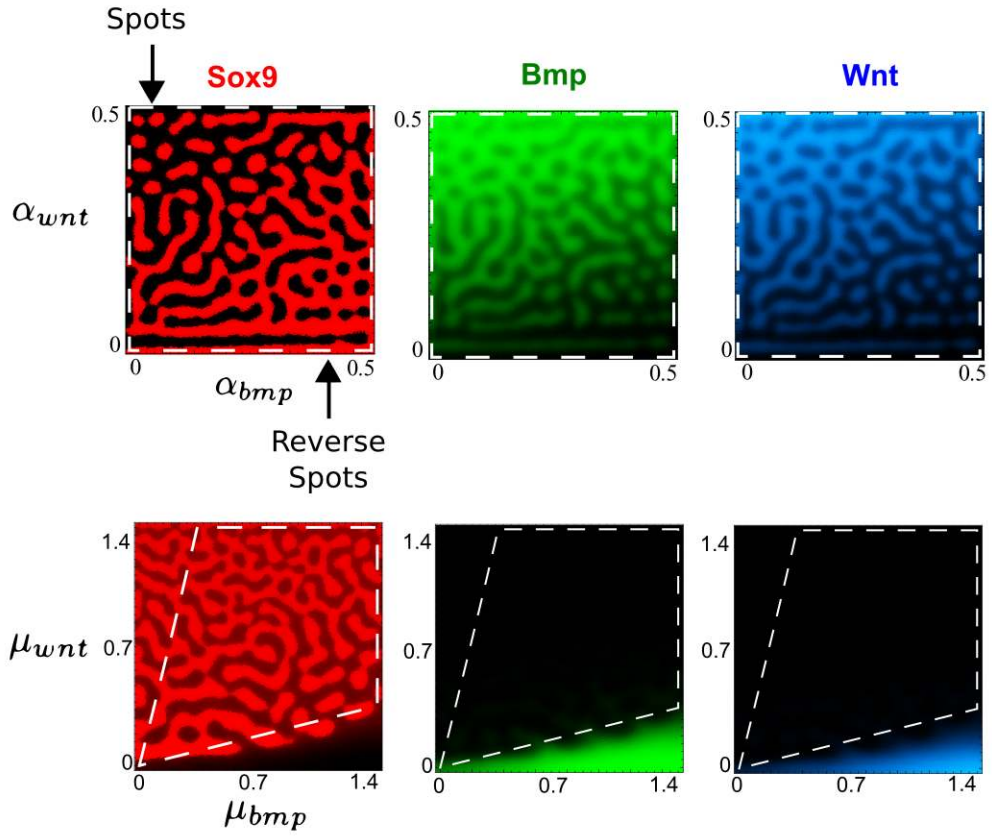

Figure 3.22: Analytically derived Turing spaces (white dashed line) are overlapped with the final time-point of a numerical simulations where one parameter varies along the x direction and another parameter along the y direction. Concentrations of $sox9, bmp$ and wnt are showed respectively in red, green and blue. Top row: variation of the production rates α_{bmp} and α_{wnt}. Starting from the parameters in Table 3.2, the systems always produce a Turing instability (the dashed line includes the entire space). However, different qualitative patterns are observed: when $\alpha_{wnt} \gg \alpha_{bmp}$ spots are formed, when $\alpha_{wnt} \ll \alpha_{bmp}$ reverse spots are formed and when $\alpha_{wnt} \sim \alpha_{bmp}$ stripes are obtained. Bottom row: variation of the decay rates μ_{bmp} and μ_{wnt}, when $\mu_{bmp} \gg \mu_{bmp}$ Sox9 is very low and no pattern is formed, this region is outside the Turing space (white dashed line).

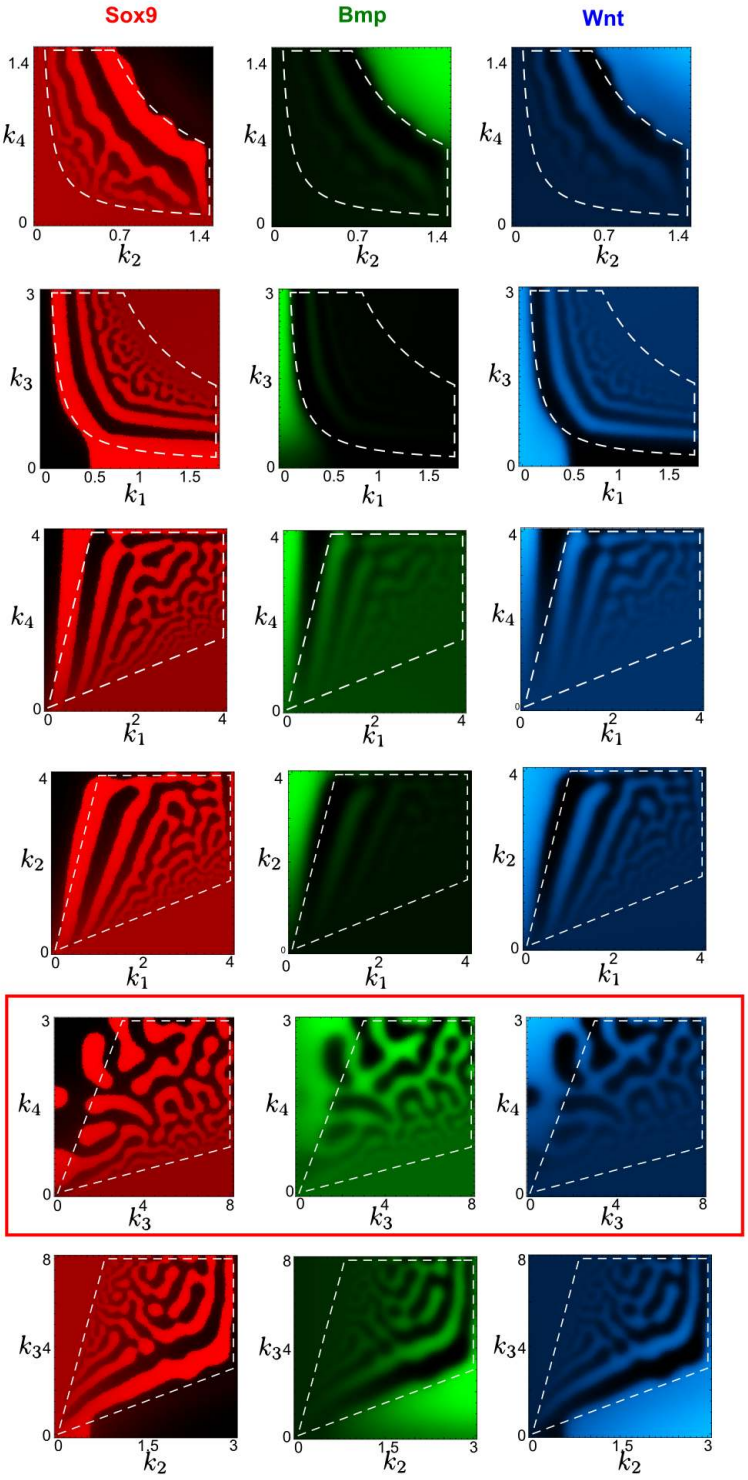

Figure 3.23: The behavior of the system when k_1, k_2, k_3, k_4 are changed (six parameter couples are shown). Outlined in red: the parameters that align the stripes towards the direction of change.

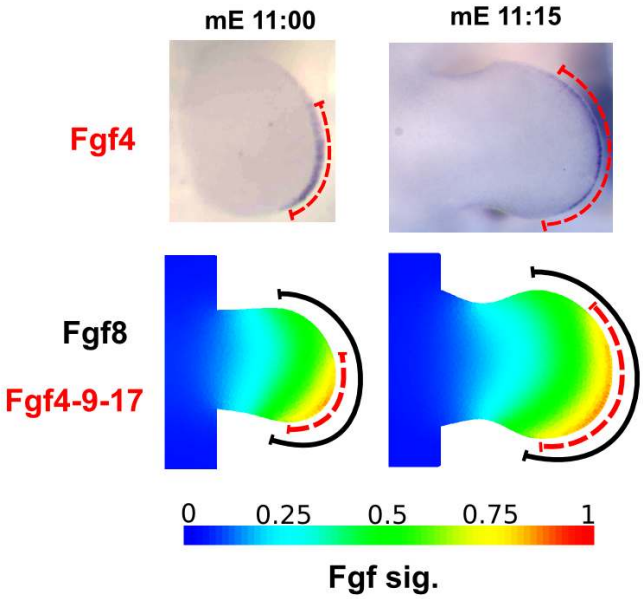

Figure 3.24: On the top row in-situ hybridizations for Fgf4. The dashed red line highlights the region along the AER where Fgf4 is expressed. On the bottom row, the black line shows the region under the AER where $\alpha_{fgf8} > 0$, while the dashed red line shows the region where $\alpha_{fgf4} > 0$. The colored pattern represent the simulated Fgf signaling gradient obtained by diffusion of a cumulative term that considers both production terms.

The simulated $fgfsig$ gradient is used to change the reaction parameters of the system (3.25) in a spatially graded manner. As in the case of the two-reactant model presented in section 3.1, the Fgf-signaling gradient is used as a Positional Information signal that modulates the Turing system along the space. Such modulation is implemented by setting the reaction parameters to default values that do not produce a Turing pattern and by using $fgfsig$ to move the system inside the diffusion-driven instability region, see Figure 3.25. In agreement with the static simulations, the numerical simulations on the MorphoMovie reveal that k_3 and k_4 are the best parameter to achieve modulation of wavelength to align the stripes towards the gradient.

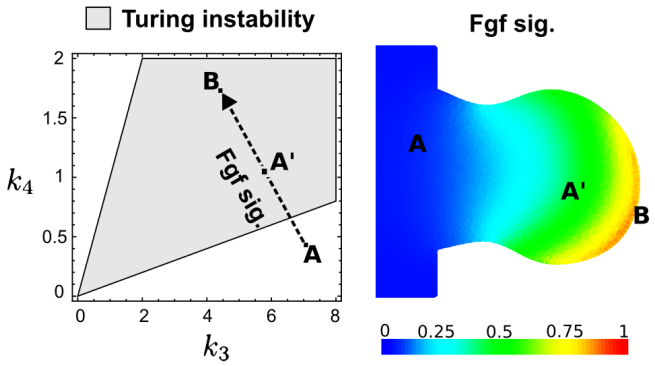

Figure 3.25: On the left, a graph shows the Turing instability region (gray color) as k_3 and k_4 are varied. The black dashed line represents the change in k_3 and k_4 promoted by $fgfsig$ to go from no-Turing instability (A) to a Turing instability (B), an intermediate point (A') is showed. On the right, an example of simulated $fgfsig$, the points (A) (A') (B) are highlighted along the gradient.

The modulation is implemented by rewriting the system (3.25) as follows:

$$\begin{aligned}
\frac{\partial sox9}{\partial t} &= k_1 bmp - k_2 wnt - sox9^3 \\
\frac{\partial bmp}{\partial t} &= \alpha_{bmp} - (k_3 - k^1_{fgf} fgfsig) sox9 - \mu_{bmp} bmp + D_{bmp} \nabla^2 bmp \\
\frac{\partial wnt}{\partial t} &= \alpha_{wnt} - (k_4 + k^2_{fgf} fgfsig) sox9 - \mu_{wnt} wnt + D_{wnt} \nabla^2 wnt
\end{aligned} \tag{3.30}$$

with the parameter in table 3.1 except for $k_3 = 7, k_4 = 0.45$ and the new parameters $k^1_{fgf} = 2.5$ and $k^2_{fgf} = 1.25$. The simulation on the growing model shows that when k_3 is increased and k_4 is decreased, the wavelength is increased in a P-D graded manner and the stripes align towards distal tip assuming a radial conformation, see Figure 3.26. However, the pattern that is formed shows a greater variability in comparison with the case where Turing activity was restricted by Hoxd13, see Figure 3.27.

In the next section I develop a model where both Fgf-signaling and Hoxd13 modulate the Turing mechanism.

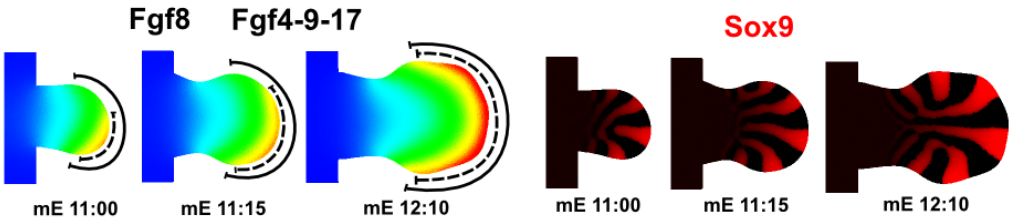

Figure 3.26: Left, an Fgf-signaling gradient (blue=0, red=1) is simulated by diffusing Fgfs from the regions that express Fgf8 (full line) and Fgf4-9-17 (dashed line). Right, simulated Sox9 concentrations (red) show a distally-oriented pattern with bigger wavelength towards the distal tip.

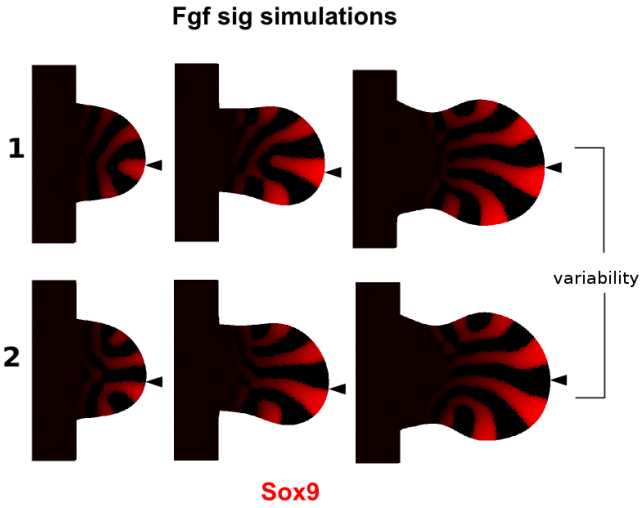

Figure 3.27: Two simulation runs with the Fgf-signaling gradient that modulate the Turing mechanism. Although distal bifurcation are prevented and the patterns align radially, a high degree of variability in the pattern is observed, see the black arrows.

3.3.4.4 Using Hoxd13 and Fgfs together

The simulations presented in the previous sections revealed that when the Turing mechanism is modulated by Hoxd13 a reproducible arrangement of the pattern is obtained. However, when the A-P expansion of the autopod increases stripe bifurcations occur at the distal tip. Conversely, when the system is modulated by Fgf-signaling, distal bifurcations are prevented but the arrangement of the pattern is more variable. In this section I develop a model which combines Hoxd13 and Fgf-signaling to avoid distal digit bifurcations and to obtain reliable patterning. The model produces digit patterning dynamics that capture most of the features of the experimental Sox9 expression patterns.

Similarly to the model presented in the article in section 3.1, I rewrite the equations of system (3.25) as following:

$$\begin{aligned}
\frac{\partial sox9}{\partial t} &= k_1 bmp - k_2 wnt - sox9^3 \\
\frac{\partial bmp}{\partial t} &= \alpha_{bmp} - (k_3 - k^1_{hoxfgf} hoxd13fgfsig) sox9 - \mu_{bmp} bmp + D_{bmp}\nabla^2 bmp \\
\frac{\partial wnt}{\partial t} &= \alpha_{wnt} - (k_4 + k^2_{hoxfgf} hoxd13fgfsig) sox9 - \mu_{wnt} wnt + D_{wnt}\nabla^2 wnt
\end{aligned} \tag{3.31}$$

with the parameter set presented in Table 3.1 except for $k_3 = 7, k_4 = 0.45$ and the two new parameters $k^1_{hoxfgf} = 2.5$ and $k^2_{hoxfgf} = 1.25$. As expected, this model forms a reproducible pattern with stripes that aligns radially and increase the wavelength in a P-D graded manner. The patterns highly resemble the expression of Sox9 in the digital region up to E12. However, in later points the pattern disorganizes and shows proximal bifurcations and/or stripe bending, see Figure 3.28A. Intriguingly, this behavior correlates with the proximal expansion of Hoxd13, see the graphs in Figure 3.28A, suggesting the hypothesis that to reproduce the experimental pattern of Sox9 until late developmental stages (E12.5), Fgf-signaling must be up-regulated in coordination with the proximal expansion of Hoxd13. This idea is consistent with the fact that Fgfs are progressively up-regulated in the AER by the Shh-Grem-Fgf positive feedback loop [Bénazet et al., 2009, Sun et al., 2002, Verheyden and Sun, 2008], and fits with the hypothesis that the Fgf-signaling is involved in P-D patterning [Mercader et al., 2000, Tabin and Wolpert, 2007] by directly or indirectly promoting the expression of Hoxd13.

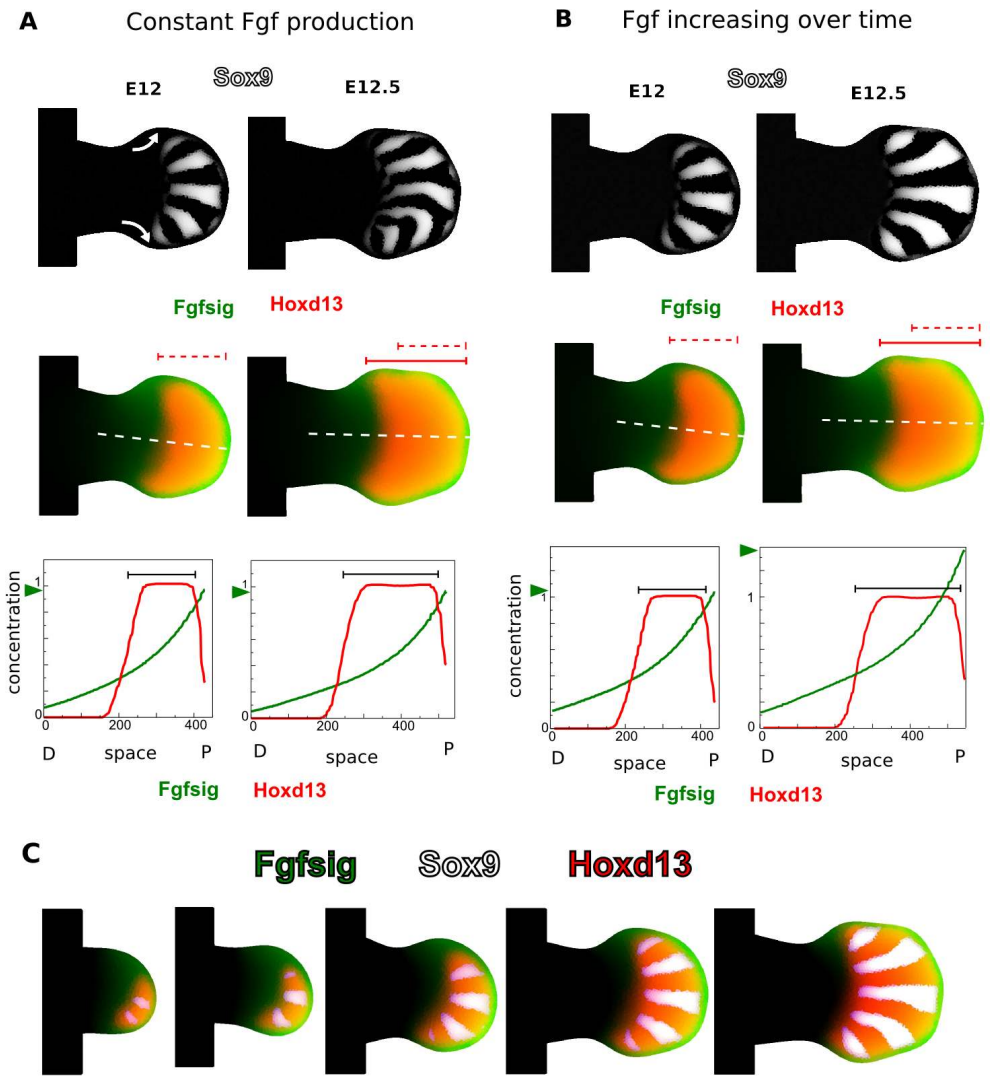

Figure 3.28: Simulated Sox9 concentrations (white), Fgf-signaling (green) and Hoxd13 (red) at E12 and E12.5. A) Case with constant Fgf production: the Sox9 pattern orients radially (see white arrows at E12) and distal bifurcations are prevented, but at E12.5 when Hoxd13 expands and Fgf-signaling remains constant (see graph) the pattern disorganizes. B-C) Case with Fgf production increasing over time (see green arrows in the graphs): the Sox9 pattern orients radially even at E12.5

To validate this hypothesis, I simulate a new Fgf-signaling gradient by progressively increasing $fgf8$ and $fgf4$ in later time points. This is done by rewriting the terms α_{fgf8} and α_{fgf4} in equation (3.29) as follows:

$$\begin{aligned} \alpha_{fgf8} &= 0.7 + \Delta_{fgf8}\frac{t - t_1}{t_2 - t_1} \\ \alpha_{fgf4} &= 0.3 + \Delta_{fgf4}\frac{t - t_1}{t_2 - t_1} \end{aligned} \tag{3.32}$$

where t is the current time in the simulation, t_1, t_2 define the temporal interval when the productions are increased and $\Delta_{fgf8}, \Delta_{fgf4}$ define the strength in Fgf increase. Using an Fgf-signaling gradient obtained with $\Delta_{fgf8} = \Delta_{fgf4} = 0.15$, $t_1 = 17200$ (E12) and $t_2 = 18000$ (E12.5), stripe bending at later time points is indeed prevented, see Figure 3.28B. Strikingly, by combining these Positional Information signals with the Turing mechanism a highly reproducible arrangement of the pattern that reflects the experimental expression of Sox9 is obtained, see Figure 3.28C

To summarize, when Hoxd13 and Fgf-signaling are coordinated to modulate the Turing system (see Figure 3.29A), results that agree with the experimental patterns of Sox9 are obtained at all stages of development. This can be seen by comparing the simulated Sox9 pattern in Figure 3.29B, with the experimental expression patterns of Sox9 in Figure 3.29C. In particular, the simulation reproduces the progressive formation of digits in the anterior part of the autopod, the final formation of digit 1 and digit 5 (black arrows in Figure 3.29B), the radial orientation of digits at later stages and the complementary patterns between Sox9, Bmps and Wnt.

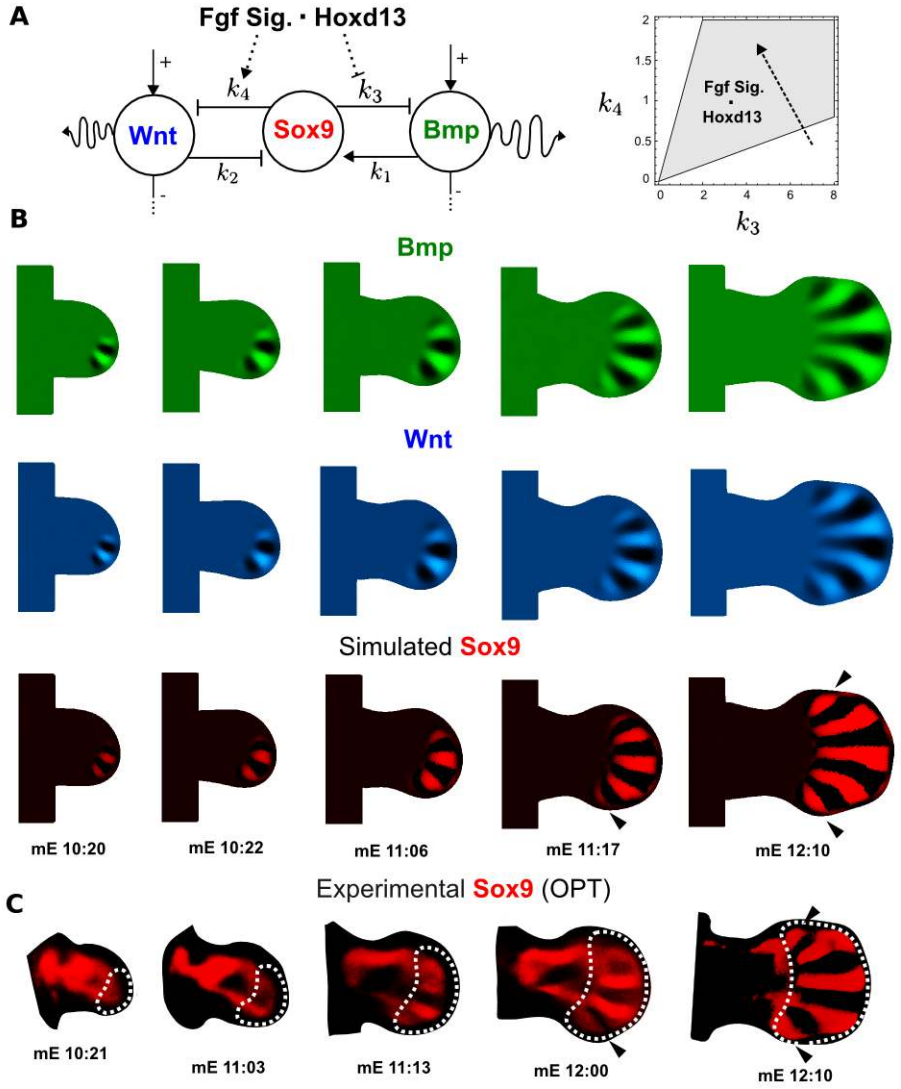

Figure 3.29: A) The Fgf-signaling gradient and Hoxd13 patterns modulate the reaction parameters of the Turing model by increasing k4 and decreasing k1, shown by the network diagram on the left. In this way the system moves into the Turing instability region, see the graph on the right where the dashed line shows the action of Fgf-signaling and Hoxd13 to move the system into the Turing space (gray region). B) Concentrations of Bmp2 (green), Wnt (blue) and Sox9 (red) in the simulation with Fgf-signaling and Hoxd13 that modulate the Turing network. C) Experimental expression pattern of Sox9 (red) scanned with OPT. The simulated Sox9 pattern recapitulates the main features of the experimental Sox9 digit pattern (outlined by the white dotted line). Black arrows mark the late appearance of digit 5 and digit 1 in the simulation and in experimental patterns.

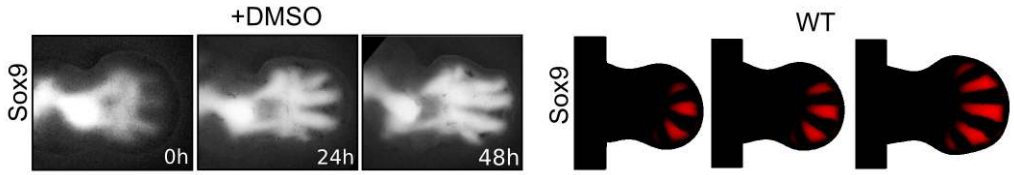

Figure 3.30: Control situations: 48h of Sox9-EGP limb culture with DMSO added to the medium (left) and simulation of the system 3.31 (right).

3.3.5 Model predictions vs experimental perturbations

A critical test to evaluate the final model (3.31) is to check whether it can predict the spatio-temporal dynamics of digit patterning under different experimental perturbations. Limb cultures of Sox9-EGFP mouse are a perfect tool to monitor the expression of Sox9. By culturing E11.5 limbs for 48h, the progressive appearance of the digital pattern could be observed in-vitro for the first time (Figure 3.30). Similar cultures were performed with several experimental perturbations and compared with simulated perturbations from E11.5.

When LDN, an inhibitor of Bmp-signaling, was added in limb culture a progressive down-regulation of Sox9 in the autopod which resulted in complete disappearance of the digits by 48h (Figure 3.31A), was observed. Similarly when Bmp-signaling was prevented in the simulation by setting $k_1 = 0$ at E11.5, the digital pattern progressively disappeared over time (Figure 3.31A). Consistently, when Bmp-signaling was locally increased by implanting Bmp2 soaked beads in limb culture a rapid local up-regulation of Sox9 was observed (Figure 3.31B). Similar results were obtained by placing virtual beads that released Bmp in the simulation (Figure 3.31B).

Virtual beads were defined by taking advantage of the triangle correspondence map provided by our limb growth model, which allows us to track a part of tissue from E10.5 to E12.5 (virtual fate map). By marking a set of triangles at E10.5 and realistically tracking their fates until E12.5, I defined a region that represented a Bmp bead where the system (3.31) was modified as:

$$\begin{aligned} \frac{\partial sox9}{\partial t} &= 0 \\ \frac{\partial bmp}{\partial t} &= 0.6 \\ \frac{\partial wnt}{\partial t} &= 0 \end{aligned} \tag{3.33}$$

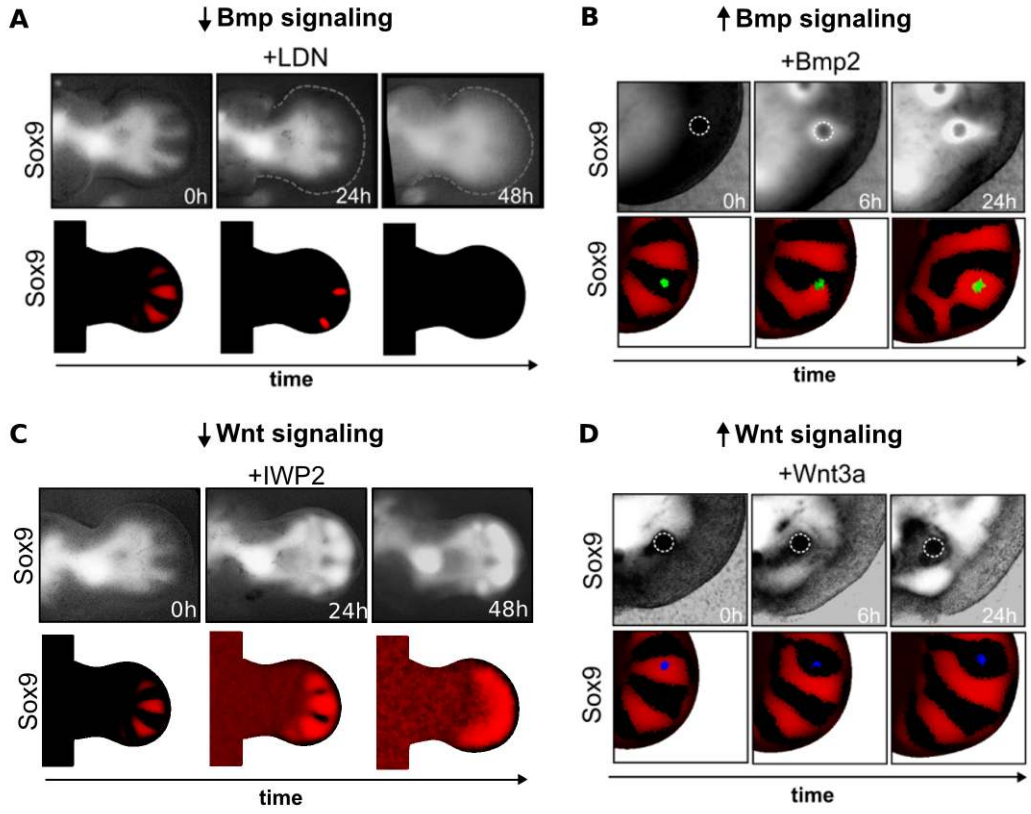

Figure 3.31: Simulated Sox9 concentrations (red) are compared with Sox9-EGP limb cultures (black and white pictures) in various perturbations. The Turing system (3.31) is used in all cases. A) Addition of the LDN, a Bmp-signaling inhibitor, shows a down-regulation of Sox9 and loss of the digital pattern by 48h. A simulation with impaired Bmp-signaling shows a similar gradual loss of digit patterning. Dashed lines highlight the outline of the limb. B) Implantation of a Bmp2-soaked bead (white dashed circle) shows progressive local up-regulation of Sox9. In the simulation, a virtual bead (green) that releases Bmp induces a similar progressive Sox9 up-regulation. C) Addition of IWP2, an inhibitor of Wnt secretion, promotes Sox9 up-regulation and expansion of the digits, which fuse to form a continuous domain of Sox9 expression in the autopod by 48h. When Wnt production is reduced in the model, remarkably similar dynamics are observed. D) Implantation of a Wnt3a-soaked bead (white dashed circle) shows progressive local down-regulation of Sox9. A virtual bead (blue) that releases Wnt stimulates a similar progressive Sox9 down-regulation.

When IWP2, which inhibits Wnt secretion, was added to limb cultures we observed an up-regulation of Sox9 and a progressive expansion of each digit that resulted in a continuous Sox9 domain by 48h (Figure 3.31C). Strikingly, when Wnt production is reduced in the simulation by setting $\alpha_{wnt} = -3$ at E11.5, similar spatio-temporal dynamics are obtained (Figure 3.31C). Both in the experiments and in simulations, interdigital Wnt-signaling is an essential part of the Turing system, without which digit patterning is lost. Consistently, when Wnt-signaling was locally increased by implanting Wnt3a soaked beads in limb culture, a progressive down-regulation of Sox9 was observed over time (Figure 3.31D). Similar results were obtained in the simulation by placing virtual beads that released Wnt (Figure 3.31D) by modifying the system (3.31) as:

$$\begin{aligned} \frac{\partial sox9}{\partial t} &= 0 \\ \frac{\partial bmp}{\partial t} &= 0 \\ \frac{\partial wnt}{\partial t} &= 1.5 \end{aligned} \tag{3.34}$$

Finally, in agreement with the study presented in section 3.1 the model predicts that a reduction of the Hox dosage reduces the wavelength. Our previous study showed that the effect of Distal Hox genes removal was more evident when growth deficiencies were rescued by using the Gli3-/- background (where growth of the handplate is increased). I compare simulations of the new model with a distal Hox mutant with the Gli3+/- background, which has an handplate A-P size that is comparable to the wildtype situation. In the dynamic simulation, the experimental expression patterns of Hoxd13 are used to represent the effect of both Hoxa13 and Hoxd13, which are known have redundant functions [Fromental-Ramain et al., 1996]. I therefore model the Gli3+/- Hoxa13+/- Hoxd11-13-/- mutant with a general reduction in Hoxd13 obtained by rewriting $hoxd13$ as $\frac{hoxd13}{2}$, see Figure 3.32A.

The dynamic model also predicts that an increase in Fgf-signaling should promote a bigger wavelength. Since alteration of Fgf-signaling in the limb would cause a change in limb growth which would compromise interpretation of the results, we tested the effect of Fgf-signaling in Micromass culture. When progressively more Fgf4 was added to the medium we observed an increase in wavelength that was in close agreement with simulations inside a squared domain (Figure 3.32B). Because simulations of the Micromass culture situation had no experimental expression patterns of Hoxd13 and Fgf-signaling, I implemented the effect of Fgf-signaling by mimicking the change in k_3 and k_4 as in the dynamic

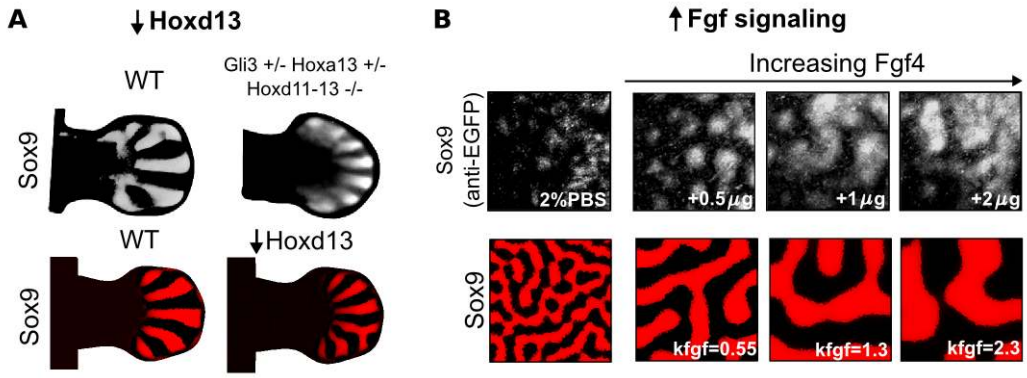

Figure 3.32: A) Top, Sox9 expression (red) in the WT and in the Gli3+/- Hoxa13+/- Hoxd11-13 -/- mutant. As shown in section 3.1, reduction of Hox dosage promotes the formation more thinner digits. Bottom, when Hoxd13 is reduced in the simulation (Khox=0.5) the model forms an increased number of thinner digits. B) Micromass cultures of Sox9-EGP autopod cells with increasing concentration of Fgf4 added to the medium, create patterns with increasing wavelength. Two-dimensional simulations of the model with increasing Fgf influence produce Sox9 patterns (red) with increasing wavelength.

limb simulation according to the following equations:

$$\begin{aligned}
\frac{\partial sox9}{\partial t} &= k_1 bmp - k_2 wnt - sox9^3 \\
\frac{\partial bmp}{\partial t} &= \alpha_{bmp} - (k_3 - k_{fgf} 1.75) sox9 - \mu_{bmp} bmp + D_{bmp} \nabla^2 bmp \\
\frac{\partial wnt}{\partial t} &= \alpha_{wnt} - (k_4 + k_{fgf} 0.875) sox9 - \mu_{wnt} wnt + D_{wnt} \nabla^2 wnt
\end{aligned} \tag{3.35}$$

By varying k_{fgf} these equations defined parameter sets that lay in the same trajectory promoted by the Fgf-signaling in the wild type limb simulation.

3.3.6 Robustness of the model

The linear stability analysis presented in section 3.3.2.2 shows that when $f_{sox9} = 0$ and $D_{sox9} = 0$ the Turing instability condition (3.8) is relaxed to (3.12). This implies that the Turing model (3.25) has particularly large diffusion-driven instability parameter space and suggests that it should implement a very robust Turing mechanism. To test this hypothesis I perform numerical simulations with different amount of Gaussian noise on Bmp, $Sox9$ and Wnt. The model (3.25) can be written as a system of stochastic partial differential equation (SPDEs) as follows:

$$\begin{aligned}
\frac{\partial sox9}{\partial t} &= f(sox9, bmp, wnt) + \eta(t, sox9) \\
\frac{\partial bmp}{\partial t} &= g(sox9, bmp, wnt) + D_{bmp}\nabla^2 bmp + \eta(t, bmp) \\
\frac{\partial wnt}{\partial t} &= h(sox9, bmp, wnt) + D_{wnt}\nabla^2 wnt + \eta(t, wnt)
\end{aligned} \tag{3.36}$$

where $f(sox9, bmp, wnt), g(sox9, bmp, wnt), h(sox9, bmp, wnt)$ the reaction terms presented in equation (3.31) and $\eta(t, sox9), \eta(t, bmp), \eta(t, wnt)$ are noise terms written as:

$$\begin{aligned}
\eta(t, sox9) &= \upsilon \quad sox9 \quad W_t^s \\
\eta(t, bmp) &= \upsilon \quad bmp \quad W_t^b \\
\eta(t, wnt) &= \upsilon \quad wnt \quad W_t^w
\end{aligned} \tag{3.37}$$

with W_t^s, W_t^b, W_t^w that represent random Wiener processes and υ that is a constant between 0 and 1 that defines the amount of multiplicative noise (intrinsic noise) in the system. At every integration step, the system of SPDEs is solved similarly to the Euler Maruyama method as follows: let define Δt_n as the time-step used by the numerical integration method at the iteration n, the noise terms $\eta(t, sox9), \eta(t, bmp), \eta(t, wnt)$ can be calculated by sampling the normally distributed random variables W_n^s, W_n^b, W_n^w with expected value 0 and variance Δt_n. This random variables represent the change in concentration given by the Wiener processes in the interval Δt_n (E.g. $W_{t+\Delta t_n}^s - W_t^s$).

By varying υ different amount of noise can be introduced, see Figure 3.33. Remarkably, the model is able to form a digit pattern even when $\upsilon = 0.5$, that represents 50% of multiplicative noise, see Figure 3.33. Strikingly, in this extremely noisy scenario the stereotypical spatio-temporal dynamics of Sox9 are highly compromised but a normal Sox9 digit pattern is formed at the final time-point (E12.5).

In the next chapter I discuss this dynamic Turing model and its limitations.

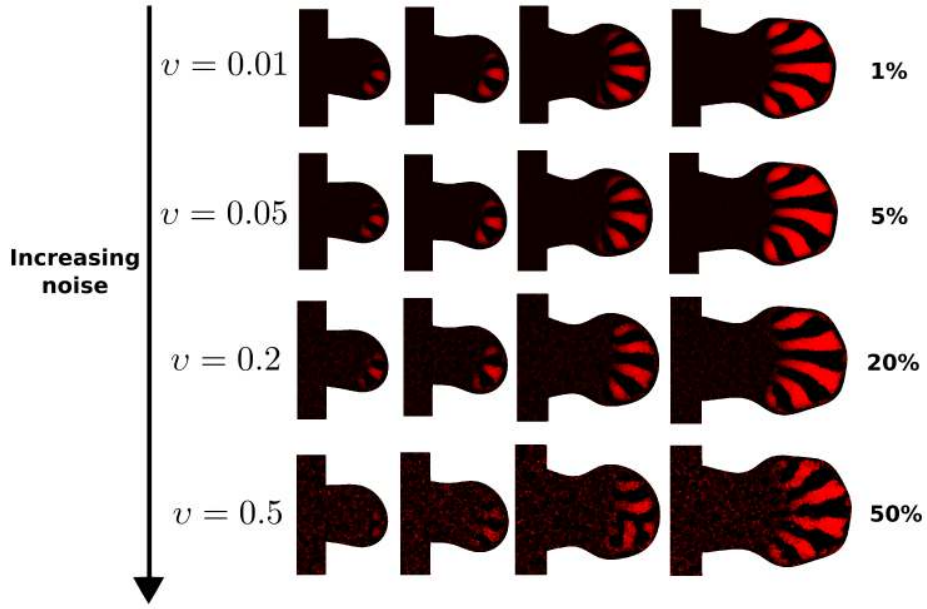

Figure 3.33: Simulation with progressively increasing noise, Sox9 concentration in red. The model produces a correct digit pattern even with $\upsilon = 0.5$ that corresponds to 50% of multiplicative noise.

Chapter 4

DISCUSSION

Understanding the mechanisms that underlie the development of organs and tissues from an homogeneous population of cells is one of the main goals of developmental biology. Two alternative theories have been proposed to explain this phenomena: the Positional Information model of Lewis Wolpert and the reaction-diffusion model of Alan Turing. Traditionally, these two theories have not been considered as alternative explanations for the same patterning task. The Wolpert model was proposed to be mostly relevant to regionalization (e.g. positioning the head at one end of the embryo, and the tail at the other), while Turing mechanisms were considered relevant to repetitive, periodic patterns (such as the zebra's stripes). In the vertebrate limb, digit patterning has been explained using both models and for a long time these two theories were seen as competing against each other. On one hand, the mirror image duplication observed upon anterior grafting of the ZPA was proposed as a paradigmatic example to support the positional information model. On the other hand, the formation of relatively normally patterned digits in re-aggregated limbs (up to thirty in Xenopus) strongly supported a self-organizing Turing mechanism.

In this study, I used computational modeling to explore to what extent these two models could be reconciled to explain digit patterning. Although, digit patterning had traditionally been explained by a positional information gradient of Sonic hedgehog (Shh), it was also proposed that a Turing mechanism could be responsible for the establishment of the digital vs inter-digital fates along the A-P axis. Nevertheless, in many of the developmental systems where Turing mechanisms were proposed to play a role, the repeated periodic patterns did not have a stereotypical arrangement (E. g. feather buds, hair follicles, fish stripes).

How could a Turing mechanism, which produces highly variable patterns, be responsible for the reliable specification of the digits?

An answer to this question came by analyzing the Distal Hox mutants produced by the laboratory of Marian Ros at the University of Cantabria. The progressive removal of Distal Hox genes, revealed that Hox dosage negatively correlated with the number of digits and the probability of distal digit bifurcations. In particular, we found that as Hox genes were removed a supernumerary number of thinner digit was formed, up to fourteen digits in one limb, and digit bifurcations were often observed in the distal part of the limb. These results were very difficult to reconcile with the Positional Information model and suggested that Distal Hox genes could act as modulators of a Turing mechanism responsible for the periodic digit pattern. By developing a simple Turing model that would confirm this hypothesis, I found that to avoid distal digit bifurcations the wavelength of the Turing mechanism had to be modulated in a proximal-distal (P-D) graded manner. An extensive computational analysis revealed that increasing the wavelength in P-D graded manner with an AER-signal was not only able to avoid digit bifurcations but also helped to obtain a reproducible digit pattern. Because there was no evidence for a P-D graded Hox expression, the simplest interpretation of this model was that the wavelength had to be modulated by both the Hox genes (explaining the global reduction in wavelength in the mutants) and fibroblast growth factor (FGF) signaling (explaining the P-D gradient). A Simulation of Hox dosage reduction in this combined model was indeed able to reproduce the polydactyly and the digit bifurcations observed upon Distal Hox removal.

As discussed in section 1.1.2.3, the idea of combining Positional Information with a Turing mechanism was already proposed thirty years ago by Lewis Wolpert [Wolpert, 1989] and has recently been re-proposed in several studies [Kondo and Miura, 2010, Miura, 2013]. Our study however, represents the first concrete example of a model that combines these two theories and implements a reliable patterning system.

Lewis Wolpert in his original work was also intrigued by another question: how could embryos of different sizes produce similar patterns with likely the same positional information system?

Wolpert proposed that this problem, known as scale-invariance, could be solved by coupling the positional-information gradients with growth, for example by having shorter-range gradients in smaller organism and longer-range gradients in bigger organism, see section 1.2.3. In addition, he proposed that not only the patterning systems had to be re-scaled according to the embryo size, but that such re-scaling had to be coordinated along the different axis to maintain the proportions. To solve this problem, Wolpert suggested that the interpretation of the gradients could be coupled along the different axis, see section 1.2.3. In Drosophila, some of Wolpert's hypothesis have been confirmed, however the mechanism that

control scale-invariance and maintenance of proportion during development remain largely unknown. Limb development is a Morphodynamic system in which digit patterning and limb outgrowth are happening simultaneously. This makes the problem of scale-invariance and proportion maintenance not only relevant for the final digital pattern but also for the early patterning phases when the digit pattern is being formed. In the limb, both concepts can be seen as part of the more general problem of "coordination between patterning and growth".

To explore the mechanism that may achieved such coordination in the limb, I extended my digit patterning model to consider an accurate simulation of limb growth. This comprehensive Morphodynamic model considered a new set of Turing equations derived from molecular data, a time-course of Hoxd13 expression patterns and a simulated Fgf-signaling gradient based on experimental expression of Fgf4 and Fgf8. Similarly to the model presented in our previous study, the Hoxd13 expression defined the region where the patterning mechanism was active while Fgf-signaling promoted a P-D graded wavelength to avoid digit bifurcations. Strikingly, to obtain patterning dynamics in agreement with the spatio-temporal expression of Sox9, the simulated Fgf-signaling gradient had to be highly coordinated with the experimental expression pattern of Hoxd13 at all stages of development. In particular, I found that to avoid proximal and distal bifurcations, Fgf-signaling had to be up-regulated in coordination with the proximal expansion of Hoxd13 and the A-P expansion of the autopod, see the section 3.3.4.4. According to our model, the expression of Fgfs has to increase over time and has to be strongly coupled with the molecular marker which defines the digital region (Hoxd13) and with limb growth. In agreement with this hypothesis, previous studies have shown that Fgfs promote growth [Martin, 1998] and promote the specification of the distal P-D segment [Mercader et al., 2000, Tabin and Wolpert, 2007]. Moreover, it has been proposed that the positive feedback between Fgf and Shh increases AER-Fgf concentration during limb outgrowth. Taken together, these observations suggest that Fgfs have three parallel roles: they promote growth, they promote the proximal expansion of autopod markers (Hoxd13) and according to our model they also increase the wavelength of the digits, see Figure 4.1. I propose that these three roles implement an effective coordination between patterning and growth (Figure 4.1A, right). On one side, this mechanism explains the normal dynamic patterning of Sox9 (Figure 4.1B), and on the other side it implements an Fgf-based strategy to achieve scale-invariance in embryos of different size (Figure 4.1C).

This idea represents the first concrete example of a digit patterning mechanism that is able to maintain the proportions along different axis. In the original hypothesis of Wolpert the maintenance of proportions along the different axis

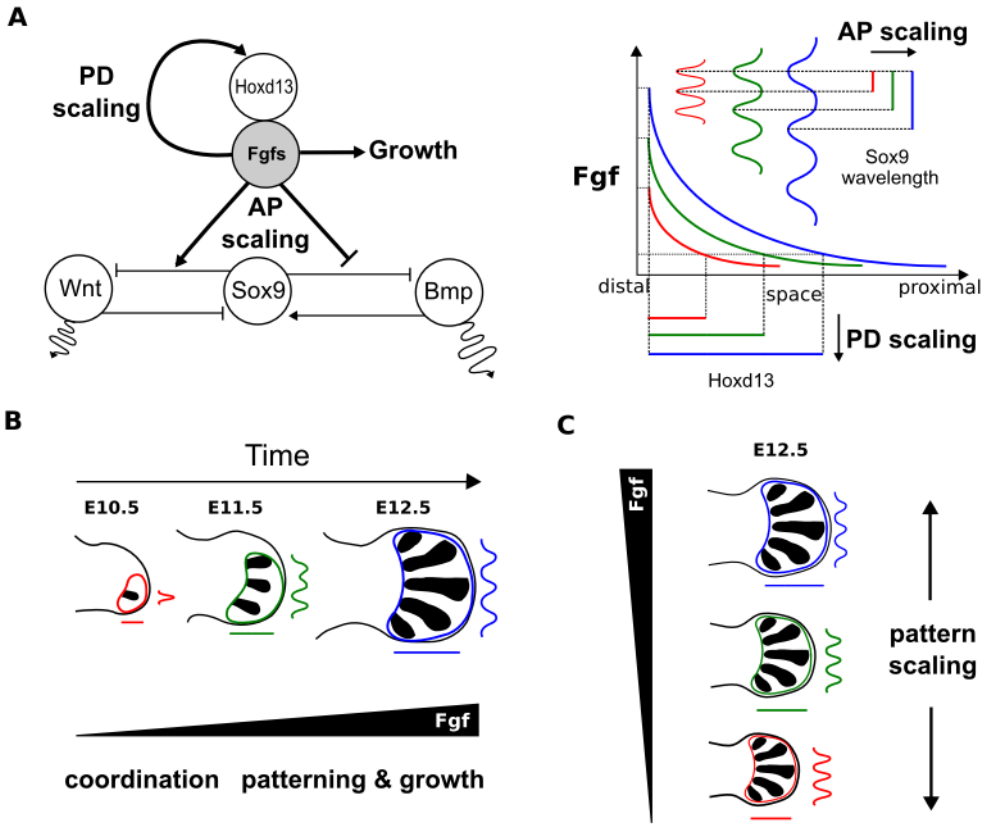

Figure 4.1: A) Left, a scheme summarizes the three roles of Fgfs proposed by previous work and by our model: Fgfs promote growth, they promote distal P-D markers (E.g Hoxd13) and they promote a larger wavelength by modulating the Turing network. Right, according to these roles, when increasingly stronger Fgf-signaling gradient are considered (red weak, green medium, blue strong) the digit pattern scales simultaneously along the A-P (bigger-wavelength) and along the P-D (more extended Hoxd13). This suggests that Fgfs orchestrates patterning and growth. B) Our simulations suggest that patterning and growth are coordinated by progressively stronger Fgf-signaling during limb development. C) Modulations of Fgfs to control both growth and AP-PD patterning is a perfect strategy to maintain proportions and scale the digit patterns across embryos of different sizes.

was achieved by coupling the interpretation of independent Positional Information systems, see Figure 1.14. Intriguingly, according to our model, in the limb the proportions are maintained by considering two different interpretation mechanisms under the same Positional Information gradient, the Fgf-signaling. On one side, the Fgf-signaling acts as as a positional information gradient for a simple threshold-response mechanism that regulates the expression of Hoxd13 and therefore the digital region. On the other side, the Fgf-signaling gradient modulates the wavelength of an interpretation mechanism based on a Turing model. In this way, a simple regionalization along the Proximal-Distal (P-D) axis and more complex isomorphic pattern along the Anterior- Posterior (A-P) axis are coordinated by the same signaling gradient which also controls growth. The final pattern, not only is simultaneously scaled along the P-D and the A-P axis as the signaling gradient changes (see Figure 4.1A), but it is also arranged in a extremely reproducible radial manner along the two axis. Furthermore, as shown in section 3.3.6, this radial disposition is extremely robust to noise. Obtaining these stereotypical curved digit morphologies with a more classical threshold-response Positional Information system would required a large number of gradients and a very complex set of interpretation rules.

This study not only explored the mechanism that underlie the coordination between growth and patterning, but it also helped to identify which molecules implement the Turing network. A key strategy to identify the Turing molecules was to restrict the possible candidates by defining temporal and spatial constrains. Firstly we ensured that candidate molecules were patterned as soon as the skeletal marker Sox9 showed a digital pattern. Secondly, a mathematical analysis determined which topologies and which spatial patterns were compatible with the formation of a Turing pattern. By comparing these constraints with descriptive and functional experiments we provide evidence that Bmps, Sox9 and Wnts form the Turing network that controls digit patterning. Our study reveals the main feedbacks involved in digit patterning, however other regulatory links could confer extra redundancy or robustness to the system. For example it is well known that ligands of the Tgf-β family can form homo and hetero-dimers [Lin et al., 2006] which may confer extra specificity to their signaling. In addition, other diffusible molecules like Activin and Tgf-βs can modulate Smad-signaling during chondrogenesis [Montero et al., 2008]. These complex signaling dynamics may underlie the non-trivial redundancy between Bmp2, Bmp4 and Bmp7 that leads the loss of only the posterior digits in Bmp2/4 double mutants and in syndactyly/polydactyly in the case of Bmp4/7 and Bmp2/7 double mutants [Bandyopadhyay et al., 2006].

Our network also suggests a mechanistic link between the molecular patterning of the digits and the onset of mesenchymal condensations. It is known that complexes between Beta-catenin and cadherins at the cell wall promote mesenchymal condensations [Hülsken et al., 1994, Kemler, 1993], but the frequency

of these complexes is reduced in response to Wnt signaling [Bienz, 2005]. The Bmp-Sox9-Wnt Turing network forms a periodic pattern where Wnt-signaling activity is higher in the interdigital tissue. This suggests that together with the specification of the digits a rapid difference in adhesivity between digital and interdigital cells may develop to drive the formation of digital condensations.

4.1 Limitations of the models and future directions

An obvious limitation of the models presented in this thesis is their high abstraction level. A considerable part of my work has been to create a more realistic Turing model made of a three-reactant Turing network with a non-diffusible component (Sox9). Several further improvements can be introduced to make the model more realistic, but while they will be extremely useful to elucidate the molecular basis the Turing mechanisms, they will also prevent most analytical approaches. A key aspect to further improve the model will be to find the best trade-off between introducing additional details and having a model that can be managed analytically.

Nevertheless, if we just concentrate on the possible extension that can make a Turing model more realistic, we can envision many different possibilities. If we take for example a simple Activator-Inhibitor model (AI), showed in Figure 4.2A, a number of alternative implementation can be imagined.

A first extension can be formulated by considering that, although most Turing models (including those developed in this study) abstract cell-communication with a simple diffusion process, most biological systems implement cell to cell communication with cell signaling. Therefore, a more realistic AI model can be formulated by considering ligand-receptor dynamics. This would require modeling the production of ligands inside the cells, their transport to the external environment and they binding with receptors to trigger a specific signaling cascade on another cells. Such changes could be implemented by transforming the AI network presented in 4.2A into the network showed in the left part of Figure 4.2B. The model requires at least six reactants: two diffusible signaling molecules u_{out}, v_{out}, two transcription factors u_{in}, v_{in} and two receptors RU, RV. The free diffusion of u and v across the cells, which approximates the developmental field as a continuum, is substituted with extracellular diffusion and cell-signaling mediated by the ligands u_{out}, v_{out} and their receptors RU, RV. The signaling promotes expression of the transcription factors u_{in}, v_{in} that interact in way that mirrors the classic AI model.

This new formulation increases the complexity of model but at the same time opens a whole new set of possible implementations for the main feedbacks of the Turing network. For example, an alternative implementation for the auto-

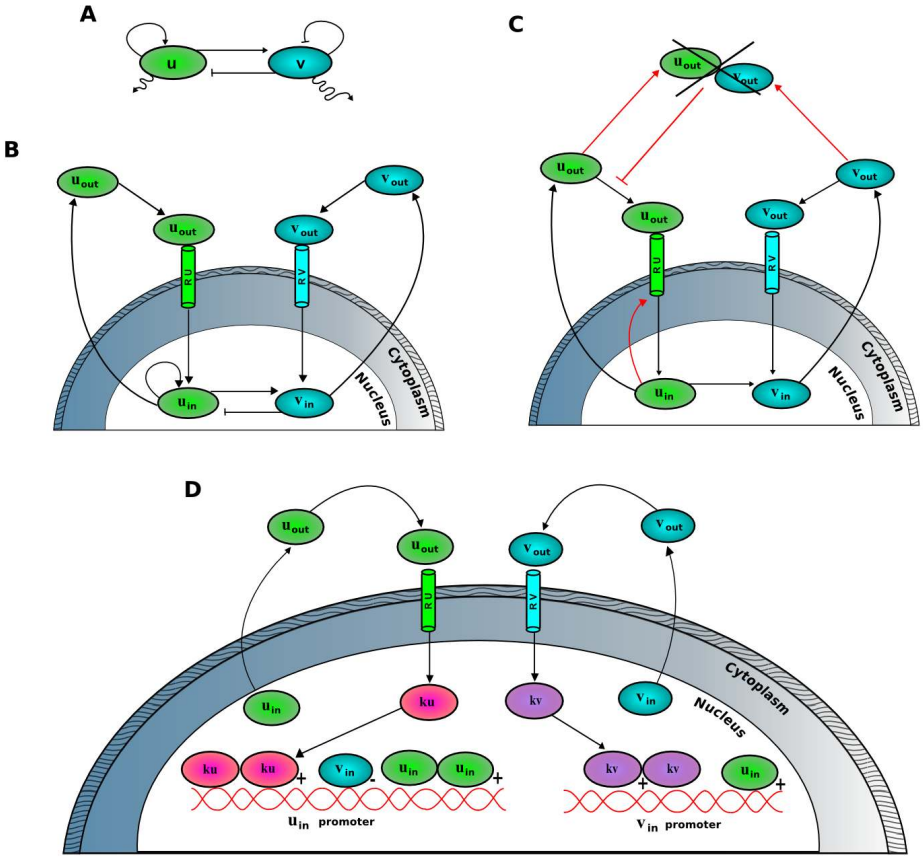

Figure 4.2: A) A schematic representation of the classic Activator-Inhibitor model: the activator (u) activates its inhibitor (v), cell communication is implemented by the free diffusion of u and v between cells. B) An extension to the classic Activator-Inhibitor model to consider ligand-receptor dynamics: the freely diffusible molecules u and v are replaced with two non-diffusible transcription factors (u_{in}, v_{in}) and two diffusible ligands (u_{out}, v_{out}), cell-communication is triggered when ligands bind to the correspondent receptors (RU, RV). C) Another possible implementation for an Activator-Inhibitor model with ligand-receptor dynamics: the autoactivation of u is implemented by the positive feedback between u_{in} and RU, the negative feedback of v on u is implemented by the sequestration of u_{out} when it is bound with v_{out}. D) It has been proposed that models with high cooperativity can form a Turing pattern even when the diffusion constants are very similar [Engelhardt, 2001]. Following this idea, the formulation of Activator-Inhibitor model with ligand-receptor dynamics can be extended to consider cooperativity between the molecules ku and kv that regulates u_{in}, v_{in} at the promoter level.

activation of u can be achieved by a positive feedback on the receptor and the inhibition of u can be obtained with sequestration of u_{out} by v_{out} (assuming that $v_{out} \gg u_{out}$), see Figure 4.2C. Very few example of Turing models that explicitly consider ligand-receptor dynamics can be found in literature [Klika et al., 2012, Rauch and Millonas, 2004] and none of them has been confirmed experimentally.

Another alternative to the classic AI model can be formulated by considering that in real biological systems the difference between the diffusion of the two ligands u_{out}, v_{out} is limited by the fact that most signaling molecules have comparable diffusion coefficients. In this case, following the study presented in [Engelhardt, 2001] we may imagine that the conditions that are required for a diffusion-driven instability can be achieved by high cooperativity in the regulation terms rather than a big difference in diffusion constants. High cooperativity levels could be obtained by explicitly representing the regulation of u_{in}, v_{in} at the promoter level. Additional reactants, for example the kinases ku and kv, could act in a synergistic manner to regulate the production of u_{in}, v_{in}, see Figure 4.2D. Modeling this process would introduce regulation terms with higher non-linearities that allow to obtain a diffusion-driven instability even with smaller differences between the diffusion coefficients.

Ligand-receptor dynamics is not the only alternative to the communication based on free diffusion across cells. Another possibility is to consider direct cell to cell communications. Very recently, it has been showed that in the limb Sonic Hedge Hog (Shh) is diffused by active transport between cells [Sanders et al., 2013] trough filopodia contacts that are established between mesenchymal cells. An alternative implementation to the ligand-receptor signaling can be therefore formulated by considering a systems where the diffusion of u_{out}, v_{out} is substituted by a propagating cascade of cell to cell communications, see Figure 4.3. This alternative implementation opens interesting possibilities because it provides a plausible biological basis for the regulation of the communication processes. For example, it is easier to imagine that the different communication range required to form a Turing pattern could be effectively implemented by a difference in filopodia extension rather than a difference in diffusion coefficients. Another interesting possibility is that cells can be polarized and can protrude the filopodia in a preferential direction. This implies that the communication process can happen along one preferential direction which will ultimately reduce to a Turing models with anisotropic diffusion. Various two-dimensional numerical studies [Bose and Chaudhuri, 1997, Shoji and Iwasa, 2003] revealed that Turing models with anisotropic diffusion exhibit interesting properties like the ability to orient the stripes in a specific direction.

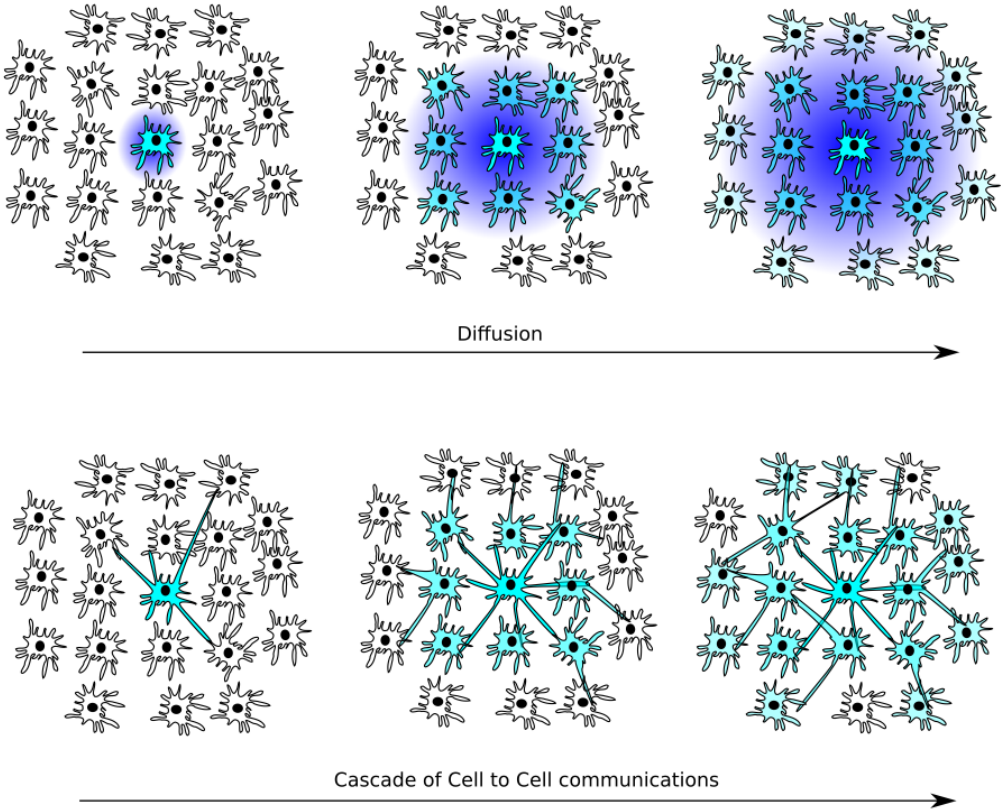

Figure 4.3: First row: an example of free diffusion between cells, a cell in the center (light blue cell) diffuses a signal (blue) that spreads over the developmental field and is received by the other cells. Second row: an example of direct cell to cell communication, a cell in the center (light blue cell) communicates with its neighbors by extending filopodia, the neighbors propagate the signal by protruding filopodia. Eventually, the signal spreads over the developmental field.

The alternative implementations discussed above all require cells to be explicatively represented in the model. While this is indeed extremely useful to investigate the cellular behaviors that can affect a Turing mechanism, it also requires a simulation formalism that models the tissue at the cellular level. Finite element simulations like those presented in this study, usually consider that each triangle represents a piece of tissue which contains a number cells. Modeling single cells requires the use of another formalism, for example the Cellular-Potts model [Graner and Glazier, 1992] or physical models based on strings [Weliky and Oster, 1990]. These model have been used with success to model developmental systems with epithelium-like tissues where cells were densely packed in grid conformation. However, to the best of my knowledge there is no formalism that has been proposed to explicitly represents mesenchymal cells that can protrude filopodia and can mix with their neighbors.

Another limitation of the Morphodynamic model presented in this study is that the patterning events do not feedback into the growth model. In section 1.2.1, I showed that in a full Morphodynamic system, morphogenesis and patterning can feedback into each other. In the Morphodynamic model presented in this study, I used an accurate limb growth model derived from clonal data and experimental limb morphologies. This growth model allowed me to explore the influence of morphogenetic events on the patterning system and in particular to explore how the Turing model behaved when the limb was growing. However, it did not allow me to explore the opposite influence, that is how the patterning system could affect growth. This is due to the fact that the limb growth model was given in input to the patterning simulation as a fixed growth map (the MorphoMovie). To consider a complete Morphodynamic model, it would be necessary to develop a real dynamic simulation of limb growth that would be executed in parallel to the patterning process.

This type of model will also be crucial to investigate the mechanism of scale-invariance and maintenance of proportion that have emerged from this study.

4.2 Conclusions

In summary, this study has presented a possible implementation for some of the hypothesis that have been proposed to explain limb development in the last thirty years. In particular, it has addressed three main points: i) it has shown a possible way in which the Positional Information model can be combined with a Turing mechanism to specify the digits, ii) it has proposed a way to coordinate digit patterning and limb growth to achieve scale-invariance and maintenance of proportions, iii) together with the experimental work of Jelena Raspopovic, it has identified the main genes that implement the Turing network and the Positional

Information that drive digit patterning.

A common theme behind these topics has been the use of computational modeling, which has mainly served as a modern version of a classic cartoon of developmental biology rather than a tool to make quantitative predictions. The models presented in this work do not pretend to be an exhaustive representation of reality, as Turing once said, models are "a simplification and an idealization, and consequently a falsification"[Turing, 1952]. It is a common misconception nowadays to consider that computational models have to be able to make extremely precise quantitative predictions in order to be useful. This study has showed that models can also be extremely useful to formulate formal qualitative descriptions of our hypothesis, which in contrast to cartoons and descriptions in natural language can be evaluated and confuted with simulations.

To conclude, it is often quoted that our assumptions are as good as our data and I like to think that in the near future it will be quite common to say that our hypotheses are as good as our models.

Bibliography

Abu-Arish, A., Porcher, A., Czerwonka, A., Dostatni, N., and Fradin, C. (2010). High mobility of bicoid captured by fluorescence correlation spectroscopy: implication for the rapid establishment of its gradient. *Biophysical journal*, 99(4):L33–L35.

Ahn, K., Mishina, Y., Hanks, M. C., Behringer, R. R., and Crenshaw, E. B. (2001). Bmpr-ia signaling is required for the formation of the apical ectodermal ridge and dorsal-ventral patterning of the limb. *Development*, 128(22):4449–4461.

Akam, M. (1987). The molecular basis for metameric pattern in the drosophila embryo. *Development*, 101(1):1–22.

Akiyama, H. (2008). Control of chondrogenesis by the transcription factor sox9. *Modern Rheumatology*, 18(3):213–219.

Akiyama, H., Chaboissier, M.-C., Martin, J. F., Schedl, A., and de Crombrugghe, B. (2002). The transcription factor sox9 has essential roles in successive steps of the chondrocyte differentiation pathway and is required for expression of sox5 and sox6. *Genes and development*, 16(21):2813–2828.

Akiyama, H., Kim, J.-E., Nakashima, K., Balmes, G., Iwai, N., Deng, J. M., Zhang, Z., Martin, J. F., Behringer, R. R., Nakamura, T., et al. (2005). Osteochondroprogenitor cells are derived from sox9 expressing precursors. *Proceedings of the National Academy of Sciences of the United States of America*, 102(41):14665–14670.

Akiyama, H., Lyons, J. P., Mori-Akiyama, Y., Yang, X., Zhang, R., Zhang, Z., Deng, J. M., Taketo, M. M., Nakamura, T., Behringer, R. R., et al. (2004). Interactions between sox9 and beta-catenin control chondrocyte differentiation. *Genes and development*, 18(9):1072–1087.

Akiyama, H., Stadler, H. S., Martin, J. F., Ishii, T. M., Beachy, P. A., Nakamura, T., and de Crombrugghe, B. (2007). Misexpression of sox9 in mouse limb

bud mesenchyme induces polydactyly and rescues hypodactyly mice. *Matrix biology*, 26(4):224–233.

Alber, M., Glimm, T., Hentschel, H., Kazmierczak, B., Zhang, Y.-T., Zhu, J., and Newman, S. A. (2008). The morphostatic limit for a model of skeletal pattern formation in the vertebrate limb. *Bulletin of mathematical biology*, 70(2):460–483.

Arques, C. G., Doohan, R., Sharpe, J., and Torres, M. (2007). Cell tracing reveals a dorsoventral lineage restriction plane in the mouse limb bud mesenchyme. *Development*, 134(20):3713–3722.

Badugu, A., Kraemer, C., Germann, P., Menshykau, D., and Iber, D. (2012). Digit patterning during limb development as a result of the bmp-receptor interaction. *Scientific reports*, 2.

Balaskas, N., Ribeiro, A., Panovska, J., Dessaud, E., Sasai, N., Page, K. M., Briscoe, J., and Ribes, V. (2012). Gene regulatory logic for reading the sonic hedgehog signaling gradient in the vertebrate neural tube. *Cell*, 148(1):273–284.

Balme, D. M. (2002). *Historia Animalium: Text*. Number v. 1, bks. 1-10 in Cambridge classical texts and commentaries. Cambridge University Press.

Bandyopadhyay, A., Tsuji, K., Cox, K., Harfe, B. D., Rosen, V., and Tabin, C. J. (2006). Genetic analysis of the roles of bmp2, bmp4, and bmp7 in limb patterning and skeletogenesis. *PLoS genetics*, 2(12):e216.

Barna, M. and Niswander, L. (2007). Visualization of cartilage formation: insight into cellular properties of skeletal progenitors and chondrodysplasia syndromes. *Developmental cell*, 12(6):931–941.

Barrio, R. A., Varea, C., Aragón, J. L., and Maini, P. K. (1999). A Two-dimensional Numerical Study of Spatial Pattern Formation in Interacting Turing Systems. *Bull. Math. Biol.*, 61:483–505.

Barrow, J. R., Thomas, K. R., Boussadia-Zahui, O., Moore, R., Kemler, R., Capecchi, M. R., and McMahon, A. P. (2003). Ectodermal wnt3/beta-catenin signaling is required for the establishment and maintenance of the apical ectodermal ridge. *Genes and development*, 17(3):394–409.

Bastida, M. F., Sheth, R., and Ros, M. A. (2009). A bmp-shh negative-feedback loop restricts shh expression during limb development. *Development*, 136(22):3779–3789.

Becker, P. and Field, R. J. (1985). Stationary concentration patterns in the oregonator model of the belousov-zhabotinsky reaction. *J. Phys. Chem.*, (89):118–28.

Belousov, B. P. (1959). Periodically acting reaction and its mechanism. *Collection of Abstracts on Radiation Medicine*, (147):145.

Bénazéraf, B., Francois, P., Baker, R. E., Denans, N., Little, C. D., and Pourquié, O. (2010). A random cell motility gradient downstream of fgf controls elongation of an amniote embryo. *Nature*, 466(7303):248–252.

Bénazet, J.-D., Bischofberger, M., Tiecke, E., Gonçalves, A., Martin, J. F., Zuniga, A., Naef, F., and Zeller, R. (2009). A self-regulatory system of interlinked signaling feedback loops controls mouse limb patterning. *Science*, 323(5917):1050–1053.

Bénazet, J.-D., Pignatti, E., Nugent, A., Unal, E., Laurent, F., and Zeller, R. (2012). Smad4 is required to induce digit ray primordia and to initiate the aggregation and differentiation of chondrogenic progenitors in mouse limb buds. *Development*, 139(22):4250–4260.

Bienz, M. (2005). Beta-catenin: a pivot between cell adhesion and wnt signalling. *Current Biology*, 15(2):R64–R67.

Boehm, B., Rautschka, M., Quintana, L., Raspopovic, J., Jan, Ž., and Sharpe, J. (2011). A landmark-free morphometric staging system for the mouse limb bud. *Development*, 138(6):1227–1234.

Boehm, B., Westerberg, H., Lesnicar-Pucko, G., Raja, S., Rautschka, M., Cotterell, J., Swoger, J., and Sharpe, J. (2010). The role of spatially controlled cell proliferation in limb bud morphogenesis. *PLoS biology*, 8(7):e1000420.

Bose, I. and Chaudhuri, I. (1997). Effect of randomness and anisotropy on turing patterns in reaction-diffusion systems. *Physical Review E*, 55(5):5291–5296.

Boulet, A. M., Moon, A. M., Arenkiel, B. R., and Capecchi, M. R. (2004). The roles of fgf4 and fgf8 in limb bud initiation and outgrowth. *Developmental biology*, 273(2):361–372.

Capellini, T. D., Di Giacomo, G., Salsi, V., Brendolan, A., Ferretti, E., Srivastava, D., Zappavigna, V., and Selleri, L. (2006). Pbx1/pbx2 requirement for distal limb patterning is mediated by the hierarchical control of hox gene spatial distribution and shh expression. *Development*, 133(11):2263–2273.

Carkett, M., Logan, M., et al. (2011). 1, 2, 3: Counting the fingers on a chicken wing. *Genome biology*, 12(10):130.

Chaturvedi, R., Huang, C., Izaguirre, J., Newman, S., Glazier, J., and Alber, M. (2004). A hybrid discrete-continuum model for 3-d skeletogenesis of the vertebrate limb. *Cellular Automata*, pages 543–552.

Chiang, C., Litingtung, Y., Harris, M. P., Simandl, B. K., Li, Y., Beachy, P. A., and Fallon, J. F. (2001). Manifestation of the limb prepattern: limb development in the absence of sonic hedgehog function. *Developmental biology*, 236(2):421–435.

Child, C. M. (1941). Patterns and problems of development.

Chimal-Monroy, J., Rodriguez-Leon, J., Montero, J., Ganan, Y., Macias, D., Merino, R., and Hurle, J. (2003). Analysis of the molecular cascade responsible for mesodermal limb chondrogenesis: sox genes and bmp signaling. *Developmental biology*, 257(2):292–301.

Christley, S., Alber, M. S., and Newman, S. A. (2007). Patterns of mesenchymal condensation in a multiscale, discrete stochastic model. *PLoS computational biology*, 3(4):e76.

Cickovski, T. M., Huang, C., Chaturvedi, R., Glimm, T., Hentschel, H. G. E., Alber, M. S., Glazier, J. A., Newman, S. A., and Izaguirre, J. A. (2005). A framework for three-dimensional simulation of morphogenesis. *Computational Biology and Bioinformatics, IEEE/ACM Transactions on*, 2(4):273–288.

Cohn, M. J. (2000). Developmental biology: Giving limbs a hand. *Nature*, 406(6799):953–954.

Cottrill, C. P., Archer, C. W., and Wolpert, L. (1987). Cell sorting and chondrogenic aggregate formation in micromass culture. *Developmental biology*, 122(2):503–515.

Crampin, E. J., Gaffney, E. A., and Maini, P. K. (1999). Reaction and diffusion on growing domains: scenarios for robust pattern formation. *Bulletin of mathematical biology*, 61(6):1093–1120.

Dahn, R. D. and Fallon, J. F. (2000). Interdigital regulation of digit identity and homeotic transformation by modulated bmp signaling. *Science*, 289(5478):438–441.

D'Arcy, W. T. (1963). *On growth and form*. Cambridge Univ Press.

Davey, M., Paton, I., Yin, Y., Schmidt, M., Bangs, F., Morrice, D., Smith, T., Buxton, P., Stamataki, D., Tanaka, M., et al. (2006). The chicken talpid3 gene

encodes a novel protein essential for hedgehog signaling. *Genes and development*, 20(10):1365–1377.

Day, T. F., Guo, X., Garrett-Beal, L., and Yang, Y. (2005). Wnt/β-catenin signaling in mesenchymal progenitors controls osteoblast and chondrocyte differentiation during vertebrate skeletogenesis. *Developmental cell*, 8(5):739–750.

De Kepper, P., Castets, V., Dulos, E., and Boissonade, J. (1991). Turing-type chemical patterns in the chlorite-iodide-malonic acid reaction. *Physica D: Nonlinear Phenomena*, 49(1):161–169.

De Lachapelle, A. M. and Bergmann, S. (2010). Precision and scaling in morphogen gradient read-out. *Molecular systems biology*, 6(1).

Delise, A. M. and Tuan, R. S. (2002). Analysis of n-cadherin function in limb mesenchymal chondrogenesis in vitro. *Developmental dynamics*, 225(2):195–204.

Dillon, R., Maini, P., and Othmer, H. (1994). Pattern formation in generalized turing systems. *Journal of Mathematical Biology*, 32(4):345–393.

Dillon, R. and Othmer, H. G. (1999). A mathematical model for outgrowth and spatial patterning of the vertebrate limb bud. *Journal of theoretical biology*, 197(3):295–330.

Drocco, J. A., Grimm, O., Tank, D. W., and Wieschaus, E. (2011). Measurement and perturbation of morphogen lifetime: effects on gradient shape. *Biophysical journal*, 101(8):1807–1815.

Dudley, A. T., Ros, M. A., and Tabin, C. J. (2002). A re-examination of proximodistal patterning during vertebrate limb development. *Nature*, 418(6897):539–544.

Duprez, D., Coltey, M., Amthor, H., Brickell, P., and Tickle, C. (1996). Bone morphogenetic protein-2 (bmp-2) inhibits muscle development and promotes cartilage formation in chick limb bud cultures. *Developmental biology*, 174(2):448–452.

Ede, D. and Law, J. (1969). Computer simulation of vertebrate limb morphogenesis. *Nature*, 221(5177):244.

Engelhardt, R. (2001). High cooperativity as origin of pattern complexity. *Modeling in Biotechnology*, pages 263–267.

Field, R. J. and Noyes, R. M. (1974). Oscillations in chemical systems. IV. Limit cycle behavior in a model of a real chemical reaction. *J. Chem. Phys.*, 60:8.

Fitzhugh, R. (1961). Impulses and Physiological States in Theoretical Models of Nerve Membrane. *Biophysical Journal*, 1(6):445–466.

Frohnhöfer, H. G. and Nüsslein-Volhard, C. (1986). Organization of anterior pattern in the drosophila embryo by the maternal gene bicoid. *Nature*, 324:120–125.

Fromental-Ramain, C., Warot, X., Messadecq, N., LeMeur, M., Dollé, P., and Chambon, P. (1996). Hoxa-13 and hoxd-13 play a crucial role in the patterning of the limb autopod. *Development*, 122(10):2997–3011.

Galloway, J. L., Delgado, I., Ros, M. A., and Tabin, C. J. (2009). A reevaluation of x-irradiation-induced phocomelia and proximodistal limb patterning. *Nature*, 460(7253):400–404.

Ganan, Y., Macias, D., Duterque-Coquillaud, M., Ros, M., and Hurle, J. (1996). Role of tgf beta s and bmps as signals controlling the position of the digits and the areas of interdigital cell death in the developing chick limb autopod. *Development*, 122(8):2349–2357.

Geduspan, J. S. and MacCabe, J. A. (1987). The ectodermal control of mesodermal patterns of differentiation in the developing chick wing. *Developmental biology*, 124(2):398–408.

Geduspan, J. S. and Maccabe, J. A. (1989). Transfer of dorsoventral information from mesoderm to ectoderm at the onset of limb development. *The Anatomical Record*, 224(1):79–87.

Gibson-Brown, J. J., Agulnik, S. I., Chapman, D. L., Alexiou, M., Garvey, N., Lee, S. M., and Papaioannou, V. E. (1996). Evidence of a role for t-box genes in the evolution of limb morphogenesis and the specification of forelimb/hindlimb identity. *Mechanisms of development*, 56(1):93–101.

Gierer, A. (1981). Generation of biological patterns and form: some physical, mathematical, and logical aspects. *Prog Biophys Mol Biol*, 37(1):1–47.

Gierer, A. and Meinhardt, H. (1972). A theory of biological pattern formation. *Biological Cybernetics*, 12(1):30–39.

Gimp (1). The gnu image manipulation program. `http://www.gimp.org/`.

Graner, F. and Glazier, J. A. (1992). Simulation of biological cell sorting using a two-dimensional extended potts model. *Physical review letters*, 69(13):2013.

Gray, P. and Scott, S. K. (1985). Sustained oscillations and other exotic patterns of behavior in isothermal reactions. *J.Phys.Chem.*, 89:22.

Gregor, T., Bialek, W., van Steveninck, R. R. d. R., Tank, D. W., and Wieschaus, E. F. (2005). Diffusion and scaling during early embryonic pattern formation. *Proceedings of the National Academy of Sciences of the United States of America*, 102(51):18403–18407.

Grigoryan, T., Wend, P., Klaus, A., and Birchmeier, W. (2008). Deciphering the function of canonical wnt signals in development and disease: conditional loss- and gain-of-function mutations of β-catenin in mice. *Genes and development*, 22(17):2308–2341.

Grima, R. (2008). Multiscale modeling of biological pattern formation. *Current topics in developmental biology*, 81:435–460.

Gros, J., Hu, J. K.-H., Vinegoni, C., Feruglio, P. F., Weissleder, R., and Tabin, C. J. (2010). Wnt5a/jnk and fgf/mapk pathways regulate the cellular events shaping the vertebrate limb bud. *Current Biology*, 20(22):1993–2002.

Grüneberg, H. (1951). Embryos and ancestors. revised edition, 1951. *The Eugenics Review*, 43(3):155.

Hardin, P. E. (2005). The circadian timekeeping system of Drosophila. *Current biology : CB*, 15(17).

Harfe, B. D., Scherz, P. J., Nissim, S., Tian, H., McMahon, A. P., and Tabin, C. J. (2004). Evidence for an expansion-based temporal shh gradient in specifying vertebrate digit identities. *Cell*, 118(4):517–528.

Hens, J. R., Wilson, K. M., Dann, P., Chen, X., Horowitz, M. C., and Wysolmerski, J. J. (2005). Topgal mice show that the canonical wnt signaling pathway is active during bone development and growth and is activated by mechanical loading in vitro. *Journal of Bone and Mineral Research*, 20(7):1103–1113.

Hentschel, H., Glimm, T., Glazier, J. A., and Newman, S. A. (2004). Dynamical mechanisms for skeletal pattern formation in the vertebrate limb. *Proceedings of the Royal Society B: Biological Sciences*, 271(1549):1713.

Hill, T. P., Später, D., Taketo, M. M., Birchmeier, W., and Hartmann, C. (2005). Canonical wnt/β-catenin signaling prevents osteoblasts from differentiating into chondrocytes. *Developmental cell*, 8(5):727–738.

Hornbruch, A. and Wolpert, L. (1970). Cell division in the early growth and morphogenesis of the chick limb. *Nature*, 226(5247):764.

Hörstadius, S. (1936). Weitere studien über die determination im verlaufe der eiachse bei seeigeln. *Development Genes and Evolution*, 135(1):40–68.

Houchmandzadeh, B., Wieschaus, E., and Leibler, S. (2002). Establishment of developmental precision and proportions in the early drosophila embryo. *Nature*, 415(6873):798–802.

Houchmandzadeh, B., Wieschaus, E., and Leibler, S. (2005). Precise domain specification in the developing drosophila embryo. *Physical Review E*, 72(6):061920.

Hu, H., Hilton, M. J., Tu, X., Yu, K., Ornitz, D. M., and Long, F. (2005). Sequential roles of hedgehog and wnt signaling in osteoblast development. *Development*, 132(1):49–60.

Hülsken, J., Birchmeier, W., and Behrens, J. (1994). E-cadherin and apc compete for the interaction with beta-catenin and the cytoskeleton. *The Journal of Cell Biology*, 127(6):2061–2069.

Ingham, P. (1988). The molecular genetics of embryonic pattern formation in drosophila.

Iron, D., Wei, J., and Winter, M. (2004). Stability analysis of turing patterns generated by the schnakenberg model. *Journal of mathematical biology*, 49(4):358–390.

Izaguirre, J. A., Chaturvedi, R., Huang, C., Cickovski, T., Coffland, J., Thomas, G., Forgacs, G., Alber, M., Hentschel, G., Newman, S. A., et al. (2004). Compucell, a multi-model framework for simulation of morphogenesis. *Bioinformatics*, 20(7):1129–1137.

Jaeger, J. (2011). The gap gene network. *Cellular and Molecular Life Sciences*, 68(2):243–274.

Jaeger, J. and Martinez-Arias, A. (2009). Getting the measure of positional information. *PLoS biology*, 7(3):e1000081.

JavaMorph (1). Picture merging by interpolated deformation. `http://code.google.com/p/javamorph/`.

Johnston, D. S., Driever, W., Berleth, T., Richstein, S., and Nüsslein-Volhard, C. (1989). Multiple steps in the localization of bicoid rna to the anterior pole of the drosophila oocyte. *Development*, 107(Supplement):13–19.

Johnston, D. S. and Nüsslein-Volhard, C. (1992). The origin of pattern and polarity in the drosophila embryo. *Cell*, 68(2):201–219.

Kawakami, Y., Capdevila, J., Buscher, D., Itoh, T., Esteban, C. R., and Belmonte, J. C. I. (2001). Wnt signals control fgf-dependent limb initiation and aer induction in the chick embryo. *Cell*, 104(6):891–900.

Keller, P. J. (2013). Imaging morphogenesis: Technological advances and biological insights. *Science*, 340(6137).

Kemler, R. (1993). From cadherins to catenins: cytoplasmic protein interactions and regulation of cell adhesion. *Trends in Genetics*, 9(9):317–321.

Kerner, B. S. and Osipov, V. V. (1994). *Autosolitons: A New Approach to Problems of Self-Organization and Turbulence*. Fundamental Theories of Physics. Springer.

Kerszberg, M. and Wolpert, L. (2007). Specifying positional information in the embryo: looking beyond morphogens. *Cell*, 130(2):205–209.

Khokha, M. K., Hsu, D., Brunet, L. J., Dionne, M. S., and Harland, R. M. (2003). Gremlin is the bmp antagonist required for maintenance of shh and fgf signals during limb patterning. *Nature genetics*, 34(3):303–307.

Kiskowski, M. A., Alber, M. S., Thomas, G. L., Glazier, J. A., Bronstein, N. B., Pu, J., and Newman, S. A. (2004). Interplay between activator-inhibitor coupling and cell-matrix adhesion in a cellular automaton model for chondrogenic patterning. *Developmental biology*, 271(2):372–387.

Klika, V., Baker, R. E., Headon, D., and Gaffney, E. A. (2012). The influence of receptor-mediated interactions on reaction-diffusion mechanisms of cellular self-organisation. *Bulletin of mathematical biology*, 74(4):935–957.

Kondo, S. and Miura, T. (2010). Reaction-diffusion model as a framework for understanding biological pattern formation. *Science*, 329(5999):1616–1620.

Kraus, P., Fraidenraich, D., and Loomis, C. A. (2001). Some distal limb structures develop in mice lacking sonic hedgehog signaling. *Mechanisms of development*, 100(1):45–58.

Kuchen, E. E., Fox, S., de Reuille, P. B., Kennaway, R., Bensmihen, S., Avondo, J., Calder, G. M., Southam, P., Robinson, S., Bangham, A., et al. (2012). Generation of leaf shape through early patterns of growth and tissue polarity. *Science*, 335(6072):1092–1096.

Leloup, J. C., Gonze, D., and Goldbeter, A. (1999). Limit Cycle Models for Circadian Rhythms Based on Transcriptional Regulation in Drosophila and Neurospora. *Biological Rhythms*, 14:433–448.

Leonard, C. M., Fuld, H. M., Frenz, D. A., Downie, S. A., Massague, J., and Newman, S. A. (1991). Role of transforming growth factor-beta in chondrogenic pattern formation in the embryonic limb: Stimulation of mesenchymal condensation and fibronectin gene expression by exogenenous tgf-beta and evidence for endogenous tgf-b-like activity. *Developmental biology*, 145(1):99–109.

Lewandoski, M., Sun, X., and Martin, G. R. (2000). Fgf8 signalling from the aer is essential for normal limb development. *Nature genetics*, 26(4):460–463.

Lewis, J. (1975). Fate maps and the pattern of cell division: a calculation for the chick wing-bud. *Journal of embryology and experimental morphology*, 33(2):419–434.

Lin, S. J., Lerch, T. F., Cook, R. W., Jardetzky, T. S., and Woodruff, T. K. (2006). The structural basis of tgf-beta, bone morphogenetic protein, and activin ligand binding. *Reproduction*, 132(2):179–190.

Litingtung, Y., Dahn, R. D., Li, Y., Fallon, J. F., and Chiang, C. (2002). Shh and gli3 are dispensable for limb skeleton formation but regulate digit number and identity. *Nature*, 418(6901):979–983.

Liu, J., He, F., and Ma, J. (2011). Morphogen gradient formation and action: insights from studying bicoid protein degradation. *Fly*, 5(3):242–246.

Liu, J. and Ma, J. (2010). Fates-shifted is an f-box protein that targets bicoid for degradation and regulates developmental fate determination in drosophila embryos. *Nature cell biology*, 13(1):22–29.

Logan, M. (2003). Finger or toe: the molecular basis of limb identity. *Development*, 130(26):6401–6410.

Loomis, C., Harris, E., Michaud, J., Wurst, W., Hanks, M., and Joyner, A. (1996). The mouse engrailed-1 gene and ventral limb patterning. *Nature*, 382(6589):360–363.

Lotka, A. J. (1910). Contribution to the Theory of Periodic Reactions. *The Journal of Physical Chemistry*, 14(3):271–274.

Lu, P., Minowada, G., and Martin, G. R. (2006). Increasing fgf4 expression in the mouse limb bud causes polysyndactyly and rescues the skeletal defects that result from loss of fgf8 function. *Development*, 133(1):33–42.

Maini, P. K. (1991). A comparison of reaction diffusion and mechanochemical models for limb development. In *Developmental Patterning of the Vertebrate Limb*, pages 161–163. Springer.

Maini, P. K., Benson, D. L., and Sherratt, J. A. (1992). Pattern formation in reaction-diffusion models with spatially inhomogeneous diffusion coefficients. *Mathematical Medicine and Biology*, 9(3):197–213.

Maini, P. K. and Solursh, M. (1991). ellular mechanisms of pattern formation in the developing limb. In *International Review of Cytology*, volume 129, pages 91–133.

Martin, G. R. (1998). The roles of fgfs in the early development of vertebrate limbs. *Genes and development*, 12(11):1571–1586.

Meinhardt, H. (1982). *Models of biological pattern formation*. Academic Press.

Meinhardt, H. (2004). Out-of-phase oscillations and traveling waves with unusual properties: the use of three-component systems in biology. *Physica D: Nonlinear Phenomena*, 199(1):264–277.

Menshykau, D., Kraemer, C., and Iber, D. (2012). Branch mode selection during early lung development. *PLoS computational biology*, 8(2):e1002377.

Mercader, N., Leonardo, E., Piedra, M. E., Martinez-A, C., Ros, M., and Torres, M. (2000). Opposing ra and fgf signals control proximodistal vertebrate limb development through regulation of meis genes. *Development*, 127(18):3961–3970.

Mercader, N., Selleri, L., Criado, L. M., Pallares, P., Parras, C., Cleary, M. L., and Torres, M. (2009). Ectopic meis1 expression in the mouse limb bud alters pd patterning in a pbx1-independent manner. *International Journal of Developmental Biology*, 53(8):1483.

Merino, R., Macias, D., Ganan, Y., Rodriguez-Leon, J., Economides, A., Rodriguez-Esteban, C., Izpisua-Belmonte, J., and Hurle, J. (1999). Control of digit formation by activin signalling. *Development*, 126(10):2161–2170.

Michos, O., Panman, L., Vintersten, K., Beier, K., Zeller, R., and Zuniga, A. (2004). Gremlin-mediated bmp antagonism induces the epithelial-mesenchymal feedback signaling controlling metanephric kidney and limb organogenesis. *Development*, 131(14):3401–3410.

Mikels, A. and Nusse, R. (2006). Wnts as ligands: processing, secretion and reception. *Oncogene*, 25(57):7461–7468.

Minguillon, C., Del Buono, J., and Logan, M. P. (2005). Tbx5 and tbx4 are not sufficient to determine limb-specific morphologies but have common roles in initiating limb outgrowth. *Developmental cell*, 8(1):75–84.

Miura, T. (2013). Turing and wolpert work together during limb development. *Science signaling*, 6(270):pe14.

Miura, T. and Maini, P. K. (2004). Speed of pattern appearance in reaction-diffusion models: implications in the pattern formation of limb bud mesenchyme cells. *Bulletin of mathematical biology*, 66(4):627–649.

Miura, T. and Shiota, K. (2000). Tgf acts as an activator molecule in reaction-diffusion model and is involved in cell sorting phenomenon in mouse limb micromass culture. *Developmental Dynamics*, 217(3):241–249.

Miura, T., Shiota, K., Morriss-Kay, G., and Maini, P. K. (2006). Mixed-mode pattern in doublefoot mutant mouse limb - turing reaction-diffusion model on a growing domain during limb development. *Journal of theoretical biology*, 240(4):562–573.

Montero, J. A., Lorda-Diez, C. I., Gañan, Y., Macias, D., and Hurle, J. M. (2008). Activin/tgf-beta and bmp crosstalk determines digit chondrogenesis. *Developmental biology*, 321(2):343–356.

Moon, A. M. and Capecchi, M. R. (2000). Fgf8 is required for outgrowth and patterning of the limbs. *Nature genetics*, 26(4):455–459.

Morisalo, D. and Anderson, K. V. (1995). Signaling pathways that establish the dorsal-ventral pattern of the drosophila embryo. *Annual review of genetics*, 29(1):371–399.

Morishita, Y. and Iwasa, Y. (2008). Growth based morphogenesis of vertebrate limb bud. *Bulletin of mathematical biology*, 70(7):1957–1978.

Moussian, B. and Roth, S. (2005). Dorsoventral axis formation in the drosophila embryo-shaping and transducing a morphogen gradient. *Current biology*, 15(21):R887–R899.

Murray, J. D. (1989). *Mathematical biology*. Biomathematics (Berlin). Springer London, Limited.

Murray, J. D. (2012). Vignettes from the field of mathematical biology: the application of mathematics to biology and medicine. *Interface Focus*, 2(4):397–406.

Murray, J. D., Maini, P., and Tranquillo, R. (1988). Mechanochemical models for generating biological pattern and form in development. *Physics Reports*, 171(2):59–84.

Murray, J. D. and Maini, P. K. (1989). Pattern formation mechanisms - a comparison of reaction diffusion and mechanochemical models.

Nahmad, M. and Stathopoulos, A. (2009). Dynamic interpretation of hedgehog signaling in the drosophila wing disc. *PLoS biology*, 7(9):e1000202.

Nelson, W. J. and Nusse, R. (2004). Convergence of wnt, beta-catenin, and cadherin pathways. *Science*, 303(5663):1483–1487.

Newman, S. A. (1996). Sticky fingers: Hox genes and cell adhesion in vertebrate limb development. *Bioessays*, 18(3):171–174.

Newman, S. A. and Frisch, H. (1979). Dynamics of skeletal pattern formation in developing chick limb. *Science*, 205(4407):662–668.

Nicolis, G. (1970). Thermodynamic theory of stability, structure and fluctuations. *Pure and Applied Chemistry*, (22):379–392.

Nicolis, G. and Prigogine, I. (1977). *Self-organization in nonequilibrium systems: from dissipative structures to order through fluctuations*. A Wiley-Interscience Publication. Wiley.

Niederreither, K., Subbarayan, V., Dollé, P., and Chambon, P. (1999). Embryonic retinoic acid synthesis is essential for early mouse post-implantation development. *Nature genetics*, 21(4):444–448.

Niederreither, K., Vermot, J., Schuhbaur, B., Chambon, P., and Dollé, P. (2002). Embryonic retinoic acid synthesis is required for forelimb growth and anteroposterior patterning in the mouse. *Development*, 129(15):3563–3574.

Nissim, S., Hasso, S. M., Fallon, J. F., and Tabin, C. J. (2006). Regulation of gremlin expression in the posterior limb bud. *Developmental biology*, 299(1):12–21.

Niswander, L. (2002). Interplay between the molecular signals that control vertebrate limb development. *International Journal of Developmental Biology*, 46(7):877–882.

Ochoa-Espinosa, A., Yu, D., Tsirigos, A., Struffi, P., and Small, S. (2009). Anterior-posterior positional information in the absence of a strong bicoid gradient. *Proceedings of the National Academy of Sciences*, 106(10):3823–3828.

Olsson, L. (2007). A clash of traditions: the history of comparative and experimental embryology in sweden as exemplified by the research of gösta jägersten and sven hörstadius. *Theory in Biosciences*, 126(4):117–129.

Oster, G. F., Murray, J. D., and Harris, A. (1983). Mechanical aspects of mesenchymal morphogenesis. *Journal of embryology and experimental morphology*, 78(1):83–125.

Ovchinnikov, D. A., Selever, J., Wang, Y., Chen, Y.-T., Mishina, Y., Martin, J. F., and Behringer, R. R. (2006). Bmp receptor type ia in limb bud mesenchyme regulates distal outgrowth and patterning. *Developmental biology*, 295(1):103–115.

Pan, Q., Yu, Y., Chen, Q., Li, C., Wu, H., Wan, Y., Ma, J., and Sun, F. (2008). Sox9, a key transcription factor of bone morphogenetic protein-2-induced chondrogenesis, is activated through bmp pathway and a ccaat box in the proximal promoter. *Journal of cellular physiology*, 217(1):228–241.

Parr, B. A. and McMahon, A. P. (1995). Dorsalizing signal wnt-7a required for normal polarity of d–v and a–p axes of mouse limb. *Nature*, 374(6520):350–353.

Parr, B. A., Shea, M. J., Vassileva, G., and McMahon, A. P. (1993). Mouse wnt genes exhibit discrete domains of expression in the early embryonic cns and limb buds. *Development*, 119(1):247–261.

Pearson, J. E. (1993). Complex patterns in a simple system. *Science*, 261:189.

Pizette, S. and Niswander, L. (2000). Bmps are required at two steps of limb chondrogenesis: formation of prechondrogenic condensations and their differentiation into chondrocytes. *Developmental biology*, 219(2):237–249.

Popławski, N. J., Swat, M., Scott Gens, J., and Glazier, J. A. (2007). Adhesion between cells, diffusion of growth factors, and elasticity of the aer produce the paddle shape of the chick limb. *Physica A: Statistical Mechanics and its Applications*, 373:521–532.

Porcher, A., Abu-Arish, A., Huart, S., Roelens, B., Fradin, C., and Dostatni, N. (2010). The time to measure positional information: maternal hunchback is required for the synchrony of the bicoid transcriptional response at the onset of zygotic transcription. *Development*, 137(16):2795–2804.

Porcher, A. and Dostatni, N. (2010). The bicoid morphogen system. *Current Biology*, 20(5):R249–R254.

Prigogine, I. and Lefever, R. (1968). Symmetry breaking instabilities in dissipative systems II. *J. Chem. Phys.*, 48(4):1695–1700.

Probst, S., Kraemer, C., Demougin, P., Sheth, R., Martin, G. R., Shiratori, H., Hamada, H., Iber, D., Zeller, R., and Zuniga, A. (2011). Shh propagates distal limb bud development by enhancing cyp26b1-mediated retinoic acid clearance via aer-fgf signalling. *Development*, 138(10):1913–1923.

Qian, H. and Murray, J. D. (2001). A simple method of parameter space determination for diffusion-driven instability with three species. *Appl. Math. Lett.*, 14(4):405–411.

Rauch, E. M. and Millonas, M. M. (2004). The role of trans-membrane signal transduction in turing-type cellular pattern formation. *Journal of theoretical biology*, 226(4):401–407.

Reinitz, J., Kosman, D., Vanario-Alonso, C. E., Sharp, D. H., et al. (1998). Stripe forming architecture of the gap gene system. *Developmental Genetics*, 23(1):11–27.

Riddle, R. D., Ensini, M., Nelson, C., Tsuchida, T., Jessell, T. M., and Tabin, C. (1995). Induction of the lim homeobox gene lmx1 by wnt6a establishes dorsoventral pattern in the vertebrate limb. *Cell*, 83(4):631–640.

Riddle, R. D., Johnson, R. L., Laufer, E., and Tabin, C. (1993). Sonic hedgehog mediates the polarizing activity of the zpa. *Cell*, 75(7):1401–1416.

Robert, B. (2007). Bone morphogenetic protein signaling in limb outgrowth and patterning. *Development, growth & differentiation*, 49(6):455–468.

Rolland-Lagan, A.-G., Bangham, J. A., and Coen, E. (2003). Growth dynamics underlying petal shape and asymmetry. *Nature*, 422(6928):161–163.

Ros, M. A., López-Martínez, A., Simandl, B. K., Rodriguez, C., Belmonte, J. I., Dahn, R., and Fallon, J. F. (1996). The limb field mesoderm determines initial limb bud anteroposterior asymmetry and budding independent of sonic hedgehog or apical ectodermal gene expressions. *Development*, 122(8):2319–2330.

Rovinskii, A. (1987). Turing bifurcation and stationary patterns in the ferroin-catalyzed belousov-zhabotinskii reaction. *Journal of Physical Chemistry*, 91(17):4606–4613.

Salazar-Ciudad, I., Jernvall, J., and Newman, S. A. (2003). Mechanisms of pattern formation in development and evolution. *Development*, 130(10):2027–2037.

Sanders, T. A., Llagostera, E., and Barna, M. (2013). Specialized filopodia direct long-range transport of shh during vertebrate tissue patterning. *Nature*, 497(7451):628–632.

Sanz-Ezquerro, J. J. and Tickle, C. (2003). Fgf signaling controls the number of phalanges and tip formation in developing digits. *Current biology*, 13(20):1830–1836.

Satnoianu, R. A., Menzinger, M., and Maini, P. K. (2000). Turing instabilities in general systems. *Journal of Mathematical Biology*, 41(6):493–512.

Saunders, J. W. (1948). The proximo-distal sequence of origin of the parts of the chick wing and the role of the ectoderm. *Journal of Experimental Zoology*, 108(3):363–403.

Saunders, J. W. and Gasseling, M. (1968). Ectodermal-mesenchymal interactions in the origin of limb symmetry. *Epithelial-mesenchymal interactions*, pages 78–97.

Saunders, J. W. and Reuss, C. (1974). Inductive and axial properties of prospective wing-bud mesoderm in the chick embryo. *Developmental biology*, 38(1):41–50.

Scherz, P. J., Harfe, B. D., McMahon, A. P., and Tabin, C. J. (2004). The limb bud shh-fgf feedback loop is terminated by expansion of former zpa cells. *Science*, 305(5682):396–399.

Scherz, P. J., McGlinn, E., Nissim, S., and Tabin, C. J. (2007). Extended exposure to sonic hedgehog is required for patterning the posterior digits of the vertebrate limb. *Developmental biology*, 308(2):343–354.

Schnakenberg, J. (1979). Simple chemical reaction systems with limit cycle behaviour. *Journal of Theoretical Biology*, 81(3):389–400.

Scholarpedia (1). `http://www.scholarpedia.org/article/Gierer-Meinhardt_model`.

Searls, R. L. and Janners, M. Y. (1971). The initiation of limb bud outgrowth in the embryonic chick. *Developmental biology*, 24(2):198–213.

Sharpe, J. (2011). Two ways to use imaging: focusing directly on mechanism, or indirectly via behaviour? *Current opinion in genetics & development*, 21(5):523–529.

Shoji, H. and Iwasa, Y. (2003). Pattern selection and the direction of stripes in two-dimensional turing systems for skin pattern formation of fishes. *Forma*, 18(1):3–18.

Summerbell, D. and Lewis, J. (1975). Time, place and positional value in the chick limb-bud. *Journal of embryology and experimental morphology*, 33(3):621–643.

Summerbell, D., Lewis, J., and Wolpert, L. (1973). Positional information in chick limb morphogenesis. *Nature*, 244:492–496.

Summerbell, D. and Wolpert, L. (1972). Cell density and cell division in the early morphogenesis of the chick wing. *Nature*, 239(88):24–26.

Summerhurst, K., Stark, M., Sharpe, J., Davidson, D., and Murphy, P. (2008). 3d representation of wnt and frizzled gene expression patterns in the mouse embryo at embryonic day 11.5 (ts19). *Gene Expression Patterns*, 8(5):331–348.

Sun, X., Mariani, F. V., and Martin, G. R. (2002). Functions of fgf signalling from the apical ectodermal ridge in limb development. *Nature*, 418(6897):501–508.

Suzuki, T., Hasso, S. M., and Fallon, J. F. (2008). Unique smad1/5/8 activity at the phalanx-forming region determines digit identity. *Proceedings of the National Academy of Sciences*, 105(11):4185–4190.

Szalai, I., Cuiñas, D., Takács, N., Horváth, J., and De Kepper, P. (2012). Chemical morphogenesis: recent experimental advances in reaction–diffusion system design and control. *Interface Focus*, 2(4):417–432.

Tabin, C. and Wolpert, L. (2007). Rethinking the proximodistal axis of the vertebrate limb in the molecular era. *Genes and development*, 21(12):1433–1442.

Tarchini, B., Duboule, D., and Kmita, M. (2006). Regulatory constraints in the evolution of the tetrapod limb anterior–posterior polarity. *Nature*, 443(7114):985–988.

te Welscher, P., Fernandez-Teran, M., Ros, M. A., and Zeller, R. (2002). Mutual genetic antagonism involving gli3 and dhand prepatterns the vertebrate limb bud mesenchyme prior to shh signaling. *Genes & development*, 16(4):421–426.

ten Berge, D., Brugmann, S. A., Helms, J. A., and Nusse, R. (2008). Wnt and fgf signals interact to coordinate growth with cell fate specification during limb development. *Development*, 135(19):3247–3257.

Tickle, C. (1981). The number of polarizing region cells required to specify additional digits in the developing chick wing. *Nature*, 289(5795):295.

Tickle, C. (2005). Making digit patterns in the vertebrate limb. *Nature Reviews Molecular Cell Biology*, 7(1):45–53.

Tickle, C., Alberts, B., Wolpert, L., Lee, J., et al. (1982). Local application of retinoic acid to the limb bond mimics the action of the polarizing region. *Nature*, 296:564–566.

Tickle, C., Shellswell, G., Crawley, A., and Wolpert, L. (1976). Positional signalling by mouse limb polarising region in the chick wing bud. *Nature*, 259(5542):396–397.

Tickle, C., Summerbell, D., and Wolpert, L. (1975). Positional signalling and specification of digits in chick limb morphogenesis. *Nature*, 254(5497):199–202.

Topol, L., Chen, W., Song, H., Day, T. F., and Yang, Y. (2009). Sox9 inhibits wnt signaling by promoting beta-catenin phosphorylation in the nucleus. *Journal of Biological Chemistry*, 284(5):3323–3333.

Towers, M., Mahood, R., Yin, Y., and Tickle, C. (2008). Integration of growth and specification in chick wing digit-patterning. *Nature*, 452(7189):882–886.

Turing, A. M. (1952). The chemical basis of morphogenesis. *Philosophical Transactions of the Royal Society of London, Biological Sciences*, 237(641):37–72.

Vakulenko, S., Reinitz, J., Radulescu, O., et al. (2009). Size regulation in the segmentation of drosophila: interacting interfaces between localized domains of gene expression ensure robust spatial patterning. *Physical review letters*, 103(16):168102.

Varjosalo, M. and Taipale, J. (2008). Hedgehog: functions and mechanisms. *Genes and development*, 22(18):2454–2472.

Verheyden, J. M. and Sun, X. (2008). An fgf/gremlin inhibitory feedback loop triggers termination of limb bud outgrowth. *Nature*, 454(7204):638–641.

Vogel, A., Rodriguez, C., Warnken, W., and Izpisua Belmonte, J. (1995). Dorsal cell fate specified by chick lmx1 during vertebrate limb development. *Nature*, 378(6558):716–720.

VTK (1). The vizualization toolkit. `http://www.vtk.org/`.

Waddington, C. H. (1940). *Organisers & genes*. Cambridge University Press, Cambridge.

Wan, M. and Cao, X. (2005). Bmp signaling in skeletal development. *Biochemical and biophysical research communications*, 328(3):651–657.

Weliky, M. and Oster, G. (1990). The mechanical basis of cell rearrangement. *Development*, 109(2):373–386.

White, K. A. J. and Gilligan, C. A. (1998). Spatial heterogeneity in three species, plant-parasite-hyperparasite, systems. *Philosophical Transactions of the Royal Society of London. Series B: Biological Sciences*, 353(1368):543–557.

Wikipedia (1). `http://en.wikipedia.org/wiki/Belousov%E2%80%93Zhabotinsky_reaction`.

Wilby, O. (1977). A model for the control of limb growth and development. *Vertebrate limb and somite morphogenesis*, pages 229–244.

Wilby, O. and Ede, D. (1975). A model generating the pattern of cartilage skeletal elements in the embryonic chick limb. *Journal of theoretical biology*, 52(1):199–217.

Wilkins, A. S. (2002). *The evolution of developmental pathways*. Sunderland, Massachusetts, USA: Sinauer Associates Inc.

Wolpert, L. (1968). The french flag problem: a contribution to the discussion on pattern development and regulation. *Towards a theoretical biology*, 1:125–133.

Wolpert, L. (1969). Positional information and the spatial pattern of cellular differentiation. *Journal of theoretical biology*, 25(1):1–47.

Wolpert, L. (1989). Positional information revisited. *Development*, 107(Supplement):3–12.

Wolpert, L., Clarke, M., and Hornbruch, A. (1972). Positional signalling along hydra. *Nature*, 239(91):101–105.

Wolpert, L. and Hornbruch, A. (1981). Positional signalling along the antero-posterior axis of the chick wing. the effect of multiple polarizing region grafts. *Journal of Embryology and Experimental Morphology*, 63(1):145–159.

Wolpert, L., Tickle, C., Sampford, M., and Lewis, J. (1979). The effect of cell killing by x-irradiation on pattern formation in the chick limb. *Journal of embryology and experimental morphology*, 50(1):175–198.

Wyngaarden, L. A., Vogeli, K. M., Ciruna, B. G., Wells, M., Hadjantonakis, A.-K., and Hopyan, S. (2010). Oriented cell motility and division underlie early limb bud morphogenesis. *Development*, 137(15):2551–2558.

Yi, S. E., Daluiski, A., Pederson, R., Rosen, V., and Lyons, K. M. (2000). The type i bmp receptor bmprib is required for chondrogenesis in the mouse limb. *Development*, 127(3):621–630.

Yokoyama, H., Endo, T., Tamura, K., Yajima, H., and Ide, H. (1998). Multiple digit formation in xenopus limb bud recombinants. *Developmental biology*, 196(1):1–10.

Yoon, B. S. and Lyons, K. M. (2004). Multiple functions of bmps in chondrogenesis. *Journal of cellular biochemistry*, 93(1):93–103.

Zehentner, B. K., Dony, C., and Burtscher, H. (1999). The transcription factor sox9 is involved in bmp-2 signaling. *Journal of Bone and Mineral research*, 14(10):1734–1741.

Zeller, R. (2004). It takes time to make a pinky: unexpected insights into how shh patterns vertebrate digits. *Science Signaling*, 2004(259):pe53.

Zhabotinsky, A. M. (1964). Periodical process of oxidation of malonic acid solution. *Biophysics*, (9):306–311.

Zhu, J., Nakamura, E., Nguyen, M.-T., Bao, X., Akiyama, H., and Mackem, S. (2008). Uncoupling sonic hedgehog control of pattern and expansion of the developing limb bud. *Developmental cell*, 14(4):624–632.

Zhu, J., Zhang, Y.-T., Alber, M. S., and Newman, S. A. (2010). Bare bones pattern formation: a core regulatory network in varying geometries reproduces major features of vertebrate limb development and evolution. *PLoS One*, 5(5):e10892.

Zhu, J., Zhang, Y.-T., Newman, S., and Alber, M. (2009). A finite element model based on discontinuous galerkin methods on moving grids for vertebrate limb pattern formation. *Mathematical Modelling of Natural Phenomena*, 4(04):131–148.

Zuzarte-Luis, V. and Hurle, J. M. (2005). Programmed cell death in the embryonic vertebrate limb. In *Seminars in cell & developmental biology*, volume 16, pages 261–269. Elsevier.

Zwilling, E. (1964). Development of fragmented and of dissociated limb bud mesoderm. *Developmental Biology*, 9(1):20–37.

Appendix

Important acronyms:

AER = Apical Ectodermal Ridge
AI = Activator-Inhibitor
A-P = Anterior-Posterior
Bmp = Bone Morphogenetic Protein
D-V = Dorsal-Ventral
Fgf = Fibroblast Growth Factor
LPM = Lateral Plate Mesoderm
MC = Mechanochemical
P-D = Proximal-Distal
PI = Positional Information
RA = Retinoic Acid
RD = Reaction-Diffusion
SD = Substrate-Depletion
WT = Wild Type
ZPA = Zone of Polarizing Activity